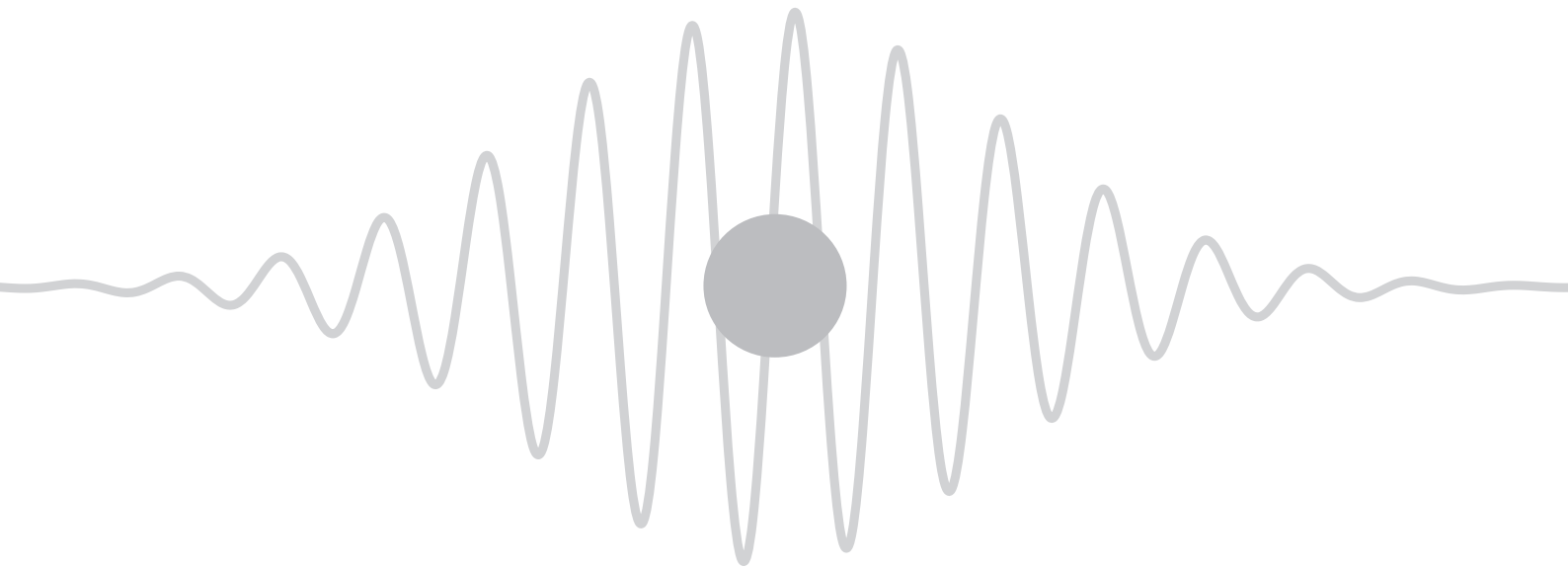


VAHID ANSARI

QUANTUM OPTICS WITH TEMPORAL MODES

QUANTUM OPTICS WITH TEMPORAL MODES



Der Naturwissenschaftlichen Fakultät
der Universität Paderborn
zur
Erlangung des Doktorgrades Dr. rer. nat.
vorgelegt von

VAHID ANSARI

ABSTRACT

The photonic time-frequency degree of freedom is a powerful resource for implementing high-dimensional quantum information processing. In particular, field-orthogonal pulsed temporal modes offer a flexible framework compatible with both long-distance fibre networks and integrated waveguide devices. In order for it to be fully utilised, techniques must be developed which can reliably generate diverse quantum states of light and accurately measure complex temporal waveforms. A promising toolbox to accomplish this is nonlinear processes driven by spectrally shaped pump pulses in group-velocity engineered waveguides. In this thesis, we show how tailoring the phasematching conditions of parametric downconversion and sum-frequency generation, as well as pulse shaping techniques, create new possibilities for generating highly pure single photons, for flexible temporal-mode entanglement, and for accurate measurement of time-frequency photon states.

ZUSAMMENFASSUNG

Die photonische Zeit-Frequenz Freiheitsgrad ist ein leistungsfähiger Werkzeug, der sich für die Implementierung hochdimensionalen Quanteninformationsverarbeitung eignet. Insbesondere die sogenannten feldorthogonalen Temporal Modes bieten einen flexiblen Rahmen, den mit sowohl Glasfasernetzen, als auch integrierte Wellenleiter-Geräte kompatibel sind. Um diese Potential vollständig auszunutzen, müssen Methoden und Techniken entwickelt werden, die in der Lage sind, diverse Quantenzustände von Licht zuverlässig zu generieren und komplexe temporale Waveforms akkurat zu messen. Ein vielversprechendes Mittel, dieses zu ermöglichen, bieten nichtlineare Prozessen an, die über spektral geformten Pump-Pulse in Gruppengeschwindigkeit-optimierten Wellenleitern angetrieben werden. In dieser Dissertation zeigen wir, wie sozusagen *maßgeschneiderte (tailored)* Phasenanpassung für die parametrischen Downconversion und Summenfrequenzerzeugung, wie auch Pulsformung-Techniken, neue Möglichkeiten erlauben bei der Produktion reiner einzelnen Photonen, sowie auch bei der flexiblen Verschränkung von Temporal Modes und akkuraten Messungen von Zeit-Frequenz-Zuständen der Photonen.

CONTENTS

I QUANTUM OPTICS WITH TEMPORAL MODES

1	INTRODUCTION	3
1.1	Temporal modes of light	3
1.2	Chronocyclic Wigner function	4
1.3	Shaping ultrashort pulses	4
1.4	Characterising ultrashort pulses	5
2	CREATING QUANTUM STATES OF LIGHT WITH CONTROLLED TEMPORAL MODES	9
2.1	Temporal-mode structure of parametric down conversion	9
2.2	Group-velocity matching for single-mode emission	12
2.3	The problem with side lobes	15
2.4	Controlled generation of temporal modes	16
3	MEASURING PHOTONIC TEMPORAL MODES OF QUANTUM STATES	23
3.1	Measurement tomography of a quantum pulse gate	26
3.2	Temporal-mode tomography and purification of quantum light	33
4	CONCLUSION AND OUTLOOK	41
	BIBLIOGRAPHY	43

II PUBLICATIONS

5	AUTHOR PUBLICATIONS AND CONTRIBUTIONS	57
5.1	Main publications	57
5.2	Other publications	58
6	OPT. EXPRESS 26(3), 2764-2774 (2018)	61
7	NAT. COMMUN. 8, 14288 (2017)	73
8	PHYS. REV. A 96, 063817 (2017)	81
9	ARXIV:1607.03001V2 (2018)	91
10	OPTICA 5 (5), 534 (2018)	103

Part I

QUANTUM OPTICS WITH TEMPORAL MODES

INTRODUCTION

1.1 TEMPORAL MODES OF LIGHT

Let us consider the temporal modes of a quanta of electric field i.e. single photons. If we neglect all degrees of freedom except time, the quantum state of a single photon in a specific temporal-mode is

$$|\psi_j\rangle = \hat{A}_j^\dagger |0\rangle, \quad (1.1)$$

where the quantum operator \hat{A}^\dagger defines the *temporal-mode* of the photon such as

$$\hat{A}_j^\dagger = \int dt \tilde{f}_j(t) \hat{A}^\dagger(t), \quad (1.2)$$

where $\tilde{f}_j(t)$ the temporal shape of the wave packet and $\hat{A}_j^\dagger(t)$ is a creation operator for a single photon at time t [11]. Although this fully describe the photon's temporal-mode, depending on the problem at hand it can be useful to express the field in the frequency domain. Through a Fourier transformation we can rewrite \hat{A}^\dagger in the frequency space as

$$\hat{A}_j^\dagger = \int \frac{d\omega}{2\pi} f_j(\omega) \hat{a}^\dagger(\omega), \quad (1.3)$$

where $f_j(\omega)$ is the complex spectral amplitude of the wave packet and $\hat{a}^\dagger(\omega)$ is the monochromatic creation operator. The operators \hat{A}_j and $\hat{a}(\omega)$ both satisfy bosonic commutation relations. With this definition, we can write the state of any single-photon in terms of superposition of temporal-modes

$$|\Psi\rangle = \sum_j c_j \hat{A}_j^\dagger |0\rangle, \quad (1.4)$$

where $\{\hat{A}_j^\dagger\}$ create a complete basis.

These temporal-modes of light accommodate a versatile resource for information encoding in quantum and classical information sciences. The description of the temporal-modes of quantum light formulated here can be easily translated to classical light, where e.g. $f_j(\omega)$ define the temporal-modes of our classical field. In any case, the information is encoded in the complex time-frequency amplitude of photons. Like spatial encodings, the Hilbert space available in the Fourier-conjugate time and frequency domains is in-principle unbounded, allowing for high-dimensional encodings. Unlike spatial encodings, time-frequency encodings are intrinsically compatible

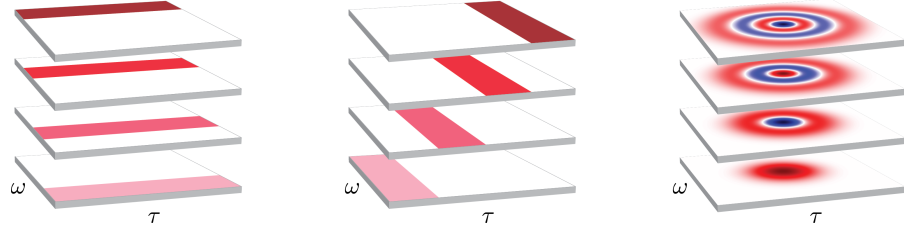


Figure 1.1: Temporal-mode encodings visualised in time-frequency space. Orthogonal temporal mode bases can be constructed through slicing bins in frequency or time, as in (a) and (b), or through intensity-overlapping but field-orthogonal waveforms, such as the Hermite-Gauss pulsed modes in (c).

with waveguides and fibre transmission. Temporal-mode bases can take on a variety of forms, such as discrete time or frequency bins or intensity-overlapping Hermite-Gaussian modes, as illustrated in Fig. 1.1, so long as the waveforms provide an orthonormal basis.

1.2 CHRONOCYCLIC WIGNER FUNCTION

A nice mathematical formalism to visualise ultrashort temporal-modes is the chronocyclic Wigner function [65]. The real-valued Wigner distribution function can be defined as

$$W(t, \omega) = \frac{1}{2\pi} \int f\left(\omega + \frac{\omega'}{2}\right) f^*\left(\omega - \frac{\omega'}{2}\right) e^{-i\omega't} d\omega'. \quad (1.5)$$

The temporal and spectral intensities of the a pulse can be easily calculated by tracing the Wigner function over the conjugate variable. In Fig. 1.1 (c) we show the Wigner function for the first four Hermite-Gaussian modes.

1.3 SHAPING ULTRASHORT PULSES

Many different experimental techniques exist for pulse shaping [62, 94, 95], where the practicality of each method depend on the required temporal resolution and the temporal duration of the pulses. In the context of this thesis, we work with ultrashort pulses of duration from 100 to 10,000 femtoseconds. Since the existing electronics technology is not fast enough to modulate such short pulses directly in time, typically frequency-domain methods are chosen to shape these pulses.

Here we use 4f-setups with a spatial light modulator (SLM) at the Fourier plane to shape the desired spectral amplitude and phase [28, 92], as outlined in Fig. 1.2. As an example, to shape pulses from a titanium:sapphire (Ti:Sa) oscillator (Coherent Chameleon Ultra II) with a central wavelength of 850 nm, our 4f-setup consist of a magnifying telescope with a magnification of three, a holographic diffraction

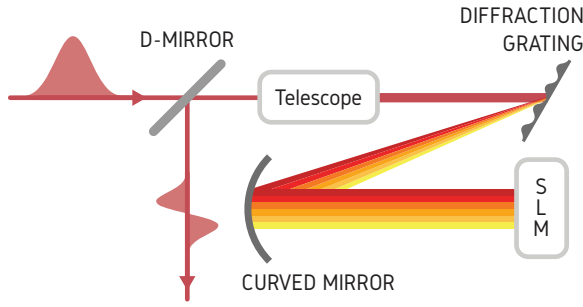


Figure 1.2: Ultrashort pulse shaping. We use a reflective spatial light modulator (SLM) in a folded 4f-setup to shape the spectral amplitude and phase of the pulses. A telescope is used to match the size of each frequency component with SLM's pixels to get an optimum resolution. The SLM reflects the beam at a slightly different angle which displaces the reflected beam vertically and allows us to collect the reflected beam with a d-shaped mirror.

grating with 2000 lines per mm, a cylindrical silver mirror with a focal length of 300 mm and a reflective liquid crystal on silicon spatial light modulator (Hamamatsu X10468-07 LCoS-SLM). This configuration provide a pulse shaper with a spectral resolution of about 33 picometres or 87 GHz which corresponds to a temporal window of about 31 picoseconds.

1.4 CHARACTERISING ULTRASHORT PULSES

Similar to pulse shaping methods, there are also many techniques developed to fully characterise optical fields [62, 87]. In the context of this thesis, we widely used spectral interferometry [27] in the alignment procedure of pulse shapers and to characterise the shaped pulses. The outline of this method is depicted in Fig. 1.3. We mix an *unknown* pulse $f(\omega) = |f(\omega)|e^{i\phi(\omega)}$ with a *known* reference pulse $f_r(\omega) = |f_r(\omega)|e^{i\phi_r(\omega)}$ with a controllable time delay τ on a beamsplitter. Then we measure the interferogram on an optical spectrometer. The obtained interferogram can be expresses as

$$\begin{aligned} I(\omega) &= |f(\omega) + f_r(\omega) e^{i\omega\tau}| \\ &= |f(\omega)|^2 + |f_r(\omega)|^2 + 2 |f(\omega)| |f_r(\omega)| \cos[\phi(\omega) - \phi_r(\omega) - \omega\tau]. \end{aligned} \quad (1.6)$$

With a complete and priori knowledge of the reference field, we can reconstruct the complex spectral field of the unknown pulse. This can be easily achieved by a Fourier analysis of the interferogram [53, 82]. In Fig. 1.4 we plot a few experimentally shaped and characterised pulses with the methods described in this chapter.

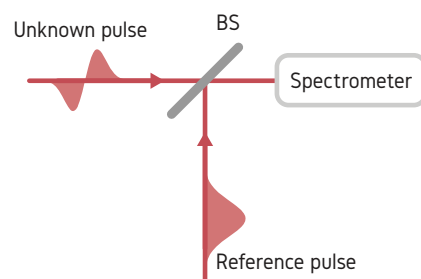


Figure 1.3: A sketch of the spectral interferometry setup. The pulse under characterisation is interfered with a known reference on a beam-splitter (BS). The beam from an output port of the beamsplitter is then measured on an optical spectrometer. Through a Fourier analysis of the interferogram, the complex spectral field of the unknown pulse can be reconstructed.

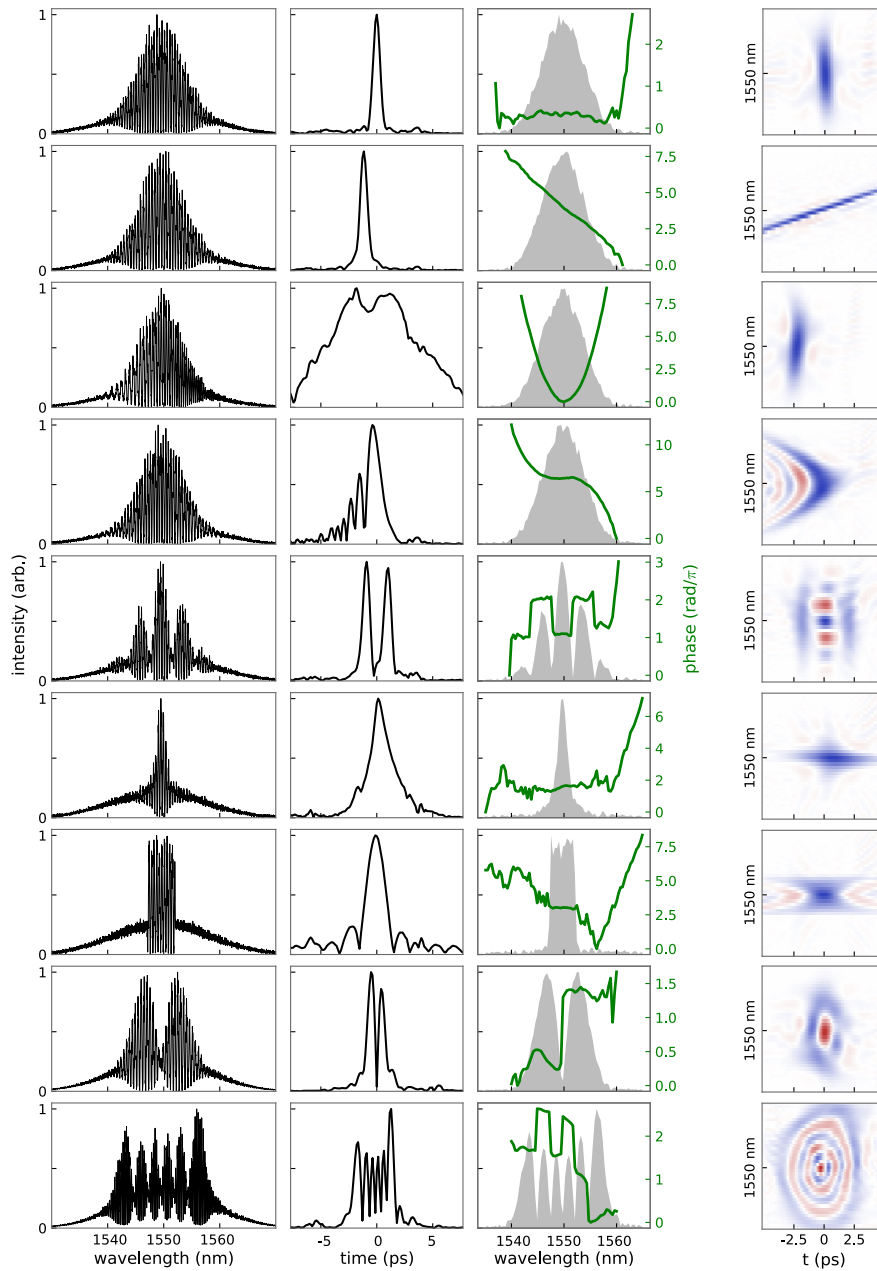


Figure 1.4: Gallery of ultrashort pulses, characterised by spectral interferometry. Columns are: $I(\omega)$ the interferogram, $\tilde{f}(t)$ the temporal profile, $f(\omega)$ the spectral amplitude and phase, and $W(t, \omega)$ the Wigner function. Rows correspond to: (a) Gaussian, (b) Gaussian with a linear phase, (c) Gaussian with a quadratic phase, (d) Gaussian with a cubic phase, (e) time-bins, (f) Lorentzian distribution, (g) boxcar function in frequency, (h) first-order Hermite-Gaussian, (i) fifth-order Hermite-Gaussian pulses.

CREATING QUANTUM STATES OF LIGHT WITH CONTROLLED TEMPORAL MODES

DECLARATION

The ideas and content presented in this chapter are partly taken from the following publications:

1. Vahid Ansari, *et al*, Opt. Express 26(3), 2764-2774 (2018).
 2. Vahid Ansari, *et al*, Optica 5, 534 (2018).
-

2.1 TEMPORAL-MODE STRUCTURE OF PARAMETRIC DOWN CONVERSION

In this section we describe the TM structure of photon-pair states generated in PDC, where a photon from a bright classical pump pulse decays with a small probability inside a nonlinear optical medium, e.g. a nonlinear waveguide, into a pair of daughter photons typically called *signal* and *idler*, as sketched in Fig. 2.1a. PDC is a well-understood process, capable of generating photons with a rich TM structure at room temperature. Moreover, PDC can be used to generate a plethora of quantum states, including heralded single photons, squeezed states, and maximally entangled states. These properties have cemented PDC as the workhorse in many quantum optics laboratories.

Restricting our model to the generation of photon pairs and assuming spatially single-mode emission, e.g. by realising the PDC in a weakly pumped waveguide, the type-II PDC process can be described by the interaction Hamiltonian

$$\hat{H}_{\text{PDC}} = \mathcal{B} \int d\omega_s d\omega_i f(\omega_s, \omega_i) \hat{a}^\dagger(\omega_s) \hat{b}^\dagger(\omega_i) + \text{h.c.}, \quad (2.1)$$

and the generated state can be written as

$$|\psi\rangle_{\text{PDC}} = \mathcal{B} \int d\omega_s d\omega_i f(\omega_s, \omega_i) \hat{a}^\dagger(\omega_s) \hat{b}^\dagger(\omega_i) |vac\rangle, \quad (2.2)$$

where $\hat{a}^\dagger(\omega_s)$ and $\hat{b}^\dagger(\omega_i)$ are standard creation operators that generate a signal photon at ω_s and an idler photon at ω_i , \mathcal{B} is the optical gain or efficiency of the process which includes the second-order nonlinearity and the pump power, and $f(\omega_s, \omega_i)$ is the complex-valued joint spectral amplitude (JSA), normalised to $\int d\omega_s d\omega_i |f(\omega_s, \omega_i)|^2 = 1$. The JSA describes the entangled time-frequency structure of the

PDC state, and is essential for describing PDC in cases with a broadband pump pulse [35].

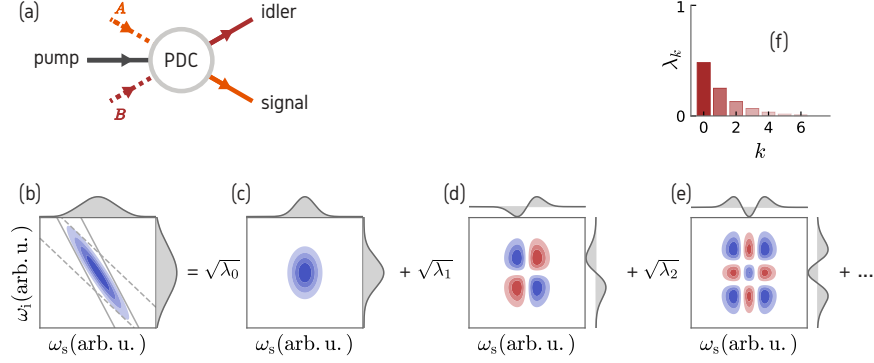


Figure 2.1: Joint spectral amplitude, temporal modes, and Schmidt coefficients of a non-engineered PDC process. (a) Outline of a PDC process with the three involved fields. (b) The JSA and its marginal distributions which is the product of pump (dashed lines) and phase-matching (solid lines) functions and, in this case, exhibits frequency anti-correlations between signal and idler frequencies. The Schmidt decomposition of this Gaussian JSA is given by Hermite-Gaussian functions, with the first three TM pairs shown in (c-e). (f) The first seven Schmidt coefficients λ_k . The decomposition of this example yields an effective mode number of $K \approx 3.14$.

The JSA itself can be written as a product of the pump envelope function $\alpha(\omega_s + \omega_i)$ and the phase-matching function $\phi(\omega_s, \omega_i)$, such that

$$f(\omega_s, \omega_i) = \alpha(\omega_s + \omega_i)\phi(\omega_s, \omega_i). \quad (2.3)$$

Here, $\alpha(\omega_s + \omega_i)$ is the slowly varying envelope of the broadband pump and reflects energy conservation during the PDC, and the phase-matching $\phi(\omega_s, \omega_i)$ expresses the momentum conservation between involved fields and the dispersion properties of nonlinear medium. The phase-matching function can be written as

$$\phi(\omega_s, \omega_i) = \int_0^L dz \chi(z) \exp [i\Delta k(\omega_s, \omega_i)z], \quad (2.4)$$

where $\Delta k(\omega_s, \omega_i) = k_p(\omega_s + \omega_i) - k_s(\omega_s) - k_i(\omega_i)$ is the phase mismatch, L is the length of the nonlinear medium, and $\chi(z) = \pm 1$ describes the orientation of the ferroelectric domains of the crystal. A periodic modulation of $\chi(z)$, with a period Λ , is called *periodic poling*[41]. This poling adds an additional component of the form $k_{\text{QPM}} = 2\pi/\Lambda$ to the phase mismatch such that $\Delta k(\omega_s, \omega_i) \mapsto \Delta k(\omega_s, \omega_i) + 2\pi/\Lambda$, allowing the center frequencies of the phase-matched process to be tuned. In this case, the resulting phase-matching function is given by

$$\phi(\omega_s, \omega_i) = \frac{1}{L} \text{sinc} \left(\frac{\Delta k(\omega_s, \omega_i)L}{2} \right) e^{i\Delta k(\omega_s, \omega_i)\frac{L}{2}}. \quad (2.5)$$

The sinc profile of the phasematching function has significant implications which will be discussed in Section 2.3. However, to simplify the equations and plots in this thesis, we usually employ a Gaussian approximation of the phasematching function.

In 2000, Law and co-workers examined the time-frequency structure of the JSA through the *Schmidt decomposition*, defining two-photon entanglement in terms of temporal modes [51]. For this, the JSA is decomposed into two sets of orthonormal basis functions $\{g^{(s)}\}$ and $\{h^{(i)}\}$ for signal and idler, and we write

$$f(\omega_s, \omega_i) = \sum_k \sqrt{\lambda_k} g_k^{(s)}(\omega_s) h_k^{(i)}(\omega_i), \quad (2.6)$$

where $\sum_k \lambda_k = 1$. With this we define broadband TM operators

$$\hat{A}_k^\dagger = \int d\omega_s g_k^{(s)}(\omega_s) \hat{a}^\dagger(\omega_s), \quad (2.7)$$

$$\hat{B}_k^\dagger = \int d\omega_i h_k^{(i)}(\omega_i) \hat{b}^\dagger(\omega_i), \quad (2.8)$$

and consequently obtain

$$|\psi\rangle_{\text{PDC}} = \sum_k \sqrt{\lambda_k} \hat{A}_k^\dagger \hat{B}_k^\dagger |0\rangle. \quad (2.9)$$

This means that a PDC photon pair is generated in the k -th TM pair with a probability of λ_k . An example of a typical JSA together with its Schmidt decomposition is given in Fig. 2.1b. For a typical Gaussian JSA, the Schmidt modes are given by Hermite-Gauss functions, which overlap in both spectral and temporal intensity. Note that the Schmidt decomposition holds only if the global two-photon state is itself pure, and is not general for multipartite scenarios [39].

The Schmidt decomposition of the joint spectral amplitude provides an essential link between the continuous time-frequency description and a discretised temporal-mode picture. Such a transition is necessary for describing mode-multiplexed systems, where each Schmidt mode can be thought of as an independent information carrier. Such multiplexed systems are useful for communication networks [29] and essential to generate highly entangled cluster states for measurement-based quantum computation [60, 97], where utilising the time-frequency domain allows for operations to take place in a single spatial mode.

In the low-gain PDC regime, the Schmidt decomposition of the JSA can be linked directly to the amount of time-frequency entanglement present in the two-photon system. The Schmidt number, defined as $K = 1/\sum_k \lambda_k^2$, quantifies the effective number of TM pairs required to describe the properties of the generated state, with $K = 1$ for a single-mode (separable) state and $K \gg 1$ for a multimode (entangled) state. The Schmidt number is related to the spectral purity of the

individual signal photons generated, which are generally described by the mixed density matrix

$$\hat{\rho}_s = \text{Tr}_i(\hat{\rho}_{\text{PDC}}) = \sum_k \lambda_k |A_k\rangle\langle A_k| \quad (2.10)$$

with a purity of

$$\mathcal{P}_s = \text{tr}(\hat{\rho}_s^2) = \frac{1}{K}. \quad (2.11)$$

For PDC-generated photons, this quantity is directly experimentally accessible through the marginal second-order correlation function (i.e. unheralded signal photons) as $g^{(2)}(0) = 1 + \mathcal{P}_s$ [16, 24].

In summary, we have introduced the continuous time-frequency structure of PDC and connected it to the discrete TM picture through the Schmidt decomposition. Such analysis naturally describes the two-photon entanglement from PDC and the spectral purity of the generated photons. In most configurations, PDC generates highly correlated states with a large Schmidt number, yielding low-purity heralded photons if no additional spectral filtering is applied. We will shift our focus in the next section to how proper engineering of the PDC process can overcome this limitation and facilitate the direct generation of pure single photons.

2.2 GROUP-VELOCITY MATCHING FOR SINGLE-MODE EMISSION

Although multimode PDC states with usual frequency correlations, as shown in Fig. 2.1, have found many applications in quantum sciences [31, 63], full control over the modal structure of the PDC state would make a new range of applications possible. For example, high-visibility quantum interference between distinct nodes in a photonic network requires pure PDC sources, i.e. sources that emit in a single temporal mode. Without dispersion engineering, intrinsic frequency anti-correlations between signal and idler are imposed by energy conservation of the pump, reflected by the -45° angle of the pump function in the joint spectral amplitude (see Fig. 2.1), resulting in highly multimode systems. To realise single-mode PDC, researchers have tailored the phasematching function to produce separable JSAs, allowing for high-quality heralded photons without any need for additional spectral filtering.

At the turn of the millennium, several groups studied the spectral characteristics of PDC photon pairs and identified a connection between the photon spectra and the dispersion of the nonlinear medium [26, 32, 44]. It was shown that with a properly selected non-linear material, polarisations, and photon central frequencies the frequency correlations between the signal and idler photons can be eliminated [34]. Later this work was further developed in [89], where the authors

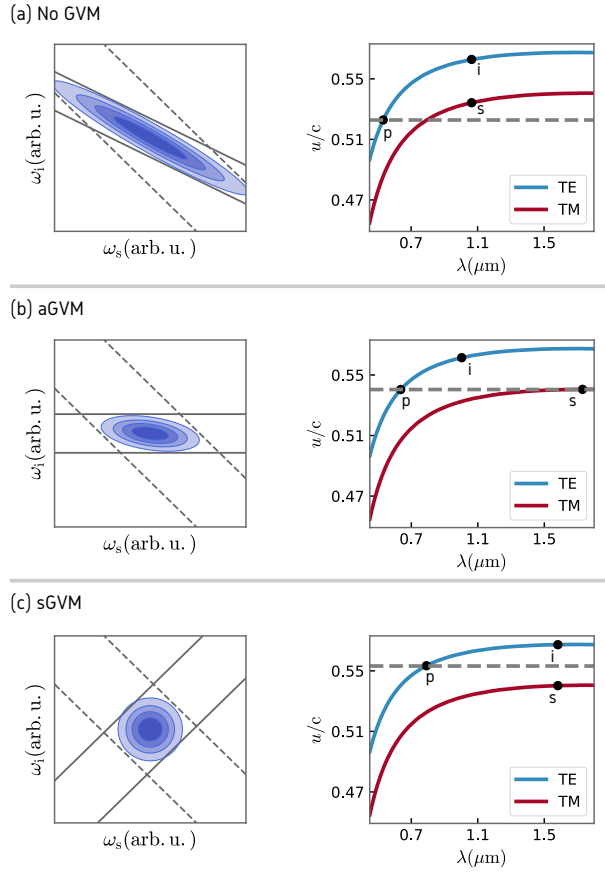


Figure 2.2: Three different group-velocity matching condition. The JSA of each case is plotted on the left side, with the respective group velocities u_j of the pump, signal, and idler fields plotted on the right side. The group velocities (normalised over the speed of light in vacuum) are exemplary for TE and TM-polarised light in a z-cut potassium titanyl phosphate (KTP). (a) Typically without dispersion engineering, the long-wavelength signal and idler photons both have a larger group velocity than the pump ($\xi > 0$). This leads to a negative phasematching angle and consequently to a correlated JSA as shown on the left. In this example, $\xi \approx 0.4$. (b) In the case of aGVM ($\xi \rightarrow 0$), one photon (here the signal) propagates at the same velocity as the pump. This yields a phasematching function that is aligned with the signal or idler frequency axis. If the pump spectral bandwidth is larger than the phasematching bandwidth, a separable JSA is generated. (c) For sGVM ($\xi \rightarrow -1$), the group velocity of the pump lies between the group velocities of signal and idler. This leads to a $+45^\circ$ phasematching angle and, given that the pump spectral bandwidth matches the phasematching bandwidth, a separable JSA with potentially indistinguishable signal and idler.

showed that the relationship between the group-velocities of interacting fields plays an essential role to tailor the phasematching function $\phi(\omega_s, \omega_i)$ and consequently the JSA.

To understand the underlying physics, we perform a Taylor expansion of the phase mismatch (defined in Sec. 2.1) up to the first order. Assuming that the process is perfectly phasematched at the center frequencies and that dispersion through the nonlinear medium is negligible, we obtain

$$\Delta k(\omega_s, \omega_i) \approx (u_s^{-1} - u_p^{-1})\omega_s + (u_i^{-1} - u_p^{-1})\omega_i, \quad (2.12)$$

where the $u_j \equiv \frac{\partial \omega_j}{\partial k_j}$ are the group-velocities of the pump, signal, and idler fields. In this context, it is useful to define the group-velocity-mismatch contrast ζ as

$$\zeta = \frac{u_s^{-1} - u_p^{-1}}{u_i^{-1} - u_p^{-1}}. \quad (2.13)$$

The group-velocity mismatch contrast is related to the angle of the phasematching function in the (ω_s, ω_i) -plane by $\theta_{\text{PM}} = -\arctan(\zeta)$ [89].

Among all possible group-velocity arrangements, two special cases received particular attention. In the first case, dubbed *asymmetric group-velocity matching* (aGVM), the pump propagates with the same group velocity as either the signal photon ($\zeta \rightarrow 0$) or the idler photon ($\zeta \rightarrow \infty$). If the pump is group-velocity matched to the signal photon, the JSA from Eq. (2.3) is reduced to

$$f(\omega_s, \omega_i) \approx \alpha(\omega_s + \omega_i)\phi(\omega_i). \quad (2.14)$$

As seen in Fig. 2.2(b), as the phasematching bandwidth shrinks to be much narrower than the pump bandwidth, the JSA becomes more and more separable. The single-modedness of the system can be increased by using wider pump bandwidths or tightening the phasematching function with longer nonlinear interactions [89]. In this scenario, the signal and idler photon will have drastically different spectral bandwidths.

In the second case, the group velocity of the pump is exactly between the group velocities of signal and idler ($\zeta \rightarrow -1$), referred to as *symmetric group-velocity matching* (sGVM) or *extended phasematching*, which results in a JSA of the form

$$f(\omega_s, \omega_i) \approx \alpha(\omega_s + \omega_i)\phi(\omega_s - \omega_i). \quad (2.15)$$

As seen in Fig. 2.2(c), if the phasematching bandwidth equals the pump bandwidth, the JSA is a perfectly separable circle, allowing for pure single photons with identical spectral properties. This phasematching configuration also allows for two-photon states with positive spectral correlations (and negative temporal correlations) when

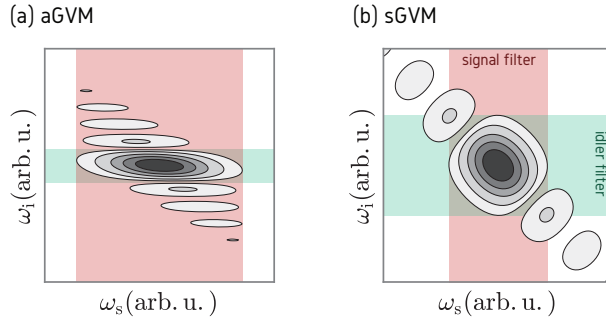


Figure 2.3: Joint spectral amplitudes (absolute value) with standard periodic poling and filters on the individual photons. (a) In an aGVM source, the idler can be filtered to remove the side lobes and herald pure signal photons. However, filtering on the signal arm cannot be used to remove the side lobes. (b) In sGVM sources, the JSA is symmetric. Filtering either signal or idler leaves the other with a purity of about 94%.

the pump is broader than the phasematching function [24, 49, 56], useful for certain quantum synchronisation and dispersion-cancellation techniques.

2.3 THE PROBLEM WITH SIDE LOBES

To put these results into context, we next consider the limitations imposed by the phasematching function in Eq. 2.5. In Fig. 2.3, we plot the JSAs resulting from this phasematching function, along with possible broadband spectral filtering. It becomes immediately obvious that the side lobes of the sinc-shaped phasematching function introduce undesired frequency anti-correlations, limiting the maximum purity of heralded photons to around 86% in the sGVM case. With filters chosen to transmit the main peak of the JSA but block as many of the correlated side lobes as possible, it is possible to increase the source performance, but limitations are still present. In the case of aGVM depicted in Fig. 2.3(a), the idler filter can be chosen to be much narrower than the signal filter. In this example, if the idler is filtered and serves as a herald, the maximum purity for the heralded signal increases to 97%. In contrast, if the signal is filtered and serves as a herald, the heralded idler photon has a maximum purity of about 92%. Note that this value can be increased with a larger pump bandwidth. In the sGVM example shown in Fig. 2.3(b), the signal and idler photons are indistinguishable, and the filtering shown in either case leaves the other photon with a purity of about 94% when heralded. We note that these numbers can be further increased when choosing smaller filter bandwidths at the cost of decreased heralding rates [61, 88].

2.4 CONTROLLED GENERATION OF TEMPORAL MODES

Finally we want to highlight two possibilities to accurately control the generated PDC state beyond separability. For applications that exploit TMs as encoding basis, the targeted generation of states with a user-defined TM structure is highly desirable. Complementary techniques arise for PDC state engineering through spectrally shaping the pump pulse in aGVM and sGVM sources, the former providing pure shaped single photons while the latter provides flexible sources for high-dimensional TM entanglement.

In the aGVM case, as seen in Eq. 2.14, the spectrum of the idler photon is nearly entirely dependent on the phasematching while the spectrum of the signal photon is dependent on the shape of the pump. By manipulating the spectral shape of the pump, the shape of the signal photon can be programmed on-the-fly, as seen in Fig. 2.4(a-c). So long as the phasematching is narrow relative to the finest features of the desired spectral shape, the JSA remains separable.

In the following, we utilise a aGVM phasematching based on the in-house fabricated unpoled KTP waveguides and emits in the near-infrared telecommunications regime. we generate heralded photons which inherit the temporal shape of the pump pulse.

To measure joint spectral intensity (JSI) distribution $|f(\omega_s, \omega_i)|^2$, we combine a monochromator in the idler arm with a time-of-flight spectrometer in the signal arm [7]. In the time-of-flight spectrometer we use a highly dispersive fibre to map the spectrum into the temporal profile which can be resolved directly in time on SNSPDs. We use a 4.3 km long fibre with a total dispersion of 0.3 ns/nm which, alongside with 70 ps timing resolution of SNSPD, constitute a spectrometer with a resolution of about 0.2 nm. The measured JSIs with the pump field in the first four Hermite-Gauss modes and five frequency bins are plotted in Fig. 2.5. The Schmidt number inferred from these JSIs shows a spectral purity of more than 0.98, which provides an upper bound on the spectral purity.

As discussed in the theory section, spectral correlations between PDC photons leads to impurity of the heralded single photons. Although the JSI measurement provide important information about the spectral correlation of the PDC photons, it is blind to the spectral phase of the photons and is also limited by the resolution of the spectrometers. A better measure of any underlying correlations of the PDC photons is the second-order correlation function $g^{(2)}(0)$ of signal or idler photons, as measured with a 50/50 fibre coupler [16, 85]. The $g^{(2)}(0)$ measurement probes the photon number statistics of unheralded beams (signal or idler) and can discriminate between a single-mode PDC state with $g^{(2)}(0) = 2$ and a highly multimode state with $g^{(2)}(0) = 1$. In Fig. 2.6 we plot the $g^{(2)}(0)$ of the both PDC photons with the pump pulse in different orders of

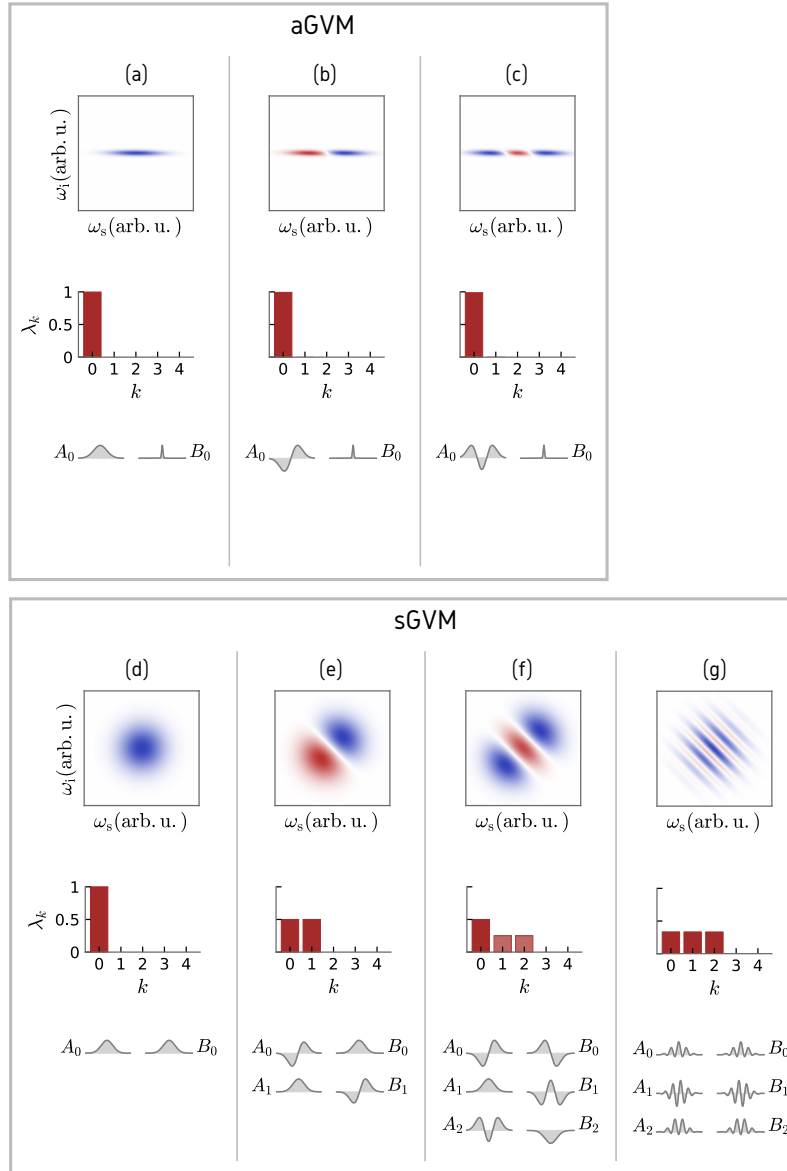


Figure 2.4: Orchestrating Schmidt modes via group-velocity matching and pump pulse shaping. (a-c) JSAs for a PDC source with an aGVM setting. The weights of the first five Schmidt modes λ_k are shown under each JSA. The state remains single-mode regardless of the pump shape. The only significant Schmidt modes of signal A_0 and idler B_0 photons are shown at the bottom. The idler photon shape is invariant to the pump, while the TM of the signal photon reflects the TM of the pump field. (e-g) A sGVM PDC can be used to control the exact number of excited temporal modes. For example, driving the source with a first-order Hermite-Gaussian pump pulse as in (e) results in exactly two TMs. This can be extended with higher orders of Hermite-Gaussian pulses as in (f), but different Schmidt modes are not occupied with a same probability. A balanced Schmidt mode distribution can be achieved when the source is pumped with time-bin superpositions, as in (g).

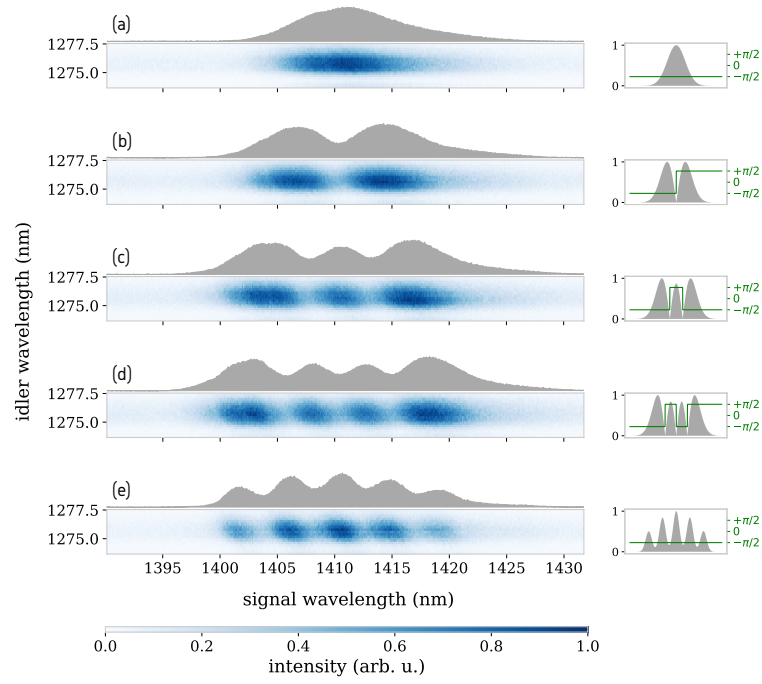


Figure 2.5: A few examples of the measured joint spectral intensities (JSIs), with the marginal spectral distribution of signal photon above in grey. The pump mode for each JSI is shown on the right side, where the grey shaded area is the spectral amplitude and the green line is the spectral phase. The pump modes are as the following: (a) Gaussian, (b) 1st-order Hermite-Gaussian, (c) 2nd-order Hermite-Gaussian, (d) 3rd-order Hermite-Gaussian, (e) frequency bins, with Schmidt numbers: $K_a = 1.01$, $K_b = 1.01$, $K_c = 1.02$, $K_d = 1.02$, $K_e = 1.02$.

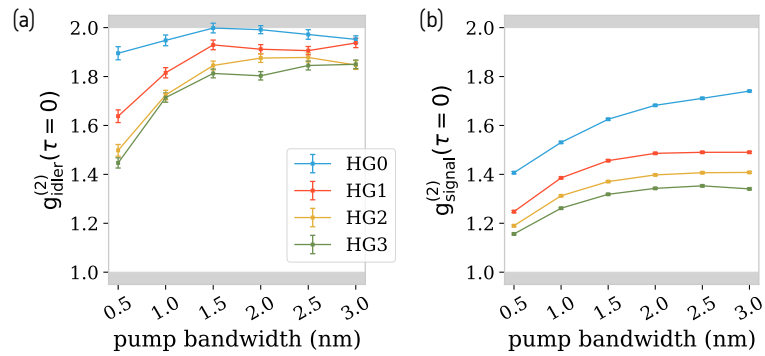


Figure 2.6: The second-order correlation measurements of the idler and signal photons with the pump set to different bandwidths and different orders of Hermite-Gaussian modes. The error bars for the $g_{\text{signal}}^{(2)}(\tau = 0)$ are smaller than the markers.

Hermite-Gauss modes and bandwidths ranging from 0.5 nm to 3 nm. With a narrow pump bandwidth, energy correlations remain in the PDC state which are exhibited in lower $g^{(2)}(0)$ values. For the idler photon, we spectrally filter the asymmetric phasematching side-lobes (see Fig. 2.3), and we achieve the highest $g^{(2)}(0)$ of 1.99 ± 0.02 with a 1.5 nm broad Gaussian pump pulse, which reduces to 1.93 ± 0.02 , 1.85 ± 0.02 , and 1.81 ± 0.02 for the first, second, and third order Hermite-Gauss modes, respectively. This reduction in the $g^{(2)}(0)$ value is also expected from theory. With increasing order of Hermite-Gauss modes, these function feature more complex structures spanned over a broader frequency range which inevitably increases the frequency anti-correlations between signal and idler (see Fig. 2.1(a)). Despite this, it is possible to achieve a high purity with an appropriately designed crystal length.

The $g^{(2)}(0)$ of signal photons, plotted in Fig. 2.6(b), is considerably lower. This is due to the presence of the phasematching side-lobes which cannot be simply filtered for the signal photons (see Fig. 2.3(b)). While the signal photons are themselves less pure, the high $g^{(2)}(0)$ of the idler indicates that the shaped signal photons are highly pure when heralded by an idler detection. However, this purity comes at a cost of heralding efficiency. Enhancing the waveguide fabrication technology or using methods such as noncritical phasematching [54] or aperiodic poling [22, 33] may be able to eliminate these unwanted spectral features to produce filter-free heralded photons with high purities and arbitrary temporal shapes.

On the other hand, PDC states that comprise a user-defined number of TMs can be generated in the sGVM configuration. Again, this is achieved by spectral shaping of the pump pulses. One example of this is a PDC driven by a pump pulse with a first-order Hermite-Gaussian spectrum [11], as depicted in Fig. 2.4(e). In this case, the generated state is a TM Bell-state of the form

$$|\psi\rangle_{\text{Bell}} = \frac{1}{\sqrt{2}} (|0\rangle_s |1\rangle_i + e^{i\varphi} |1\rangle_s |0\rangle_i), \quad (2.16)$$

where $|0\rangle_j$ ($|1\rangle_j$) labels the j photon occupying a Gaussian (first-order Hermite-Gaussian) spectrum and $j=(s,i)$. To add additional TMs to this state, it is sufficient to increase the order of the Hermite-Gaussian spectrum of the pump pulse, which is easily achieved with conventional pulse shaping [94]. Although this provides a state with finite number of Schmidt modes, the generated TMs are generally not equally occupied (i.e. they can have different $\sqrt{\lambda_k}$) [11], and thus the generated TMs are not maximally entangled. Another alternative pump shape to control the Schmidt modes is superposition of time bins or, equivalently, cosine functions in the frequency domain, as shown in Fig. 2.4(g) [64]. This provides a flexible and versatile source that generates maximally entangled states with an arbitrary dimension without the need for changing any hardware. In Fig. 2.7, we plot

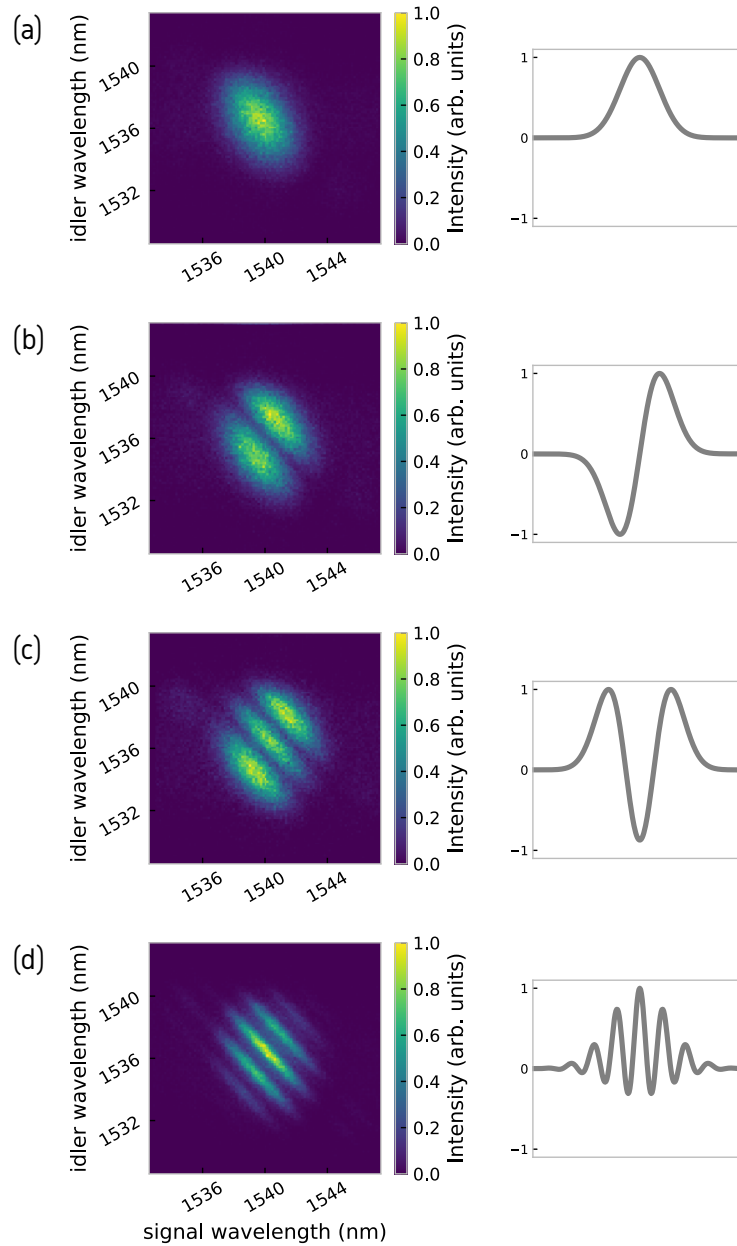


Figure 2.7: Examples of the measured joint spectral intensities (JSIs), for sGVM PDC. The pump mode for each JSI is shown on the right side; (a) Gaussian, (b) 1st-order Hermite-Gaussian, (c) 2nd-order Hermite-Gaussian, (d) superposition of cosine functions with a Gaussian envelope.

a few experimentally measured PDC JSIs, created under sGVM in a ppKTP waveguide [5, 36].

To conclude, PDC state engineering is now at a point where we can exert close-to arbitrary control over the TM structure of the generated state. This brings into reach the realisation of TM based QIP applications and provides us with a very clean laboratory system for the generation of Hilbert spaces with well-defined dimensions.

MEASURING PHOTONIC TEMPORAL MODES OF QUANTUM STATES

DECLARATION

The ideas and content presented in this chapter are partly taken from the following publications:

1. Vahid Ansari, *et al*, Phys. Rev. A 96, 063817 (2017).
 2. Vahid Ansari, *et al*, arXiv:1607.03001v2 (2018).
 3. Markus Allgaier, *et al*, Nat. Commun. 8, 14288 (2017).
 4. Vahid Ansari, *et al*, Optica 5, 534 (2018).
-

With the ability to generate single photons in arbitrary TMs, the next step for complete TM-based QIP is a quantum device capable of accessing a TM out of a multimode input. In other words, we require a special quantum mechanical beam splitter that operates on a customisable basis of TMs. A promising tool to build such a device is engineered frequency conversion.

Frequency conversion (FC) has been recognised as means to translate the central frequency of a photonic quantum state while preserving its non-classical signatures. The first proposal in 1990 considered the frequency-translation of squeezed states of light[47]. Different experiments have since confirmed that FC retains the quadrature squeezing[9, 40, 55, 93], quantum coherence and entanglement[19, 38, 70, 84], the anti-bunching of single photons[6, 98], and non-classical photon correlations[59, 69]. Since FC can be highly efficient[67, 90, 91], it provides a useful tool for improved detection schemes[1, 50, 52, 77, 86] and an interface for dissimilar nodes in future quantum networks[15, 18, 20, 30, 42, 43, 48, 58, 78, 81, 83].

However, there is more to frequency conversion. In 2010, Raymer and co-workers proposed an interpretation of FC as a two-colour beam splitter[71], enabling for example Hong-Ou-Mandel interference[37] of photons of different colour. If the FC is set to 50% efficiency, and if two monochromatic photons which are centred at the two linked frequencies (red and blue) are sent into the process, simultaneous SFG/DFG occurs and both photons will exit the FC either at the blue frequency or the red frequency. The conversion process links the two frequency bands in a beamsplitter fashion, as has been demonstrated with single-photon signals exhibiting Ramsey interference[17] and two-colour Hong-Ou-Mandel interference[45].

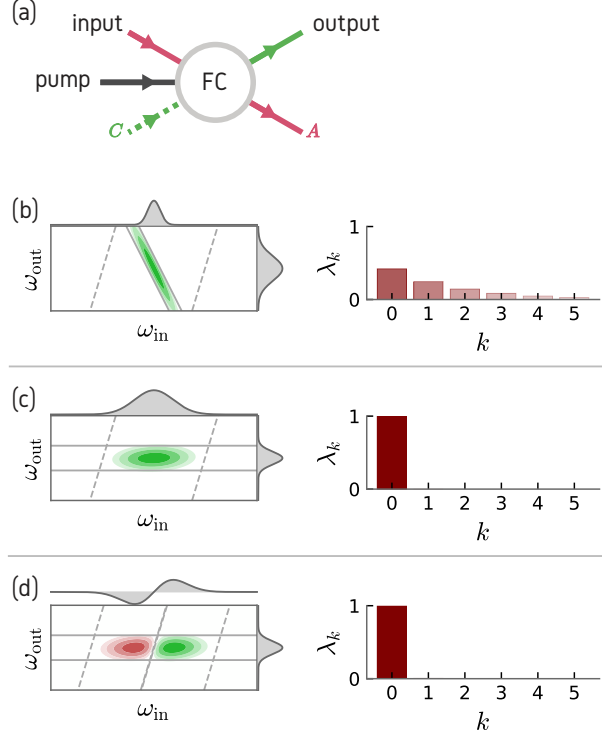


Figure 3.1: Frequency conversion process and its transfer function. (a) Outline of a general frequency conversion process with pump, input and output fields. (b to d) Sum-frequency conversion transfer functions $F(\omega_{\text{in}}, \omega_{\text{out}})$ with its marginal distributions (left) and its first few Schmidt coefficients $\sqrt{\lambda_k}$. (b) A non-engineered SFG with significant frequency correlations and a $K \approx 3.7$. (c) and (d) present a tailored SFG process with aGVM condition with pump functions $a(\omega_{\text{out}} - \omega_{\text{in}})$ of Gaussian and first-order Hermite-Gauss, respectively, and a $K \approx 1.01$.

Inspired by the previously outlined work in PDC engineering, the mode structure of FC can be tailored through dispersion engineering. It turns out that a configuration that is similar to asymmetric group-velocity matching facilitates single-mode operation: when the input signal propagates through the nonlinear medium at the same velocity as the bright pump but the output is group-velocity mismatched, one specific TM is selected and converted to the output frequency, while all other TMs are simply transmitted[23]. The single-mode FC has been dubbed the *quantum pulse gate* (QPG) to reflect that it selects, or gates, one broadband TM.

In the following we briefly outline the QPG formalism. The interaction Hamiltonian that describes a general FC process is given by

$$\hat{H}_{\text{int}} = \theta \int d\omega_{\text{in}} d\omega_{\text{out}} F(\omega_{\text{in}}, \omega_{\text{out}}) \hat{a}(\omega_{\text{in}}) \hat{c}^\dagger(\omega_{\text{out}}) + \text{h.c.}, \quad (3.1)$$

where \hat{a} and \hat{c} are annihilation operators in the input and upconverted modes, respectively, and θ is a coupling of the process incorporating the power of the QPG pump and the strength of the material nonlinearity. The *transfer function* $F(\omega_{\text{in}}, \omega_{\text{out}})$ describes the mapping from input to output frequencies, analogous to the JSA in PDC processes. The transfer function, as in the case of PDC, is a product of pump amplitude and phasematching

$$F(\omega_{\text{in}}, \omega_{\text{out}}) = \alpha(\omega_{\text{out}} - \omega_{\text{in}})\phi(\omega_{\text{in}}, \omega_{\text{out}}). \quad (3.2)$$

Similar to PDC, we can apply a Schmidt decomposition to the mapping function and define our operators in the TM basis, obtaining

$$\hat{H}_{\text{int}} = \theta \sum_{k=0}^{\infty} \sqrt{\lambda_k} \hat{A}_k \hat{C}_k^\dagger + \text{h.c.}, \quad (3.3)$$

with $\sum_k \lambda_k = 1$. Despite the similarity to the Schmidt decomposition of the PDC state as formulated in Eq. (3.3), there is a fundamental difference in the meaning of the decomposition and the Schmidt modes in each case. While the PDC decomposition expresses the modes of a *state*, in the case of the FC we have a *SFG operation*. The Hamiltonian in Eq. (3.3) generates operator transformations

$$\hat{A}_k \rightarrow \cos(\sqrt{\lambda_k}\theta) \hat{A}_k + \sin(\sqrt{\lambda_k}\theta) \hat{C}_k, \quad (3.4)$$

$$\hat{C}_k \rightarrow \cos(\sqrt{\lambda_k}\theta) \hat{C}_k - \sin(\sqrt{\lambda_k}\theta) \hat{A}_k. \quad (3.5)$$

These can be interpreted as k independent beam splitters with reflectivities $\sin^2(\sqrt{\lambda_k}\theta)$, which connect the input \hat{A}_k to an output \hat{C}_k .

As previously derived for PDC, the phasematching function can be written in terms of the group-velocity mismatch, $\Delta k(\omega_{\text{in}}, \omega_{\text{out}})$. Assuming that the nonlinear medium is periodically poled to ensure phasematching at the centre frequencies, this phase mismatch can be written to first order in analogy to Eq. 2.12 as

$$\Delta k(\omega_s, \omega_i) \approx (u_{\text{in}}^{-1} - u_{\text{p}}^{-1})\omega_{\text{in}} - (u_{\text{out}}^{-1} - u_{\text{p}}^{-1})\omega_{\text{out}}. \quad (3.6)$$

For the case of asymmetric group-velocity matching (aGVM) case where the input signal propagates at the same velocity as the pump ($u_{\text{in}} = u_{\text{p}}$), the first-order phasematching function is only dependent on the up-converted frequency $\phi(\omega_{\text{in}}, \omega_{\text{out}}) \approx \tilde{\phi}(\omega_{\text{out}})$. If the phasematching is spectrally narrow enough that the output frequency spread is negligible compared to the input, the contribution of the pump field is approximately dependent on only the central frequency of the up-converted field, $\alpha(\omega_{\text{out}} - \omega_{\text{in}}) \approx \tilde{\alpha}(\omega_{\text{in}})$. If these approximations hold, the transfer function can be rewritten simply as

$$F(\omega_{\text{in}}, \omega_{\text{out}}) \approx \tilde{\alpha}(\omega_{\text{in}})\tilde{\phi}(\omega_{\text{out}}). \quad (3.7)$$

As the phasematching function tightens, the transfer function becomes more and more separable, as illustrated in Fig.3.1(c,d).

For a separable transfer function, the Schmidt decomposition yields only one single non-zero Schmidt coefficient and the interaction Hamiltonian reduces to the desired QPG Hamiltonian,

$$\hat{H}_{\text{QPG}} = \theta \hat{A}_0 \hat{C}_0^\dagger + \text{h.c.} \quad (3.8)$$

and we obtain the following operator transformations

$$\hat{A}_0 \rightarrow \cos(\theta) \hat{A}_0 + \sin(\theta) \hat{C}_0, \quad (3.9)$$

$$\hat{C}_0 \rightarrow \cos(\theta) \hat{C}_0 - \sin(\theta) \hat{A}_0, \quad (3.10)$$

$$\hat{A}_k \rightarrow \hat{A}_k \text{ for } k \neq 0, \quad (3.11)$$

$$\hat{C}_k \rightarrow \hat{C}_k \text{ for } k \neq 0. \quad (3.12)$$

Hence, the ideal QPG selects one single input TM and converts it to an output TM with an efficiency of $\sin^2(\theta)$, while all orthogonal TMs pass through the QPG unconverted and undisturbed. The selected input TM \hat{A}_0 is defined by the shape of the bright pump pulse that drives the conversion ($\tilde{\alpha}(\omega_{\text{in}})$), whereas the shape of the output TM \hat{C}_0 is given by the envelope of the phasematching function ($\tilde{\phi}(\omega_{\text{out}})$) [12, 23]. By shaping the spectral amplitude and phase of the QPG pump pulse, the mode selected by the QPG can be adapted on-the-fly. While most works have motivated the QPG towards Hermite-Gauss TMs, it can also be set to select arbitrary superpositions as well as entirely different mode bases (e.g. time-frequency bins) by reshaping the pump pulse. While other group-velocity conditions exist which enable nearly single-mode sum-frequency generation, the aGVM case outlined here has been shown to be optimal [72].

An ideal QPG operation, as described in Eq. (3.8), requires a perfect GVM between the pump and input. To quantify this, we can redefine the group-velocity mismatch contrast, was introduced in Eq. (2.13), as

$$\tilde{\zeta} = \frac{u_{\text{in}}^{-1} - u_{\text{p}}^{-1}}{u_{\text{out}}^{-1} - u_{\text{p}}^{-1}}. \quad (3.13)$$

A aGVM condition between the pump and input fields means $\tilde{\zeta} \rightarrow 0$. This definition can help us to study the feasibility of building a QPG in different non-linear materials with different dispersion properties.

3.1 MEASUREMENT TOMOGRAPHY OF A QUANTUM PULSE GATE

Recently, quantum pulse gate (QPG) devices have been demonstrated by several groups by employing dispersion-engineered frequency conversion between a strong shaped driving pump field and a coherent signal state at single-photon level intensities [14, 57, 68, 73, 80] or with heralded single photons from a parametric down-conversion source

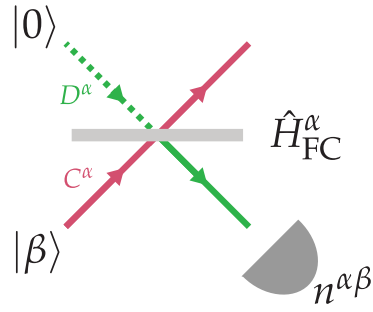


Figure 3.2: Outline of QPG operation. The QPG is a beamsplitter operating on a TM defined by the index α . For the measurement tomography, we send coherent states $|\beta\rangle$ to the QPG and at the converted (reflected) port we measure the number of converted photons using a bucket detector, noted as $n^{\alpha\beta}$.

[5]. In these experiments, TM selectivity with reasonable efficiencies has been shown, but the coherences between all possible TMs have not been investigated in detail. This is, however, an essential ingredient for the realisation of any application based on a high-dimensional alphabet rather than on simple add/drop-type multiplexing of information channels. An easy example is polarisation tomography, where measurements have to be carried out in all three mutually unbiased bases (MUBs) — horizontal/vertical, diagonal/anti-diagonal, right-circular/left-circular — in order to retrieve full information on the state under investigation.

Here, we reconstruct all measurement operators of a QPG operating on both a five-dimensional and seven-dimensional TM Hilbert space. Our QPG is based on dispersion-engineered sum-frequency generation in a titanium-indiffused lithium niobate waveguide, and we use sets of weak coherent states which span a tomographically complete set of MUBs to characterise the device. Afterwards, we use the retrieved measurement operators of our QPG to perform TM state tomography of randomly chosen TM states in an up to seven-dimensional Hilbert space with average fidelities of 0.99. This combines, for the first time, the necessary ingredients for high-dimensional QIS with single-photon TMs and paves the way towards future applications of this technology.

The outline of our experiment is shown in 3.2. The QPG is implemented through a type-II sum-frequency process in an in-house built 17 mm LiNbO_3 crystal with titanium indiffused waveguides and a poling period of $4.4 \mu\text{m}$. Further experimental details are given in Chapter 8.

We shape both the pump (denoted by superscript α) and the input (denoted by β) to span a complete set of mutually unbiased bases (MUBs) [8]. These have the property that for a dimension d , there are $(d + 1)$ bases such that overlaps between states from different

bases are always $1/d$, hence unbiased. This ensures that the space is uniformly probed. Furthermore, the total set is tomographically overcomplete, helping to reduce systematic experimental errors. Since for each pump shape, we have to run the full characterisation with $(d + 1)d$ input modes, the total number of measurements for $d = 5$ and $d = 7$ are 900 and 3136, respectively. For each of them, we record counts (denoted by $n^{\alpha\beta}$) for about 1 s at count rates up to 10^5 counts/s. This corresponds to a FC efficiency of about five percent, which is solely limited by the pump pulse energy of about 5 pJ in the our current experimental setup. Despite the relatively low conversion efficiency, a short measurement time is possible owing to high detection efficiency of the SiAPD. Since the count rates are directly proportional to the powers of the pump and the input, we record both values after the waveguide and normalise the count rates accordingly to account for small drifts in the setup (with the magnitude of less than 10%). It worth mentioning that one can also use symmetric informationally complete POVMs (SIC-POVMs) as the tomography bases [79]. The main advantage of the SIC-POVMs is that, contrary to MUBs, they exist for any arbitrary dimension [76].

To find QPG's measurement operators \hat{M}^α from the data we perform a weighted least squares fit

$$\min_{\hat{M}^\alpha} \sum_{\beta} \frac{|f^{\alpha\beta} - \langle \beta | \hat{M}^\alpha | \beta \rangle|^2}{f^{\alpha\beta}}, \quad (3.14)$$

where $f^{\alpha\beta}$ are normalised count rates and \hat{M}^α is constrained to be Hermitian and positive semidefinite. Since each setting α is an independent measurement, we do not put a constraint on the sum of operators. In Fig. 3.3 we show the first eigenmodes of all measurement operators for seven dimensions. They closely resemble the ideal MUB states. Additionally, the matrix of projections of MUB POVM elements $|\phi_i\rangle\langle\phi_j|^2$ which shows the orthogonality of the basis is given in Fig. 3.3.

To quantify how accurate the results are, we calculate the purities $\mathcal{P}^\alpha = \text{tr}([\hat{M}^\alpha]^2) / \text{tr}(\hat{M}^\alpha)^2$ and the fidelities $\mathcal{F}^\alpha = \sqrt{\langle \alpha | \hat{M}^\alpha | \alpha \rangle / \text{tr}(\hat{M}^\alpha)}$ with the ideal operators $|\alpha\rangle\langle\alpha|$. We perform the characterisation in five and seven dimensions, whereas for five dimensions we also compare the two experimental settings with and without a spectral filter in the output mode. The spectral filter blocks the side lobes of the phasematching (see Fig. 3 in Chapter 8). The average values with their respective standard deviations are listed in Table 3.1. For comparison we also show theoretical values assuming the aGVM condition, a Gaussian phasematching function and perfect pump shaping. The imperfections in this case originate from the fact that the phasematching is only about five times narrower than the pump, leading to correlations in the transfer function and multimode performance of the QPG. These correlations also explains why suppressing the side lobes of the

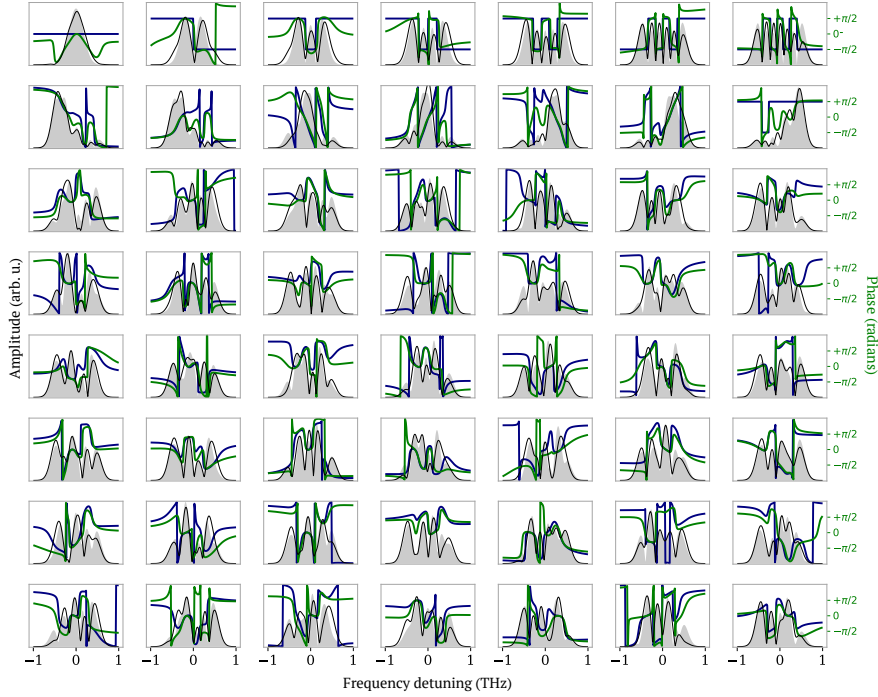


Figure 3.3: The first eigenvectors of the 7×6 measurement operators. For each plot, the x-axis corresponds to the frequency detuning (from the central frequency) and the y-axis to the amplitude and phase. Black and green lines are the measured amplitudes and phases, respectively; shaded areas and blue lines correspond to the theoretical MUB modes. Note that the phase is 2π periodic, which is also the interval of the y-axis. Please note that phases are only meaningful when a significant amplitude is present.

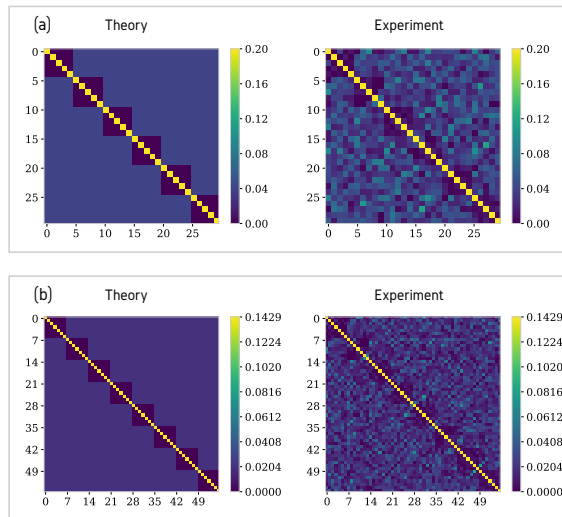


Figure 3.4: Matrix of projections of MUB POVM elements for five (a) and seven (b) dimensions.

Table 3.1: Purities and fidelities of QPG measurement operators.

d	5 (unfiltered)	5	7
$\mathcal{P}_{\text{measured}}$	0.719 ± 0.064	0.920 ± 0.024	0.811 ± 0.035
$\mathcal{F}_{\text{measured}}$	0.778 ± 0.086	0.912 ± 0.046	0.847 ± 0.042
$\mathcal{P}_{\text{theory}}$		0.939 ± 0.026	0.909 ± 0.035
$\mathcal{F}_{\text{theory}}$		0.979 ± 0.008	0.971 ± 0.010

output spectrum improves the purity from 0.72 to 0.92. A comparison of the eigenmodes for these two cases shows that the first eigenmode hardly changes. Thus the spectral filtering suppresses the higher order spectral modes introduced by the side lobes of the phasematching, or in other words drives the QPG closer to single-modeness. Going from five to seven dimensions slightly lowers both the purities and the fidelities. One reason is that the richer spectral structure of the pump at higher dimensions, again, will introduce some spectral correlations in the transfer function which also reduce the theoretical values. However, the expected reduction is smaller than what we measure. Imperfections in the pulse shaping are a greater problem for higher dimensions. With the increase of dimensionality, the total bandwidth both in time and frequency increases which requires the relative phases and amplitudes to be accurate over a broader range in both time and frequency. To improve the single-mode operation of QPG, one can use a longer waveguide which gives a narrower phase-matching bandwidth. Furthermore, the measurement time increases drastically which makes the experiment more susceptible to drifts in the setup. With the current experimental setup, the seven dimensional characterisation takes about 2 hours.

The overall high fidelities we measure in this work demonstrates that the QPG can operate on arbitrary TMs in a selective way. The fidelities also quantify the mode selectivity since the normalised conversion efficiency is given by \mathcal{F}^2 . In the five-dimensional case, that means that the desired mode gets converted with 83% efficiency and any orthogonal mode gets converted with less than 17%. However, with the measurement operators we have much more information than just the mode selectivity. For a task like state tomography, the QPG operation can be calibrated for small experimental errors, as we have here. All we need is mode sensitivity and the knowledge of our mode detector, which we have with the matrices \hat{M}^a .

In the following we investigate the performance of the QPG for state tomography. For this purpose, we prepare states like $\hat{\rho} = |\beta\rangle\langle\beta|$, which are different from the characterisation set we use for the measurement tomography. To ensure fair benchmarking we prepare twenty different input states where half of them are generated randomly.

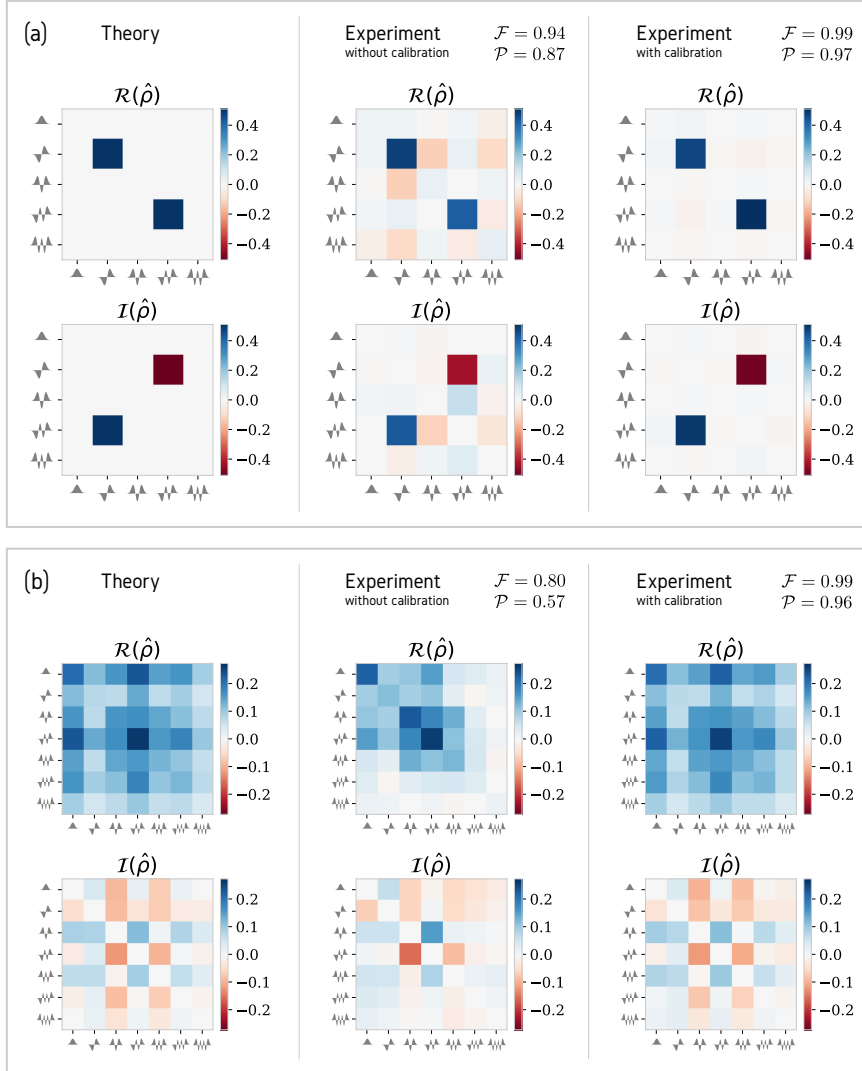


Figure 3.5: Two examples of state tomography with QPG in the Hermite-Gaussian basis in five (a) and seven (b) dimensions. State vectors corresponding to each density matrix is detailed in Chapter 8 (Appendix). For each state the theoretical density matrix (left), the reconstructed density matrix without QPG calibration (middle) and the reconstructed density matrix with QPG calibration (right) are plotted.

Table 3.2: Measured purities and fidelities of state tomography.

d	5 (unfiltered)	5	7
\mathcal{P}	0.68 ± 0.079	0.753 ± 0.098	0.619 ± 0.052
\mathcal{F}	0.742 ± 0.126	0.879 ± 0.041	0.813 ± 0.031

Table 3.3: Measured purities and fidelities of state tomography with calibrated QPG.

d	5 (unfiltered)	5	7
\mathcal{P}	0.931 ± 0.038	0.972 ± 0.016	0.957 ± 0.017
\mathcal{F}	0.971 ± 0.015	0.991 ± 0.005	0.988 ± 0.004

Then we use the $(d + 1)d$ QPG settings α to reconstruct the input state. We measure the normalised probabilities f^α and minimise

$$\min_{\hat{\rho}} \sum_{\alpha} \frac{|f^\alpha - \text{tr}(\hat{\rho} \hat{M}^\alpha)|^2}{f^\alpha}, \quad (3.15)$$

under the constraints that $\hat{\rho}$ is Hermitian, positive semidefinite and $\text{tr}(\hat{\rho}) = 1$. First, we assume a perfect QPG with ideal measurement operators and reconstruct the input states. Since the prepared inputs are coherent states in well-defined TMs, we expect to reconstruct pure states. The average fidelities and their standard deviations measured for all input states are listed in Table 3.2, which shows a modest fidelity of the reconstructed state with respect to the prepared state. This is because the slight multimodeness of the QPG operation, translates into the mixedness of the reconstructed states and leads to inaccurate tomography.

To improve the quality of the state tomography we can use the characterised measurement operators of the QPG in Eq. (3.15). Table 3.3 summarises the outcome. The improvement is striking. We obtain fidelities of 0.99 with the actual input state. Two example of such states are shown in Fig. 3.5. The decrease in fidelity from five to seven dimensions is almost negligible and even without filtering, the values are still very high. This shows the power of proper detector calibration for state tomography. The outstanding fidelities suggest that the state tomography with QPG can be scaled up to higher dimensions. However performing a complete measurement tomography for higher dimensions, with the current experimental configuration, would require an impractically long measurement time. This is primarily a technical challenge to decrease the switching time of the SLMs and increase the count rates per second. From the numeric point of view, measurement tomography becomes time consuming very quickly. Here, one could switch to pattern tomography [75], which circumvents this tedious step by fitting the detector response

pattern directly. We tested this approach as well and obtained similar fidelities as shown in Table 3.3.

3.2 TEMPORAL-MODE TOMOGRAPHY AND PURIFICATION OF QUANTUM LIGHT

To fully exploit the temporal mode structure of quantum light, it is necessary to both control the modal structure of quantum light sources and develop matched mode-selective measurement methods. In order to perform projective measurements onto arbitrary temporal modes, techniques are needed which can identify and remove a specific desired mode from a mixture or superposition. Furthermore, operations on photonic temporal modes must not introduce noise in order to leave the fragile quantum nature of the light intact. Sum-frequency generation with tailored group-velocity relationships and shaped ultrafast pulses provides a capable toolbox for these tasks [2, 21, 23, 66, 72, 99]. Notably, a sum-frequency process between a weak photonic signal and a shaped strong measurement pulse with matched group velocities has been shown to act as mode-selective coupling between an upconverted frequency band and the temporal mode defined by the shaped strong pulse [23, 72]. This process, dubbed the *quantum pulse gate* (QPG), is capable of selectively addressing individual temporal modes and can be used as a temporal-mode analyser for communication networks [99] or as an add-drop component to build general unitaries and quantum logic gates for a desired temporal-mode basis [11, 13]. Recent QPG experiments have shown highly efficient and highly selective operations on coherent light pulses [14, 25, 46, 57, 74, 80] and its effectiveness as a measurement device for unknown superpositions [4] and a mode-selective photon subtractor [68].

In this section, we show a complete set of tools to generate, manipulate, and measure the temporal-mode structure of single photons with a high degree of control. The outline of our scheme is depicted in Fig. 3.6. Single photons are heralded from an engineered PDC source where we orchestrate the modal structure of the photon pair by spectral modulation of the pump field. Regardless of the temporal mode structure of the PDC photons, we show that the QPG can select a single temporal mode from a mixture, demonstrating its usefulness as a temporal-mode projective measurement and as a purifier. We then use a QPG to tomographically reconstruct the seven-dimensional temporal-mode density matrix of heralded single photons, showing that QPG measurements are sensitive to time-frequency structure of light beyond intensity-only measurements. Finally, through the correlation function measurements, we show that the QPG can change the modal structure of the transmitted photon state, either acting as a mode cleaner or increasing the mixedness

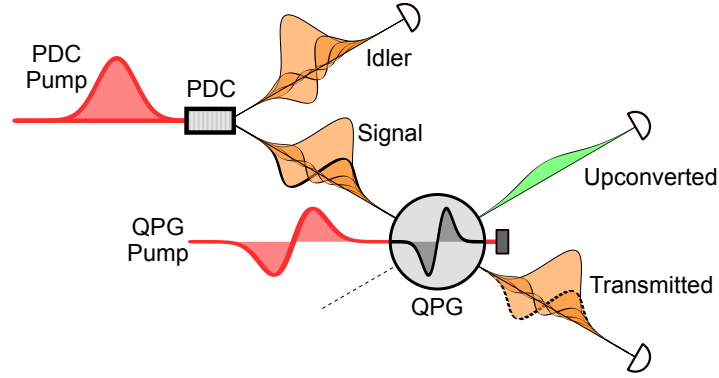


Figure 3.6: **Temporal mode selection with a quantum pulse gate.** The two-photon state resulting from parametric downconversion (PDC) has a multimode structure defined by the pump field and nonlinear phasematching. The quantum pulse gate (QPG) selects a single mode (the first-order Hermite-Gauss for example, in bold) from this superposition and upconverts it to a higher frequency, while the unselected modes transmit unaffected. Changing the shape of the QPG pump changes which temporal mode the QPG selects.

depending on its programmable operation. We measure high signal-to-noise ratios and high contrast between mode selections while operating on quantum light, definitively positioning the QPG as an invaluable resource for pulsed quantum information science.

The group-velocity matching condition can be met in periodically poled lithium niobate (PPLN) waveguides, which also provide the spatial confinement necessary for long nonlinear interaction lengths. In our experimental setup, detailed in the appendix, we make use of type-II group-velocity matching between a 1540-nm photonic input and an 876-nm QPG pump, as in Refs. [4, 14]. To implement the QPG, we use a 17-mm PPLN waveguide with a $4.4 \mu\text{m}$ poling period built in-house. We measure upconverted output pulses at 558 nm with a 61-pm (59 GHz) bandwidth (full-width at half-maximum), significantly narrower than the 4.9-nm (620 GHz) bandwidth of the input photons. Although similar conditions can be met in other materials using near-degenerate type-0 or type-I processes [25, 46, 57], our scheme avoids the challenge of isolating the single-photon signal from the second harmonic of the QPG pump.

We use spatial-light-modulator-based pulse shapers to define both the spectral amplitude and phase of the PDC and QPG pump pulses [62, 94]. With this flexibility in hand, we selected four PDC states to illustrate the versatility of the QPG. The joint spectral intensity $|f(\omega_s, \omega_i)|^2$ for each is shown on the right side of Fig. 3.7, as measured with dispersive time-of-flight spectrometers [7]. Firstly, we set the PDC pump bandwidth such that the generated two-photon state is nearly spectrally separable [36], as seen in Fig. 3.7a. In this sce-

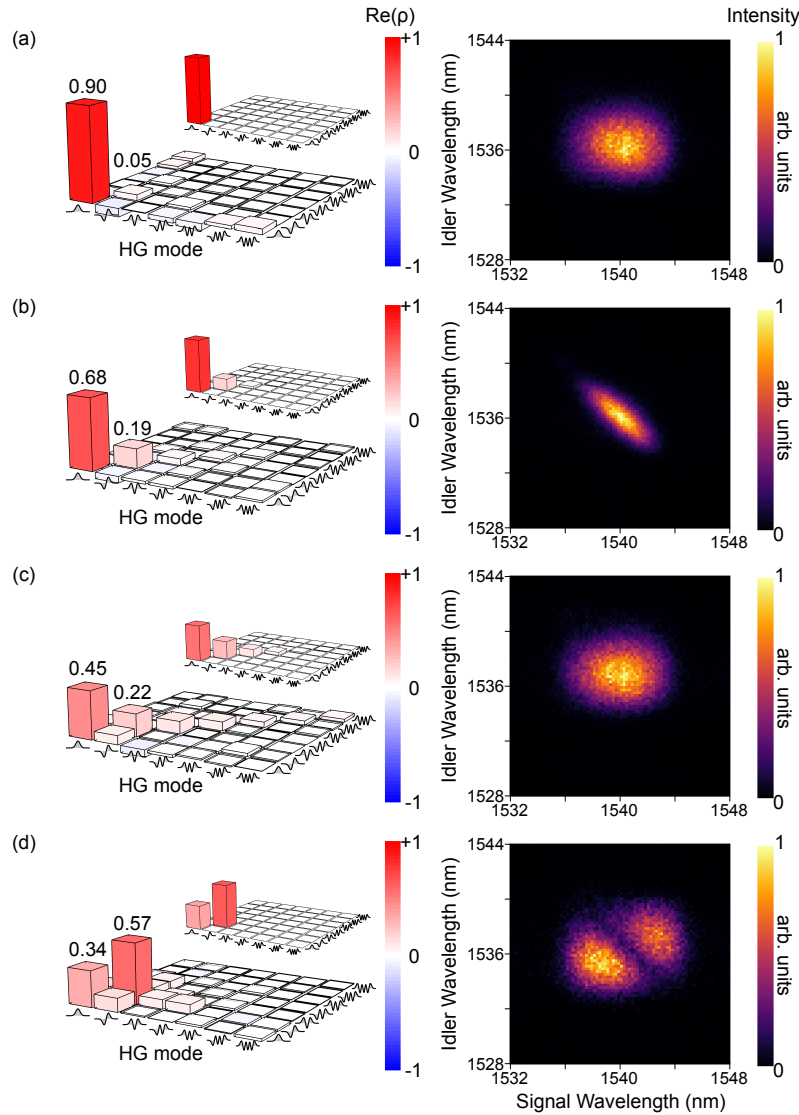


Figure 3.7: **Joint spectral intensities and reconstructed temporal-mode density matrices.** The real part of the seven-dimensional one-photon temporally reconstructed density matrices (left), joint spectral intensities (right), and theoretically expected density matrices (inset) for four PDC states: (a) a separable PDC state, (b) a PDC state with spectral anti-correlations from a narrow-bandwidth pump, (c) a PDC state with spectral phase correlations from a chirped pump, and (d) a PDC state pumped with a higher-order mode. The values of the first two diagonal entries are explicitly labelled above the density matrix. Imaginary components of the reconstructed density matrices are small and found in the appendix.

nario, we expect that a single temporal mode dominates the PDC state. A singular value decomposition of the joint spectral intensity predicts a purity of 0.995, but measured $g^{(2)} = 1 + P$ (corrected for detector dark counts) corresponds to a significantly lower purity of

0.929 ± 0.008 , potentially due to high-order phase correlations or degenerate background processes.

By shaping the QPG pump to project onto a set of Hermite-Gauss spectral shapes, we expect to significantly higher upconversion probabilities for the lowest-order Gaussian mode. We find that, when measuring in coincidence with an idler detection, the Gaussian projection indeed provides more counts than the first-order Hermite-Gaussian projection by a factor of 19.3 (12.8 dB), with even stronger suppression for higher-order modes. This demonstrates simultaneously the high mode separability of our device and the single-mode character of our PDC state. With a coherent-state input signal from a commercial pulse shaper instead of PDC photons, the suppression factor increases to 111 (20.5 dB). The upconverted signal is cleanly separated from all background sources, even for a PDC-generated average photon number of $\langle n \rangle \approx 0.16$. The signal-to-noise ratio (including detector dark counts and noise from the QPG pump) is over 70:1 without heralding and increases to over 900:1 when gated by an idler detection.

While joint spectral intensity measurements provide important information about the two-photon PDC state, they potentially hide significant information about the spectral phase to which mode-selective measurement would be sensitive. To demonstrate the effectiveness of the QPG for quantum state characterisation, we reconstruct the density matrix of the signal photons, as seen on the left-hand side of Fig. 3.7. By shaping the QPG pump, we project onto the first seven Hermite-Gauss temporal modes as well as a tomographically complete set of superpositions, totalling 56 measurements [8, 96]. The time-frequency waveforms chosen span eight mutually unbiased seven-dimensional bases. The density matrices were then reconstructed from the heralded counts in the upconverted mode using a maximum-likelihood approach [3]. As the tomography measurements are made on one photon of a PDC pair, we expect to reconstruct mixed density matrices with purities consistent with the measured $g^{(2)}$. For the separable PDC state of Fig. 3.7a, we reconstruct a density matrix with a purity of $\text{tr}(\rho^2) = 0.896 \pm 0.006$, lower than the expected value of 0.929 ± 0.008 . Discrepancies between the tomographically reconstructed purities and the $g^{(2)}$ values arise from somewhat diminished mode selectivity for the higher-order projections [4], to which characterisation of single-mode behaviour is particularly sensitive.

Next, we increase the number of modes present in the PDC state in three different ways, and show that the QPG measurements are sensitive to all three. First, we narrow the bandwidth of the PDC pump to produce a multimode PDC state with spectral intensity anticorrelations. The inseparability of this system can be seen directly in the joint spectral intensity of Fig. 3.7b as well as in the $g^{(2)}$ -inferred pu-

rity of 0.528 ± 0.009 , which matches the purity of the reconstructed density matrix, 0.523 ± 0.008 .

Intensity correlations are not the only available avenue for increasing the mode number of a PDC state. By adding quadratic spectral phase (chirp) to the PDC pump, we introduce phase correlations between the signal and idler photons. Note that this phase does not affect the joint spectral intensity, as seen in Fig. 3.7c. However, the added phase drastically decreases the $g^{(2)}$, with a measured purity of 0.327 ± 0.005 . Through tomography, we find that the QPG measurements are also sensitive to this phase, with a reconstructed purity of 0.317 ± 0.005 , similar to the $g^{(2)}$ -inferred purity. This result explicitly demonstrates the limitations of spectral intensity measurements for benchmarking pure single photons and the necessity of spectral phase control.

In each of the previous cases, the expected primary temporal mode of the PDC state is approximately Gaussian, with higher-order contributions falling off exponentially with mode number. In practical applications, it is often desirable to produce photon pairs in a restricted subspace, for example to create maximally entangled Bell states and their high-dimensional equivalents. As a final example, we produce a state with contributions from principally two temporal modes by shaping the PDC into the first-order Hermite-Gauss function, as seen in Fig. 3.7d. This pump shape is expected to produce photon pairs in the time-frequency Bell state, with similar weights in the zeroth- and first-order HG modes [11]. The reconstructed density matrix from the QPG measurements shows that the modal content of the PDC state is principally confined to these two modes, and the purities inferred from the $g^{(2)}$ and the tomography for this state are, respectively, 0.498 ± 0.006 and 0.531 ± 0.004 , consistent with half of a highly entangled qubit pair. The imbalance between the first two modes can be attributed to a non-ideal group-velocity relationship between signal and idler in the PDC process (i.e. a non-45-degree phasematching angle [36]), and is consistent with the density matrix expected from the joint spectral intensity.

To demonstrate the potential of the QPG for state purification, we measure the $g^{(2)}$ of the upconverted photons for the QPG pump in the first two Hermite-Gauss modes, as shown in Fig. 3.8. If the QPG selects a single mode from the input mixture, we expect that the upconverted photons themselves will be highly pure. Indeed, the $g^{(2)}$ of the upconverted light confirms a purity of at least 0.9 for both the zeroth- and first-order HG modes, regardless of the PDC state under interrogation. For example, for the correlated spectral intensity of case (b), the $g^{(2)}$ of the upconverted light when the Gaussian mode is selected is 1.95 ± 0.04 , which increases to 2.04 ± 0.04 after dark-count subtraction. The purity of the upconverted light remains high when the first-order HG mode is selected. The high $g^{(2)}$ values

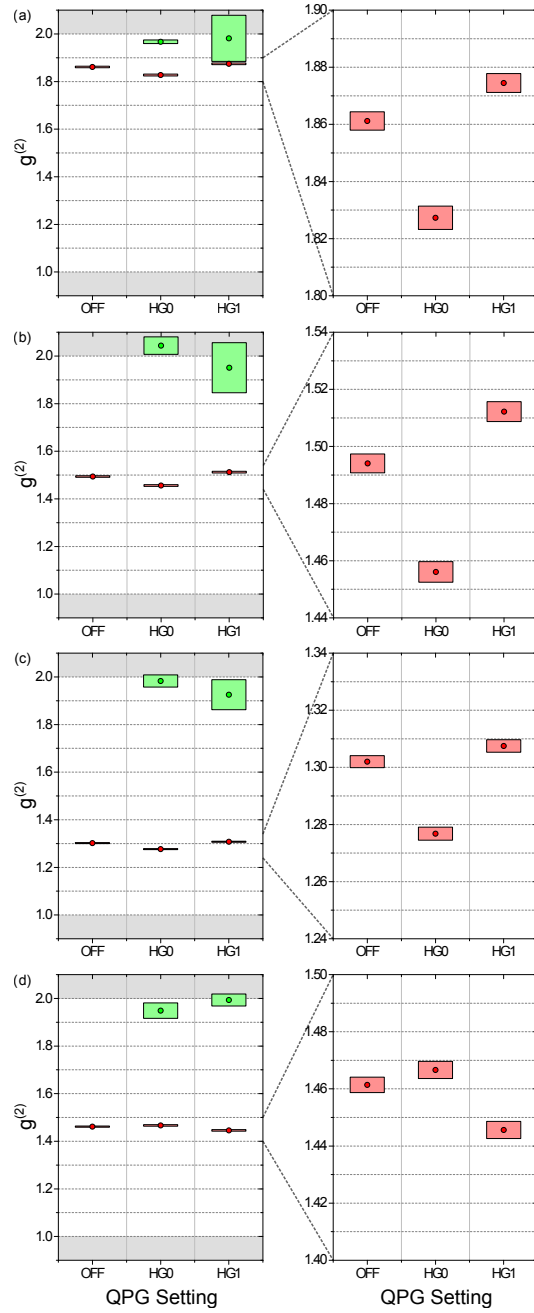


Figure 3.8: **Second-order correlation functions of transmitted and upconverted photons.** The marginal $g^{(2)}$ s of the upconverted (green) and transmitted (red) PDC photons are shown for the four PDC states corresponding to Fig. 3.7a-d with the QPG pump pulse delayed relative to the signal photons ('OFF') and shaped to the first two Hermite-Gauss temporal modes ('HGO' and 'HG1'). The right side of the figure shows the same data rescaled to highlight the changes in the $g^{(2)}$ of the transmitted photons. The data presented is dark-count background subtracted and the error bars are found assuming Poissonian noise.

measured here conclusively show both that the QPG indeed selects a single mode and that the upconverted mode retains the thermal photon statistics of PDC, with very little noise introduced by the process.

Finally, we show through the $g^{(2)}$ that the modal structures of the transmitted photons are significantly altered by the QPG. If a mixture of modes is dominated by one mode, partially removing that mode from the mixture will increase the mixedness of the remaining distribution, akin to the Procrustean method of entanglement concentration [10]. For the decorrelated PDC state of case (a), we measured the conversion efficiency through the depletion of the transmitted signal as approximately 22%. This partial removal of the primary mode indeed results in a significant decrease in the $g^{(2)}$ of the unconverted transmitted signal photons, as seen on the right-hand side of Fig. 3.8, consistent with the efficiency measured from the input depletion. Conversely, removing the first-order HG mode removes amplitude from the secondary Schmidt coefficient, which increases the relative amplitude of the primary Schmidt mode. This is seen in cases (a-c) to increase the overall purity of the transmitted photon state, demonstrating that the QPG can act as a temporal mode cleaner even for the non-converted photons. In case (d), the first-order HG mode is present in a larger proportion than the Gaussian component, and the opposite trend is seen. This is consistent with the reconstructed density matrix of Fig. 3.7d. This directly demonstrates that the QPG can be used to remove modal components from a single-photon state, an essential task for mode-selective add/drop functionality.

We have shown that the quantum pulse gate can be used to directly manipulate and measure the temporal modal structure of single-photon states. By projecting over a complete set of temporal modes and superpositions, we reconstructed seven-dimensional temporal-mode density matrices for PDC photons with a variety of modal structures. We have demonstrated that the output of the pulse gate is nearly completely purified regardless of the input, positioning the quantum pulse gate as a powerful tool for photonic quantum state engineering. We have also demonstrated through changes in the second-order correlation function that the quantum pulse gate modifies the modal structure of the input photons, establishing the QPG as a novel device for both entanglement concentration and state purification. Future work will focus on improving the efficiency and extending the accessible dimensionality of the quantum pulse gate to fully realise its potential for time-frequency mode-selective measurement, as a conversion interface and add/drop device for temporally encoded quantum networks, and as a platform for high-dimensional quantum state characterisation.

CONCLUSION AND OUTLOOK

In this thesis we demonstrated a complete framework for generating and measuring photon temporal modes. Through dispersion-engineered waveguides we constructed photon-pair sources with near arbitrary control over the temporal modes of the emitted photons and the entanglement between them. Then we incorporated similar methods into sum-frequency generation, providing the necessary tools to manipulate and measure temporal-modes of the generated photons.

In Chapter 1 we introduced the temporal modes of a single quantum of light and its presentation through the chronocyclic Wigner function. Then we introduced the methods used in this thesis to shape and characterise bright ultrashort pulses. In Chapter 2, we reviewed the basic theory behind the temporal-mode structure of photon pairs generated via parametric downconversion. By engineering the group-velocity relation between the three optical fields involved in the nonlinear process in a KTP waveguide, we generated separable PDC photons in arbitrary temporal modes capable of providing the high-visibility quantum interference necessary for multiphoton quantum networks. Exploiting a different group-velocity relation, it was also shown that the number of excited temporal-modes and their entanglement structure can be controlled.

In Section 3, we used similar dispersion engineering methods in sum-frequency generation to realise a quantum pulse gate; a versatile tool capable of manipulating and measuring the temporal-mode structure of single photons. We experimentally characterised the measurement operators of a QPG in up to seven dimensions, enabling accurate temporal-mode state tomography of single photons with fidelities above 0.99. By projecting over a complete set of temporal modes and superpositions, we reconstructed seven-dimensional temporal-mode density matrices for PDC photons with a variety of modal structures. We have demonstrated that the output of the pulse gate is nearly completely purified regardless of the input, positioning the quantum pulse gate as a powerful tool for photonic quantum state engineering. We have also demonstrated through changes in the second-order correlation function that the quantum pulse gate modifies the modal structure of the input photons, establishing the quantum pulse gate as a novel device for both entanglement concentration and state purification.

Many challenges remain to push toward practical application. The major benefits of encoding quantum information in temporal-modes appears when we employ a high-dimensional space (large alphabet).

However, devices that can isolate a single temporal mode are difficult to scale, requiring multiple shaped pulses and physical media to construct a multi-output measure. Techniques which demultiplex a set of pulsed temporal modes into spatial or spectral bins, equivalent to the orbital angular momentum mode sorter in space, are essential to scale these techniques to high-dimensional networks. A promising avenue for these temporal-mode demultiplexers is through multiplexed phasematching structures. Furthermore, extending the access of temporal-mode selective devices to pico- or nanosecond regime can also benefit long-distance quantum communication where these pulses can more efficiently be coupled to memory-based interfaces and are less jitter-sensitive, but requires advancement in pulse shaping techniques. Temporal-mode encoding can also enable another range of applications in quantum computation or simulation; where compared to spatial-mode encoding, more scalable optical networks can be implemented with efficient time-frequency encoding. Here the challenge is to build a network of many mode-selective devices, phase shifters, beam-splitters, etc., that efficiently operate on many single-photons. To construct such networks, recent technological developments in photonic integrated circuits seem to offer a promising future.

BIBLIOGRAPHY

- [1] Marius A Albota and Franco NC Wong. "Efficient single-photon counting at $1.55 \mu\text{m}$ by means of frequency upconversion." In: *Optics letters* 29.13 (2004), pp. 1449–1451.
- [2] Markus Allgaier, Vahid Ansari, Linda Sansoni, Christof Eigner, Viktor Quiring, Raimund Ricken, Georg Harder, Benjamin Brecht, and Christine Silberhorn. "Highly efficient frequency conversion with bandwidth compression of quantum light." In: *Nature Communications* 8 (2017), p. 14288. ISSN: 2041-1723.
- [3] Joseph B Altepeter, Evan R Jeffrey, and Paul G Kwiat. "Photonic state tomography." In: *Advances in Atomic, Molecular, and Optical Physics* 52 (2005), pp. 105–159.
- [4] Vahid Ansari, Georg Harder, Markus Allgaier, Benjamin Brecht, and Christine Silberhorn. "Temporal-mode measurement tomography of a quantum pulse gate." In: *Physical Review A* 96.6 (2017), p. 063817.
- [5] Vahid Ansari, John M Donohue, Markus Allgaier, Linda Sansoni, Benjamin Brecht, Jonathan Roslund, Nicolas Treps, Georg Harder, and Christine Silberhorn. "Tomography and purification of the temporal-mode structure of quantum light." In: *arXiv preprint arXiv:1607.03001* (2018).
- [6] Serkan Ates, Imad Agha, Angelo Gulinatti, Ivan Rech, Matthew T Rakher, Antonio Badolato, and Kartik Srinivasan. "Two-photon interference using background-free quantum frequency conversion of single photons emitted by an InAs quantum dot." In: *Physical review letters* 109.14 (2012), p. 147405.
- [7] Malte Avenhaus, Andreas Eckstein, Peter J Mosley, and Christine Silberhorn. "Fiber-assisted single-photon spectrograph." English. In: *Optics Letters* 34.18 (2009), pp. 2873–2875.
- [8] Somshubhro Bandyopadhyay, P Oscar Boykin, Vwani Roychowdhury, and Farrokh Vatan. "A new proof for the existence of mutually unbiased bases." In: *Algorithmica* 34.4 (2002), pp. 512–528.
- [9] Christoph Baune, Jan Gniesmer, Axel Schönbeck, Christina E Vollmer, Jaromír Fiurášek, and Roman Schnabel. "Strongly squeezed states at 532 nm based on frequency up-conversion." In: *Optics express* 23.12 (2015), pp. 16035–16041.
- [10] Charles H Bennett, Herbert J Bernstein, Sandu Popescu, and Benjamin Schumacher. "Concentrating partial entanglement by local operations." In: *Physical Review A* 53.4 (1996), p. 2046.

- [11] B Brecht, Dileep V Reddy, C Silberhorn, and M G Raymer. "Photon temporal modes: A complete framework for quantum information science." In: *Physical Review X* 5.4 (2015), p. 041017.
- [12] Benjamin Brecht, Andreas Eckstein, and Christine Silberhorn. "Controlling the correlations in frequency upconversion in PPLN and PPKTP waveguides." In: *Physica Status Solidi (C) Current Topics in Solid State Physics* 8.4 (2011), pp. 1235–1238. ISSN: 18626351.
- [13] Benjamin Brecht, Andreas Eckstein, Andreas Christ, Hubertus Suche, and Christine Silberhorn. "From quantum pulse gate to quantum pulse shaper—engineered frequency conversion in nonlinear optical waveguides." In: *New Journal of Physics* 13.6 (2011), p. 065029. ISSN: 1367-2630.
- [14] Benjamin Brecht, Andreas Eckstein, Raimund Ricken, Viktor Quiring, Hubertus Suche, Linda Sansoni, and Christine Silberhorn. "Demonstration of coherent time-frequency Schmidt mode selection using dispersion-engineered frequency conversion." In: *Physical Review A* 90.3 (2014), p. 030302. ISSN: 1050-2947.
- [15] Y-H Cheng, Tim Thomay, Glenn S Solomon, Alan L Migdall, and Sergey V Polyakov. "Statistically background-free, phase-preserving parametric up-conversion with faint light." In: *Optics express* 23.14 (2015), pp. 18671–18678.
- [16] Andreas Christ, Kaisa Laiho, Andreas Eckstein, Katiúscia N Cassemiro, and Christine Silberhorn. "Probing multimode squeezing with correlation functions." In: *New Journal of Physics* 13.3 (2011), p. 033027.
- [17] Stéphane Clemmen, Alessandro Farsi, Sven Ramelow, and Alexander L. Gaeta. "Ramsey Interference with Single Photons." In: *Physical Review Letters* 117.22 (2016), p. 223601. ISSN: 0031-9007.
- [18] Noé Curtz, Rob Thew, Christoph Simon, Nicolas Gisin, and Hugo Zbinden. "Coherent frequency-down-conversion interface for quantum repeaters." In: *Optics express* 18.21 (2010), pp. 22099–22104.
- [19] Kristiaan De Greve, Leo Yu, Peter L McMahon, Jason S Pelc, Chandra M Natarajan, Na Young Kim, Eisuke Abe, Sebastian Maier, Christian Schneider, Martin Kamp, Sven Höfling, Robert H Hadfield, Alfred Forchel, M M Fejer, and Yoshihisa Yamamoto. "Quantum-dot spin-photon entanglement via frequency down-conversion to telecom wavelength." In: *Nature* 491 (7424 2012), pp. 421–425. ISSN: 1476-4687.
- [20] Yu Ding and ZY Ou. "Frequency downconversion for a quantum network." In: *Optics letters* 35.15 (2010), pp. 2591–2593.
- [21] John M Donohue, Megan Agnew, Jonathan Lavoie, and Kevin J Resch. "Coherent ultrafast measurement of time-bin encoded photons." In: *Physical review letters* 111.15 (2013), p. 153602.

- [22] Annamaria Dosseva, Łukasz Cincio, and Agata M. Brańczyk. "Shaping the joint spectrum of down-converted photons through optimized custom poling." In: *Physical Review A* 93.1 (2016), p. 013801. ISSN: 2469-9926.
- [23] Andreas Eckstein, Benjamin Brecht, and Christine Silberhorn. "A quantum pulse gate based on spectrally engineered sum frequency generation." In: *Optics Express* 19.15 (2011), p. 13770. ISSN: 1094-4087.
- [24] Andreas Eckstein, Andreas Christ, Peter J. Mosley, and Christine Silberhorn. "Highly efficient single-pass source of pulsed single-mode twin beams of light." In: *Physical Review Letters* 106.1 (2011), p. 013603. ISSN: 00319007.
- [25] "Engineering temporal-mode-selective frequency conversion in nonlinear optical waveguides: from theory to experiment." In: *Optics Express* 25.11 (2017), p. 12952.
- [26] Reinhard Erdmann, David Branning, Warren Grice, and I. A. Walmsley. "Restoring dispersion cancellation for entangled photons produced by ultrashort pulses." In: *Physical Review A - Atomic, Molecular, and Optical Physics* 62.5 (2000), p. 053810. ISSN: 10502947.
- [27] Cl Froehly, A Lacourt, and J Ch Vienot. "Notions de réponse impulsionnelle et de fonction de transfert temporelles des pupilles optiques, justifications expérimentales et applications." In: *J. Opt.(Paris)* 4 (1973), pp. 183–196.
- [28] Eugene Frumker and Yaron Silberberg. "Phase and amplitude pulse shaping with two-dimensional phase-only spatial light modulators." English. In: *JOSA B* 24.12 (Dec. 2007), pp. 2940–2947.
- [29] Joe Ghalbouni, Imad Agha, Robert Frey, Eleni Diamanti, and Isabelle Zaquine. "Experimental wavelength-division-multiplexed photon-pair distribution." In: *Opt. Lett.* 38.1 (2013), pp. 34–36.
- [30] G Giorgi, P Mataloni, and F De Martini. "Frequency hopping in quantum interferometry: efficient up-down conversion for qubits and ebits." In: *Physical review letters* 90.2 (2003), p. 027902.
- [31] Vittorio Giovannetti, Seth Lloyd, and Lorenzo Maccone. "Quantum-enhanced positioning and clock synchronization." In: *Nature* 412.6845 (2001), pp. 417–419.
- [32] Vittorio Giovannetti, Lorenzo Maccone, Jeffrey H. Shapiro, and Franco N. C. Wong. "Extended phase-matching conditions for improved entanglement generation." In: *Physical Review A* 66 (2002), p. 043813. ISSN: 1050-2947.

- [33] Francesco Graffitti, Dmytro Kundys, Derryck T Reid, Agata M Brańczyk, and Alessandro Fedrizzi. "Pure down-conversion photons through sub-coherence-length domain engineering." In: *Quantum Science and Technology* 2.3 (2017), p. 035001. ISSN: 2058-9565.
- [34] W. P. Grice, A. B. U'Ren, and I. A. Walmsley. "Eliminating frequency and space-time correlations in multiphoton states." In: *Physical Review A. Atomic, Molecular, and Optical Physics* 64.6 (2001), p. 063815. ISSN: 10502947.
- [35] W. Grice and I. Walmsley. "Spectral information and distinguishability in type-II down-conversion with a broadband pump." In: *Phys. Rev. A* 56.2 (1997), pp. 1627–1634. ISSN: 1050-2947.
- [36] Georg Harder, Vahid Ansari, Benjamin Brecht, Thomas Dirmeier, Christoph Marquardt, and Christine Silberhorn. "An optimized photon pair source for quantum circuits." In: *Optics Express* 21.12 (2013), pp. 13975–13985. ISSN: 1094-4087.
- [37] CK Hong, Zhe-Yu Ou, and Leonard Mandel. "Measurement of subpicosecond time intervals between two photons by interference." In: *Physical review letters* 59.18 (1987), p. 2044.
- [38] T Honjo, H Takesue, H Kamada, Y Nishida, O Tadanaga, M Asobe, and K Inoue. "Long-distance distribution of time-bin entangled photon pairs over 100 km using frequency up-conversion detectors." In: *Optics express* 15 (21 2007), pp. 13957–13964. ISSN: 1094-4087.
- [39] Ryszard Horodecki, Paweł Horodecki, Michał Horodecki, and Karol Horodecki. "Quantum entanglement." In: *Rev. Mod. Phys.* 81.2 (2009), p. 865.
- [40] Jianming Huang and Prem Kumar. "Observation of quantum frequency conversion." In: *Physical review letters* 68.14 (1992), p. 2153.
- [41] David S Hum and Martin M Fejer. "Quasi-phasematching." In: *Comptes Rendus Physique* 8.2 (2007), pp. 180–198.
- [42] Rikizo Ikuta, Yoshiaki Kusaka, Tsuyoshi Kitano, Hiroshi Kato, Takashi Yamamoto, Masato Koashi, and Nobuyuki Imoto. "Wide-band quantum interface for visible-to-telecommunication wavelength conversion." English. In: *Nature Communications* 2 (2011), p. 1544.
- [43] Rikizo Ikuta, Toshiki Kobayashi, Shuto Yasui, Shigehito Miki, Taro Yamashita, Hirotaka Terai, Mikio Fujiwara, Takashi Yamamoto, Masato Koashi, Masahide Sasaki, Zhen Wang, and Nobuyuki Imoto. "Frequency down-conversion of 637 nm light to the telecommunication band for non-classical light emitted from NV centers in diamond." In: *Optics express* 22 (9 2014), pp. 11205–11214. ISSN: 1094-4087.

- [44] Timothy Keller and Morton Rubin. "Theory of two-photon entanglement for spontaneous parametric down-conversion driven by a narrow pump pulse." In: *Physical Review A* 56.2 (1997), pp. 1534–1541. ISSN: 1050-2947.
- [45] Toshiki Kobayashi, Rikizo Ikuta, Shuto Yasui, Shigehito Miki, Taro Yamashita, Hirotaka Terai, Takashi Yamamoto, Masato Koashi, and Nobuyuki Imoto. "Frequency-domain Hong–Ou–Mandel interference." In: *Nature Photonics* 10.7 (2016), pp. 441–444.
- [46] Abijith S Kowligy, Paritosh Manurkar, Neil V Corzo, Vesselin G Velez, Michael Silver, Ryan P Scott, S J B Yoo, Prem Kumar, Gregory S Kanter, and Yu-Ping Huang. "Quantum optical arbitrary waveform manipulation and measurement in real time." In: *Optics Express* 22.23 (2014), p. 27942. ISSN: 1094-4087.
- [47] Prem Kumar. "Quantum frequency conversion." In: *Optics Letters* 15.24 (1990), p. 1476. ISSN: 0146-9592.
- [48] Paulina S Kuo, Jason S Pelc, Oliver Slattery, Yong-Su Kim, M M Fejer, and Xiao Tang. "Reducing noise in single-photon-level frequency conversion." English. In: *Optics Letters* 38.8 (2013), pp. 1310–1312.
- [49] Onur Kuzucu, Franco N C Wong, Sunao Kurimura, and Sergey Tovstonog. "Joint temporal density measurements for two-photon state characterization." In: *Physical Review Letters* 101.15 (2008), p. 153602. ISSN: 00319007.
- [50] Carsten Langrock, Eleni Diamanti, Rostislav V Roussev, Yoshihisa Yamamoto, Martin M Fejer, and Hiroki Takesue. "Highly efficient single-photon detection at communication wavelengths by use of upconversion in reverse-proton-exchanged periodically poled LiNbO₃ waveguides." In: *Optics letters* 30.13 (2005), pp. 1725–1727.
- [51] C. K. Law, I. A. Walmsley, and J. H. Eberly. "Continuous Frequency Entanglement: Effective Finite Hilbert Space and Entropy Control." In: *Physical Review Letters* 84.23 (2000), pp. 5304–5307. ISSN: 0031-9007.
- [52] Matthieu Legré, Rob Thew, Hugo Zbinden, and Nicolas Gisin. "High resolution optical time domain reflectometer based on 1.55 μm up-conversion photon-counting module." In: *Optics express* 15.13 (2007), pp. 8237–8242.
- [53] L Lepetit, G Chériaux, and M Joffre. "Linear techniques of phase measurement by femtosecond spectral interferometry for applications in spectroscopy." In: *JOSA B* 12.12 (1995), pp. 2467–2474.
- [54] EJ Lim, S Matsumoto, and MM Fejer. "Noncritical phase matching for guided-wave frequency conversion." In: *Applied physics letters* 57.22 (1990), pp. 2294–2296.

- [55] Wenyuan Liu, Ning Wang, Zongyang Li, and Yongmin Li. "Quantum frequency up-conversion of continuous variable entangled states." In: *Applied Physics Letters* 107.23 (2015), p. 231109.
- [56] Thomas Lutz, Piotr Kolenderski, and Thomas Jennewein. "Demonstration of spectral correlation control in a source of polarization-entangled photon pairs at telecom wavelength." In: *Optics letters* 39.6 (2014), pp. 1481–1484.
- [57] Paritosh Manurkar, Nitin Jain, Michael Silver, Yu-Ping Huang, Carsten Langrock, Martin M Fejer, Prem Kumar, and Gregory S Kanter. "Multidimensional mode-separable frequency conversion for high-speed quantum communication." In: *Optica* 3.12 (2016), pp. 1300–1307.
- [58] Nicolas Maring, Pau Farrera, Kutlu Kutluer, Margherita Mazzera, Georg Heinze, and Hugues de Riedmatten. "Photonic quantum state transfer between a cold atomic gas and a crystal." In: *Nature* 551.7681 (2017), p. 485.
- [59] H J McGuinness, Michael G Raymer, C J McKinstrie, and S Radic. "Quantum Frequency Translation of Single-Photon States in a Photonic Crystal Fiber." English. In: *Physical Review Letters* 105.9 (2010), p. 093604.
- [60] Nicolas C Menicucci, Peter van Loock, Mile Gu, Christian Weedbrook, Timothy C Ralph, and Michael A Nielsen. "Universal quantum computation with continuous-variable cluster states." In: *Phys. Rev. Lett.* 97.11 (2006), p. 110501.
- [61] Evan Meyer-Scott, Nicola Montaut, Johannes Tiedau, Linda Sansoni, Harald Herrmann, Tim J Bartley, and Christine Silberhorn. "Limits on the heralding efficiencies and spectral purities of spectrally filtered single photons from photon-pair sources." In: *Physical Review A* 95.6 (2017), p. 061803.
- [62] Antoine Monmayrant, Sébastien Weber, and Béatrice Chatel. "A newcomer's guide to ultrashort pulse shaping and characterization." English. In: *Journal of Physics B: Atomic, Molecular and Optical Physics* 43.10 (2010), p. 103001.
- [63] Maged B Nasr, Bahaa EA Saleh, Alexander V Sergienko, and Malvin C Teich. "Demonstration of dispersion-canceled quantum-optical coherence tomography." In: *Physical review letters* 91.8 (2003), p. 083601.
- [64] Giuseppe Patera, Carlos Navarrete-Benlloch, Germán J de Valcárcel, and Claude Fabre. "Quantum coherent control of highly multipartite continuous-variable entangled states by tailoring parametric interactions." In: *The European Physical Journal D-Atomic, Molecular, Optical and Plasma Physics* 66.9 (2012), pp. 1–14.

- [65] J Paye. "The chronocyclic representation of ultrashort light pulses." In: *IEEE Journal of Quantum Electronics* 28.10 (1992), pp. 2262–2273.
- [66] Avi Pe'er, Barak Dayan, Asher A. Friesem, and Yaron Silberberg. "Temporal Shaping of Entangled Photons." In: *Physical Review Letters* 94.7 (2005), p. 073601. ISSN: 0031-9007.
- [67] J S Pelc, L Ma, C R Phillips, Q Zhang, C Langrock, O Slattery, X Tang, and M M Fejer. "Long-wavelength-pumped upconversion single-photon detector at 1550 nm: performance and noise analysis." English. In: *Optics Express* 19.22 (2011), pp. 21445–21456.
- [68] Young-Sik Ra, Clément Jacquard, Adrien Dufour, Claude Fabre, and Nicolas Treps. "Tomography of a Mode-Tunable Coherent Single-Photon Subtractor." In: *Physical Review X* 7.3 (2017), p. 031012. ISSN: 2160-3308.
- [69] Matthew T Rakher, Lijun Ma, Oliver Slattery, Xiao Tang, and Kartik Srinivasan. "Quantum transduction of telecommunications-band single photons from a quantum dot by frequency upconversion." In: *Nature Photonics* 4.11 (2010), pp. 786–791.
- [70] Sven Ramelow, Alessandro Fedrizzi, Andreas Poppe, Nathan K Langford, and Anton Zeilinger. "Polarization-entanglement-conserving frequency conversion of photons." In: *Physical Review A* 85.1 (2012), p. 013845.
- [71] M.G. Raymer, S.J. van Enk, C.J. McKinstrie, and H.J. McGuinness. "Interference of two photons of different color." In: *Optics Communications* 283.5 (2010), pp. 747–752. ISSN: 00304018.
- [72] D V Reddy, M G Raymer, C. J. McKinstrie, L Mejling, and K. Rottwitt. "Temporal mode selectivity by frequency conversion in second-order nonlinear optical waveguides." In: *Optics Express* 21.11 (2013), p. 13840. ISSN: 1094-4087.
- [73] Dileep V Reddy and Michael G Raymer. "Photonic temporal-mode multiplexing by quantum frequency conversion in a dichroic-finesse cavity." In: *arXiv preprint arXiv:1708.01705* (2017).
- [74] Dileep V Reddy and Michael G Raymer. "Temporal-mode-selective optical Ramsey interferometry via cascaded frequency conversion." In: *arXiv:1710.06736* (2017).
- [75] J Rehacek, D Mogilevtsev, and Z Hradil. "Operational Tomography: Fitting of Data Patterns." English. In: *Physical Review Letters* 105.1 (2010), p. 010402.
- [76] Joseph M Renes, Robin Blume-Kohout, A J Scott, and Carlton M Caves. "Symmetric informationally complete quantum measurements." English. In: *Journal of Mathematical Physics* 45.6 (2004), pp. 2171–2180.

- [77] Rostislav V Roussev, Carsten Langrock, Jonathan R Kurz, and MM Fejer. "Periodically poled lithium niobate waveguide sum-frequency generator for efficient single-photon detection at communication wavelengths." In: *Optics letters* 29.13 (2004), pp. 1518–1520.
- [78] Helge Rütz, Kai-Hong Luo, Hubertus Suche, and Christine Silberhorn. "Quantum frequency conversion between infrared and ultraviolet." In: *Physical Review Applied* 7.2 (2017), p. 024021.
- [79] A J Scott and M Grassl. "Symmetric informationally complete positive-operator-valued measures: A new computer study." English. In: *Journal of Mathematical Physics* 51.4 (2010), p. 042203.
- [80] Amin Shahverdi, Yong Meng Sua, Lubna Tumeh, and Yu-Ping Huang. "Quantum Parametric Mode Sorting: Beating the Time-Frequency Filtering." In: *Scientific Reports* 7.1 (2017), p. 6495. ISSN: 2045-2322.
- [81] Fabian Steinlechner, Nathaniel Hermosa, Valerio Pruneri, and Juan P Torres. "Frequency conversion of structured light." In: *Scientific reports* 6 (2016).
- [82] Mitsuo Takeda, Hideki Ina, and Seiji Kobayashi. "Fourier-transform method of fringe-pattern analysis for computer-based topography and interferometry." In: *JosA* 72.1 (1982), pp. 156–160.
- [83] Hiroki Takesue. "Single-photon frequency down-conversion experiment." In: *Physical Review A* 82.1 (2010), p. 013833.
- [84] S Tanzilli, Wolfgang Tittel, M Halder, O Alibart, P Baldi, N Gisin, and H Zbinden. "A photonic quantum information interface." In: *Nature* 437.7055 (2005), pp. 116–120.
- [85] P R Tapster and J G Rarity. "Photon statistics of pulsed parametric light." English. In: *Journal of Modern Optics* 45.3 (1998), pp. 595–604.
- [86] Robert Thomas Thew, S Tanzilli, L Krainer, SC Zeller, A Rochas, I Rech, S Cova, Hugo Zbinden, and Nicolas Gisin. "Low jitter up-conversion detectors for telecom wavelength GHz QKD." In: *New Journal of Physics* 8.3 (2006), p. 32.
- [87] R Trebino, P Bownan, P Gabolde, X Gu, S Akturk, and M Kimmel. "Simple devices for measuring complex ultrashort pulses." English. In: *Laser & Photonics Reviews* 3.3 (Apr. 2009), pp. 314–342.
- [88] Alfred B U'Ren, Konrad Banaszek, and Ian A Walmsley. "Photon engineering for quantum information processing." In: *Quantum Information and Computation* 3 (2003), p. 480.

- [89] A. B. U'ren, C Silberhorn, K Banaszek, I A Walmsley, R Erdmann, W P Grice, and M G Raymer. "Generation of Pure-State Single-Photon Wavepackets by Conditional Preparation Based on Spontaneous Parametric Downconversion." In: *Laser Physics* 15.1 (2005), pp. 146–161.
- [90] Aaron P VanDevender and Paul G Kwiat. "Quantum transduction via frequency upconversion (Invited)." English. In: *JOSA B* 24.2 (2007), pp. 295–299.
- [91] Aaron P Vandevender and Paul G Kwiat. "High efficiency single photon detection via frequency up-conversion." In: *Journal of Modern Optics* 51.9-10 (2004), pp. 1433–1445.
- [92] Joshua C Vaughan, Thomas Hornung, T Feurer, and Keith A Nelson. "Diffraction-based femtosecond pulse shaping with a two-dimensional spatial light modulator." English. In: *Optics Letters* 30.3 (Feb. 2005), pp. 323–325.
- [93] Christina E Vollmer, Christoph Baune, Aiko Sambrowski, Tobias Eberle, Vitus Händchen, Jaromír Fiurášek, and Roman Schnabel. "Quantum up-conversion of squeezed vacuum states from 1550 to 532 nm." In: *Physical review letters* 112 (7 2014), p. 073602. ISSN: 1079-7114.
- [94] A. M. Weiner. "Femtosecond pulse shaping using spatial light modulators." In: *Rev. Sci. Instrum.* 71.5 (2000), pp. 1929–1960.
- [95] Andrew M Weiner. "Ultrafast optical pulse shaping: A tutorial review." In: *Optics Communications* 284.15 (2011), pp. 3669–3692.
- [96] William K Wootters and Brian D Fields. "Optimal state-determination by mutually unbiased measurements." In: *Annals of Physics* 191.2 (1989), pp. 363–381.
- [97] Shota Yokoyama, Ryuji Ukai, Seiji C Armstrong, Chanond Sornphiphatphong, Toshiyuki Kaji, Shigenari Suzuki, Jun-ichi Yoshikawa, Hidehiro Yonezawa, Nicolas C Menicucci, and Akira Furusawa. "Ultra-large-scale continuous-variable cluster states multiplexed in the time domain." In: *Nat. Photon.* 7.12 (2013), pp. 982–986.
- [98] Sebastian Zaske, Andreas Lenhard, Christian A Keßler, Jan Kettler, Christian Hepp, Carsten Arend, Roland Albrecht, Wolfgang-Michael Schulz, Michael Jetter, Peter Michler, and Christoph Becher. "Visible-to-telecom quantum frequency conversion of light from a single quantum emitter." In: *Physical review letters* 109 (14 2012), p. 147404. ISSN: 1079-7114.
- [99] Z Zheng and AM Weiner. "Spectral phase correlation of coded femtosecond pulses by second-harmonic generation in thick nonlinear crystals." In: *Optics letters* 25.13 (2000), pp. 984–986.

ACKNOWLEDGMENTS

First, I would like to express my sincere gratitude to Christine Silberhorn for her guidance, patience, and continuous support over the years which gave me the liberty of pursuing crazy and the most fun research ideas.

I want to thank Benjamin Brecht for writing proposals that funded my curiosity; Georg Harder for the car (also other stuff); Kai-Hong-Luo and family for fun work-weekends; Regina Kruse for the *this means you!* sticker on the blue lab; Andreas Christ for keep asking me about experimental progress on time-ordering; Christof Eigner for the nice summer hike in Sauerland; Michael Stefszky for delicious Lamington and then destroying it with Vegemite; Thomas Nitsche for confusing everyone with puns; Viktor Quiring and Raimund Ricken for the magical work in the cleanroom; Markus Allgaier for keeping the dye in the laser; John M Donohue for the *Love letter*; Matteo Santandrea for the amazing KTP waveguide; Linda Sansoni for making Tiramisu; Marcello Massaro for his special expertise during our trip; Johannes Tiedau for discovering RPyC; Irmgard Zimmermann, Rita Prevor, Kerstin Falke, and Nadine Schwarz for taking away the bureaucratic pain. I am also grateful to many others for helping me during my PhD including Harald Herrmann, Jano Gil López, Laura Padberg, Stephan Krapick, Malte Avenhaus, Kaisa Laiho, Tim Bartley, Sonja Barkhofen, Evan Meyer-Scott, Mahnaz Doostdar, Melanie Engelkemeier, Felix vom Bruch, Jan Philipp Höpker, Frederik Thiele, Nicola Montaut, Fabian Katschmann, Helge Rütz, Andreas Schreiber, Hubertus Suche, Thomas Dirmeier, Ganaël Roeland, Marco Barbieri, Emanuele Rocchia, Saleh Rahimi, Nicolas Quesada, and Jan Sperling.

I would like to thank Teresa for her patience and support. Last but not least, I am grateful to my parents and my sister for giving me love and support.

Part II

PUBLICATIONS

AUTHOR PUBLICATIONS AND CONTRIBUTIONS

5.1 MAIN PUBLICATIONS

Ideas, methods, and results presented in this thesis have appeared previously in the following publications.

- [1] V. Ansari and E. Roccia and M. Santandrea and M. Doostdar and C. Eigner and L. Padberg and I. Gianani and M. Sbroscia and J. M. Donohue and L. Mancino and M. Barbieri and C. Silberhorn. “Heralded generation of high-purity ultrashort single photons in programmable temporal shapes.” In: *Optics Express* 26.3, p. 2764 (2018).
- The original idea was conceived by E.R. and M.B.. V.A. and M.D. designed and constructed the experimental setup. V.A., E.R., and M.D. carried out the experiment. M.S., C.E., and L.P. fabricated the waveguided crystal. V.A. wrote the manuscript with contributions from M.B., E.R., and J.M.D.. M.B. and C.S. supervised the project. All authors contributed to the discussion of results and commented on the manuscript.
- [2] M Allgaier, V Ansari, L Sansoni, C Eigner, V Quiring, R Ricken, G Harder, B Brecht, and C Silberhorn. “Highly efficient frequency conversion with bandwidth compression of quantum light.” In: *Nature Communications* 8, p. 14288 (2017).
- V.A. designed and constructed the experimental setup. M.A. and V.A. carried out the experiment. M.A. and G.H. wrote the manuscript. C.E., V.Q. and R.R. fabricated the lithium niobate waveguide. C.S. supervised the project. All authors contributed to the discussion of results and commented on the manuscript.
- [3] V Ansari, G Harder, M Allgaier, B Brecht, and C Silberhorn. “Temporal-mode measurement tomography of a quantum pulse gate.” In: *Physical Review A* 96.6, p. 063817 (2017).
- V.A. designed and constructed the experimental setup. V.A. and G.H. carried out the experiment and co-wrote the manuscript. C.S. supervised the project. All authors contributed to the discussion of results and commented on the manuscript.
- [4] V Ansari, J M Donohue, M Allgaier, L Sansoni, B Brecht, J Roslund, N Treps, G Harder, and C Silberhorn. “Tomography and purification of the temporal-mode structure of quantum light.” In: *arXiv preprint arXiv:1607.03001* (2018).
- V.A. designed and constructed the experimental setup. V.A., J.M.D, and G.H. carried out the experiment and wrote the manuscript.

C.S. supervised the project. All authors contributed to the discussion of results and commented on the manuscript.

- [5] V Ansari, J M Donohue, B Brecht, and C Silberhorn. "Tailoring nonlinear processes for quantum optics with pulsed temporal-mode encodings." In: *Optica* 5(5), 534 (review article) (2018).
- V.A., J.M.D, and B.B. co-wrote the manuscript. C.S. supervised the project and helped refining the article.

5.2 OTHER PUBLICATIONS

The following publications are also developed during my PhD but are not the main focus of this thesis and thus are not included here.

- [1] V Ansari, B Brecht, G Harder, and C Silberhorn. "Probing spectral-temporal correlations with a versatile integrated source of parametric down-conversion states." In: *arXiv preprint arXiv:1404.7725* (2014).
- V.A. and G.H. carried out the experiment. V.A. wrote the manuscript with contributions from B.B. and G.H.. C.S. supervised the project. All authors contributed to the discussion of results and commented on the manuscript.
- [2] G Harder, V Ansari, TJ Bartley, B Brecht, and C Silberhorn. "Harnessing temporal modes for multi-photon quantum information processing based on integrated optics." In: *Phil. Trans. R. Soc. A* 375.2099, p. 20160244 (2017).
- G.H. wrote the manuscript with contributions from V.A.. C.S. supervised the project. All authors contributed to the discussion of results and commented on the manuscript.
- [3] J Sperling, M Bohmann, W Vogel, G Harder, B Brecht, V Ansari, and C Silberhorn. "Uncovering quantum correlations with time-multiplexed click detection." In: *Physical review letters* 115.2, p. 023601 (2015).
- J.S. wrote the manuscript with contributions from M.B. and G.H.. C.S. supervised the project. All authors contributed to the discussion of results and commented on the manuscript.
- [4] M Allgaier, V Ansari, C Eigner, V Quiring, R Ricken, J M Donohue, T Czerniuk, M Aßmann, M Bayer, B Brecht, and C Silberhorn. "Streak camera imaging of single photons at telecom wavelength." In: *Applied Physics Letters* 112.3, p. 031110 (2018).
- M. Allgaier and V.A. carried out the experiment, with the help of T.C. and M. Aßmann to operate and install the streak camera. C.E., V.Q., and R.R. fabricated the lithium niobate sample. M. Allgaier wrote the manuscript. M.B. and C.S. supervised the project. All authors contributed to the discussion of results and commented on the manuscript.

- [5] M Allgaier, G Vigh, V Ansari, C Eigner, V Quiring, R Ricken, B Brecht, and C Silberhorn. “Fast time-domain measurements on telecom single photons.” In: *Quantum Science and Technology* 2.3, p. 034012 (2017).
- M.A. and G.V. carried out the experiment with contributions from V.A., C.E., V.Q., and R.R. fabricated the lithium niobate sample. M.A. wrote the manuscript. C.S. supervised the project. All authors contributed to the discussion of results and commented on the manuscript.
- [6] J Tiedau, V S Shchesnovich, D Mogilevtsev, V Ansari, G Harder, T Bartley, N Korolkova, and C Silberhorn. “Trading quantum states for temporal profiles: tomography by the overlap.” In: *New J. Phys.* 20 033003 (2018).
- J.T. carried out the experiment, with contributions from V.A. and T.B.. J.T. and V.S. wrote the manuscript. T.B., N.K., and C.S. supervised the project. All authors contributed to the discussion of results and commented on the manuscript.

- Title: Heralded generation of high-purity ultrashort single photons in programmable temporal shapes
- Authors: Vahid Ansari, Emanuele Roccia, Matteo Santandrea, Mahnaz Doostdar, Christof Eigner, Laura Padberg, Ilaria Gianani, Marco Sbroscia, John M. Donohue, Luca Mancino, Marco Barbieri, Christine Silberhorn
- Journal: Opt. Express 26(3), 2764-2774
- Year: 2018
- Contributions: The original idea was conceived by E.R. and M.B.. V.A. and M.D. designed and constructed the experimental setup. V.A., E.R., and M.D. carried out the experiment. M.S., C.E., and L.P. fabricated the waveguided crystal. V.A. wrote the manuscript with contributions from M.B., E.R., and J.M.D.. M.B. and C.S. supervised the project. All authors contributed to the discussion of results and commented on the manuscript.

Heralded generation of high-purity ultrashort single photons in programmable temporal shapes

V. ANSARI,^{1,*} E. ROCCIA,² M. SANTANDREA,¹ M. DOOSTDAR,¹ C. EIGNER,¹ L. PADBERG,¹ I. GIANANI,² M. SBROSCIA,² J. M. DONOHUE,¹ L. MANCINO,² M. BARBIERI,² AND C. SILBERHORN¹

¹*Integrated Quantum Optics, Paderborn University, Warburger Strasse 100, 33098 Paderborn, Germany*

²*Dipartimento di Scienze, Università degli Studi Roma Tre, Via della Vasca Navale 84, 00146, Rome, Italy*

**vahid.ansari@uni-paderborn.de*

Abstract: We experimentally demonstrate a source of nearly pure single photons in arbitrary temporal shapes heralded from a parametric down-conversion (PDC) source at telecom wavelengths. The technology is enabled by the tailored dispersion of in-house fabricated waveguides with shaped pump pulses to directly generate the PDC photons in on-demand temporal shapes. We generate PDC photons in Hermite-Gauss and frequency-binned modes and confirm a minimum purity of 0.81, even for complex temporal shapes.

© 2018 Optical Society of America under the terms of the [OSA Open Access Publishing Agreement](#)

OCIS codes: (270.0270) Quantum optics; (320.7110) Ultrafast nonlinear optics; (320.5540) Pulse shaping.

References and links

1. A. N Boto, P. Kok, D. S. Abrams, S. L. Braunstein, C. P. Williams, and J. P. Dowling, "Quantum interferometric optical lithography: exploiting entanglement to beat the diffraction limit," *Phys. Rev. Lett.* **85**(13), 2733 (2000).
2. N. Treps, U. Andersen, B. Buchler, P. K. Lam, A. Maitre, H.-A. Bachor, and C. Fabre, "Surpassing the standard quantum limit for optical imaging using nonclassical multimode light," *Phys. Rev. Lett.* **88**(20), 203601 (2002).
3. N. C. Menicucci, S. T. Flammia, and O. Pfister, "One-way quantum computing in the optical frequency comb," *Phys. Rev. Lett.* **101**(13), 130501 (2008).
4. S. Rahimi-Keshari, T. C. Ralph, and C. M. Caves, "Sufficient conditions for efficient classical simulation of quantum optics," *Phys. Rev. X* **6**(2), 021039 (2016).
5. T. Jennewein, C. Simon, G. Weihs, H. Weinfurter, and A. Zeilinger, "Quantum cryptography with entangled photons," *Phys. Rev. Lett.* **84**(20), 4729–4732 (2000).
6. J. Nunn, L. J. Wright, C. Söller, L. Zhang, I. A. Walmsley, and B. J. Smith, "Large-alphabet time-frequency entangled quantum key distribution by means of time-to-frequency conversion," *Opt. Express* **21**(13), 15959–15973 (2013).
7. T. Zhong, H. Zhou, R. D. Horansky, C. Lee, V. B. Verma, A. E. Lita, A. Restelli, J. C. Bienfang, R. P. Mirin, T. Gerrits, S. W. Nam, F. Marsili, M. D. Shaw, Z. Zhang, L. Wang, D. Englund, G. W. Wornell, J. H. Shapiro, and F. N. C. Wong, "Photon-efficient quantum key distribution using time-energy entanglement with high-dimensional encoding," *New J. Phys.* **17**(2), 022002 (2015).
8. P. J. Mosley, J. Lundeen, B. Smith, P. Wasylczyk, A. B. U'Ren, C. Silberhorn, and I. A. Walmsley, "Heralded generation of ultrafast single photons in pure quantum states," *Phys. Rev. Lett.* **100**(13), 133601 (2008).
9. D. Kielpinski, J. F. Corney, and H. M. Wiseman, "Quantum optical waveform conversion," *Phys. Rev. Lett.* **106**, 130501 (2011).
10. B. Brecht, D. V. Reddy, C. Silberhorn, and M. G. Raymer, "Photon temporal modes: a complete framework for quantum information science," *Phys. Rev. X* **5**(4), 041017 (2015).
11. F. Kaneda, B. G. Christensen, J. Ju. Wong, H. S. Park, K. T. McCusker, and P. G. Kwiat, "Time-multiplexed heralded single-photon source," *Optica* **2**(12), 1010–1013 (2015).
12. R. J. A. Francis-Jones, R. A. Hoggarth, and P. J. Mosley, "All-fiber multiplexed source of high-purity single photons," *Optica* **3**(11), 1270–1273 (2016).
13. W. P. Grice, A. B. U'Ren, and I. A. Walmsley, "Eliminating frequency and space-time correlations in multiphoton states," *Phys. Rev. A* **64**(6), 063815 (2001).
14. Z. D. Walton, M. C. Booth, A. V. Sergienko, B. E. Saleh, and M. C. Teich, "Controllable frequency entanglement via auto-phase-matched spontaneous parametric down-conversion," *Phys. Rev. A* **67**(5), 053810 (2003).
15. O. Kuzucu, M. Fiorentino, M. Albota, F. N. C. Wong, and F. Kärtner, "Two-photon coincident-frequency entanglement via extended phase matching," *Phys. Rev. Lett.* **94**(8), 083601 (2005).
16. P. G. Evans, R. S. Bennink, W. P. Grice, T. S. Humble, and J. Schaake, "Bright source of spectrally uncorrelated polarization-entangled photons with nearly single-mode emission," *Phys. Rev. Lett.* **105**(25), 253601 (2010).

17. A. Eckstein, A. S. Christ, P. J. Mosley, and C. Silberhor, "Highly efficient single-pass source of pulsed single-mode twin beams of light," *Phys. Rev. Lett.* **106**(1), 013603 (2011).
18. R.-B. Jin, R. Shimizu, K. Wakui, H. Benichi, and M. Sasaki, "Widely tunable single photon source with high purity at telecom wavelength," *Opt. Express* **21**(9), 10659–10666 (2013).
19. G. Harder, V. Ansari, B. Brecht, T. Dirmeier, C. Marquardt, and C. Silberhorn, "An optimized photon pair source for quantum circuits," *Opt. Express* **21**(12), 13975–13985 (2013).
20. F. Kaneda, K. Garay-Palmett, A. B. U'Ren, and P. G. Kwiat, "Heralded single-photon source utilizing highly nondegenerate, spectrally factorable spontaneous parametric downconversion," *Opt. Express* **24**(10), 10733–10747 (2016).
21. J. B. Spring, P. L. Mennea, B. J. Metcalf, P. C. Humphreys, J. C. Gates, H. L. Rogers, C. Söller, B. J. Smith, W. S. Kolthammer, P. G. R. Smith, and I. A. Walmsley, "Chip-based array of near-identical, pure, heralded single-photon sources," *Optica* **4**(1), 90–96 (2017).
22. M. Bellini, F. Marin, S. Viciani, A. Zavatta, and F. T. Arecchi, "Nonlocal pulse shaping with entangled photon pairs," *Phys. Rev. Lett.* **90**(4), 043602 (2003).
23. A. Pe'er, B. Dayan, A. A. Friesem, and Y. Silberberg, "Temporal shaping of entangled photons," *Phys. Rev. Lett.* **94**(7), 073601 (2005).
24. S.-Y. Baek, O. Kwon, and Y.-H. Kim, "Temporal shaping of a heralded single-photon wave packet," *Phys. Rev. A* **77**(1), 013829 (2008).
25. J. M. Lukens, A. Dezfooliyani, C. Langrock, M. M. Fejer, D. E. Leaird, and A. M. Weiner, "Orthogonal spectral coding of entangled photons," *Phys. Rev. Lett.* **112**(13), 133602 (2014).
26. C. Bernhard, B. Bessire, T. Feurer, and A. Stefanov, "Shaping frequency-entangled qubits," *Phys. Rev. A* **88**(3), 032322 (2013).
27. A. B. U'Ren, K. Banaszek, and I. A. Walmsley, "Photon engineering for quantum information processing," *Quantum Inf. Comput.* **3**, 480 (2003).
28. E. Meyer-Scott, N. Montaut, J. Tiedau, L. Sansoni, H. Herrmann, T. J. Bartley, and C. Silberhorn, "Limits on the heralding efficiencies and spectral purities of spectrally filtered single photons from photon-pair sources," *Phys. Rev. A* **95**(6), 061803 (2017).
29. A. Acín, N. Brunner, N. Gisin, S. Massar, S. Pironio, and V. Scarani, "Device-independent security of quantum cryptography against collective attacks," *Phys. Rev. Lett.* **98**(23), 230501 (2007).
30. M. Lucamarini, G. Vallone, I. Gianani, P. Mataloni, and G. Di Giuseppe, "Device-independent entanglement-based Bennett 1992 protocol," *Phys. Rev. A* **86**(3), 032325 (2012).
31. Michael Varnava, Daniel E Browne, and Terry Rudolph, "How good must single photon sources and detectors be for efficient linear optical quantum computation?" *Phys. Rev. Lett.* **100**(6), 060502 (2008).
32. Y.-X. Gong, X.-B. Zou, T. C. Ralph, S.-N. Zhu, and G.-C. Guo, "Linear optical quantum computation with imperfect entangled photon-pair sources and inefficient non-photon-number-resolving detectors," *Phys. Rev. A* **81**(5), 052303 (2010).
33. Th. Jennewein, M. Barbieri, and A. G. White, "Single-photon device requirements for operating linear optics quantum computing outside the post-selection basis," *J. Mod. Opt.* **58**(3-4), 276–287 (2011).
34. J. M. Donohue, M. Mastrovich, and K. J. Resch, "Spectrally engineering photonic entanglement with a time lens," *Phys. Rev. Lett.* **117**(24), 243602 (2016).
35. N. Matsuda, "Deterministic reshaping of single-photon spectra using cross-phase modulation," *Sci. Adv.* **2**(3), e1501223 (2016).
36. M. Allgaier, V. Ansari, L. Sansoni, C. Eigner, V. Quiring, R. Ricken, G. Harder, B. Brecht, and C. Silberhorn, "Highly efficient frequency conversion with bandwidth compression of quantum light," *Nat. Commun.* **8**, 14288 (2017).
37. V. Averchenko, D. Sych, G. Schunk, U. Vogl, C. Marquardt, and G. Leuchs, "Temporal shaping of single photons enabled by entanglement," *Phys. Rev. A* **96**(4), 043822 (2017).
38. K. A. G. Fisher, D. G. England, J.-P. W. MacLean, P. J. Bustard, K. J. Resch, and B. J. Sussman, "Frequency and bandwidth conversion of single photons in a room-temperature diamond quantum memory," *Nat. Commun.* **7**, 11200 (2016).
39. M. Karpiński, Mi. Jachura, L. J Wright, and B. J Smith, "Bandwidth manipulation of quantum light by an electro-optic time lens," *Nat. Photonics* **11**, 53–57 (2017).
40. P. T. Callahan, K. Safak, P. Battle, T. D. Roberts, and F. X. Kärtner, "Fiber-coupled balanced optical cross-correlator using PPKTP waveguides," *Opt. Express* **22**(8), 9749–9758 (2014).
41. C. K. Law, I. A. Walmsley, and J. H. Eberly, "Continuous frequency entanglement: effective finite hilbert space and entropy control," *Phys. Rev. Lett.* **84**(23), 5304–5307 (2000).
42. J. H. Eberly, "Schmidt analysis of pure-state entanglement," *Laser Phys.* **16**(6), 921–926 (2006).
43. A. Christ, K. Laiho, A. Eckstein, K. N. Cassemiro, and C. Silberhorn, "Probing multimode squeezing with correlation functions," *New J. Phys.* **13**(3), 033027 (2011).
44. W. Mauerer, M. Avenhaus, W. Helwig, and C. Silberhorn, "How colors influence numbers: Photon statistics of parametric down-conversion," *Phys. Rev. A* **80**(5), 053815 (2009).
45. A. B. U'Ren, C. Silberhorn, K. Banaszek, I. A. Walmsley, R. K. Erdmann, W. P. Grice, and M. G. Raymer, "Generation of pure-state single-photon wavepackets by conditional preparation based on spontaneous parametric downconversion," *Laser Phys.* **15**(1), 146–161 (2005).

46. J. C. Vaughan, T. Hornung, T. Feurer, and K. A. Nelson, "Diffraction-based femtosecond pulse shaping with a two-dimensional spatial light modulator," *Opt. Lett.* **30**(3), 323–325 (2005).
47. E. Frumker and Y. Silberberg, "Phase and amplitude pulse shaping with two-dimensional phase-only spatial light modulators," *J. Opt. Soc. Am. B* **24**(12), 2940–2947 (2007).
48. M. Takeda, H. Ina, and S. Kobayashi, "Fourier-transform method of fringe-pattern analysis for computer-based topography and interferometry," *J. Opt. Soc. Am. A* **72**(1), 156–160 (1982).
49. R. Regener and W. Sohler, "Loss in low-finesse Ti:LiNbO₃ optical waveguide resonators," *Appl Phys B-Lasers O.* **36**(3), 143–147 (1985).
50. D.N. Klyshko, "Use of two-photon light for absolute calibration of photoelectric detectors," *Quantum Electron.* **10**(9), 1112–1117 (1980).
51. X. Cao, J. Natour, R. V. Ramaswamy, and R. Srivastava, "Effect of waveguide uniformity on phase matching for frequency conversion in channel waveguides," *Appl. Phys. Lett.* **58**(21), 2331–2333 (1991).
52. S. Helmfrid, G. Arvidsson, and J. Webjörn, "Influence of various imperfections on the conversion efficiency of second-harmonic generation in quasi-phase-matching lithium niobate waveguides," *J. Opt. Soc. Am. B* **10**(2), 222–229 (1993).
53. M. L. Bortz, S.J. Field, M. M. Fejer, D. W. Nam, R. G. Waarts, and D.F. Welch, "Noncritical quasi-phase-matched second harmonic generation in an annealed proton-exchanged LiNbO₃ waveguide," *IEEE J. Quantum Electron.* **30**(12), 2953–2960 (1994).
54. I. Cristiani, C. Liberale, V. Degiorgio, G. Tartarini, and P. Bassi, "Nonlinear characterization and modeling of periodically poled lithium niobate waveguides for 1.5- μ m-band cascaded wavelength conversion," *Opt. Commun.* **187**(1), 263–270 (2001).
55. E. J. Lim, S. Matsumoto, and M. M. Fejer, "Noncritical phase matching for guided-wave frequency conversion," *Appl. Phys. Lett.* **57**(22), 2294–2296 (1990).
56. K. Laiho, A. Christ, K. N. Cassemiro, and C. Silberhorn, "Testing spectral filters as Gaussian quantum optical channels," *Opt. Lett.* **36**(8), 1476–1478 (2011).
57. M. Avenhaus, A. Eckstein, P. J. Mosley, and C. Silberhorn, "Fiber-assisted single-photon spectrograph," *Opt. Lett.* **34**(18), 2873–2875 (2009).
58. P. R. Tapster and J. G. Rarity, "Photon statistics of pulsed parametric light," *J. Mod. Opt.* **45**(3), 595–604 (1998).
59. A. Dosseva, L. Cincio, and A. M. Brańczyk, "Shaping the joint spectrum of down-converted photons through optimized custom poling," *Phys. Rev. A* **93**(1), 013801 (2016).
60. F. Graffitti, D. Kundys, D. T. Reid, A. M. Brańczyk, and A. Fedrizzi, "Pure down-conversion photons through sub-coherence-length domain engineering," *Quantum Science and Technology* **2**(3), 035001 (2017).

1. Introduction

Preparing single photons in pure and controlled spectral-temporal modes is a key requirement for quantum photonic technologies. Diverse applications including quantum-enhanced metrology [1,2], quantum computation [3,4], and quantum encryption [5–7] rely on high-contrast interference through stable sources of pure single photons. In addition, widely customisable and precisely controllable temporal-mode shaping is necessary to ensure mode matching between individual sources [8], facilitate coupling between nodes in a quantum network [9], and enable temporal-mode based quantum communication [10] and source multiplexing [11, 12], among other applications. Furthermore, sources with high brightness are essential for scalable performance, and spatially single-mode behaviour is necessary for coupling to optical fibre networks and integrated waveguide devices.

Sources based on parametric downconversion (PDC) have granted a simple solution to heralded single-photon generation for decades, but have not yet satisfied all of the above requirements simultaneously. Most PDC sources generate photons with strong spectral correlations which is undesirable for heralded single-photon sources. However, it is possible to minimise the spectral correlation in crystals offering specific dispersion properties along with an adapted pump bandwidth [8, 13–21]. This specific dispersion property is linked to the group velocities of the pump and the PDC photons and can be summarised in two categories: matching the group velocity of the pump photon with one of the PDC photons [8, 20], or having the group velocity of the pump between the two PDC photons [15, 17–19].

On the other hand, efficient temporal-mode shaping of the PDC photons is more challenging. Existing methods to create a broadband single photon in an arbitrary temporal mode rely on carving out the desired mode from the original wavepacket as depicted in Fig. 1(a), which

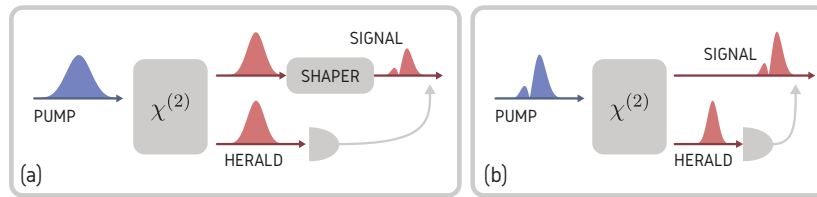


Fig. 1. Heralded source of temporally shaped single-photons. (a) The desired temporal mode can be carved out of PDC photons after the generation, which inevitably reduces the heralding efficiency. (b) With an appropriately designed pump field and group-velocity engineered nonlinear medium, the PDC photons are emitted directly in a desired temporal shape. In both scenarios the purity of heralded single photon rely on the separability of the PDC state in terms of signal and herald fields.

can be accurately achieved by temporal or spectral modulation of the photon [22–26]. This method, however, necessarily introduces loss and leads to a reduced rate of prepared photons [27] and a low pair-symmetric heralding efficiencies [28]; this poses a practical limit for many experiments such as device-independent quantum cryptography [29,30] and optical quantum computing [31–33]. Temporal manipulation is also possible with shaped-pulse mediated nonlinear interactions [9,34–37], Raman interfaces [38], or ultrafast electro-optic modulation [39], but these methods are experimentally challenging to implement without prohibitive loss. To minimise the potential for photon loss, a source which generates heralded photons in a customisable and pure spectral state is highly desirable.

In this letter, we take a novel approach to directly create PDC photons with tailored temporal-modes. Through group-velocity matching two of the interacting fields in the PDC process, we generate heralded photons which inherit the temporal shape of the pump pulse, as sketched in Fig. 1(b). We show through joint spectral measurements and second-order photon number correlations that the photons are generated in a highly pure state. We explicitly demonstrate the versatility of our source design by generating photons with customised temporal shapes, such as broadband Hermite-Gaussian temporal modes and narrow frequency bins. Our source is based on the in-house fabricated unpoled KTP waveguides and emits in the near-infrared telecommunications regime, making it a prime candidate for use in long-distance quantum protocols and fibre-based networks. Our result bridges an important gap in quantum state engineering of time-frequency modes, and enables a range of quantum photonic applications that require temporal-mode matching.

2. Theory

The PDC process in the waveguides happens when the energy conservation $\omega_p = \omega_s + \omega_i$ and the momentum conservation $k_p = k_s + k_i$ between the three fields — pump, signal, and idler — are satisfied. The momentum conservation with waveguided collinear propagation is typically achieved with quasi-phasematching through periodic poling. In our case, we consider a type-II PDC process where momentum conservation is enabled by birefringent phasematching without a need for periodic poling. The waveguided structure we consider is made with a z-cut KTP substrate and waveguides fabricated along the x-axis of the crystal with rubidium ion exchange. To calculate the effective refractive indices of the optical fields inside of the Rb:KTP waveguide, we use a commercial finite-element mode solver along with a model for the refractive index profile provided in [40]. Theoretically calculated phasematched type-II processes for different pump wavelengths are plotted in Fig. 2(a) as solid lines, where we also experimentally verified our model (see the caption).

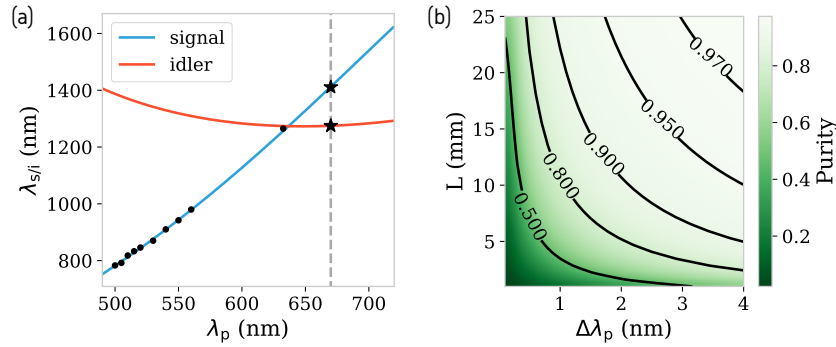


Fig. 2. (a) Birefringent phasematched type-II PDC processes in the KTP waveguide versus pump wavelength. The pump and idler photons are TE polarised and the signal photon is TM polarised. The dots correspond to experimentally measured PDC photons with a tunable pulsed pump laser and a single-photon sensitive spectrometer. The data point at the degeneracy point, however, is measured by means of second harmonic generation with a pulsed pump at the central wavelength of 1275 nm. The error bars are smaller than the markers. To generate a single-mode JSA we use the AGVM condition which holds for a pump wavelength of 670 nm (indicated with the vertical dashed line) and a signal and idler wavelengths of 1411 nm and 1276 nm, respectively (star markers). (b) Theoretical spectral purity of the JSA for different pump bandwidths $\Delta\lambda_p$ and crystal lengths L .

The Hamiltonian of type-II PDC process is

$$\hat{H}_{\text{PDC}} \propto \iint f(\omega_s, \omega_i) \hat{a}_{\text{TM}}^\dagger(\omega_s) \hat{a}_{\text{TE}}^\dagger(\omega_i) d\omega_s d\omega_i + \text{h.c.}, \quad (1)$$

where $a^\dagger(\omega)$ is the standard creation operator at frequency ω . The joint spectral amplitude (JSA) function

$$f(\omega_s, \omega_i) = \alpha(\omega_s + \omega_i) \phi(\omega_s, \omega_i), \quad (2)$$

describes the spectral-temporal properties of the PDC state, where $\alpha(\omega_s + \omega_i)$ is the ultrashort pump amplitude function and $\phi(\omega_s, \omega_i)$ is the phasematching function expressing the momentum conservation between the fields in the waveguide. Due to energy conservation, PDC sources typically exhibit spectral correlations. However, many applications benefit from spectrally pure single-photon states with separable JSAs of the form

$$f(\omega_s, \omega_i) \approx g(\omega_s) h(\omega_i), \quad (3)$$

which can be achieved by dispersion engineering.

The strength of spectral correlations in the PDC state can be quantified by a Schmidt decomposition of the JSA function [41, 42]. This defines the Schmidt number K as the effective number of temporal-modes in the state. An experimentally accessible method to measure the Schmidt number and the purity \mathcal{P} of the PDC photons is by means of second-order correlation function $g^{(2)}(\tau = 0)$ of unheralded signal or idler photons as [43]

$$\mathcal{P} = \frac{1}{K} = g^{(2)}(0) - 1. \quad (4)$$

In the case of spectrally pure PDC state with $K = 1$, the partial trace of the PDC state exhibits thermal photon number statistics corresponding to $g^{(2)}(0) = 2$. With a multimode state, we would

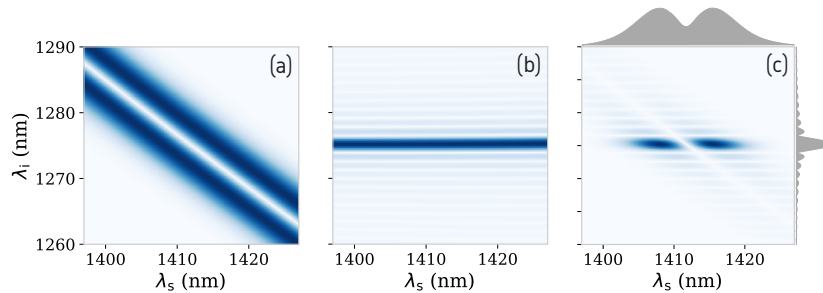


Fig. 3. (a) The absolute value of the pump spectrum $|\alpha(\omega_p = \omega_s + \omega_i)|$ with the first-order Hermite-Gaussian profile with FWHM of 2 nm. (b) Phasematching function $|\phi(\omega_s, \omega_i)|$ of a KTP waveguide with a length of 16 mm. (c) Theoretical joint spectral amplitude $|f(\omega_s, \omega_i)|$ of the PDC state and its marginal distributions. The modelled JSA shows a Schmidt number of $K = 1.087$ and a spectral purity of $\mathcal{P} = 0.919$. All functions are plotted against wavelengths (instead of angular frequencies ω_j) to provide a convenient comparison with the experimental data.

measure a convolution of all the different thermal photon statistics, since the detector cannot discriminate each mode, which results in a Poissonian photon-number distribution and a $g^{(2)}(0)$ that approaches 1 [44].

To realise a single-mode JSA we exploit a phasematching with matched group-velocities of pump and signal fields, known as the asymmetric group-velocity matching (AGVM) condition [45]. This condition holds for a pump wavelength of 670 nm (TE polarised) and a signal wavelength of 1411 nm (TM polarised), which are marked with stars in Fig. 2(a). In order to find the experimental settings for an optimum spectral purity, we calculate \mathcal{P} for different pump pulse bandwidths and crystal lengths as plotted in Fig. 2(b). In our experimental implementation, we use the AGVM condition with a pump spectral FWHM of 2 nm and a crystal length of 16 mm. This configuration leads to a nearly single-mode JSA as plotted in Fig. 3, where we plot the JSA function with the pump in the first-order Hermite-Gauss mode. From the JSA and its marginal distributions in Fig. 3(c), it is clear that the phasematching function is mapped onto the idler photon, while the spectral profile of the pump is imparted into the signal photon. A similar AGVM condition can be also achieved in a periodically poled bulk KTP but at wavelengths outside of the telecom bands [20]. Additionally, the waveguided structure, in comparison to bulk, accommodates a longer interaction length and a stronger field confinement, allowing for higher parametric gains and narrower phasematching functions. Note that a narrow phasematching is crucial for high fidelity shaping of the signal photon.

3. Experiment

The outline of the experimental setup is given in Fig. 4. To prepare the pump of the PDC process, we take ultrashort pulses at the central wavelength of 670 nm (from a frequency doubled optical parametric oscillator) (Coherent Chameleon OPO with APE HarmoniXX) and use a pulse shaper to carve out the desired temporal modes. The pulse shaper is a folded 4f-setup consist of a magnifying telescope, a holographic diffraction grating with 2000 lines per mm (Spectrogon), a cylindrical silver mirror and a two-dimensional reflective liquid crystal on silicon spatial light modulator (Hamamatsu X10468-07 LCoS-SLM) [46, 47]. This 4f-setup has a spectral resolution of 35 pm which along with the initial 6 nm bandwidth of our laser system, allows us to accurately prepare e.g. Hermite-Gaussian pulses of up to fourth order with 2 nm of FWHM for the Gaussian profile. We use spectral interferometry to characterise the performance of the pulse shaper and

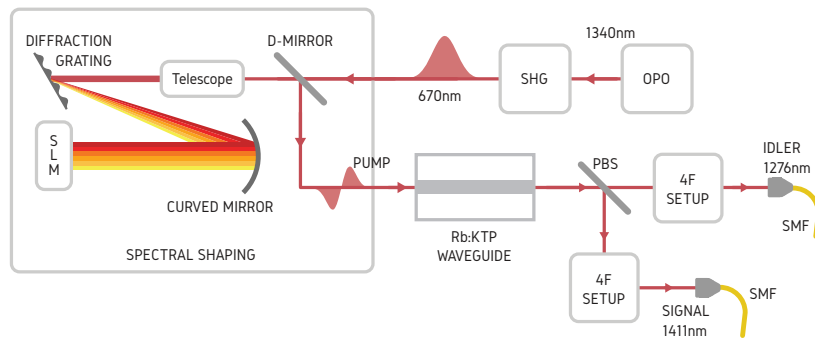


Fig. 4. Experimental setup. To prepare ultrashort pump pulses at 670 nm we take second harmonics (SHG) of an optical parametric oscillator (OPO). In the spectral shaping setup, we use a reflective spatial light modulator (SLM) in a folded 4f-setup to shape the spectral amplitude and phase of the pump field. A telescope is used to match the size of each frequency component with SLM's pixels to get an optimum resolution. The SLM reflects the beam at a slightly different angle which displaces the reflected beam vertically and allows us to collect the reflected beam with a d-shaped mirror. The generated PDC photons are separated on a broadband polarising beamsplitter (PBS). We use 4f-setsups for both PDC photons to filter the undesirable background. Finally each beam is coupled into single-mode fibres (SMF) for telecom wavelengths.

ensure a dispersion-free alignment [48].

The heart of the experiment is a 16 mm long in-house built Rb:KTP waveguide with a nominal width of $3\ \mu\text{m}$ and depth of $5\ \mu\text{m}$, designed to be spatially single-mode over the whole telecom range for both TE and TM polarisations. The sample is produced in a two-step process. At first, KTP sample with dimensions of about $20 \times 6 \times 1\ \text{mm}^3$ is immersed in a pure KNO_3 melt to homogenize the sample composition. In a second step, after a titanium mask is patterned on the +c face of the sample using standard photolithography to define waveguide structures with different widths, the sample is immersed in a $\text{RbNO}_3/\text{KNO}_3/\text{Ba}(\text{NO}_3)_2$ melt, where K^+ ions in the crystal are exchanged with Rb^+ ions present in the melt. After removing the Ti mask, the sample facets are polished to provide a smooth surface suitable for free space coupling and fibre pigtailling.

To couple the laser to the waveguide, we use a aspheric lens with a focal length of 8 mm. Using the Fabry-Perot interferometric method [49] we measure internal waveguide average losses of 0.85 dB/cm (with a minimum of 0.66 dB/cm and a maximum of 1.15 dB/cm) and 0.67 dB/cm (with a minimum of 0.53 dB/cm and a maximum of 0.78 dB/cm) at 1550 nm for TE and TM polarisations, respectively. To estimate the maximum achievable coupling efficiency of the waveguide mode into the standard single-mode telecom fibre (SMF-28) we use bright lasers matched with central frequencies of the PDC photons and measure coupling efficiencies of 0.65 and 0.60 for idler (TE) and signal (TM) photons, respectively. This is due to asymmetry of the waveguide mode which can be designed to be more symmetric at any chosen wavelength by modifying the fabrication parameters e.g. the diffusion depth. The waveguide used in this work has a more symmetric mode profile at 1550 nm where we measure a coupling efficiency of more than 0.80.

3.1. Heralding efficiency and brightness

To spectrally filter the pump field and the parasitic background noise, we use folded 4f-setsups in each arm, aligned around the central frequencies of PDC photons. The total transmissions

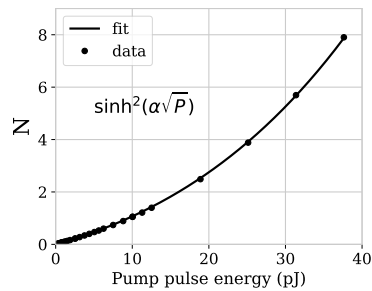


Fig. 5. Mean photon number N of one PDC arm versus pump pulse energy. The pump pulse energy is measured after the waveguide to account for the incoupling loss. The only fit parameter used for the fitting function $\sinh^2(\alpha\sqrt{P})$ is $\alpha = 0.28$.

of 4f-setups are 0.26 and 0.30 for signal and idler photons, respectively, owing principally to a low diffraction efficiency of the diffraction gratings. The PDC photons are then detected with fibre coupled superconducting nanowire single photon detectors (SNSPD) (Photon Spot) with system detection efficiencies of 0.41 and 0.55 at 1276 nm and 1411 nm, respectively. With this configuration we measure Klyshko efficiencies (coincidences over the single counts of each arm [50]) of $(8 \pm 0.01)\%$ and $(5 \pm 0.02)\%$ for signal and idler photons, respectively. A normalisation over the transmission of 4f-setups (which can be replaced with bandpass filters with very high transmissivities) and detection efficiencies suggests that these Klyshko efficiencies can be improved to around 56% and 40% for signal and idler photons, respectively. These efficiencies can be further improved by using anti-reflective coatings on the KTP waveguide facet and the fibres.

To benchmark the brightness of the source, in in Fig. 5 we plot the generated mean photon number versus pump pulse energy. For this measurement, we calibrate the detected counts using the Klyshko method [50]. When we drive the waveguide with a pump pulse energy of 37.5 pJ, the source generates states with a mean photon number of about 8. The mean photon number follows the expected curve for a single-mode source at relatively low pump powers. The comparably high brightness of the source is due to long waveguide length, the use of birefringent phasematching, and the relatively single-mode character of the source.

3.2. Spectral characterisation

To measure the spectrum of the idler photon, we use the 4f-setup in the monochromator configuration, with a spectral resolution of 0.2 nm. With the AGVM condition, as can be seen in Fig. 3(c), the spectrum of the idler photon echoes the phasematching function $\phi(\omega_s, \omega_i)$. The measured spectrum of the idler photon and its theoretical counterpart are plotted in Fig. 6(a). The discrepancy between experiment and theory can be explained by considering the waveguide inhomogeneities [51–54]. Inhomogeneity of the waveguide channel, e.g. non-uniform width or depth, can change the effective refractive index along the propagation direction and consequently distort the phasematching function. This can be understood by regarding the inhomogeneous waveguide as many short homogeneous segments with different phasematching conditions $\Delta k(\omega_s, \omega_i) = k_p(\omega_s + \omega_i) - k_s(\omega_s) - k_i(\omega_i)$. The overall phasematching distribution then would be a sum of all of these segments, which is a coherent mixture of many sinc-shaped functions with different widths and central frequencies. This depends on the exact form of inhomogeneities, but in general these inhomogeneities effectively broaden the phasematching function. A known solution to this is to design the waveguide geometry insensitive to these inhomogeneities (known as noncritical phase-matching) [53, 55]. We are currently conducting a comprehensive study of

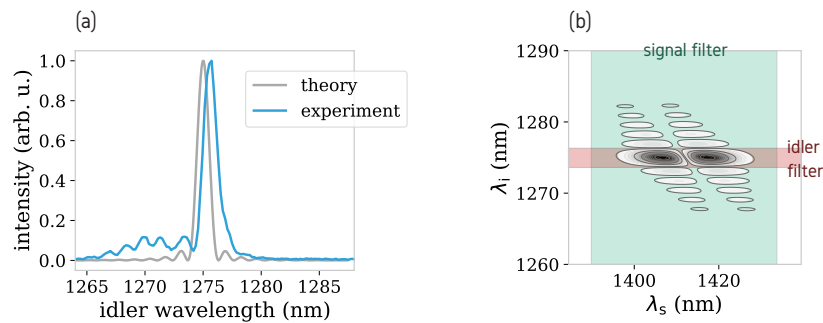


Fig. 6. (a) Theoretical and experimentally measured phasematching functions $|\phi(\omega_s, \omega_i)|$. (b) A contour plot of the theoretical JSA function and the bandpass filters to remove the phasematching sidelobes. The widths of filters in signal and idler arms are 45 nm and 3 nm, respectively. Without any spectral filtering, the JSA features a Schmidt number $K = 1.12$ which increases to $K = 1.03$ when the idler filter is applied. Due to the specific distribution of JSA, filtering the signal photons cannot remove the phasematching sidelobes.

this matter.

The broadened phasematching with asymmetric side-lobes, seen in Fig. 6(a), diminishes the spectral purity and the fidelity of single photon shaping, hence we use spectral filtering (with a width of 3 nm) on the idler photons to remove the side-lobes, as shown in Fig. 6(b). From the distribution of the JSA, it is evident that removing the phasematching sidelobes is only possible by filtering the idler photons. This filtering, however, results in an imbalanced Schmidt number K between the signal and idler photons [56]. Nonetheless, since we are interested in heralding signal photons upon detection of idler photons, the heralded photons inherit the lowest Schmidt number K , which consequently yields a high purity.

To measure joint spectral intensity (JSI) distribution $|f(\omega_s, \omega_i)|^2$, we combine the monochromator in the idler arm with a time-of-flight spectrometer in the signal arm [57]. In the time-of-flight spectrometer we use a highly dispersive fibre to map the spectrum into the temporal profile which can be resolved directly in time on SNSPDs. We use a 4.3 km long fibre with a total dispersion of 0.3 ns/nm which, alongside with 70 ps timing resolution of SNSPD, constitute a spectrometer with a resolution of about 0.2 nm. The measured JSIs with the pump field in the first four Hermite-Gauss modes and five frequency bins are plotted in Fig. 7. The Schmidt number inferred from these JSIs shows a spectral purity of more than 0.98, which provides an upper bound on the spectral purity.

3.3. Purity and second-order correlation function

As discussed in the theory section, spectral correlations between PDC photons leads to impurity of the heralded single photons. Although the JSI measurement provides important information about the spectral correlation of the PDC photons, it is blind to the spectral phase of the photons and is also limited by the resolution of the spectrometers. A better measure of any underlying correlations of the PDC photons is the second-order correlation function $g^{(2)}(0)$ of signal or idler photons, as measured with a 50/50 fibre coupler [43, 58]. The $g^{(2)}(0)$ measurement probes the photon number statistics of unheralded beams (signal or idler) and can discriminate between a single-mode PDC state with $g^{(2)}(0) = 2$ and a highly multimode state with $g^{(2)}(0) = 1$. In Fig. 8 we plot the $g^{(2)}(0)$ of the both PDC photons with the pump pulse in different orders of Hermite-Gauss modes and bandwidths ranging from 0.5 nm to 3 nm. With a narrow pump bandwidth, energy correlations remain in the PDC state which are exhibited in lower $g^{(2)}(0)$

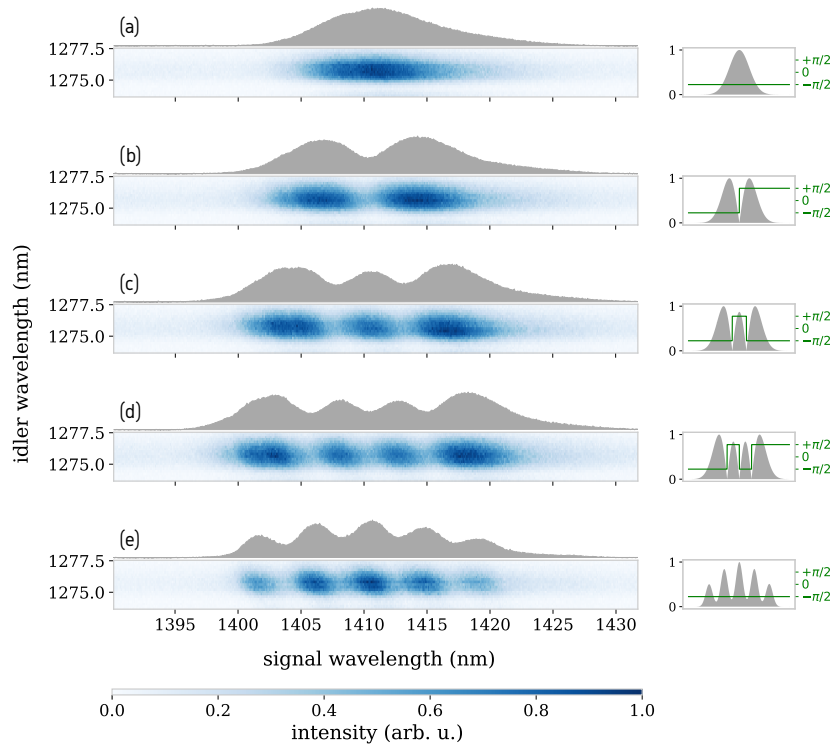


Fig. 7. A few examples of the measured joint spectral intensities (JSIs), with the marginal spectral distribution of signal photon above in grey. The pump mode for each JSI is shown on the right side, where the grey shaded area is the spectral amplitude and the green line is the spectral phase. The pump modes are as the following: (a) Gaussian, (b) 1st-order Hermite-Gaussian, (c) 2nd-order Hermite-Gaussian, (d) 3rd-order Hermite-Gaussian, (e) frequency bins, with Schmidt numbers: $K_a = 1.01$, $K_b = 1.01$, $K_c = 1.02$, $K_d = 1.02$, $K_e = 1.02$.

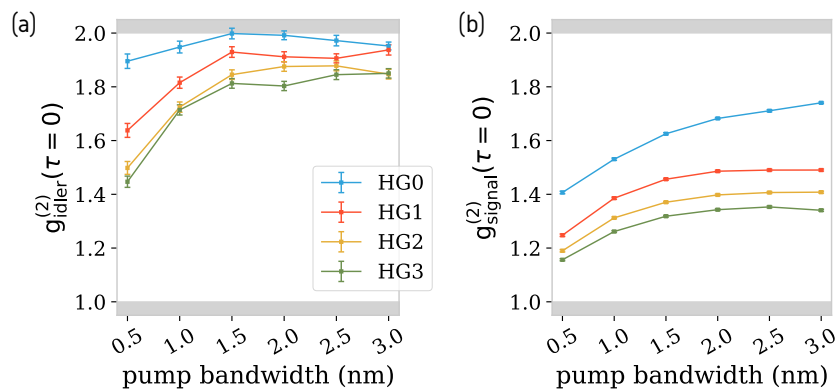


Fig. 8. The second-order correlation measurements of the idler and signal photons with the pump set to different bandwidths and different orders of Hermite-Gaussian modes. The error bars for the $g_{\text{signal}}^{(2)}(\tau = 0)$ are smaller than the markers.

values. For the idler photon, we spectrally filter the asymmetric phasematching side-lobes (see Fig. 6), and we achieve the highest $g^{(2)}(0)$ of 1.99 ± 0.02 with a 1.5 nm broad Gaussian pump pulse, which reduces to 1.93 ± 0.02 , 1.85 ± 0.02 , and 1.81 ± 0.02 for the first, second, and third order Hermite-Gauss modes, respectively. The corresponding purities can be calculated through Eq. (4). This reduction in the $g^{(2)}(0)$ value is also expected from theory. With increasing order of Hermite-Gauss modes, these function feature more complex structures spanned over a broader frequency range which inevitably increases the frequency anti-correlations between signal and idler (see Fig. 3(a)). Despite this, it is possible to achieve a high purity with an appropriately designed crystal length.

The $g^{(2)}(0)$ of signal photons, plotted in Fig. 8(b), is considerably lower. This is due to the presence of the phasematching side-lobes which cannot be simply filtered for the signal photons (see Fig. 6(b)). While the signal photons are themselves less pure, the high $g^{(2)}(0)$ of the idler indicates that the shaped signal photons are highly pure when heralded by an idler detection. However, this purity comes at a cost of heralding efficiency. Enhancing the waveguide fabrication technology or using methods such as noncritical phasematching [55] or aperiodic poling [59, 60] may be able to eliminate these unwanted spectral features to produce filter-free heralded photons with high purities and arbitrary temporal shapes.

3.4. Conclusion

We have shown that heralded single photons can be generated in arbitrary temporal modes using pulse shaping and KTP waveguides with an optimised dispersion. Through joint spectral intensity measurements, we have verified that the spectral shape of the pump pulse is faithfully imparted onto the signal photon. Second-order photon number correlations measurements show that the heralded photon state is highly pure and suitable for use in quantum networks. Our integrated source is based on birefringent phasematching and emits within the telecommunications band. Future work will focus on adapting the source with periodic poling to optimise the emission wavelengths for available photon detectors and customise the joint spectral amplitude to eliminate the need for filtering. With these optimisations, the source presented here will prove to be a vital component in applications such as temporal-mode based quantum communication and mode matching between quantum interfaces.

Funding

Gottfried Wilhelm Leibniz-Preis; European Union's Horizon 2020 Research and Innovation Programme (665148).

Acknowledgments

E.R. thanks the integrated quantum optics group for their hospitality during the completion of this work. We thank Fabio Sciarrino for fruitful discussion.

- Title:** Highly efficient frequency conversion with bandwidth compression of quantum light
- Authors:** Markus Allgaier, Vahid Ansari, Linda Sansoni, Christof Eigner, Viktor Quiring, Raimund Ricken, Georg Harder, Benjamin Brecht, Christine Silberhorn
- Journal:** Nature Communications 8, 14288
- Year:** 2017
- Contributions:** V.A. designed and constructed the experimental setup. M.A. and V.A. carried out the experiment. M.A. and G.H. wrote the manuscript. C.E., V.Q. and R.R. fabricated the lithium niobate waveguide. C.S. supervised the project. All authors contributed to the discussion of results and commented on the manuscript.

ARTICLE

Received 8 Oct 2016 | Accepted 16 Dec 2016 | Published 30 Jan 2017

DOI: 10.1038/ncomms14288

OPEN

Highly efficient frequency conversion with bandwidth compression of quantum light

Markus Allgaier¹, Vahid Ansari¹, Linda Sansoni¹, Christof Eigner¹, Viktor Quiring¹, Raimund Ricken¹, Georg Harder¹, Benjamin Brecht^{1,2} & Christine Silberhorn¹

Hybrid quantum networks rely on efficient interfacing of dissimilar quantum nodes, as elements based on parametric downconversion sources, quantum dots, colour centres or atoms are fundamentally different in their frequencies and bandwidths. Although pulse manipulation has been demonstrated in very different systems, to date no interface exists that provides both an efficient bandwidth compression and a substantial frequency translation at the same time. Here we demonstrate an engineered sum-frequency-conversion process in lithium niobate that achieves both goals. We convert pure photons at telecom wavelengths to the visible range while compressing the bandwidth by a factor of 7.47 under preservation of non-classical photon-number statistics. We achieve internal conversion efficiencies of 61.5%, significantly outperforming spectral filtering for bandwidth compression. Our system thus makes the connection between previously incompatible quantum systems as a step towards usable quantum networks.

¹Integrated Quantum Optics, Applied Physics, University of Paderborn, Paderborn 33098, Germany. ²Clarendon Laboratory, Department of Physics, University of Oxford, Oxford OX1 3PU, UK. Correspondence and requests for materials should be addressed to M.A. (email: markus.allgaier@uni-paderborn.de).

Photons play the important role of transmitting quantum information between nodes in a quantum network¹. However, systems employed for different tasks such as generation, storage and manipulation of quantum states are in general spectrally incompatible. Therefore, interfaces to adapt the central frequency and bandwidth of the photons are crucial^{2–4}. To achieve any viable bandwidth compression, the interface has to provide at least a net gain over using spectral filters. Electro-optical frequency conversion can provide such high efficiencies for bandwidth compression⁴ and shearing⁵ of quantum pulses. However, it is limited to frequency shifts of a few hundred gigahertz. Optical frequency conversion in nonlinear crystals offers both large frequency shifts as well as high conversion efficiencies^{6–10}. Operating on chirped pulses allows to perform spectral shaping¹¹, an approach with which a bandwidth compression of 40 has been demonstrated^{2,12}, however, with low efficiencies below spectral filtering. Reaching high conversion efficiencies with this method is challenging, as very broad phasematching is required, which in turn limits the allowed interaction lengths and hence the conversion efficiencies. An alternative approach is to engineer the phasematching of the sum-frequency process itself¹³ by choosing appropriate group velocity and pump-pulse conditions. Such engineering has been widely exploited for parametric downconversion (PDC)^{14–17} to produce decorrelated photon pairs efficiently. For frequency conversion, this approach has not been investigated.

The quantum pulse gate (QPG)^{9,18–20} is such a device that exploits specific group-velocity conditions: The input and the pump are group-velocity matched, while the output is strongly group-velocity mismatched. This is achieved in a type-II sum-frequency process in a periodically poled titanium-indiffused waveguide in lithium niobate. The group-velocity matching ensures that spectrally broad input pulses overlap throughout the crystal while the mismatch with the output in combination with the long interaction length inside the waveguide results in a narrow output spectrum. Furthermore, the output temporal mode, that is, the temporal or spectral amplitude of the output pulse, only depends on the phasematching and not on the pump or input fields. This allows to convert any input to the same narrow output. It can thus interface broad PDC sources as well as narrower and even dissimilar emitters, such as quantum dots.

To demonstrate the performance of the QPG as an interface, we focus on its application as a link between PDC sources and quantum memories to produce on-demand single photons. Ideally for quantum networks, single photons are generated into well-defined optical modes and feature compatibility with low-loss fibre networks. Heralded photons from engineered, single-pass PDC fulfill these requirements^{21,22}. One class of quantum memories, Raman quantum memories, can exhibit very broad spectral bandwidths of a few gigahertz²³ up to 20 GHz (refs 24,25). Long storage times have been achieved in alkali vapour memories with bandwidths of up to several gigahertz²⁶; however, these are narrowband compared with the above-mentioned PDC sources with bandwidths in the terahertz regime²². In diamond, terahertz bandwidth can be achieved²⁷, but both storage time and memory efficiency are low, such that these memories cannot be utilized in quantum networks, yet. In principle, schemes exist to match both systems directly by using a very broad memory²⁷ or strong spectral filtering of a correlated PDC source²⁸, but these come at the expense of short storage times or reduced purities through spectral filtering²⁹. A bandwidth-compressing interface between the broadband PDC sources at telecom wavelengths and the narrower quantum memories at visible or near-infrared wavelengths is therefore desirable.

We show in this work that dispersion engineering can be used to develop processes that provide spectral reshaping and high

conversion efficiencies at the same time. We demonstrate such an interface by converting single photons from 1,545 nm and a bandwidth of 1 THz to 550 nm and a bandwidth of 129 GHz under preservation of the second-order correlation function $g^{(2)}(0)$ while achieving external conversion efficiencies high enough to outperform a spectral filter producing an equivalent output spectrum.

Results

Experimental setup and spectral properties of the PDC source.

Our experimental setup is depicted in Fig. 1. We generate single photons at 1,545 nm from an 8 mm long type-II PDC source in periodically poled potassium titanyl phosphate with a poling period of 117 μm and a Klyshko efficiency³⁰ of 20.2%. The pump beam for the PDC source is created by a series of elements, starting with a Ti:Sapphire mode-locked laser, which pumps an optical parametric oscillator, followed by second-harmonic generation and bandwidth fine-tuning with a 4f spectral filter. The bandwidth is adjusted to ensure a decorrelated PDC state. We characterize the spectral properties of the PDC photons by measuring their joint spectral intensity with a time-of-flight spectrometer³¹, consisting of a pair of dispersive fibres and a low-jitter superconducting nanowire single-photon detector (SNSPD; Photon Spot). From this measurement, shown in Fig. 2a, we conclude that the bandwidth (full-width at half-maximum) of the idler photon is 963 ± 11 GHz at 1,545 nm central wavelength. Furthermore, the round shape of the joint spectral intensity and the Schmidt number³² $K = 1/\sum_k \lambda_k^2 = 1.05$ extracted from the measurement indicate that the photon pairs are indeed spectrally decorrelated. λ_k are the weights of the Schmidt modes. We keep the pulse energy of the PDC pump at a low level of 62.5 pJ to ensure that mainly photon pairs and only few higher-photon-number components are created. At the output, an 80 nm wide band-pass filter centred at 1,550 nm is used to filter out background processes while not cutting the spectrum of the actual PDC process.

The heralded idler photon is then sent to the QPG, consisting of a periodically poled 27 mm long LiNbO₃ crystal with Ti-indiffused waveguides and a poling period of 4.4 μm . It is pumped at 854 nm with light from the same Ti:Sapphire laser, which is spectrally shaped by means of another 4f line containing a liquid-crystal spatial-light modulator. The modulator can be used to adapt the QPG pump to any input. To characterize the

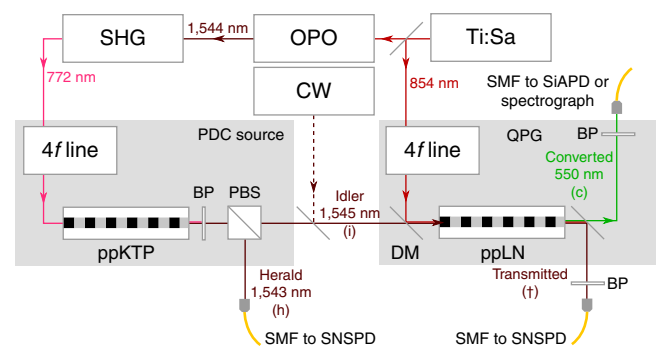


Figure 1 | Experimental setup. Setup used for characterization of the transfer function of the the quantum pulse gate (QPG) as well as the measurement of conversion efficiency, correlation functions and spectra. BP, band pass filter; CW, continuous wave laser; DM, dichroic mirror; OPO, optical parametric oscillator; PBS, polarizing beam splitter; ppKTP, periodically poled potassium titanyl phosphate crystal; ppLN, periodically poled lithium niobate crystal; SHG, second-harmonic generation; SMF, single mode fibre; Ti:Sa, Ti:Sapphire laser.

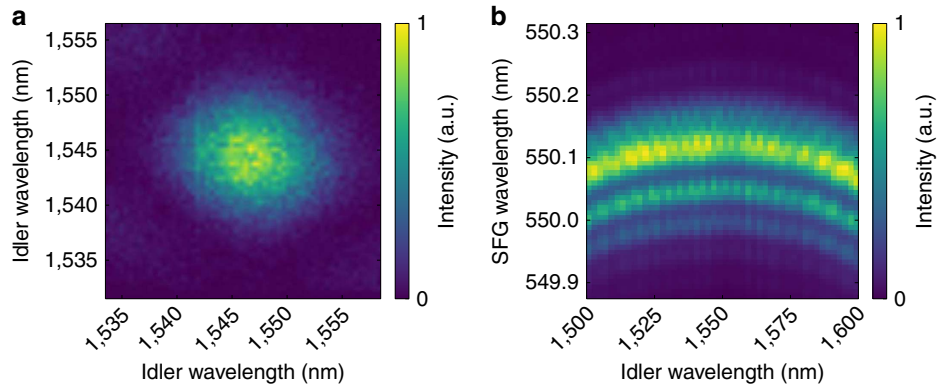


Figure 2 | Spectral characteristics of the parametric downconversion and sum-frequency generation. (a) Joint spectral intensity of the photon pairs generated in the PDC source. The spectra were measured using two dispersive fibre time-of-flight spectrometers. (b) Phasematching function of the quantum pulse gate. The spectrum of the sum-frequency generation (SFG) signal from the Ti:Sapphire laser and a tunable continuous wave telecom laser were recorded on a Czerny–Turner spectrometer.

QPG, we measure its phasematching function by recording the sum-frequency signal of a broad pump and a tunable continuous wave telecom laser on a Czerny–Turner spectrograph equipped with $2,398 \text{ lines mm}^{-1}$ grating and a single-photon-sensitive electron multiplying charge-coupled device camera. The result is shown in Fig. 2b. The horizontal orientation of the phasematching function is due to the fact that the input and pump are group-velocity matched, while the output is strongly group-velocity mismatched. This leads to the narrow spectrum of the output field while accepting a broad input field. As the slope of the phasematching function is connected to the group-velocity mismatch between input and pump, the horizontal portion on the top indicates perfect group-velocity matching, where the output spectrum depends only on the phasematching and not on the pump. This holds for a telecom input bandwidth as large as 20 nm. As the PDC photons are only 7.8 nm wide, we are well within that range and adjust the pump bandwidth accordingly to ensure maximum conversion efficiency. After the conversion, we separate both the converted and the unconverted light from the background and residual pump by means of broadband filters and couple all fields into single-mode fibres. It is noteworthy that the phasematching bandwidth and therefore the bandwidth compression depend on the sample length and could therefore be increased or decreased to get the desired output. As the group-velocity curves steepen towards shorter wavelength, moving the process in this direction would increase the group-velocity mismatch between input and output resulting in even greater bandwidth compression.

Noise properties of the conversion. To be viable as an interface in quantum networks, the device has to leave the quantum nature of the single photons untouched. To measure this, we employ photon-number statistics, namely, the heralded second-order autocorrelation function of the photons measured with a 50/50 beam splitter and two click detectors:

$$g^{(2)} = \frac{P_{cc}}{P_1 \cdot P_2}, \quad (1)$$

where P_{cc} is the coincidence probability and P_1 and P_2 the single-click probabilities. The QPG does not change the $g^{(2)}(0)$, which takes the value of 0.32 ± 0.01 both before and after the frequency conversion. With $g^{(2)}(0) < 1$, the single-photon character is verified before and after the conversion. The value before the conversion can be explained with higher photon number components. More notably, there are no measurable noise

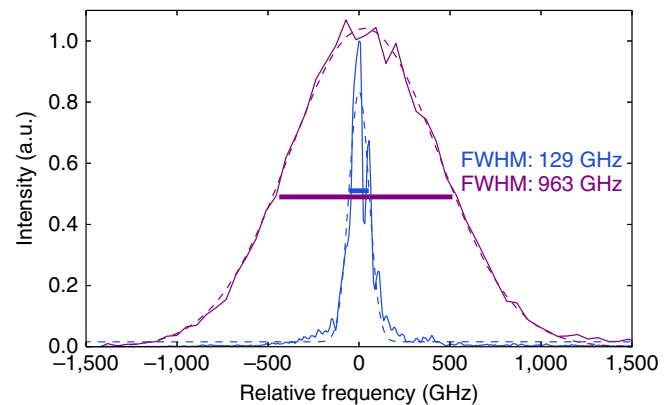


Figure 3 | Marginal spectra before and after conversion. Marginal spectra of the PDC idler photon before (magenta) and after (blue) frequency conversion in the quantum pulse gate centred around their respective centre frequencies. Dashed lines correspond to Gaussian fits from which the bandwidths were obtained. The spectrum of the idler photons were measured using a dispersive-fibre time-of-flight spectrometer. A Czerny–Turner spectrograph was used for the spectrum of the converted light.

photons added polluting the $g^{(2)}$ in the frequency conversion process.

Bandwidth compression and efficiency. To estimate the bandwidth compression, we record the spectrum of converted PDC photons with the aforementioned Czerny–Turner spectrometer. The marginal spectra of the idler photon together with the converted spectrum are depicted in Fig. 3. The converted light has a spectral bandwidth of $129 \pm 4 \text{ GHz}$ and a central wavelength of 550 nm. Compared with the original bandwidth of 963 GHz of the PDC photon, this implies a bandwidth-compression factor of 7.47 ± 0.01 .

The second, equally important figure of merit is the conversion efficiency. If the conversion efficiency is low, a simple spectral filter could outperform the device. Were the idler converted by a continuous wave pump, the bandwidth would remain constant at 963 GHz. Filtering down to 129 GHz would then imply a throughput of $13.40 \pm 0.02\%$ (the error corresponds to the fit errors for the spectral bandwidths in Fig. 3), assuming the conversion itself is lossless. To measure the conversion efficiency, we send the photons to SNSPDs and a silicon avalanche

photodiode (SiAPD) for infrared or visible photons, respectively. We estimate the internal efficiency of the process itself as well as the external efficiency including all optical loss in the setup. As a measure for the internal efficiency, we use the depletion of the transmitted light by calculating the Klyshko efficiency³⁰ η_t of the unconverted 1,545 nm light, transmitted through the QPG with the QPG pump open and blocked. The Klyshko efficiency is defined as $\eta_t = P_{cc}/P_h$, where P_{cc} is the coincidence-count probability between the herald (h) and unconverted, transmitted (t) PDC photon (refer to labels in Fig. 1) and P_h is the herald-count probability alone. From this depletion, we get the internal conversion efficiency of the process

$$\eta_{\text{int}} = 1 - \frac{\eta_t^{\text{open}}}{\eta_t^{\text{blocked}}} \quad (2)$$

where the superscript denotes whether the QPG pump was blocked, meaning that the idler mode is merely coupled and transmitted through the QPG, or open and the conversion process takes place. Using the depletion of the unconverted light has the advantage that it provides a direct measure of the internal conversion efficiency. By contrast, one would need precise knowledge of all losses to estimate it from the unconverted signal. The resulting value for the internal conversion efficiency is 61.5%.

As a measure for the external conversion efficiency, we use the ratio between the Klyshko efficiencies of the converted light η_c and the unconverted idler light before the QPG η_i , corrected only for the different detection efficiencies of the SiAPD compared with the SNSPD:

$$\eta_{\text{ext}} = \frac{\eta_c \cdot \eta_{\text{SNSPD}}}{\eta_i \cdot \eta_{\text{SiAPD}}} \quad (3)$$

where $\eta_{\text{SNSPD}} = 0.9$ and $\eta_{\text{SiAPD}} = 0.6$ are the detector efficiencies of the SNSPD and SiAPD photon detectors, respectively. This external conversion efficiency is 16.9%. Owing to some spatial mode mismatch, the coupling of the converted light into a single mode fibre is reduced compared with the unconverted light. Taking into account this reduced fibre compatibility of the green mode (50% instead of 80% for the herald), the external efficiency amounts to 27.1%. This can be seen as the free-space efficiency of the device. As all of these efficiencies result from counting sufficiently large numbers of photons, errors are negligible. The coupling of the green mode into the fibre can be further improved by optimizing the waveguide structure or the coupling optics. The

difference between the internal and the external efficiency is mainly due to linear optical losses in uncoated lenses and a 4f line band-pass filter, with a total transmission of 68% and a waveguide-incoupling efficiency of around 71%.

These conversion efficiencies show that the QPG offers useful bandwidth compression and provides a net gain over using a spectral filter. For the first time, this is realized in combination with substantial frequency conversion. This is true not only when looking at the internal conversion efficiency but even when comparing to the external conversion efficiency, which already includes all losses, such as waveguide and even fibre couplings.

Discussion

Having demonstrated a viable interface, we calculate the process parameters required to interface the proposed broadband memories in diamond based on nitrogen and silicon vacancy centres^{24,25}. The degrees of freedom available for tuning the conversion process are primarily the temperature and the choice of the nonlinear material. As a basis for this study, we use effective Sellmeier equations^{33,34} of the modes inside the waveguide. Figure 4a shows the group-velocity mismatch between PDC idler and pump at two different temperatures. The two light stripes in the colour code represent areas with zero group-velocity mismatch for 190 °C (left stripe) and 300 °C (right stripe), whereas the solid white lines indicate wavelength combination where the sum-frequency is at the desired output frequency. The main target wavelength in this work, the transition of a charge-neutral nitrogen vacancy centre (NV0) in diamond²⁴ at 574 nm, can be addressed with a group-velocity-matched sum-frequency generation process at a sample temperature of 300 °C. The PDC wavelength would be at 1,560 nm and the pump at 907 nm, well within reach of PDC sources and Ti:Sapphire laser systems. For the proof-of-principle experiment in this work, we have chosen a slightly different operating point of 190 °C as it simplifies the choice of suitable ovens and insulation materials, thus shifting the target wavelength to 550 nm. As unwanted effects such as photorefractive are only present at lower temperatures³⁵, there is no fundamental limitation for increasing the temperature as high as the Curie temperature. The alternative silicon-vacancy transition²⁵ at 738 nm cannot be reached with the birefringent properties of lithium niobate. However, lithium tantalate, a less birefringent material, supports it. The signal wavelength of this process could be at 1,278 nm and the pump wavelength at

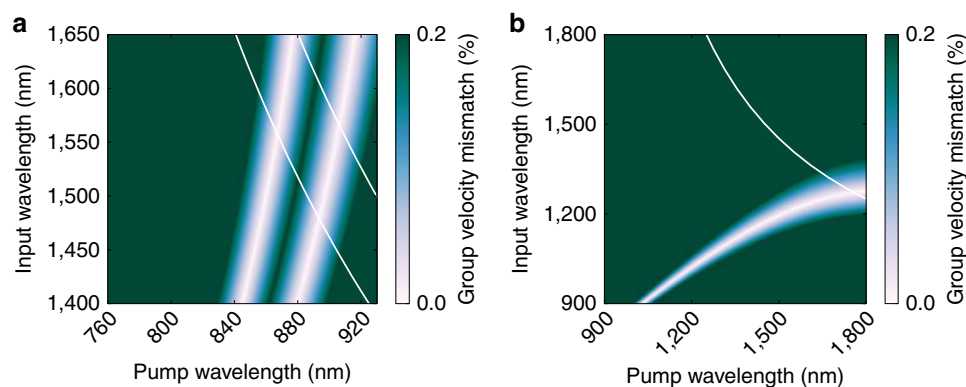


Figure 4 | Group-velocity mismatch in lithium niobate and lithium tantalate. (a) Group-velocity matching in LiTiNbO₃ between waveguide modes in ordinary and extraordinary polarization at two different temperatures (left stripe: 190 °C, right stripe: 300 °C). The solid white lines indicate wavelength combinations where the sum-frequency generation process reaches the desired wavelength of 574 nm (right line) for the transition of the charge neutral nitrogen vacancy centre or the wavelength of 550 nm (left line) chosen in this article. (b) Group-velocity matching in bulk LiTaO₃ between the ordinary and extraordinary polarization at 190 °C. Here the white line indicates an output wavelength of 738 nm, corresponding to the silicon vacancy transition in diamond.

Table 1 | Herald and coincidence count rates before and after the quantum pulse gate (QPG) used to obtain the external conversion efficiency.

	Before QPG	After QPG
Herald counts (s^{-1})	430,000	465,000
Coincidence counts (s^{-1})	86,000	10,600
Klyshko efficiency	20.2%	2.27%

Table 2 | Count and coincidence rates for measuring the second-order correlation function before and after the quantum pulse gate (QPG).

	Before QPG	After QPG
Herald counts (s^{-1})	910,000	970,000
Coincidences herald—mode1 (s^{-1})	6,900	3,900
Coincidences herald—mode2 (s^{-1})	7,200	2,780
Triple coincidences (s^{-1})	18.0	3.42

1,748 nm or vice versa. Temperature tuning of the group-velocity matching in the same way as in lithium niobate can also be considered. Figure 4b shows the parameter space for that process. Note that these numbers are based on bulk Sellmeier equations³⁶ and might slightly differ for waveguides. Apart from sum-frequency processes, difference-frequency generation can also be considered. For example, conversion of near-infrared light as emitted by semiconductor quantum dots to the telecom band can be carried out with an infrared pump such as the one employed in ref. 37. Overall, a large range of wavelengths can be covered with the available materials and realistic process parameters.

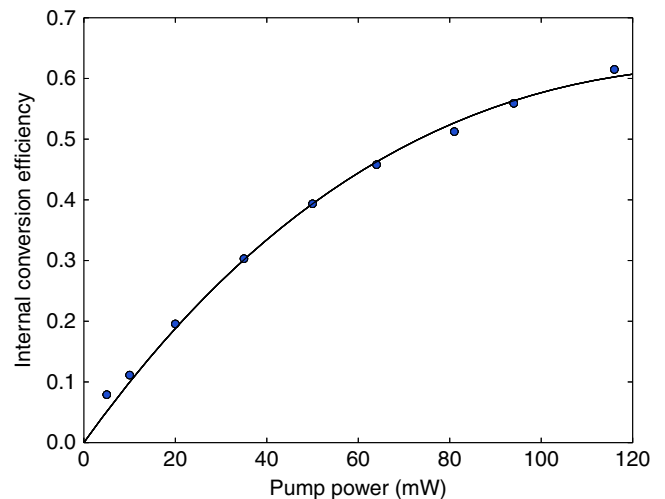
In conclusion, we have realized a device that not only offers efficient upconversion from telecom light to the visible spectrum but also useful bandwidth compression. As the phasematching bandwidth is proportional to the inverse of the sample length, the compression factor is in principle scalable. It is noteworthy that the device does not provide a fixed bandwidth ratio between input and output but rather a fixed output bandwidth, such that the same converter can be used for inputs of different bandwidth.

Methods

Laser system. The main laser system employed in the experiment is a Coherent Chameleon Ultra II Titanium Sapphire laser with an APE Compact OPO optical parametric oscillator. The pulse duration of the Ti:Sapphire oscillator is 150 fs at a repetition rate of 80 MHz. The optical parametric oscillator's pulse duration is 190 fs. Its emission at 1,545 nm is converted to 772.5 nm by a periodically poled bulk lithium niobate second-harmonic generation crystal fabricated in-house in Paderborn. The bandwidth of the 772.5 nm light used as the PDC pump is 3 nm (all bandwidths given as full-width at half-maximum). A Photonics Tunic continuous wave laser was used in the characterization of the QPG's phasematching.

Spectral pump shaping. Two 4f line pulse-shaping setups are employed in the experiment. Both use a dispersive element to separate spectral components. The spectrum is then manipulated in the focal plane of a lens. The one for the PDC pump is a folded geometry prism monochromator with an adjustable slit as described in ref. 22. The resolution is 0.7 nm. The pump for the QPG can be intensity and phase-shaped with a liquid-crystal-on-silicon-based spatial light modulator setup in a folded grating monochromator geometry with a resolution of 22 pm. In this work, the PDC pump spectrometers was set to the full 3 nm bandwidth to match the phasematching bandwidth of the PDC crystal in order to achieve a decorrelated PDC state. The QPG pump was set to 6 nm.

Photon pair source. The PDC photon pair source is a commercially available periodically poled potassium titanyl phosphate crystal with rubidium-exchanged waveguides purchased from ADVR. The crystal is 8 mm long with a poling period of 117 μm over a poled length of 6 mm. The source is pumped to produce a

**Figure 5 | Pump power dependence of the internal conversion efficiency.**

Pump power dependence of the quantum pulse gate's internal conversion efficiency. The solid line was fitted to the data and follows $0.619 \cdot \sin^2(0.130 \cdot \sqrt{P})$. Each data point was obtained by measuring the depletion of the unconverted (transmitted) beam's count rate. Poissonian distributed statistical uncertainties of the count rates are small, error bars are therefore omitted as they are smaller than the data points.

decorrelated photon pair state with a bandwidth of 7.8 nm. The Schmidt number obtained from the measured joint spectral intensity is 1.05, and the Klyshko efficiency is 20.2%. A coincidence window of 5 ns was used to obtain this number.

Time-of-flight spectrometer. The time-of-flight spectrometer consists of two dispersive fibres introducing group delays of 431 ps nm^{-1} each. The chirped photons are then detected by superconducting nanowire single-photon detectors manufactured by Photon Spot combined with a AIT TTM8000 time tagger. The convoluted jitter in the coincidence measurement is 150 ps leading to a spectral resolution of 0.35 nm.

Coincidence measurements. The coincidence window for all coincidence measurements was set to 5 ns. For the measurement of external conversion efficiencies, we measured Klyshko efficiencies, that is coincidence rates divided by herald counts. Table 1 shows the herald and coincidence count rates leading to the external efficiency discussed in the paper.

The measurements were conducted over periods of 30 s before the QPG and 46 s after, yielding 12 million and 21 million herald counts, respectively. The herald is not sent through the pulse gate; the fluctuation is due to fluctuations of the laser output power. For the $g^{(2)}$ measurement, the PDC photons in mode 1 were split up by a fibre beam splitter and all counts were conditioned on a click in the herald arm. The result was normalized over the herald counts:

$$g^{(2)} = \frac{P_{\text{hab}}}{P_{\text{ha}} \cdot P_{\text{hb}}} \cdot P_{\text{h}} \quad (4)$$

where a and b label the two modes resulting from splitting up mode 1.

The count and coincidence rates in this measurement are shown in Table 2:

The measurement durations were 57 s in front and 190 s behind the QPG, yielding a total of 52 million and 185 million herald counts, respectively. The duration of the measurement for the converted light was increased in order to yield the same statistical error for the $g^{(2)}(0)$.

Pump power dependence of conversion efficiency. Figure 5 shows the dependence of the QPG conversion efficiency on the pump power. Although the conversion probability follows a \sin^2 dependence, we cannot reach unit efficiency with the pump power available to us.

Code availability. The code used to generate the findings of this study is available from the corresponding author on reasonable request.

Data availability. The data that support the findings of this study are available from the corresponding author on reasonable request.

References

- Kimble, H. J. The quantum internet. *Nature* **453**, 1023–1030 (2008).
- Lavoie, J. *et al.* Spectral compression of single photons. *Nat. Photon.* **7**, 363–366 (2013).
- Fisher, K. A. G. *et al.* Frequency and bandwidth conversion of single photons in a room-temperature diamond quantum memory. *Nat. Commun.* **7**, 11200 (2016).
- Karpinski, M., Jachura, M., Wright, L. J. & Smith, B. J. Bandwidth manipulation of quantum light by an electro-optic time lens. *Nat. Photon* **11**, 53–57 (2017).
- Wright, L. J., Karpinski, M., Soeller, C. & Smith, B. J. Spectral shearing of quantum light pulses by electro-optic phase modulation. Preprint at <http://arxiv.org/abs/1605.00640> (2016).
- Vandevender, A. P. & Kwiat, P. G. High efficiency single photon detection via frequency up-conversion. *J. Mod. Opt.* **51**, 1433–1445 (2004).
- Albota, M. A. & Wong, F. N. C. Efficient single-photon counting at 1.55 μm by means of frequency upconversion. *Opt. Lett.* **29**, 1449–1451 (2004).
- Pelc, J. S. *et al.* Long-wavelength-pumped upconversion single-photon detector at 1550 nm: performance and noise analysis. *Opt. Express* **19**, 21445–21456 (2011).
- Brecht, B. *et al.* Demonstration of coherent time-frequency schmidt mode selection using dispersion-engineered frequency conversion. *Phys. Rev. A* **90**, 030302 (2014).
- Baune, C. *et al.* Strongly squeezed states at 532 nm based on frequency up-conversion. *Opt. Express* **23**, 16035–16041 (2015).
- Raymer, M. G. & Srinivasan, K. Manipulating the color and shape of single photons. *Phys. Today* **65**, 32–37 (2012).
- Donohue, J. M., Mazurek, M. D. & Resch, K. J. Theory of high-efficiency sum-frequency generation for single-photon waveform conversion. *Phys. Rev. A* **91**, 033809 (2015).
- Baronovski, A. P., Ladouceur, H. D. & Shaw, J. K. Analysis of cross correlation, phase velocity mismatch and group velocity mismatches in sum-frequency generation. *IEEE J Quant. Electron.* **29**, 580–589 (1993).
- Mosley, P. J. *et al.* Heralded generation of ultrafast single photons in pure quantum states. *Phys. Rev. Lett.* **100**, 133601 (2008).
- Jin, R.-B., Shimizu, R., Wakui, K., Benichi, H. & Sasaki, M. Widely tunable single photon source with high purity at telecom wavelength. *Opt. Express* **21**, 10659–10666 (2013).
- Ben Dixon, P., Shapiro, J. H. & Wong, F. N. C. Spectral engineering by Gaussian phase-matching for quantum photonics. *Opt. Express* **21**, 5879–5890 (2013).
- Bruno, N., Martin, A., Guerreiro, T., Sanguinetti, B. & Thew, R. T. Pulsed source of spectrally uncorrelated and indistinguishable photons at telecom wavelengths. *Opt. Express* **22**, 17246–17253 (2014).
- Christ, A. *et al.* in *CLEO/Europe and EQEC 2011 Conference Digest* (Optical Society of America, 2011).
- Ansari, V. *et al.* Temporal-mode tomography of single photons. Preprint at <https://arxiv.org/abs/1607.03001> (2016).
- Manurkar, P. *et al.* Multidimensional mode-separable frequency conversion for high-speed quantum communication. *Optica* **3**, 1300–1307 (2016).
- Eckstein, A., Christ, A., Mosley, P. J. & Silberhorn, C. Highly efficient single-pass source of pulsed single-mode twin beams of light. *Phys. Rev. Lett.* **106**, 013603 (2011).
- Harder, G. *et al.* An optimized photon pair source for quantum circuits. *Opt. Express* **21**, 13975–13985 (2013).
- Sprague, M. R. *et al.* Broadband single-photon-level memory in a hollow-core photonic crystal fibre. *Nat. Photon.* **8**, 287–291 (2014).
- Poem, E. *et al.* Broadband noise-free optical quantum memory with neutral nitrogen-vacancy centers in diamond. *Phys. Rev. B* **91**, 205108 (2015).
- Hepp, C. *et al.* Electronic structure of the silicon vacancy color center in diamond. *Phys. Rev. Lett.* **112**, 036405 (2014).
- Saunders, D. *et al.* Cavity-enhanced room-temperature broadband Raman memory. *Phys. Rev. Lett.* **116**, 090501 (2016).
- England, D. G., Bustard, P. J., Nunn, J., Lausten, R. & Sussman, B. J. From photons to phonons and back: a THz optical memory in diamond. *Phys. Rev. Lett.* **111**, 243601 (2013).
- Michelberger, P. S. *et al.* Interfacing GHz-bandwidth heralded single photons with a warm vapour Raman memory. *New J. Phys.* **17**, 043006 (2015).
- Christ, A., Laiho, K., Eckstein, A., Cassemiro, K. N. & Silberhorn, C. Probing multimode squeezing with correlation functions. *New J. Phys.* **13**, 033027 (2011).
- Klyshko, D. N. Use of two-photon light for absolute calibration of photoelectric detectors. *Sov. J. Quant. Electron.* **10**, 1112–1116 (1980).
- Avenhaus, M., Eckstein, A., Mosley, P. J. & Silberhorn, C. Fiber-assisted single-photon spectrograph. *Opt. Lett.* **34**, 2873–2875 (2009).
- Eberly, J. H. Schmidt analysis of pure-state entanglement. *Laser Phys.* **16**, 921–926 (2006).
- Edwards, G. J. & Lawrence, M. A temperature-dependent dispersion equation for congruently grown lithium niobate. *Opt. Quant. Electron.* **16**, 373–375.
- Jundt, D. H. Temperature-dependent Sellmeier equation for the index of refraction, n_o , in congruent lithium niobate. *Opt. Lett.* **22**, 1553–1555 (1997).
- Augstov, P. A. & Shvarts, K. K. The temperature and light intensity dependence of photorefraction in LiNbO_3 . *Appl. Phys.* **21**, 191–194 (1980).
- Abedin, K. S. & Ito, H. Temperature-dependent dispersion relation of ferroelectric lithium tantalate. *J. Appl. Phys.* **80**, 6561–6563 (1996).
- Pelc, J. S. *et al.* Downconversion quantum interface for a single quantum dot spin and 1550-nm single-photon channel. *Opt. Express* **20**, 27510–27519 (2012).

Acknowledgements

This work was funded by the Deutsche Forschungsgemeinschaft via SFB TRR 142 and via the Gottfried Wilhelm Leibniz-Preis.

Author contributions

M.A. and V.A. carried out the experiment. M.A. wrote the manuscript with support from G.H. C.E., V.Q. and R.R. fabricated the LiNbO_3 sample. L.S., G.H. and B.B. helped supervise the project. B.B. and C.S. conceived the original idea. C.S. supervised the project.

Additional information

Competing financial interests: The authors declare no competing financial interests.

Reprints and permission information is available online at <http://npg.nature.com/reprintsandpermissions/>

How to cite this article: Allgaier, M. *et al.* Highly efficient frequency conversion with bandwidth compression of quantum light. *Nat. Commun.* **8**, 14288 doi: 10.1038/ncomms14288 (2017).

Publisher's note: Springer Nature remains neutral with regard to jurisdictional claims in published maps and institutional affiliations.



This work is licensed under a Creative Commons Attribution 4.0 International License. The images or other third party material in this article are included in the article's Creative Commons license, unless indicated otherwise in the credit line; if the material is not included under the Creative Commons license, users will need to obtain permission from the license holder to reproduce the material. To view a copy of this license, visit <http://creativecommons.org/licenses/by/4.0/>

© The Author(s) 2017

Title: Temporal-mode measurement tomography of a quantum pulse gate

Authors: Vahid Ansari, Georg Harder, Markus Allgaier, Benjamin Brecht, Christine Silberhorn

Journal: Phys. Rev. A 96, 063817

Year: 2017

Contributions: V.A. designed and constructed the experimental setup. V.A. and G.H. carried out the experiment and co-wrote the manuscript. C.S. supervised the project. All authors contributed to the discussion of results and commented on the manuscript.

Temporal-mode measurement tomography of a quantum pulse gateVahid Ansari,^{1,*} Georg Harder,¹ Markus Allgaier,¹ Benjamin Brecht,^{1,2} and Christine Silberhorn¹¹*Integrated Quantum Optics, Paderborn University, Warburger Strasse 100, 33098 Paderborn, Germany*²*Clarendon Laboratory, Department of Physics, University of Oxford, Parks Road, Oxford OX1 3PU, England, United Kingdom*

(Received 15 September 2017; published 13 December 2017)

Encoding quantum information in the photon temporal mode (TM) offers a robust platform for high-dimensional quantum protocols. The main practical challenge, however, is to design a device that operates on single photons in specific TMs and all coherent superpositions. The quantum pulse gate (QPG) is a mode-selective sum-frequency generation designed for this task. Here, we perform a full modal characterization of a QPG using weak coherent states in well-defined TMs. We reconstruct a full set of measurement operators, which show an average fidelity of 0.85 to a theoretically ideal device when operating on a seven-dimensional space. Then we use these characterized measurement operators of the QPG to calibrate the device. Using the calibrated device and a tomographically complete set of measurements, we show that the QPG can perform high-dimensional TM state tomography with 0.99 fidelity.

DOI: [10.1103/PhysRevA.96.063817](https://doi.org/10.1103/PhysRevA.96.063817)**I. INTRODUCTION**

Optical quantum information science (QIS) covers a multitude of applications ranging from quantum computing and simulation over quantum metrology to quantum communications. Using photons to carry information in any of these applications, we have to choose an alphabet for information encoding. Of the four degrees of freedom—polarization, transverse electric-field distribution (two degrees of freedom), and time—polarization is more popular due to its experimental accessibility. This comes, however, with an intrinsic limitation to a two-dimensional Hilbert space, where we actually would prefer an infinite-dimensional alphabet which can increase the information capacity of each photon and can also improve the performance of quantum protocols. For this reason, recent years have seen increasing interest in alternative encodings deploying either the spatial degree of freedom or the spectral-temporal domain where the basis states are e.g., orbital angular momentum states or temporal modes (TMs), respectively. The latter are particularly appealing because they are compatible with single-mode fiber networks and are also eigenmodes of state-of-the-art photon sources based on parametric down-conversion and four-wave mixing. However, the temporal shaping and detection of single-photon wave packets in higher-dimensional spaces are challenging, as they require time-dependant operations, such as nonlinear optical interactions [1,2]. Regardless of this, TMs of single photons have been identified as a promising resource for QIS and were studied in many contexts such as high-dimensional quantum communications [3], deterministic photonic quantum gates [4], light-matter interaction [5,6], and enhanced-resolution spectroscopy [7]. Any of these applications necessarily requires the capability to prepare photons in specific TMs, defined by a complex amplitude and phase distribution of the electric field, and to perform TM-resolved measurements in both the computational and any associated superposition basis. This can be achieved with the quantum pulse gate (QPG), a device that selects a single, arbitrary TM and converts

it to a distinguishable output [1,2]. Recently, such devices have been demonstrated by several groups by employing dispersion-engineered frequency conversion between a strong shaped driving pump field and a coherent signal state at single-photon level intensities [8–12] or with heralded single photons from a parametric down-conversion source [13]. In these experiments, TM selectivity with reasonable efficiencies has been shown, but the coherences between all possible TMs have not been investigated in detail. This is, however, an essential ingredient for the realization of any application based on a high-dimensional alphabet rather than on simple add-or drop-type multiplexing of information channels. An easy example is polarization tomography, where measurements have to be carried out in all three mutually unbiased bases (MUBs)—horizontal or vertical, diagonal or antidiagonal, and right-circular or left-circular—in order to retrieve full information on the state under investigation.

In this paper, we reconstruct all measurement operators of a QPG operating on both a five-dimensional and seven-dimensional TM Hilbert space. Our QPG is based on dispersion-engineered sum-frequency generation in a titanium-indiffused lithium niobate waveguide, and we use sets of weak coherent states which span a tomographically complete set of MUBs to characterize the device. Afterwards, we use the retrieved measurement operators of our QPG to perform TM state tomography of randomly chosen TM states in an up to seven-dimensional Hilbert space with average fidelities of 0.99. This combines the necessary ingredients for high-dimensional QIS with single-photon TMs and paves the way towards future applications of this technology.

II. FREQUENCY CONVERSION AND MODE SELECTIVE MEASUREMENTS

In this section, we present the theoretical basis behind the QPG and the use of it for tomography of TM states. We express our single-photon states in terms of broadband TMs:

$$\hat{A}_i = \int f_i(\omega) \hat{a}(\omega) d\omega, \quad (1)$$

*vahid.ansari@uni-paderborn.de

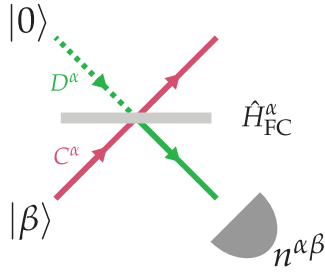


FIG. 1. Outline of QPG operation. The QPG is a beamsplitter operating on a TM defined by the index α . For the measurement tomography, we send coherent states $|\beta\rangle$ to the QPG and at the converted (reflected) port we measure the number of converted photons using a bucket detector, noted as $n^{\alpha\beta}$.

where $f_i(\omega)$ are frequency amplitudes and $\hat{a}(\omega)$ are the annihilation operators for the central frequency ω . The spectral intensity $|f_i(\omega)|^2$ can be measured with a standard spectrometer. In the following, the modes \hat{A}_i form our discrete basis of dimension d , i.e., the functions $f_i(\omega)$ are orthonormal and $0 \leq i < d$. In the experiment, we take $d = \{5, 7\}$ and $f_i(\omega)$ as Hermite-Gaussian functions of order i .

Before giving the sketch of the TM tomography, we briefly review the underlying formalism of the QPG as a mode-selective frequency conversion (FC). FC in general is a beamsplitter acting on TMs, which is described by a Hamiltonian $\hat{H}_{\text{FC}} = \theta \iint f^\alpha(\omega_{\text{in}}, \omega_{\text{out}}) \hat{a}(\omega_{\text{in}}) \hat{b}^\dagger(\omega_{\text{out}}) d\omega_{\text{in}} d\omega_{\text{out}} + \text{H.c.}$, where \hat{a} and \hat{b} are the annihilation operators for the two beamsplitter modes. The transfer function

$$f^\alpha(\omega_{\text{in}}, \omega_{\text{out}}) = \alpha(\omega_{\text{pump}}) \Phi(\omega_{\text{in}}, \omega_{\text{out}}) \quad (2)$$

is given by the pump amplitude $\alpha(\omega_{\text{pump}})$ and the phase-matching function $\Phi(\omega_{\text{in}}, \omega_{\text{out}})$ of the crystal [1,2]. We use a superscript α to indicate that we can adjust the process by shaping the pump spectrum. Using the Schmidt decomposition, the transfer function $f^\alpha(\omega_{\text{in}}, \omega_{\text{out}})$ can be decomposed into its eigenmodes defining new TM operators \hat{C}_k^α and \hat{D}_k^α , thus reducing the integral to the following sum:

$$\hat{H}_{\text{FC}}^\alpha = \theta \sum_k \lambda_k^\alpha (\hat{D}_k^\alpha)^\dagger \hat{C}_k^\alpha + \text{H.c.}, \quad (3)$$

where λ_k^α are the eigenvalues of the decomposition, normalized as $\sum_k |\lambda_k^\alpha|^2 = 1$, and θ is the gain of the process. The orthogonality of the eigenmodes ensures that we can regard the FC as independent beamsplitters with a reflectivity or conversion efficiency of $\eta_k^\alpha = \sin^2(|\theta \lambda_k^\alpha|)$. As sketched in Fig. 1, we have no input in mode D and measure the mean photon number of the converted light, which is

$$n = \sum_k \eta_k^\alpha \langle (\hat{C}_k^\alpha)^\dagger \hat{C}_k^\alpha \rangle. \quad (4)$$

To calculate what this means for a given input spectral shape, we decompose the mode β of the input state into the eigenmodes of the FC:

$$\hat{\beta} = \sum_k v_k^{\alpha\beta} \hat{C}_k^\alpha. \quad (5)$$

Then we can rewrite the mean photon number of converted light as

$$n^{\alpha\beta} = N^\beta \sum_k \eta_k^\alpha |v_k^{\alpha\beta}|^2, \quad (6)$$

where N^β is the total mean photon number of the input state and $|v_k^{\alpha\beta}|^2$ is the overlap between the input mode β and the k th eigenmode of the conversion process for a pump setting α . Interestingly, this is valid for all photon number distributions including the coherent states we use here.

We can also rewrite this in vector notation as

$$n^{\alpha\beta} = N^\beta \sum_k \eta_k^\alpha |\langle \beta | k^\alpha \rangle|^2 = \langle \beta | \hat{M}^\alpha | \beta \rangle, \quad (7)$$

where $\hat{M}^\alpha = \sum_k \eta_k^\alpha |k^\alpha\rangle \langle k^\alpha| = \sum_{ij} m_{ij}^\alpha |i\rangle \langle j|$ is our measurement operator, $|i\rangle$ is the TM basis from Eq. (1), $|\beta\rangle$ is the input state, and $|k^\alpha\rangle$ are the eigenvectors of the process. The idea of measurement tomography is to probe the matrix \hat{M}^α with different states $|\beta\rangle$. All we have to do is to generate a tomographically complete set of probe states and employ standard measurement tomography with the measured mean photon numbers for each setting, thus determining the elements m_{ij}^α . Diagonalizing this matrix, we get the FC eigenmodes $|k^\alpha\rangle$ and efficiencies η_k^α . This fully characterizes the input-mode structure of the FC. An ideal QPG has only one eigenmode, i.e., \hat{M}^α has only one nonzero eigenvalue, and the shape of the eigenmode would reflect the shape of the pump $k_0^\alpha(\omega) = \alpha(-\omega)$. This can be achieved in a three-wave mixing process with the group-velocity matching (GVM) condition between the input and the pump fields [1,2].

It is worth noting that while the number of modes of the FC is in principle infinite the probe space is only finite dimensional. Despite this, the reconstruction of the FC within the probe space is accurate. A simple example is when the TMs of the pump and input are not perfectly matched, e.g., in their central frequencies. This can change the overall conversion efficiency $\text{tr}(\hat{M}^\alpha) = \sum_k \eta_k^\alpha$ for different pump shapes α . We therefore try to match the central frequencies and bandwidths of the input and pump TMs to cover as much of the FC space as possible.

III. EXPERIMENT

The outline of the experimental setup is sketched in Fig. 2. We take ultrashort pulses from a Ti:sapphire oscillator [14] to pump an optical parametric oscillator (OPO) [15]. With this configuration we have Gaussian pulses at central wavelengths of 873 and 1550 nm, for the pump and signal fields, respectively, with amplitude full width at half maximum (FWHM) of 3.35 THz for both fields. To prepare the coherent input state, we attenuate the OPO beam to a mean photon number of 0.1 per pulse. We use a self-built pulse shaper to shape the pump and a commercial pulse shaper [16] to shape the input light pulses, with spectral resolutions of 22 and 8 pm, respectively. The self-built pulse shaper is a folded $4f$ setup consisting of a magnifying telescope, a holographic diffraction grating with 2000 lines/mm, a cylindrical silver mirror, and a reflective liquid crystal on a silicon spatial light modulator (SLM) [17]. We use spectral interferometry to ensure both pulse shapers are dispersion free. The shaping resolutions

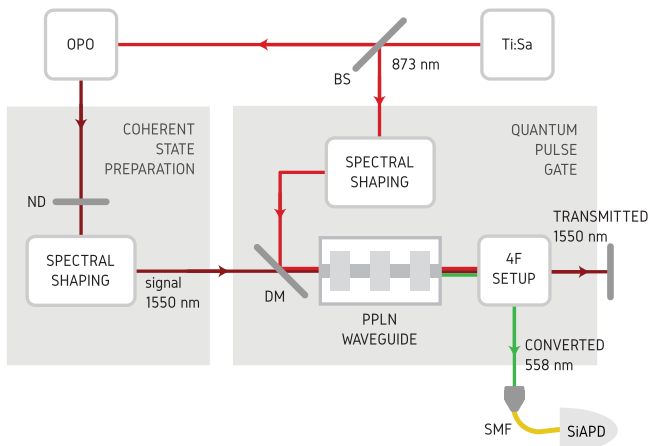


FIG. 2. Experimental setup. A femtosecond titanium:sapphire (Ti:Sa) oscillator with repetition rate of 80 MHz is used to pump an optical parametric oscillator (OPO). The pump of the QPG is obtained from a tap-off of the Ti:Sa laser. The input signal field is prepared by attenuating the OPO output to a mean photon number of 0.1 photon per pulse by using neutral density (ND) filters. For spectral shaping, we use SLMs in a folded $4f$ setup to shape the desired spectral amplitude and phase for the both fields. Then pump and input fields are combined on a dichroic mirror (DM) and coupled to an in-house built periodically poled lithium niobate (PPLN) waveguide, held at 207°C . After the PPLN waveguide, the up-converted photons with a green color are selected by a $4f$ setup and coupled to a silicon avalanche photodiode (SiAPD), through a single-mode fiber (SMF).

are better than the resolution we require in this experiment. For example, while we could prepare the 20th-order Hermite-Gaussian mode, we only use the first seven modes as our basis due to other constraints that will be discussed later. For the tomography, we choose a bandwidth of 0.4 THz (FWHM of the amplitude of the Gaussian mode) for both fields. Finally, the type-II sum-frequency process happens in an in-house built 17-mm LiNbO_3 crystal with titanium indiffused waveguides and a poling period of $4.4\ \mu\text{m}$. The waveguides are designed to be spatially single mode at 1550 nm.

The key property of a QPG is the GVM between the input and the pump [1,2]. In Fig. 3 we plot the intensity of the phase-matching function $|\Phi(\lambda_{\text{in}}, \lambda_{\text{out}})|^2$, measured with a scanning continuous-wave input laser and adjusted pump pulses on a high-resolution spectrometer. A perfect GVM condition results in zero gradient of the phase-matching function in Fig. 3. The marginal spectrum of this function, plotted on the left side in Fig. 3, shows an asymmetric structure with decaying side lobes. This can be explained by an inhomogeneity of the effective refractive index along the waveguide, equivalent to a variation of the poling period. A quadratic variation of the poling period can introduce such asymmetric side peaks. In the experiment, we also have a $4f$ setup on the sum-frequency generation (SFG) line (with a total transmissivity of about 0.55) that allows us to filter out these side lobes.

One common complication with waveguides is that different spatial mode combinations have different phase matchings. In our case, these do not overlap with the phase matching for the fundamental mode shown in Fig. 3, thus we can simply filter them out spectrally. Nevertheless, special care is taken to

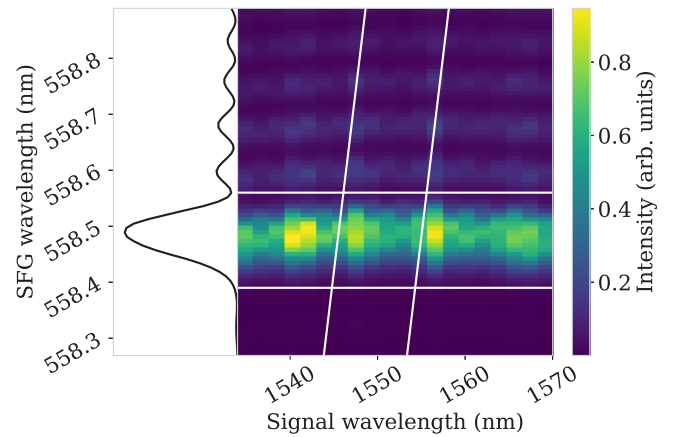


FIG. 3. Phase-matching function of the QPG. Right: The zero gradient of the phase-matching function $\Phi(\omega_{\text{in}}, \omega_{\text{out}})$ is an indicator of group-velocity matching between input signal and pump field. The diagonal white lines are marking the orientation of the pump amplitude $\alpha(\omega_{\text{out}} - \omega_{\text{in}})$ and the bandwidth we use in this paper. The horizontal white lines are showing the bandwidth of the $4f$ setup used to filter the SFG signal. Left: Marginal distribution of the plot on the right side. Asymmetries are due to inhomogeneity of the effective refractive index along the waveguide.

optimize the coupling of both beams into the waveguide for the desired process and minimize the intensity of higher-order modes.

We shape both the pump and the input to span a complete set of MUBs [18]. These have the property that for a dimension d there are $(d + 1)$ bases such that overlaps between states from different bases are always $1/d$, hence unbiased. This ensures that the space is uniformly probed. Furthermore, the total set is tomographically overcomplete, helping to reduce systematic experimental errors. Since for each pump shape we have to run the full characterization with $(d + 1)d$ input modes, the total number of measurements for $d = 5$ and 7 are 900 and 3136, respectively. For each of them, we record counts for about 1 s at count rates up to 10^5 counts/s. This corresponds to a FC efficiency of about 5%, which is solely limited by the pump pulse energy of about 5 pJ in the current experimental setup. Despite the relatively low conversion efficiency, a short measurement time is possible owing to high detection efficiency of the silicon avalanche photodiode (SiAPD). Since the count rates are directly proportional to the powers of the pump and the input, we record both values after the waveguide and normalize the count rates accordingly to account for small drifts in the setup (with the magnitude of less than 10%). It is worth mentioning that one can also use symmetric informationally complete POVMs (SIC-POVMs) as the tomography bases [19]. The main advantage of the SIC-POVMs is that, contrary to MUBs, they exist for any arbitrary dimension [20].

IV. MEASUREMENT TOMOGRAPHY OF THE QPG

To find the measurement operators \hat{M}^α from the data we perform a weighted least-squares fit:

$$\min_{\hat{M}^\alpha} \sum_{\beta} \frac{|f^{\alpha\beta} - \langle \beta | \hat{M}^\alpha | \beta \rangle|^2}{f^{\alpha\beta}}, \quad (8)$$

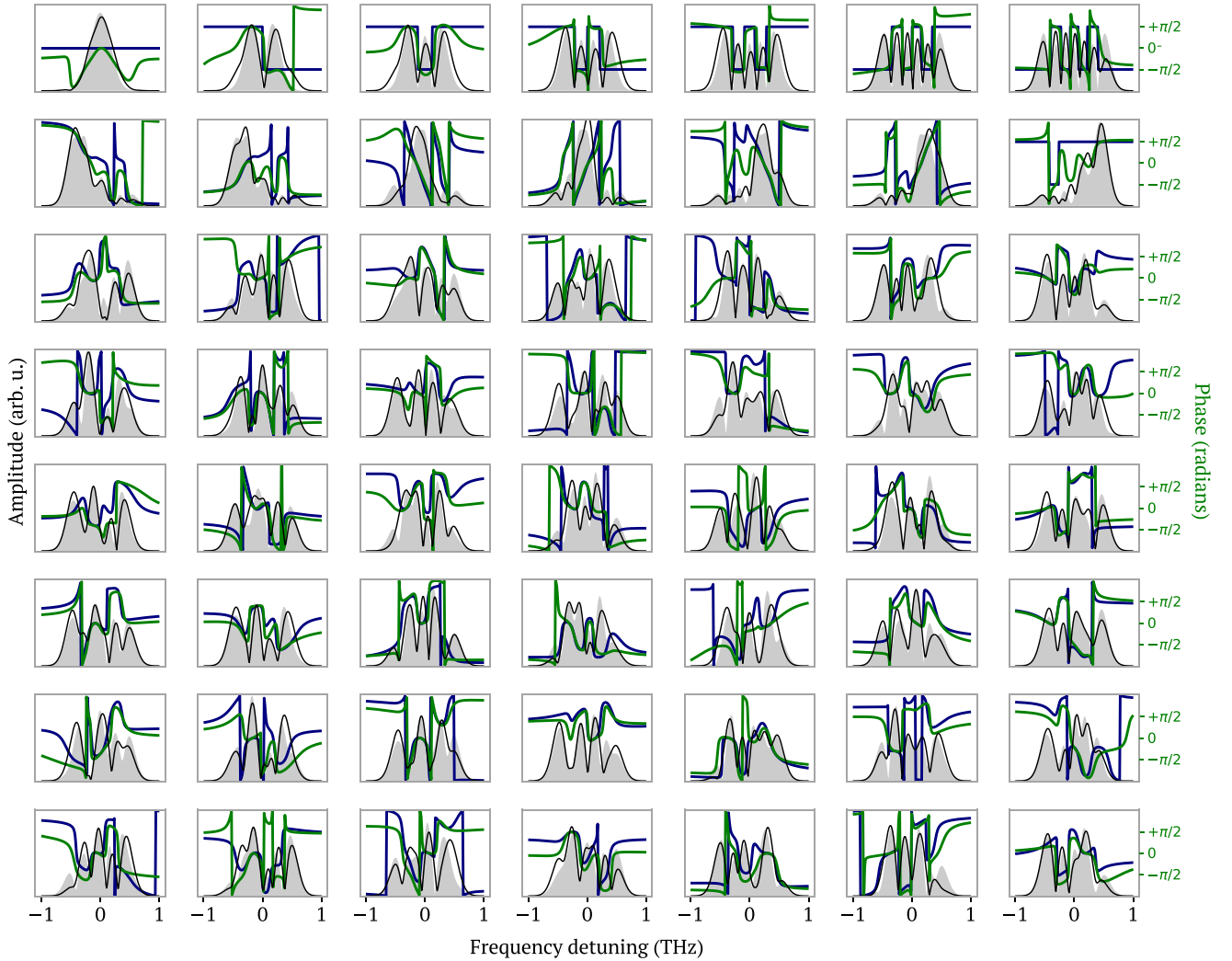


FIG. 4. The first eigenvectors of the 7×6 measurement operators. For each plot, the x axis corresponds to the frequency detuning (from the central frequency) and the y axis to the amplitude and phase. Black and green lines are the measured amplitudes and phases, respectively; shaded areas and blue lines correspond to the theoretical MUB modes. Note that the phase is 2π periodic, which is also the interval of the y axis. Please note that phases are only meaningful when a significant amplitude is present.

where $f^{\alpha\beta}$ are normalized count rates and \hat{M}^α is constrained to be Hermitian and positive semidefinite. Since each setting α is an independent measurement, we do not put a constraint on the sum of operators. In Fig. 4 we show the first eigenmodes of all measurement operators for seven dimensions. They closely resemble the ideal MUB states. Additionally, the matrix of projections of MUB POVM elements which shows the orthogonality of the basis is given in Appendix B.

To quantify how accurate the results are, we calculate the purities $\mathcal{P}^\alpha = \text{tr}([\hat{M}^\alpha]^2) / \text{tr}(\hat{M}^\alpha)^2$ and the fidelities $\mathcal{F}^\alpha = \sqrt{\langle \alpha | \hat{M}^\alpha | \alpha \rangle} / \text{tr}(\hat{M}^\alpha)$ with the ideal operators $|\alpha\rangle\langle\alpha|$. We perform the characterization in five and seven dimensions, whereas for five dimensions we also compare the two experimental settings with and without a spectral filter in the output mode. As mentioned, the spectral filter blocks the side lobes of the phase matching. The average values with their respective standard deviations are listed in Table I. For comparison we also show theoretical values assuming a Gaussian horizontal

phase matching and perfect pump shaping. The imperfections in this case originate from the fact that the phase matching is only about five times narrower than the pump, leading to correlations in the transfer function and multimode performance of the QPG. These correlations also explain why suppressing the side lobes of the output spectrum improves the purity from 0.72 to 0.92. A comparison of the eigenmodes for these two cases shows that the first eigenmode hardly changes. Thus the

TABLE I. Purities and fidelities of QPG measurement operators.

d	5 (unfiltered)	5	7
$\mathcal{P}_{\text{measured}}$	0.719 ± 0.064	0.920 ± 0.024	0.811 ± 0.035
$\mathcal{F}_{\text{measured}}$	0.778 ± 0.086	0.912 ± 0.046	0.847 ± 0.042
$\mathcal{P}_{\text{theory}}$		0.939 ± 0.026	0.909 ± 0.035
$\mathcal{F}_{\text{theory}}$		0.979 ± 0.008	0.971 ± 0.010

spectral filtering suppresses the higher-order spectral modes introduced by the side lobes of the phase matching, or in other words drives the QPG closer to single modeness. Going from five to seven dimensions slightly lowers both the purities and the fidelities. One reason is that the richer spectral structure of the pump at higher dimensions, again, will introduce some spectral correlations in the transfer function which also reduce the theoretical values. However, the expected reduction is smaller than what we measure. Imperfections in the pulse shaping are a greater problem for higher dimensions. With the increase of dimensionality, the total bandwidth both in time and frequency increases, which requires the relative phases and amplitudes to be accurate over a broader range in both time and frequency. To improve the single-mode operation of the QPG, one can use a longer waveguide which gives a narrower phase-matching bandwidth. Furthermore, the measurement time increases drastically, which makes the experiment more susceptible to drifts in the setup. With the current experimental setup, the seven-dimensional characterization takes about 2 h.

The overall high fidelities we measure in this paper demonstrate that the QPG can operate on arbitrary TMs in a selective way. The fidelities also quantify the mode selectivity since the normalized conversion efficiency is given by \mathcal{F}^2 . In the five-dimensional case, that means that the desired mode gets converted with 83% efficiency and any orthogonal mode gets converted with less than 17%. However, with the measurement operators we have much more information than just the mode selectivity. For a task like state tomography, the QPG operation can be calibrated for small experimental errors, as we have here. All we need is mode sensitivity and the knowledge of our mode detector, which we have with the matrices \hat{M}^α . In Appendix C we discuss the feasibility of this tomographic method at the presence of more significant experimental errors.

V. STATE TOMOGRAPHY WITH THE QPG

In the following we investigate the performance of the QPG for state tomography. For this purpose, we prepare states like $\hat{\rho} = |\beta\rangle\langle\beta|$, which are different from the characterization set we use for the measurement tomography. To ensure fair benchmarking we prepare 20 different input states where half of them are generated randomly. Then we use the $(d+1)d$ QPG settings α to reconstruct the input state. We measure the normalized probabilities f^α and minimize

$$\min_{\hat{\rho}} \sum_{\alpha} \frac{|f^\alpha - \text{tr}(\hat{\rho}\hat{M}^\alpha)|^2}{f^\alpha}, \quad (9)$$

under the constraints that $\hat{\rho}$ is Hermitian and positive semidefinite and $\text{tr}(\hat{\rho}) = 1$. First, we assume a perfect QPG with ideal

TABLE II. Measured purities and fidelities of state tomography.

d	5 (unfiltered)	5	7
\mathcal{P}	0.68 ± 0.079	0.753 ± 0.098	0.619 ± 0.052
\mathcal{F}	0.742 ± 0.126	0.879 ± 0.041	0.813 ± 0.031

TABLE III. Measured purities and fidelities of state tomography with calibrated QPG.

d	5 (unfiltered)	5	7
\mathcal{P}	0.931 ± 0.038	0.972 ± 0.016	0.957 ± 0.017
\mathcal{F}	0.971 ± 0.015	0.991 ± 0.005	0.988 ± 0.004

measurement operators and reconstruct the input states. Since the prepared inputs are coherent states in well-defined TMs, we expect to reconstruct pure states. The average fidelities and their standard deviations measured for all input states are listed in Table II, which shows a modest fidelity of the reconstructed state with respect to the prepared state. This is because the slight multimodeness of the QPG operation translates into the mixedness of the reconstructed states and leads to inaccurate tomography.

To improve the quality of the state tomography we can use the characterized measurement operators of the QPG in Eq. (9). Table III summarizes the outcome. The improvement is striking. We obtain fidelities of 0.99 with the actual input state. Two examples of such states are shown in Fig. 5. The decrease in fidelity from five to seven dimensions is almost negligible and, even without filtering, the values are still very high. This shows the power of proper detector calibration for state tomography. The outstanding fidelities suggest that the state tomography with QPG can be scaled up to higher dimensions. However, performing a complete measurement tomography for higher dimensions, with the current experimental configuration, would require an impractically long measurement time. This is primarily a technical challenge to decrease the switching time of the SLMs and increase the count rates per second. From the numeric point of view, measurement tomography becomes time consuming very quickly. Here, one could switch to pattern tomography [21], which circumvents this tedious step by fitting the detector response pattern directly. We tested this approach as well and obtained similar fidelities as shown in Table III.

VI. CONCLUSION

In conclusion, we experimentally characterized the measurement operators of a temporal-mode selective device in up to seven dimensions. We have shown that the device is effective in superposition bases spanning a tomographically complete set of mutually unbiased bases. Furthermore, we have shown that characterization of the measurement operators of such a device enables accurate temporal-mode state tomography, with fidelities in the 0.99 range. With such characterization, the QPG can be used to fully characterize ultrafast quantum states. Future work will focus on improving the performance of the QPG to realize its full potential for high-dimensional quantum information science with temporal modes.

ACKNOWLEDGMENTS

The authors would like to thank Saleh Rahimi-Keshari, John Donohue, Nicolas Treps, Jonathan Roslund, and Dileep

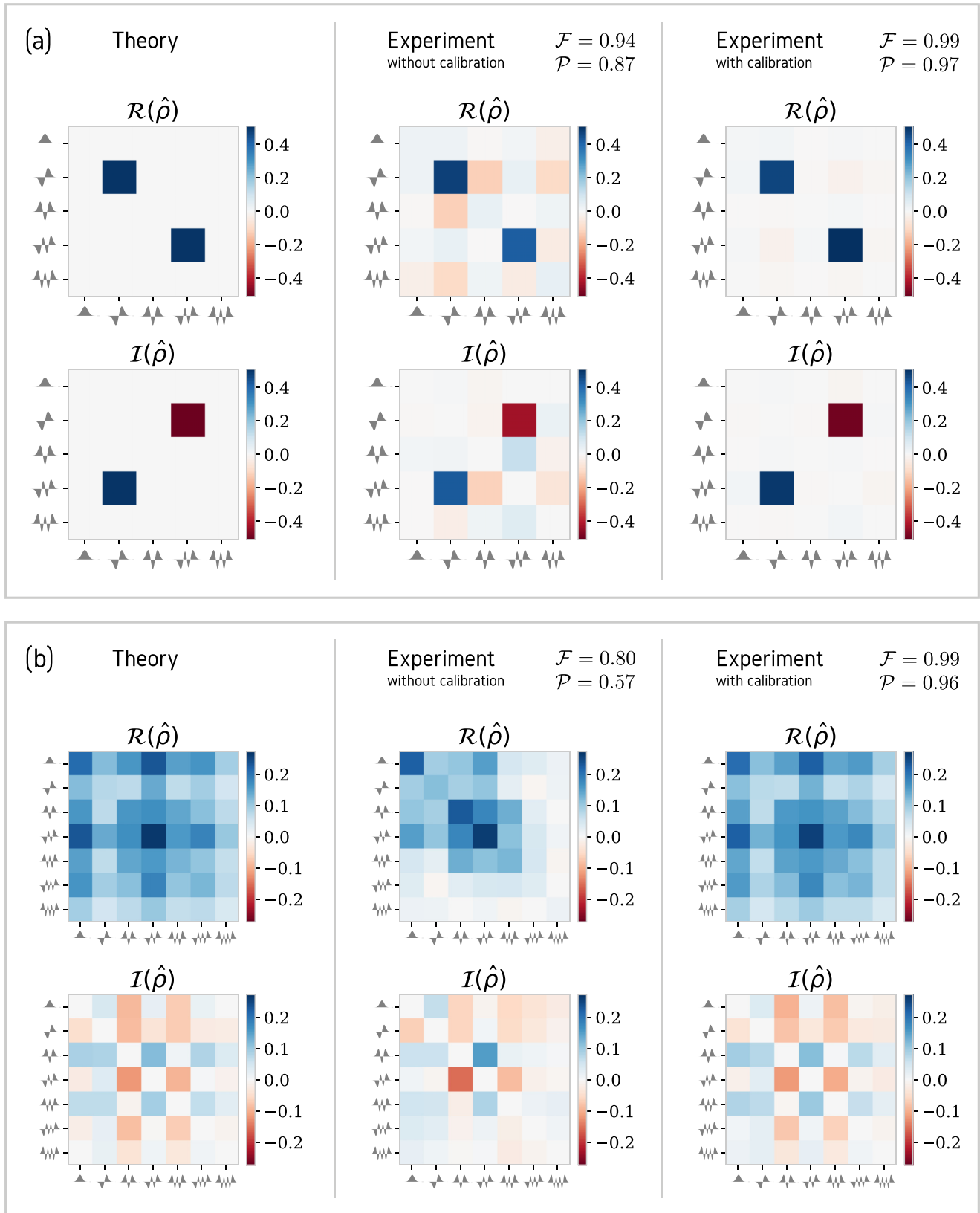


FIG. 5. Two examples of state tomography with QPG in the Hermite-Gaussian basis in five (a) and seven (b) dimensions. State vectors corresponding to each density matrix are detailed in Appendix A. For each state the theoretical density matrix (left), the reconstructed density matrix without QPG calibration (middle), and the reconstructed density matrix with QPG calibration (right) are plotted.

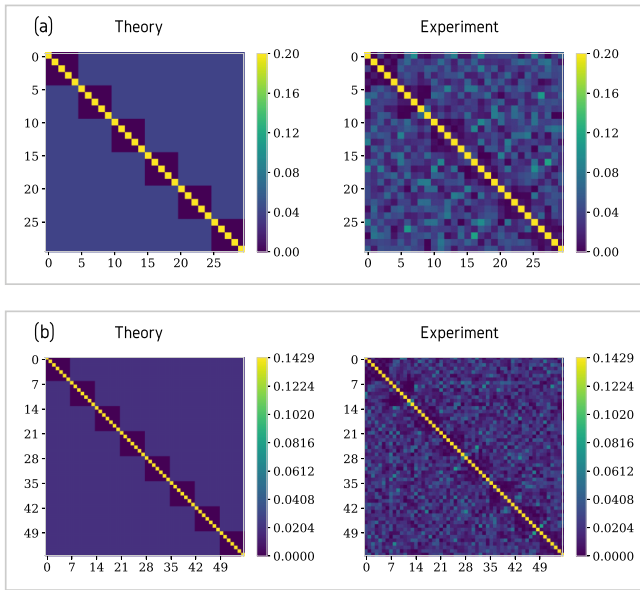


FIG. 6. Matrix of projections of MUB POVM elements for five (a) and seven (b) dimensions.

V. Reddy for helpful discussions. This research has received funding from the Gottfried Wilhelm Leibniz-Preis and from the European Unions Horizon 2020 research and innovation program under Grant No. 665148.

APPENDIX A: LIST OF STATE VECTORS

The following is the list of state vectors associated with the density matrices presented in Fig. 5, described in the Hermite-Gaussian basis:

$$|\psi_a\rangle = |1\rangle - \iota |3\rangle, \quad (\text{A1})$$

$$\begin{aligned} |\psi_b\rangle = & (0.36110833 + 0.28107443\iota) |0\rangle \\ & + (0.14599764 + 0.23536858\iota) |1\rangle \\ & + (0.39339517 + 0.05872998\iota) |2\rangle \\ & + (0.37242591 + 0.35380667\iota) |3\rangle \\ & + (0.34693250 + 0.07796563\iota) |4\rangle \\ & + (0.25172264 + 0.24799887\iota) |5\rangle \\ & + (0.16147789 + 0.12004762\iota) |6\rangle. \end{aligned} \quad (\text{A2})$$

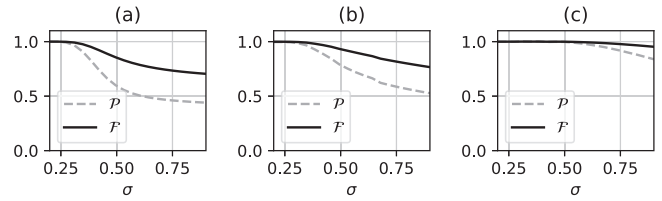


FIG. 7. The impact of an imperfect QPG (parametrized in σ with arbitrary units) on fidelity and purity of (a) measurement operators, (b) state tomography without calibration, and (c) state tomography with calibration of the POVMs. The y-axis in all cases indicates the purity or fidelity, scaling from zero to one.

APPENDIX B: MUB POVM ORTHOGONALITY

Figure 6 shows the matrix of projections of MUB POVM elements $|\phi_i\rangle\langle\phi_j|^2$ for five and seven dimensions, which is used for normalizing the data.

APPENDIX C: FEASIBILITY AGAINST EXPERIMENTAL ERRORS

In this section we briefly discuss the effectiveness of our tomographic method against the imperfections of the QPG's measurement operators. To simulate the imperfect QPG measurements, we convolve the theoretical seven-dimensional measurement operators with a Gaussian filter with a width of σ . This error model is chosen because from an operational point of view the main source of errors is the imperfect mode selectivity of the QPG. With an increasing width of the Gaussian filter, purity and fidelity of the measurement operators decline, as plotted in Fig. 7(a). In Fig. 7(b), we use these imperfect measurement operators to perform a state tomography on a pure input state in the Gaussian mode, which, as expected, shows a reduced fidelity with increasing values of σ . Finally, in Fig. 7(c), we use our knowledge of imperfect POVMs and repeat the state tomography with a calibrated QPG. For relatively small values of σ , with the purity of the measurement operators larger than about 0.6, the state tomography works with very high fidelities. However, our method breaks down for a larger amount of errors, which is considerably more than the experimental imperfections presented in this paper. With an excessive amount of experimental errors, other tomographic methods, such as Bayesian mean estimation [22], might be more effective. Nonetheless, a comprehensive theoretical evaluation of various types of error and finding the optimized tomographic method is necessary, which is beyond the scope of this paper.

- [1] B. Brecht, A. Eckstein, A. Christ, H. Suche, and C. Silberhorn, *New J. Phys.* **13**, 065029 (2011).
 [2] A. Eckstein, B. Brecht, and C. Silberhorn, *Opt. Express* **19**, 13770 (2011).
 [3] B. Brecht, D. V. Reddy, C. Silberhorn, and M. G. Raymer, *Phys. Rev. X* **5**, 041017 (2015).

- [4] T. C. Ralph, I. Söllner, S. Mahmoodian, A. G. White, and P. Lodahl, *Phys. Rev. Lett.* **114**, 173603 (2015).
 [5] J. Nunn, I. A. Walmsley, M. G. Raymer, K. Surmacz, F. C. Waldermann, Z. Wang, and D. Jaksch, *Phys. Rev. A* **75**, 011401 (2007).

- [6] Z. Zheng, O. Mishina, N. Treps, and C. Fabre, *Phys. Rev. A* **91**, 031802 (2015).
- [7] F. Schlawin, K. E. Dorfman, and S. Mukamel, *Phys. Rev. A* **93**, 023807 (2016).
- [8] B. Brecht, A. Eckstein, R. Ricken, V. Quiring, H. Suche, L. Sansoni, and C. Silberhorn, *Phys. Rev. A* **90**, 030302 (2014).
- [9] P. Manurkar, N. Jain, M. Silver, Y.-P. Huang, C. Langrock, M. M. Fejer, P. Kumar, and G. S. Kanter, *Optica* **3**, 1300 (2016).
- [10] Y.-S. Ra, C. Jacquard, A. Dufour, C. Fabre, and N. Treps, *Phys. Rev. X* **7**, 031012 (2017).
- [11] A. Shahverdi, Y. M. Sua, L. Tumeh, and Y.-P. Huang, *Sci. Rep.* **7**, 6495 (2017).
- [12] D. V. Reddy and M. G. Raymer, *Opt. Express* **25**, 12952 (2017).
- [13] V. Ansari, M. Allgaier, L. Sansoni, B. Brecht, J. Roslund, N. Treps, G. Harder, and C. Silberhorn, [arXiv:1607.03001](https://arxiv.org/abs/1607.03001).
- [14] Coherent Chameleon Ultra II.
- [15] Coherent Chameleon OPO.
- [16] Finisar waveshaper 4000.
- [17] Hamamatsu X10468-07 LCoS-SLM.
- [18] S. Bandyopadhyay, P. O. Boykin, V. Roychowdhury, and F. Vatan, *Algorithmica* **34**, 512 (2002).
- [19] A. J. Scott and M. Grassl, *J. Math. Phys.* **51**, 042203 (2010).
- [20] J. M. Renes, R. Blume-Kohout, A. J. Scott, and C. M. Caves, *J. Math. Phys.* **45**, 2171 (2004).
- [21] J. Rehacek, D. Mogilevtsev, and Z. Hradil, *Phys. Rev. Lett.* **105**, 010402 (2010).
- [22] R. Schmied, *J. Mod. Opt.* **63**, 1744 (2016).

ARXIV:1607.03001V2 (2018)

Title: Tomography and purification of the temporal-mode structure of quantum light

Authors: Vahid Ansari, John M. Donohue, Markus Allgaier, Linda Sansoni, Benjamin Brecht, Jonathan Roslund, Nicolas Treps, Georg Harder, Christine Silberhorn

Journal: arXiv:1607.03001v2 (Accepted for publication in Phys. Rev. Lett.)

Year: 2018

Contributions: V.A. designed and constructed the experimental setup. V.A., J.M.D, and G.H. carried out the experiment and wrote the manuscript. C.S. supervised the project. All authors contributed to the discussion of results and commented on the manuscript.

Tomography and purification of the temporal-mode structure of quantum light

Vahid Ansari,^{1,*} John M. Donohue,^{1,†} Markus Allgaier,¹ Linda Sansoni,¹ Benjamin Brecht,^{1,2}
Jonathan Roslund,³ Nicolas Treps,³ Georg Harder,¹ and Christine Silberhorn¹

¹*Integrated Quantum Optics, Paderborn University,
Warburger Strasse 100, 33098 Paderborn, Germany*

²*Clarendon Laboratory, Department of Physics, University of Oxford, Parks Road, OX1 3PU, United Kingdom*

³*Laboratoire Kastler Brossel, UPMC-Sorbonne Universités, CNRS,*

ENS-PSL Research University, Collège de France; CCF4, 4 Place Jussieu, 75252 Paris, France

To fully realize the potential of the time-frequency degree of freedom for photonic quantum science, techniques which selectively address the individual information-carrying modes must be established. In this work, we employ dispersion-engineered sum-frequency generation to perform temporal-mode selective measurements and manipulations on photons generated through parametric downconversion. We tailor the time-frequency mode structure of the generated photons through pump pulse shaping and confirm their structure through seven-dimensional quantum state tomography. Through changes in the second-order correlation function, we confirm that our technique manipulates and purifies the temporal structure of the overall photon state, explicitly demonstrating the effectiveness of engineered nonlinear processes for the mode manipulation of quantum states.

Single photons in clearly distinguishable, accurately controllable, and practically measurable modes are essential for photonic implementations of quantum information protocols [1]. The spectral and temporal, or time-frequency, photonic degrees of freedom offer an attractive framework for quantum communication and quantum information processing [2–5]. Unlike polarization and spatial encodings, information encoded in the time-frequency domain is robust through fiber-optic and waveguide transmission, making it a natural candidate for both long-distance quantum communication and compact integrated devices. The time-frequency basis also allows for expanded per-photon information rates and enables large-scale networking through high-dimensional encoding, multiplexing, and entanglement [6–10]. In particular, the pulsed broadband temporal mode structure provides an elegant, resource-efficient basis by encoding high-dimensional qudits in intensity-overlapping but field-orthogonal temporal waveforms [5], analogous to the orbital angular momentum spatial modes of light [11]. Due to their pulsed nature, temporal-mode encodings are an ideal choice for high repetition-rate applications and synchronizing multiple parties. Additionally, broadband temporal modes describe the natural Schmidt modes of photon pairs emitted from parametric downconversion (PDC) and spontaneous four-wave mixing [8, 12].

To fully exploit the temporal mode structure of quantum light, it is necessary to both control the modal structure of quantum light sources and develop matched mode-selective measurement methods. In order to perform projective measurements onto arbitrary temporal modes, techniques are needed which can identify and remove a specific desired mode from a mixture or superposition. Furthermore, operations on photonic temporal modes must not introduce noise in order to leave the fragile quantum nature of the light intact. Sum-frequency generation with tailored group-velocity relationships and

shaped ultrafast pulses provides a capable toolbox for these tasks [13–18]. Notably, a sum-frequency process between a weak photonic signal and a shaped strong measurement pulse with matched group velocities has been shown to act as mode-selective coupling between an unconverted frequency band and the temporal mode defined by the shaped strong pulse [15, 17]. This process, dubbed the *quantum pulse gate* (QPG), is capable of selectively addressing individual temporal modes and can be used as a temporal-mode analyzer for communication networks [13] or as an add-drop component to build general unitaries and quantum logic gates for a desired temporal-mode basis [5, 19]. Recent QPG experiments have shown highly efficient and highly selective operations on coherent light pulses [20–25] and its effectiveness as a measurement device for unknown superpositions [26] and a mode-selective photon subtractor [27]. While some of these works have used single-photon level coherent states [20, 22, 27], no existing experiments have shown temporal-mode selective manipulations and measurements of heralded single photons from PDC sources, which are necessary for entanglement-enhanced applications.

In this Letter, we show a complete set of tools to generate, manipulate, and measure the temporal-mode structure of single photons with a high degree of control. Single photons are heralded from an engineered PDC source where we orchestrate the modal structure of the photon pair by spectral modulation of the pump field. Regardless of the temporal mode structure of the PDC photons, we show that the QPG can select a single temporal mode from a mixture, demonstrating its usefulness as a temporal-mode projective measurement and as a purifier. We then use a QPG to tomographically reconstruct the seven-dimensional temporal-mode density matrix of heralded single photons, showing that QPG measurements are sensitive to time-frequency structure of light beyond

intensity-only measurements. Finally, through the correlation function measurements, we show that the QPG can change the modal structure of the transmitted photon state, either acting as a mode cleaner or increasing the mixedness depending on its programmable operation. We measure high signal-to-noise ratios and high contrast between mode selections while operating on quantum light, definitively positioning the QPG as an invaluable resource for pulsed quantum information science.

To illustrate the capability, flexibility, and sensitivity of our QPG scheme, we generate photon pairs through parametric downconversion in multiple configurations to produce varied underlying modal structures. PDC is a nonlinear process described by the Hamiltonian

$$\hat{H}_{\text{PDC}} = \iint d\omega_s d\omega_i f(\omega_s, \omega_i) \hat{a}_{\omega_s}^\dagger \hat{b}_{\omega_i}^\dagger + \text{h.c.}, \quad (1)$$

where the subscripts s and i refer to the signal and idler photons generated in modes \hat{a} and \hat{b} , respectively. The joint spectral amplitude function $f(\omega_s, \omega_i)$ describes the spectral phase and amplitude of the two-photon state, and is determined by the spectral shape of the PDC pump and the dispersive properties of the nonlinear material. While the joint spectral amplitude contains a complete description of the state in continuous time-frequency space, an equivalent discrete description can be obtained from the Schmidt decomposition [28], which re-expresses it in terms of orthonormal modes with normalized Schmidt coefficients γ_k as

$$f(\omega_s, \omega_i) = \sum_k \sqrt{\gamma_k} \psi_k(\omega_s) \phi_k(\omega_i). \quad (2)$$

Notably, for a Gaussian joint spectral amplitude, the eigenmodes are given by Hermite-Gaussian (HG) functions, as sketched in Fig. 1.

The number of effective modes in the two-photon system, K , can be defined in terms of the Schmidt coefficients and the purity P of the individual photons as

$$K = \frac{1}{P} = \frac{1}{\sum_k \gamma_k^2}. \quad (3)$$

The purity of a heralded photon generated through PDC can be experimentally measured through the second-order correlation function of one arm of the PDC (i.e. the marginal $g^{(2)}$) [29]. In the low-gain regime, the $g^{(2)}$ relates to the purity as simply $g^{(2)} = 1 + P$, as the single-mode thermal photon-number statistics ($g^{(2)} = 2$) tend toward Poissonian ($g^{(2)} = 1$) as many effective modes are mixed together.

By optimizing the group velocity relationship between the signal, idler, and PDC pump fields, it is possible to generate approximately pure heralded single photons [12, 30–32], but only for specific wavelength configurations set by available nonlinear materials. To generate approximately pure single photons, PDC photons

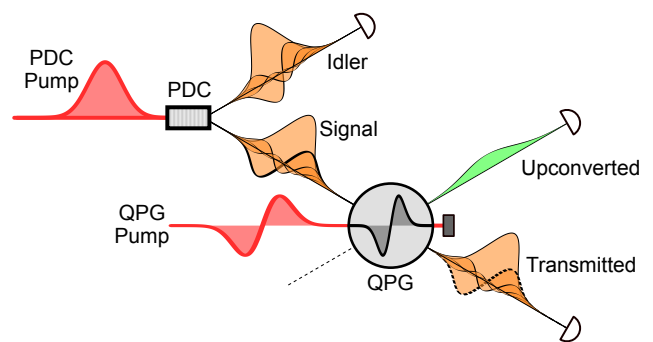


FIG. 1. **Temporal mode selection with a quantum pulse gate.** The two-photon state resulting from parametric downconversion (PDC) has a multimode structure defined by the pump field and nonlinear phasematching. The quantum pulse gate (QPG) selects a single mode (the first-order Hermite-Gauss for example, in bold) from this superposition and upconverts it to a higher frequency, while the unselected modes transmit unaffected. Changing the shape of the QPG pump changes which temporal mode the QPG selects.

are commonly spectrally filtered to be narrower than the PDC pump at the expense of heralding efficiency [33]. This tradeoff is due to the mismatch between the Schmidt modes of PDC states (broadband pulses) and the basis in which filtering is applied (spectral intensity). A temporally mode-selective device could overcome this limitation by converting one single mode to a register mode where it can be detected independently of the other modes [5, 24]. In this manner, an efficient QPG could be used to obtain highly pure PDC photons without affecting the heralding efficiency, essential for scalability in experiments requiring high-visibility interference from independent quantum sources [34, 35].

We implement a mode-selective QPG through sum-frequency generation, which can be described as an interaction between input and output fields in modes \hat{a}^\dagger and \hat{c}^\dagger by the Hamiltonian

$$\hat{H}_{\text{SFG}} \propto \iint d\omega_{\text{in}} d\omega_{\text{out}} \xi(\omega_{\text{in}}, \omega_{\text{out}}) \hat{a}_{\omega_{\text{in}}} \hat{c}_{\omega_{\text{out}}}^\dagger + \text{h.c.} \quad (4)$$

The transfer function, $\xi(\omega_{\text{in}}, \omega_{\text{out}})$, is defined by the phasematching function $\Phi(\omega_{\text{in}}, \omega_{\text{out}})$ and the spectral shape of the QPG pump, $\alpha(\omega_{\text{out}} - \omega_{\text{in}})$. If the input signal and the QPG pump travel together through the medium (i.e. are group-velocity matched), the phase-matching function can be described as a function of only the output frequency, i.e. $\Phi(\omega_{\text{in}}, \omega_{\text{out}}) \approx \bar{\Phi}(\omega_{\text{out}})$. For a sufficiently long interaction length, the output field will be temporally much longer than the input fields and thus spectrally much narrower. In this limit, the contribution of the QPG pump shape is a function of only the input field frequency, $\alpha(\omega_{\text{out}} - \omega_{\text{in}}) \approx \bar{\alpha}(\omega_{\text{in}})$, and the transfer function is completely separable.

In this case, we can describe the QPG interaction (in

the low-efficiency regime) as the single-mode broadband beamsplitter Hamiltonian with coupling constant θ ,

$$\hat{H}_{\text{QPG}} \propto i\theta \hat{A} \hat{C}^\dagger + \text{h.c.} \quad (5)$$

Eq. (5) describes a process which converts a photon in the input mode $\hat{A} = \int d\omega_{\text{in}} \bar{\alpha}(\omega_{\text{in}}) \hat{a}_{\omega_{\text{in}}}$ defined by the QPG pump spectral shape to the upconverted frequency mode $\hat{C} = \int d\omega_{\text{out}} \bar{\Phi}(\omega_{\text{out}}) \hat{c}_{\omega_{\text{out}}}$ defined by the phasematching function, and leaves all photons in orthogonal modes unaltered, as seen in Fig. 1. By measuring the upconverted frequency, the QPG facilitates a projective measurement onto a temporal mode \hat{A} that can be adjusted by shaping the spectrum of the QPG pump.

The group-velocity matching condition can be met in periodically poled lithium niobate (PPLN) waveguides, which also provide the spatial confinement necessary for long nonlinear interaction lengths. In our experimental setup, detailed in the appendix, we make use of type-II group-velocity matching between a 1540-nm photonic input and an 876-nm QPG pump, as in Refs. [20, 26]. To implement the QPG, we use a 17-mm PPLN waveguide with a 4.4 μm poling period built in-house. We measure upconverted output pulses at 558 nm with a 61-pm (59 GHz) bandwidth (full-width at half-maximum), significantly narrower than the 4.9-nm (620 GHz) bandwidth of the input photons. Although similar conditions can be met in other materials using near-degenerate type-0 or type-I processes [21–23], our scheme avoids the challenge of isolating the single-photon signal from the second harmonic of the QPG pump.

We use spatial-light-modulator-based pulse shapers to define both the spectral amplitude and phase of the PDC and QPG pump pulses [36, 37]. With this flexibility in hand, we selected four PDC states to illustrate the versatility of the QPG. The joint spectral intensity $|f(\omega_s, \omega_i)|^2$ for each is shown on the right side of Fig. 2, as measured with dispersive time-of-flight spectrometers [38]. Firstly, we set the PDC pump bandwidth such that the generated two-photon state is nearly spectrally separable [32], as seen in Fig. 2a. In this scenario, we expect that a single temporal mode dominates the PDC state. A singular value decomposition of the joint spectral intensity predicts a purity of 0.995, but measured $g^{(2)} = 1 + P$ (corrected for detector dark counts) corresponds to a significantly lower purity of 0.929 ± 0.008 , potentially due to high-order phase correlations or degenerate background processes.

By shaping the QPG pump to project onto a set of Hermite-Gauss spectral shapes, we expect to significantly higher upconversion probabilities for the lowest-order Gaussian mode. We find that, when measuring in coincidence with an idler detection, the Gaussian projection indeed provides more counts than the first-order Hermite-Gaussian projection by a factor of 19.3 (12.8 dB), with even stronger suppression for higher-order modes. This

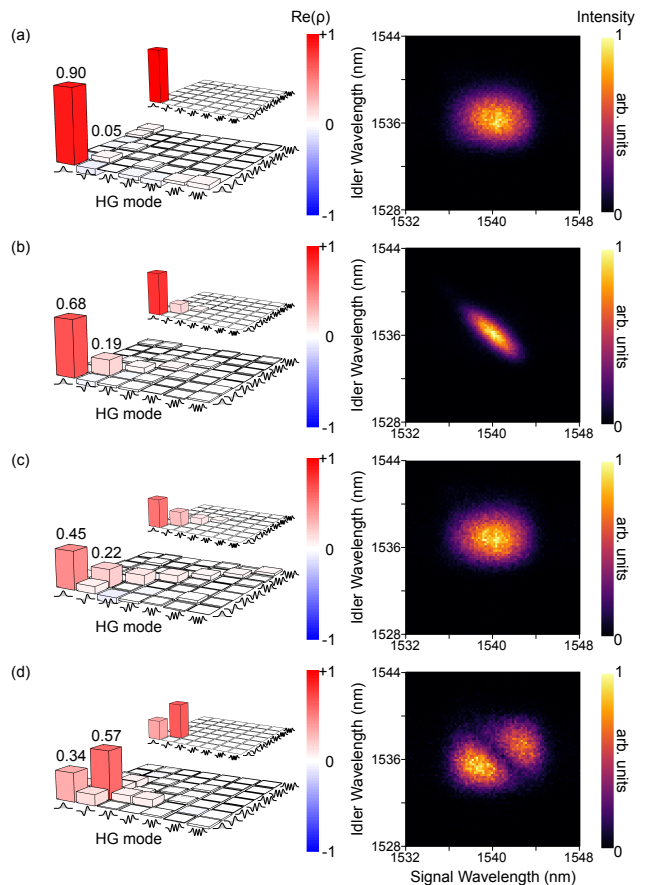


FIG. 2. **Joint spectral intensities and reconstructed temporal-mode density matrices.** The real part of the seven-dimensional one-photon temporal-mode tomographically reconstructed density matrices (left), joint spectral intensities (right), and theoretically expected density matrices (inset) for four PDC states: (a) a separable PDC state, (b) a PDC state with spectral anti-correlations from a narrow-bandwidth pump, (c) a PDC state with spectral phase correlations from a chirped pump, and (d) a PDC state pumped with a higher-order mode. The values of the first two diagonal entries are explicitly labelled above the density matrix. Imaginary components of the reconstructed density matrices are small and found in the appendix.

demonstrates simultaneously the high mode separability of our device and the single-mode character of our PDC state. With a coherent-state input signal from a commercial pulse shaper instead of PDC photons, the suppression factor increases to 111 (20.5 dB). The upconverted signal is cleanly separated from all background sources, even for a PDC-generated average photon number of $\langle n \rangle \approx 0.16$. The signal-to-noise ratio (including detector dark counts and noise from the QPG pump) is over 70:1 without heralding and increases to over 900:1 when gated by an idler detection.

While joint spectral intensity measurements provide important information about the two-photon PDC state,

they potentially hide significant information about the spectral phase to which mode-selective measurement would be sensitive. To demonstrate the effectiveness of the QPG for quantum state characterization, we reconstruct the density matrix of the signal photons, as seen on the left-hand side of Fig. 2. By shaping the QPG pump, we project onto the first seven Hermite-Gauss temporal modes as well as a tomographically complete set of superpositions, totalling 56 measurements [39, 40]. The time-frequency waveforms chosen span eight mutually unbiased seven-dimensional bases, and are sketched in the appendix. The density matrices were then reconstructed from the heralded counts in the upconverted mode using a maximum-likelihood approach [41]. As the tomography measurements are made on one photon of a PDC pair, we expect to reconstruct mixed density matrices with purities consistent with the measured $g^{(2)}$. For the separable PDC state of Fig. 2a, we reconstruct a density matrix with a purity of $\text{Tr}(\rho^2) = 0.896 \pm 0.006$, lower than the expected value of 0.929 ± 0.008 . Discrepancies between the tomographically reconstructed purities and the $g^{(2)}$ values arise from somewhat diminished mode selectivity for the higher-order projections [26], to which characterization of single-mode behaviour is particularly sensitive.

Next, we increase the number of modes present in the PDC state in three different ways, and show that the QPG measurements are sensitive to all three. First, we narrow the bandwidth of the PDC pump to produce a multimode PDC state with spectral intensity anticorrelations. The inseparability of this system can be seen directly in the joint spectral intensity of Fig. 2b as well as in the $g^{(2)}$ -inferred purity of 0.528 ± 0.009 , which matches the purity of the reconstructed density matrix, 0.523 ± 0.008 .

Intensity correlations are not the only available avenue for increasing the mode number of a PDC state. By adding quadratic spectral phase (chirp) to the PDC pump, we introduce phase correlations between the signal and idler photons. Note that this phase does not affect the joint spectral intensity, as seen in Fig. 2c. However, the added phase drastically decreases the $g^{(2)}$, with a measured purity of 0.327 ± 0.005 . Through tomography, we find that the QPG measurements are also sensitive to this phase, with a reconstructed purity of 0.317 ± 0.005 , similar to the $g^{(2)}$ -inferred purity. This result explicitly demonstrates the limitations of spectral intensity measurements for benchmarking pure single photons and the necessity of spectral phase control. More details on PDC with a chirped pump can be found in the appendix.

In each of the previous cases, the expected primary temporal mode of the PDC state is approximately Gaussian, with higher-order contributions falling off exponentially with mode number. In practical applications, it is often desirable to produce photon pairs in a restricted subspace, for example to create maximally entangled Bell states and their high-dimensional equivalents. As a fi-

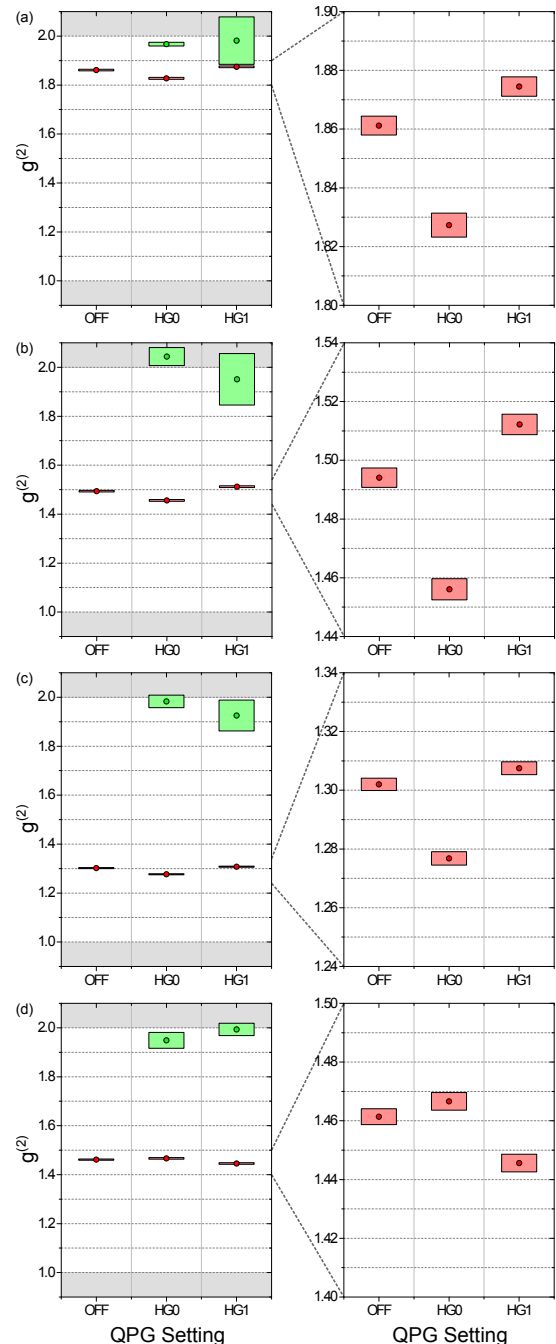


FIG. 3. **Second-order correlation functions of transmitted and upconverted photons.** The marginal $g^{(2)}$ s of the upconverted (green) and transmitted (red) PDC photons are shown for the four PDC states corresponding to Fig. 2a-d with the QPG pump pulse delayed relative to the signal photons ('OFF') and shaped to the first two Hermite-Gauss temporal modes ('HG0' and 'HG1'). The right side of the figure shows the same data rescaled to highlight the changes in the $g^{(2)}$ of the transmitted photons. The data presented is dark-count background subtracted and the error bars are found assuming Poissonian noise.

nal example, we produce a state with contributions from principally two temporal modes by shaping the PDC into the first-order Hermite-Gauss function, as seen in Fig. 2d. This pump shape is expected to produce photon pairs in the time-frequency Bell state, with similar weights in the zeroth- and first-order HG modes [5]. The reconstructed density matrix from the QPG measurements shows that the modal content of the PDC state is principally confined to these two modes, and the purities inferred from the $g^{(2)}$ and the tomography for this state are, respectively, 0.498 ± 0.006 and 0.531 ± 0.004 , consistent with half of a highly entangled qubit pair. The imbalance between the first two modes can be attributed to a non-ideal group-velocity relationship between signal and idler in the PDC process (i.e. a non-45-degree phasematching angle [32]), and is consistent with the density matrix expected from the joint spectral intensity.

To demonstrate the potential of the QPG for state purification, we measure the $g^{(2)}$ of the upconverted photons for the QPG pump in the first two Hermite-Gauss modes, as shown in Fig. 3. If the QPG selects a single mode from the input mixture, we expect that the upconverted photons themselves will be highly pure. Indeed, the $g^{(2)}$ of the upconverted light confirms a purity of at least 0.9 for both the zeroth- and first-order HG modes, regardless of the PDC state under interrogation. For example, for the correlated spectral intensity of case (b), the $g^{(2)}$ of the upconverted light when the Gaussian mode is selected is 1.95 ± 0.04 , which increases to 2.04 ± 0.04 after dark-count subtraction. The purity of the upconverted light remains high when the first-order HG mode is selected. The high $g^{(2)}$ values measured here conclusively show both that the QPG indeed selects a single mode and that the upconverted mode retains the thermal photon statistics of PDC, with very little noise introduced by the process.

Finally, we show through the $g^{(2)}$ that the modal structures of the transmitted photons are significantly altered by the QPG. If a mixture of modes is dominated by one mode, partially removing that mode from the mixture will increase the mixedness of the remaining distribution, akin to the Procrustean method of entanglement concentration [42]. For the decorrelated PDC state of case (a), we measured the conversion efficiency through the depletion of the transmitted signal as approximately 22%. This partial removal of the primary mode indeed results in a significant decrease in the $g^{(2)}$ of the unconverted transmitted signal photons, as seen on the right-hand side of Fig. 3, consistent with the efficiency measured from the input depletion. Conversely, removing the first-order HG mode removes amplitude from the secondary Schmidt coefficient, which increases the relative amplitude of the primary Schmidt mode. This is seen in cases (a-c) to increase the overall purity of the transmitted photon state, demonstrating that the QPG can act as a temporal mode cleaner even for the non-converted pho-

tons. In case (d), the first-order HG mode is present in a larger proportion than the Gaussian component, and the opposite trend is seen. This is consistent with the reconstructed density matrix of Fig. 2d. This directly demonstrates that the QPG can be used to remove modal components from a single-photon state, an essential task for mode-selective add/drop functionality.

We have shown that the quantum pulse gate can be used to directly manipulate and measure the temporal modal structure of single-photon states. By projecting over a complete set of temporal modes and superpositions, we reconstructed seven-dimensional temporal-mode density matrices for PDC photons with a variety of modal structures. We have demonstrated that the output of the pulse gate is nearly completely purified regardless of the input, positioning the quantum pulse gate as a powerful tool for photonic quantum state engineering. We have also demonstrated through changes in the second-order correlation function that the quantum pulse gate modifies the modal structure of the input photons, establishing the QPG as a novel device for both entanglement concentration and state purification. Future work will focus on improving the efficiency and extending the accessible dimensionality of the quantum pulse gate to fully realize its potential for time-frequency mode-selective measurement, as a conversion interface and add/drop device for temporally encoded quantum networks, and as a platform for high-dimensional quantum state characterization.

Acknowledgements - We thank T. Bartley, D. V. Reddy, and J. Tiedau for fruitful discussions. This research has received funding from the Deutsche Forschungsgemeinschaft (DFG) via Sonderforschungsbereich TRR 142, the Gottfried Wilhelm Leibniz-Preis, and from the European Unions (EU) Horizon 2020 research and innovation program under Grant Agreement No. 665148. J.M.D. gratefully acknowledges support from Natural Sciences and Engineering Resource Council of Canada.

* vahid.ansari@uni-paderborn.de

† john.matthew.donohue@uni-paderborn.de

- [1] P. Kok, W. J. Munro, K. Nemoto, T. C. Ralph, J. P. Dowling, and G. J. Milburn, *Reviews of Modern Physics* **79**, 135 (2007).
- [2] W. Tittel, J. Brendel, H. Zbinden, and N. Gisin, *Phys. Rev. Lett.* **81**, 3563 (1998).
- [3] J. Nunn, L. J. Wright, C. Söller, L. Zhang, I. A. Walmsley, and B. J. Smith, *Opt. Express* **21**, 15959 (2013).
- [4] J. M. Lukens, A. Dezfouliyan, C. Langrock, M. M. Fejer, D. E. Leaird, and A. M. Weiner, *Phys. Rev. Lett.* **112**, 133602 (2014).
- [5] B. Brecht, D. V. Reddy, C. Silberhorn, and M. G. Raymer, *Phys. Rev. X* **5**, 041017 (2015).
- [6] S. Yokoyama, R. Ukai, S. C. Armstrong, C. Sornphiphat-

- phong, T. Kaji, S. Suzuki, J.-i. Yoshikawa, H. Yonezawa, N. C. Menicucci, and A. Furusawa, *Nature Photonics* **7**, 982 (2013).
- [7] I. Herbauts, B. Blauensteiner, A. Poppe, T. Jennewein, and H. Huebel, *Opt. Express* **21**, 29013 (2013).
- [8] J. Roslund, R. M. De Araujo, S. Jiang, C. Fabre, and N. Treps, *Nature Photonics* **8**, 109 (2014).
- [9] T. Zhong, H. Zhou, R. D. Horansky, C. Lee, V. B. Verma, A. E. Lita, A. Restelli, J. C. Bienfang, R. P. Mirin, T. Gerrits, *et al.*, *New Journal of Physics* **17**, 022002 (2015).
- [10] S. Schwarz, B. Bessire, A. Stefanov, and Y.-C. Liang, *New Journal of Physics* **18**, 035001 (2016).
- [11] M. Agnew, J. Leach, M. McLaren, F. S. Roux, and R. W. Boyd, *Phys. Rev. A* **84**, 062101 (2011).
- [12] A. B. U'Ren, C. Silberhorn, R. Erdmann, K. Banaszek, W. P. Grice, I. A. Walmsley, and M. G. Raymer, *Laser Physics* **15**, 146 (2005).
- [13] Z. Zheng and A. Weiner, *Optics Lett.* **25**, 984 (2000).
- [14] A. Pe'er, B. Dayan, A. A. Friesem, and Y. Silberberg, *Phys. Rev. Lett.* **94**, 073601 (2005).
- [15] A. Eckstein, B. Brecht, and C. Silberhorn, *Opt. Express* **19**, 13770 (2011).
- [16] J. M. Donohue, M. Agnew, J. Lavoie, and K. J. Resch, *Phys. Rev. Lett.* **111**, 153602 (2013).
- [17] D. V. Reddy, M. G. Raymer, C. J. McKinstrie, L. Mejling, and K. Rottwitt, *Opt. Express* **21**, 13840 (2013).
- [18] M. Allgaier, V. Ansari, L. Sansoni, C. Eigner, V. Quiring, R. Ricken, G. Harder, B. Brecht, and C. Silberhorn, *Nature Comm.* **8**, 14288 (2017).
- [19] B. Brecht, A. Eckstein, A. Christ, H. Suche, and C. Silberhorn, *New J. of Phys.* **13**, 065029 (2011).
- [20] B. Brecht, A. Eckstein, R. Ricken, V. Quiring, H. Suche, L. Sansoni, and C. Silberhorn, *Phys. Rev. A* **90**, 030302 (2014).
- [21] A. S. Kowligy, P. Manurkar, N. V. Corzo, V. G. Velev, M. Silver, R. P. Scott, S. J. B. Yoo, P. Kumar, G. S. Kanter, and Y.-P. Huang, *Opt. Express* **22**, 27942 (2014).
- [22] P. Manurkar, N. Jain, M. Silver, Y.-P. Huang, C. Langrock, M. M. Fejer, P. Kumar, and G. S. Kanter, *Optica* **3**, 1300 (2016).
- [23] D. V. Reddy and M. G. Raymer, *Optics Express* **25**, 12952 (2017).
- [24] A. Shahverdi, Y. M. Sua, L. Tumei, and Y.-P. Huang, *Scientific Reports* **7**, 6495 (2017).
- [25] D. V. Reddy and M. G. Raymer, *arXiv:1710.06736* (2017).
- [26] V. Ansari, G. Harder, M. Allgaier, B. Brecht, and C. Silberhorn, *Phys. Rev. A* **96**, 063817 (2017).
- [27] Y.-S. Ra, C. Jacquard, A. Dufour, C. Fabre, and N. Treps, *Phys. Rev. X* **7**, 031012 (2017).
- [28] C. K. Law, I. A. Walmsley, and J. H. Eberly, *Phys. Rev. Lett.* **84**, 5304 (2000).
- [29] A. Christ, K. Laiho, A. Eckstein, K. N. Cassemiro, and C. Silberhorn, *New Journal of Physics* **13**, 033027 (2011).
- [30] W. P. Grice and I. A. Walmsley, *Phys. Rev. A* **56**, 1627 (1997).
- [31] O. Kuzucu, M. Fiorentino, M. A. Albota, F. N. C. Wong, and F. X. Kärtner, *Phys. Rev. Lett.* **94**, 083601 (2005).
- [32] G. Harder, V. Ansari, B. Brecht, T. Dirmeier, C. Marquardt, and C. Silberhorn, *Opt. Express* **21**, 13975 (2013).
- [33] E. Meyer-Scott, N. Montaut, J. Tiedau, L. Sansoni, H. Herrmann, T. J. Bartley, and C. Silberhorn, *Phys. Rev. A* **95**, 061803(R) (2017).
- [34] M. A. Broome, A. Fedrizzi, S. Rahimi-Keshari, J. Dove, S. Aaronson, T. C. Ralph, and A. G. White, *Science* **339**, 794 (2013).
- [35] X.-L. Wang, L.-K. Chen, W. Li, H.-L. Huang, C. Liu, C. Chen, Y.-H. Luo, Z.-E. Su, D. Wu, Z.-D. Li, *et al.*, *Physical Review Letters* **117**, 210502 (2016).
- [36] A. M. Weiner, *Rev. Sci. Instrum.* **71**, 1929 (2000).
- [37] A. Monmayrant, S. Weber, and B. Chatel, *Journal of Physics B* **43**, 103001 (2010).
- [38] M. Avenhaus, A. Eckstein, P. J. Mosley, and C. Silberhorn, *Optics Letters* **34**, 2873 (2009).
- [39] W. K. Wootters and B. D. Fields, *Annals of Physics* **191**, 363 (1989).
- [40] S. Bandyopadhyay, P. O. Boykin, V. Roychowdhury, and F. Vatan, *Algorithmica* **34**, 512 (2002).
- [41] J. B. Altepeter, E. R. Jeffrey, and P. G. Kwiat, *Advances in Atomic, Molecular, and Optical Physics* **52**, 105 (2005).
- [42] C. H. Bennett, H. J. Bernstein, S. Popescu, and B. Schumacher, *Phys. Rev. A* **53**, 2046 (1996).

Appendix

In this appendix, we provide technical details on the experimental setup, sketched in Fig. 4. In Table I, we provide measured parameters of the four PDC states explored in the main text, including the $g^{(2)}$ numbers displayed graphically in Fig. 3 of the main text. We also provide extra data detailing the purity of the PDC pump as the PDC pump is chirped, as seen in Fig. 5. In Fig. 7, we provide both the real and imaginary parts of the reconstructed seven-dimensional density matrices, and compare their eigenvalues with the expected values from the JSI. In Fig. 6, we show the projections implemented by the QPG to reconstruct the seven-dimensional density matrices.

Our experiment is driven by an 80-MHz titanium-sapphire laser (Ti:Sa, Coherent Chameleon) and OPO (APE Compact). We create the PDC pump pulses at 769 nm by frequency doubling light from the OPO in 1 mm of bulk PPLN; the fundamental of the Ti:Sa at 876 nm is used as the QPG pump. Both pulses are shaped with approximately 0.05-nm resolution using a 4f setup consisting of a 2000 lines/mm diffracting grating, a curved mirror with a 250 mm focal length, and a reflective liquid-crystal spatial light modulator (SLM, Hamamatsu LCoS) at the focal plane [36, 37]. With this setup, we can directly control the bandwidth, spectral shape, and spectral phase of the pump pulses.

The PDC photons are generated through a near-degenerate type-II process in a 8-mm long PPKTP waveguide (AdvR) with a nominal poling period of 117 μm . An 80 nm broad bandpass filter is used to remove the PDC pump, and the individual photons are separated with a polarizing beamsplitter and filtered with 3 nm bandpass filters to remove side lobes. In all cases, the PDC pump energy was approximately 15 pJ per pulse, with heralded $g_h^{(2)}$ s lying between 0.417 ± 0.003 for the spectrally decorrelated state and 0.246 ± 0.003 for the intensity-anticorrelated state. This relatively high production rate was used to enable reasonably precise unheralded $g^{(2)}$ measurements with 10-minute recording times. See Table I for all $g_h^{(2)}$ values. For ease of alignment, the signal photon path can be switched for a coherent pulse from the OPO, spectrally shaped by a commercial pulse shaper (Finisar WaveShaper 4000S). The average number of generated photons can be inferred from the two-photon cross-correlation statistics [29], with the average generation rate of $\langle n \rangle \approx 0.16$ for the decorrelated state deduced from a $g^{(1,1)} = \frac{1}{\langle n \rangle} + g^{(2)} = 8.303 \pm 0.003$.

The signal photons and the QPG pump (with an average energy-per-pulse of 250 pJ) are combined on a dichroic mirror and coupled into a 17-mm long PPLN waveguide with a poling period of 4.4 μm , fabricated in-house and designed for spatially single-mode propagation at 1540 nm. The waveguide mode of the QPG pump is imaged on a camera after the waveguide and optimized to the fundamental spatial mode. Higher-order modes produce sum-frequency signals for different time delays with central frequencies, and are filtered out of the final signal along with

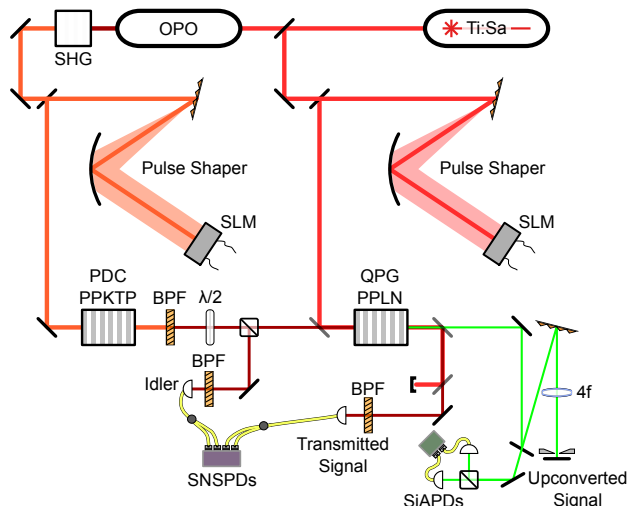


FIG. 4. **Experimental setup.** We create photon pairs through type-II PDC in an 8-mm PPKTP waveguide. By shaping the bandwidth and spectral phase of the PDC pump with a spatial light modulator (SLM) in a 4f line [36, 37], we can control the effective mode number of the generated photon pairs. The PDC pump is removed with a bandpass filter (BPF) and the photon pair is split with a polarizing beamsplitter (PBS). The signal photon is then coupled into a 17-mm PPLN waveguide acting as a quantum pulse gate (QPG), with a QPG pump shaped in both phase and amplitude by another SLM. A series of dichroic mirrors and a 4f line are used to split the upconverted and transmitted photons from the leftover QPG pump, and all photon paths are coupled into single-mode-fiber beamsplitters to measure second-order correlation functions.

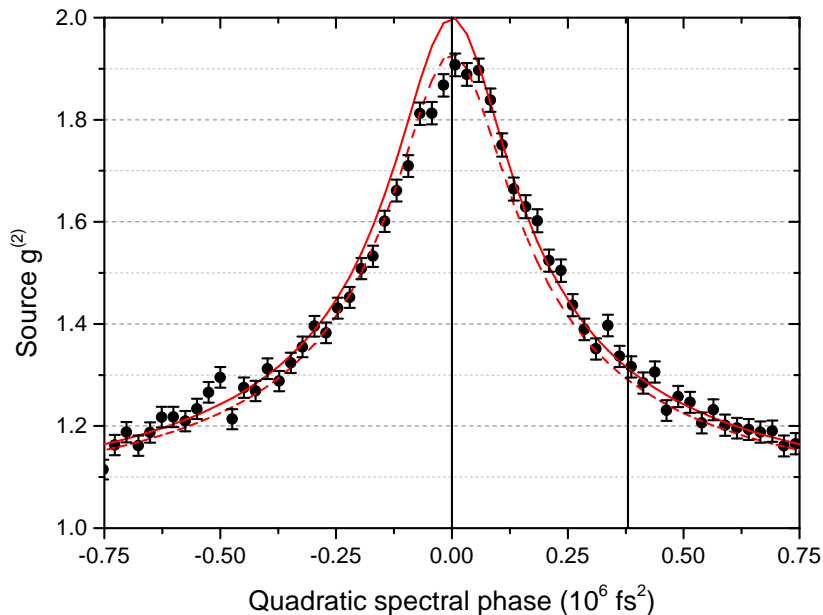


FIG. 5. **PDC source purity as spectral phase added.** The purity of the PDC source, as measured from the marginal $g^{(2)}$ of the signal photon with the QPG off, as a function of quadratic spectral phase of the form $e^{iA(\omega-\omega_0)^2}$ on the PDC pump. Five seconds of data were taken per spectral phase setting. The thick black lines represent the chirp values used for a high-purity PDC state (Case ‘a’) and a highly multimode PDC state (Case ‘c’). The solid red curve is the theoretical expectation of Eq. 6, and the dashed red curve is the same curve with Poissonian background equivalent to 4% of the total count rate added to match the peak $g^{(2)}$ of 1.929 measured in the experiment.

the second harmonic of the QPG pump by a 4f-filter. The upconverted light at 558 nm is measured on a spectrometer (Andor Shamrock SR500 spectrograph and Newton 970-BVF EMCCD camera with a 2398 lines/mm grating) to have a bandwidth of 61 pm FWHM. The 4f-filter is also used to remove spectral side lobes, which account for less than 5% of the total upconverted photons. The upconverted green photons were detected with silicon avalanche photodiodes (SiAPDs, Excelitas), while the idler and leftover signal photons were detected with superconducting nanowire single-photon detectors (SNSPDs, PhotonSpot). All three photon paths are split into two detectors to measure photon number correlations via Hanbury-Brown-Twiss interferometry [29].

The joint spectral intensities (JSIs) were measured with fiber-based time-of-flight spectrometers [38], mapping a spectral range of 1 nm at 1540 nm to a time delay of 0.42 ns. Assuming a flat spectral phase, the singular-value decomposition of the JSI predicts a spectral purity of 0.995 for the decorrelated JSI of Fig. 7a, and 0.652 for the intensity anticorrelated JSI of Fig. 7b. The marginal bandwidths (intensity FWHM) of the signal and idler photon in the decorrelated case were measured to be 4.9 nm and 3.6 nm, respectively.

To compensate for dispersive elements throughout the apparatus, the spectral phase of the PDC pump was optimized with the SLM to maximize the $g^{(2)}$ of the decorrelated state (Case ‘a’), as seen in Fig. 5. The chirp of the phase-correlated PDC state of Fig. 7c is $A = 0.38 \times 10^6 \text{ fs}^2$, where the chirp is represented as a phase in angular frequency as $\exp[iA(\omega - \omega_0)^2]$. Given a separable Gaussian PDC state with signal and idler bandwidths σ_s and σ_i (intensity standard deviation in ω), the expected purity as a function of pump chirp A is

$$P = \frac{1}{\sqrt{1 + 16A^2\sigma_s^2\sigma_i^2}}, \quad (6)$$

which is seen in Fig. 5 to match the experimental result well for large chirp values. While this result clearly shows that dispersion management of the pump is key for producing single-mode photons, it also provides an alternative avenue for generating highly entangled photon pair states. For tasks requiring highly multimode photons, this method of increasing the number of modes present can make use of the entire PDC pump bandwidth, and therefore does not significantly affect the pair generation rate of the source in power-limited situations.

The central wavelength and time delay of the QPG pump relative to the PDC signal photons were set by optimizing the ratio of upconversion between HG0 and HG1 projections. The spectral phase and bandwidth of the QPG pump

Reference	(a)	(b)	(c)	(d)
PDC Pump Shape	HG0	HG0	HG0	HG1
PDC Pump Bandwidth	1.72 nm	0.54 nm	1.49 nm	1.31 nm
PDC Pump Chirp	0	0	$0.38 \times 10^6 \text{ fs}^2$	0
QPG Pump Bandwidth	1.54 nm	1.05 nm	1.58 nm	1.30 nm
Purity of ρ from reconstruction	0.896 ± 0.006	0.523 ± 0.008	0.317 ± 0.005	0.531 ± 0.004
Expected purity from JSI	0.995	0.652	0.377*	0.542*
Transmitted $g^{(2)}$, QPG pump blocked	1.929 ± 0.008	1.528 ± 0.010	1.327 ± 0.005	1.498 ± 0.006
Transmitted $g^{(2)}$, QPG pump delayed	1.861 ± 0.003	1.494 ± 0.003	1.302 ± 0.002	1.461 ± 0.003
Transmitted $g^{(2)}$, QPG pump HG0	1.827 ± 0.004	1.456 ± 0.004	1.277 ± 0.002	1.467 ± 0.003
Transmitted $g^{(2)}$, QPG pump HG1	1.875 ± 0.003	1.512 ± 0.004	1.308 ± 0.002	1.446 ± 0.003
Upconverted $g^{(2)}$, QPG pump HG0	1.975 ± 0.015	2.044 ± 0.037	1.983 ± 0.026	1.949 ± 0.033
Upconverted $g^{(2)}$, QPG pump HG1	2.078 ± 0.194	1.951 ± 0.105	1.925 ± 0.063	1.993 ± 0.025
Transmitted $g_h^{(2)}$, QPG pump delayed	0.417 ± 0.003	0.246 ± 0.003	0.374 ± 0.002	0.393 ± 0.003
Upconverted $g_h^{(2)}$, QPG pump HG0	0.423 ± 0.005	0.319 ± 0.009	0.501 ± 0.011	0.572 ± 0.017

TABLE I. Pump bandwidths and measured $g^{(2)}$ s for the four PDC states explored in the main text, corresponding to the JSIs of Fig. 7. The error of the purity from the tomographically reconstructed density matrices ρ are found through Monte Carlo simulation assuming the coincidences measured have Poissonian error. The expected purity from the JSIs correspond to the singular value decomposition assuming a flat phase, except in cases marked (*) where faithful implementation of the intended phase is assumed. All $g^{(2)}$ values are corrected for detector dark counts assuming a 3 ns coincidence window. $g_h^{(2)}$ is the heralded second-order correlation function, which is zero for the ideal single-photon Fock state and one or greater for all classical states of light.

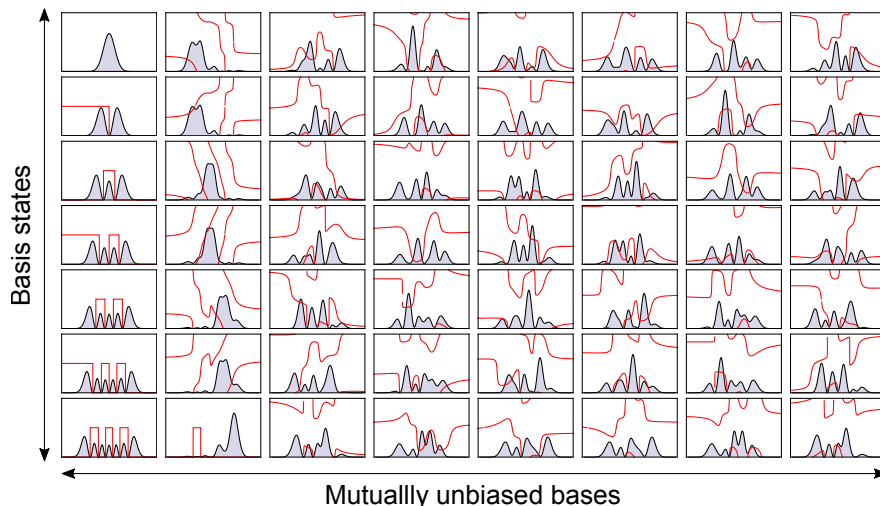


FIG. 6. **Seven-dimensional temporal-mode bases.** The spectral shapes corresponding to eight mutually unbiased seven-dimensional bases [40] as programmed for the reconstruction of Fig. 7. The black line and blue fill correspond to the intensity $|f(\omega)|^2$, and the red line corresponds to the phase on the interval $[0, 2\pi]$.

were adjusted to maximize the visibility between HG0 and HG2 projections. Pulse bandwidths as measured on a spectrometer (Andor Shamrock SR500 with a 1200 l/mm grating) are given in Table I.

For the $g^{(2)}$ measurements of Fig. 4 of the main text, the QPG is effectively set to ‘OFF’ by delaying the pump by 5 ps, where it does not interact with the PDC photons. The QPG pump is delayed rather than blocked in order to ensure all three measurements are subject to the same background noise. Coincidences are registered within a 3 ns window, and the expected dark counts outside this window are subtracted.

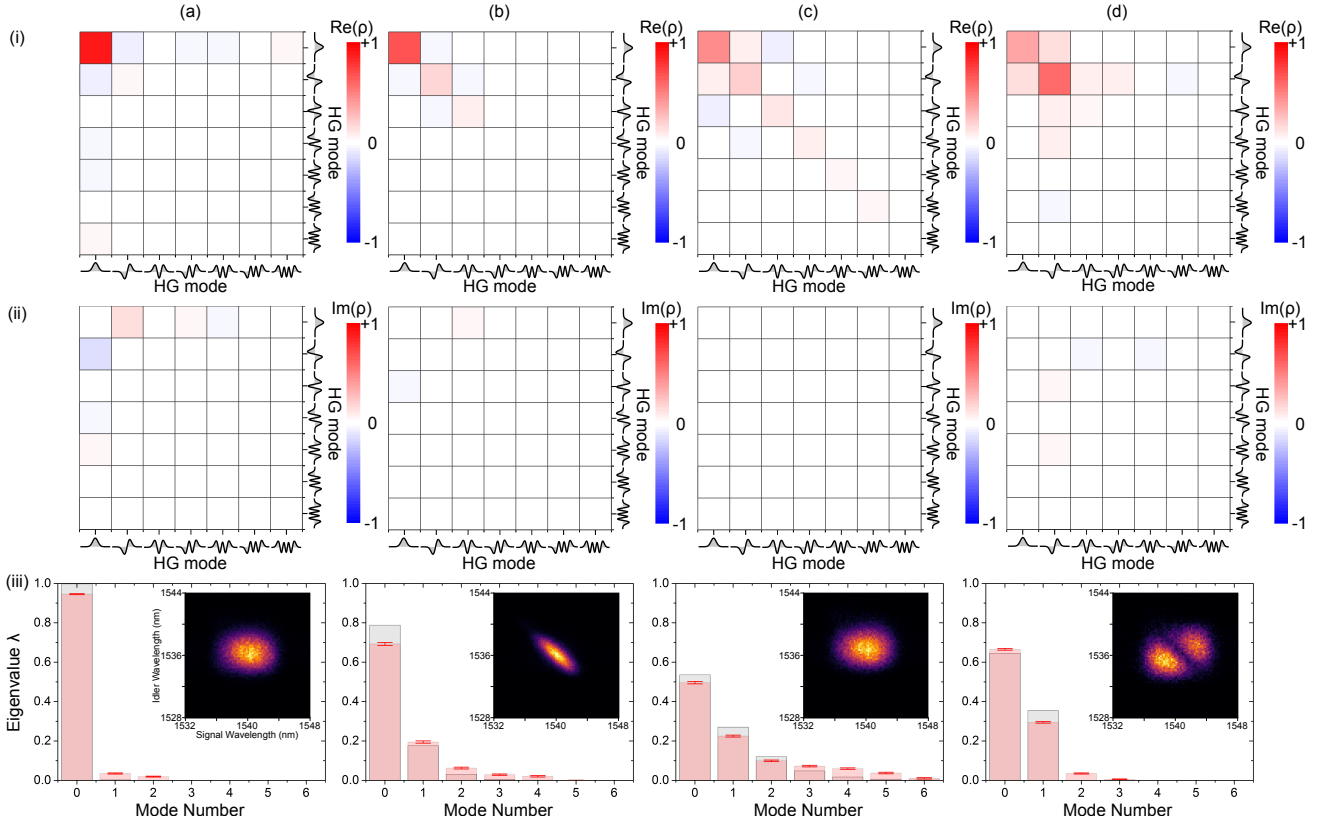


FIG. 7. **Reconstructed temporal-mode density matrices and joint spectral amplitudes.** The real (i) and imaginary (ii) parts of the reconstructed signal-photon density matrices for (a) a spectrally decorrelated PDC state, (b) an intensity-correlated state, (c) a phase-correlated state, and (d) an HG1-pumped state. The eigenvalues ($\sum \lambda = 1$) of these density matrices are shown in red in (iii), with the error bars found from Monte Carlo simulations assuming Poissonian noise. The expected one-photon density matrices from the joint spectral intensities (inset) are all diagonal with eigenvalues obtained from the singular value decomposition, as seen in gray assuming a flat phase for cases (a) and (b) and the programmed phase in (c) and (d).

Title: Tailoring nonlinear processes for quantum optics with pulsed temporal-mode encodings

Authors: Vahid Ansari, John M Donohue, Benjamin Brecht, Christine Silberhorn

Journal: Optica 5 (5), 534 (review article)

Year: 2018

Contributions: V.A., J.M.D, and B.B. co-wrote the manuscript. C.S. supervised the project and helped refining the article.



Tailoring nonlinear processes for quantum optics with pulsed temporal-mode encodings

VAHID ANSARI,^{1,*}  JOHN M. DONOHUE,¹  BENJAMIN BRECHT,²  AND CHRISTINE SILBERHORN¹ 

¹Integrated Quantum Optics, Paderborn University, Warburger Strasse 100, 33098 Paderborn, Germany

²Clarendon Laboratory, University of Oxford, Parks Road, Oxford, OX1 3PU, UK

*Corresponding author: vahid.ansari@uni-paderborn.de

Received 6 February 2018; revised 12 March 2018; accepted 30 March 2018 (Doc. ID 321344); published 2 May 2018

The time-frequency degree of freedom is a powerful resource for implementing high-dimensional quantum information processing. In particular, field-orthogonal pulsed temporal modes offer a flexible framework compatible with both long-distance fiber networks and integrated waveguide devices. In order for this architecture to be fully utilized, techniques to reliably generate diverse quantum states of light and accurately measure complex temporal waveforms must be developed. To this end, nonlinear processes mediated by spectrally shaped pump pulses in group-velocity engineered waveguides and crystals provide a capable toolbox. In this review, we examine how tailoring the phase-matching conditions of parametric downconversion and sum-frequency generation allows for highly pure single-photon generation, flexible temporal-mode entanglement, and accurate measurement of time-frequency photon states. We provide an overview of experimental progress towards these goals and summarize challenges that remain in the field. © 2018 Optical Society of America under the terms of the OSA Open Access Publishing Agreement

OCIS codes: (270.5565) Quantum communications; (130.3120) Integrated optics devices; (320.7085) Ultrafast information processing.

<https://doi.org/10.1364/OPTICA.5.000534>

1. INTRODUCTION

In any implementation of quantum information protocols, it is necessary to have access to information-carrying modes that are individually manageable and measurable in arbitrary bases. In optical implementations, it is often essential to be able to create photonic quantum states with a controlled degree of entanglement and to retain coherence among the modes over long-distance transmission. In polarization, state rotations and measurements are simple with wave plates and polarizing beam splitters, and entangled sources are straightforward to implement, but the dimensionality is limited to two. In the spatial degree of freedom, entanglement is naturally present in a high-dimensional basis of, for example, orbital angular momentum modes, and arbitrary measurements can be made with spatial light modulators. However, their complex spatial structures render them incompatible with spatially single-mode integrated devices and optical fiber networks.

Alternatively, the time-frequency (or energy-time) degree of freedom can be exploited by encoding quantum information in photonic *temporal modes* (TMs). Here, the information is encoded in the complex time-frequency amplitude of the electric field of single photons. Like spatial encodings, the Hilbert space available in the Fourier-conjugate time and frequency domains is, in principle, unbounded, allowing for high-dimensional encodings. Unlike spatial encodings, time-frequency encodings are

intrinsically compatible with waveguides and fiber transmission. Temporal-mode bases can take on a variety of forms, such as discrete time or frequency bins or intensity-overlapping pulsed temporal modes, as illustrated in Fig. 1, so long as the waveforms provide an orthonormal basis. However, controlling entanglement between and directly measuring arbitrary temporal modes presents a significant challenge for time-frequency quantum information processing.

In this mini review, we will highlight works on both the targeted generation and manipulation of TMs through controlling the group-velocity relationship in nonlinear processes. In Section 2, we summarize the basic theory behind the TM structure of photon pairs generated via parametric downconversion (PDC). Section 3 focusses on efforts towards engineering the PDC process itself, for both single-mode photon generation and to create photons with rich, programmable TM structures. In Section 4, we transfer these techniques from PDC to frequency conversion, unveiling methods to manipulate and measure the complex TM structure. Section 5 then summarizes current experimental progress on the manipulation of photonic TMs by means of frequency conversion, direct temporal manipulation, and tailored light-matter interactions. In Section 6, we overview recent experimental results, paving the way towards TM-based quantum applications. Finally, in Section 7, we will give an outlook on future steps and highlight challenges that will need to be overcome in the future.

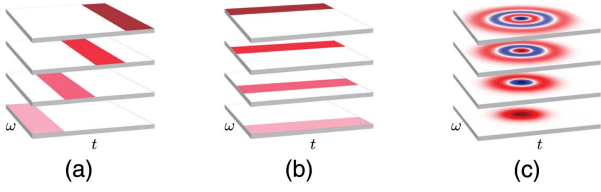


Fig. 1. Temporal-mode encodings visualized in time-frequency space. Orthogonal temporal mode bases can be constructed through slicing bins in time or frequency, as in (a) and (b), or through intensity-overlapping but field-orthogonal pulsed temporal modes, such as the Hermite–Gauss modes in (c).

2. TEMPORAL-MODE STRUCTURE OF PARAMETRIC DOWNCONVERSION

In this section, we describe the TM structure of photon-pair states generated in PDC, where a photon from a bright classical pump pulse decays with a small probability inside a nonlinear optical medium, e.g., a nonlinear waveguide, into a pair of daughter photons typically called *signal* and *idler*, as sketched in Fig. 2(a). PDC is a well-understood process, capable of generating photons with a rich TM structure at room temperature. Moreover, PDC can be used to generate a plethora of quantum states including heralded single photons, squeezed states, and maximally entangled states. These properties have cemented PDC as the workhorse in many quantum optics laboratories.

Restricting our model to the generation of photon pairs and assuming spatially single-mode emission, e.g., by realizing the PDC in a weakly pumped waveguide, the type-II PDC process can be described by the interaction Hamiltonian

$$\hat{H}_{\text{PDC}} = \mathcal{B} \int d\omega_s d\omega_i f(\omega_s, \omega_i) \hat{a}^\dagger(\omega_s) \hat{b}^\dagger(\omega_i) + \text{h.c.}, \quad (1)$$

and the generated state can be written as

$$|\psi\rangle_{\text{PDC}} = \mathcal{B} \int d\omega_s d\omega_i f(\omega_s, \omega_i) \hat{a}^\dagger(\omega_s) \hat{b}^\dagger(\omega_i) |\text{vac}\rangle, \quad (2)$$

where $\hat{a}^\dagger(\omega_s)$ and $\hat{b}^\dagger(\omega_i)$ are standard creation operators that generate a signal photon at ω_s and an idler photon at ω_i ; \mathcal{B} is the optical gain or efficiency of the process, which includes the second-order nonlinearity and the pump power; and $f(\omega_s, \omega_i)$ is the complex-valued joint spectral amplitude (JSA),

normalized to $\int d\omega_s d\omega_i |f(\omega_s, \omega_i)|^2 = 1$. The JSA describes the entangled time-frequency structure of the PDC state and is essential for describing PDC in cases with a broadband pump pulse [1].

The JSA itself can be written as a product of the pump envelope function $\alpha(\omega_s + \omega_i)$ and the phase-matching function $\phi(\omega_s, \omega_i)$, such that

$$f(\omega_s, \omega_i) = \alpha(\omega_s + \omega_i) \phi(\omega_s, \omega_i). \quad (3)$$

Here, $\alpha(\omega_s + \omega_i)$ is the slowly varying envelope of the broadband pump and reflects energy conservation during the PDC, and the phase-matching $\phi(\omega_s, \omega_i)$ expresses the momentum conservation between involved fields and the dispersion properties of the nonlinear medium. The phase-matching function can be written as

$$\phi(\omega_s, \omega_i) = \int_0^L dz \chi(z) \exp[i\Delta k(\omega_s, \omega_i)z], \quad (4)$$

where $\Delta k(\omega_s, \omega_i) = k_p(\omega_s + \omega_i) - k_s(\omega_s) - k_i(\omega_i)$ is the phase mismatch, L is the length of the nonlinear medium, and $\chi(z) = \pm 1$ describes the orientation of the ferroelectric domains of the crystal. A periodic modulation of $\chi(z)$, with a period Λ , is called *periodic poling* [2]. This poling adds an additional component of the form $k_{\text{QPM}} = 2\pi/\Lambda$ to the phase mismatch, such that $\Delta k(\omega_s, \omega_i) \mapsto \Delta k(\omega_s, \omega_i) + 2\pi/\Lambda$, allowing the center frequencies of the phase-matched process to be tuned. In this case, the resulting phase-matching function is given by

$$\phi(\omega_s, \omega_i) = \frac{1}{L} \text{sinc}\left(\frac{\Delta k(\omega_s, \omega_i)L}{2}\right) e^{i\Delta k(\omega_s, \omega_i)\frac{L}{2}}. \quad (5)$$

The sinc profile of the phase-matching function has significant implications that will be discussed in Section 3. However, to simplify the equations and plots in this article, we usually employ a Gaussian approximation of the phase-matching function.

In 2000, Law and co-workers examined the time-frequency structure of the JSA through the *Schmidt decomposition*, defining two-photon entanglement in terms of temporal modes [3]. For this, the JSA is decomposed into two sets of orthonormal basis functions $\{g^{(s)}\}$ and $\{h^{(i)}\}$ for signal and idler, respectively, and we write

$$f(\omega_s, \omega_i) = \sum_k \sqrt{\lambda_k} g_k^{(s)}(\omega_s) h_k^{(i)}(\omega_i), \quad (6)$$

where $\sum_k \lambda_k = 1$. With this we define broadband TM operators

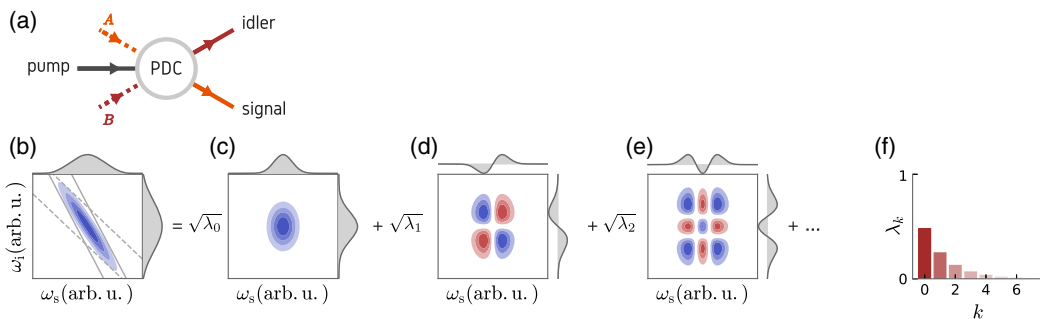


Fig. 2. Joint spectral amplitude, temporal modes, and Schmidt coefficients of a non-engineered PDC process. (a) Outline of a PDC process with the three involved fields. (b) The JSA and its marginal distributions which is the product of pump (dashed lines) and phase matching (solid lines) functions and, in this case, exhibits frequency anti-correlations between signal and idler frequencies. The Schmidt decomposition of this Gaussian JSA is given by Hermite–Gaussian functions, with the first three TM pairs shown in (c)–(e). (f) The first seven Schmidt coefficients λ_k . The decomposition of this example yields an effective mode number of $K \approx 3.14$.

$$\hat{A}_k^\dagger = \int d\omega_s g_k^{(s)}(\omega_s) \hat{a}^\dagger(\omega_s), \quad (7)$$

$$\hat{B}_k^\dagger = \int d\omega_i h_k^{(i)}(\omega_i) \hat{b}^\dagger(\omega_i), \quad (8)$$

and consequently obtain

$$|\psi\rangle_{\text{PDC}} = \sum_k \sqrt{\lambda_k} \hat{A}_k^\dagger \hat{B}_k^\dagger |0\rangle, \quad (9)$$

where we have postselected on and renormalized for two-photon emission. This means that given a PDC photon pair is generated, it is in the k th TM pair with a probability of λ_k . An example of a typical JSA together with its Schmidt decomposition is given in Fig. 2(b). For a typical Gaussian JSA, the Schmidt modes are given by Hermite–Gauss functions, which overlap in both spectral and temporal intensity.

The Schmidt decomposition of the joint spectral amplitude provides an essential link between the continuous time-frequency description and a discretised temporal-mode picture. Such a transition is necessary for describing mode-multiplexed systems, where each Schmidt mode can be thought of as an independent information carrier. Such multiplexed systems are useful for communication networks [4] and essential to generate highly entangled cluster states for measurement-based quantum computation [5–8], where utilizing the time-frequency domain allows for operations to take place in a single spatial mode. The Schmidt modes of PDC can be directly connected to the supermodes generated in a synchronously pumped optical parametric oscillator (SPOPO), where a degenerate downconversion medium is pumped below threshold in a cavity matched to the repetition rate of the driving laser system [9,10]. The eigenmode decomposition of the interaction provides the independently squeezed supermodes of the system [11,12], and their mixtures have been experimentally demonstrated to exhibit strong continuous-variable entanglement [13,14].

In the low-gain PDC regime, the Schmidt decomposition of the JSA can be linked directly to the amount of time-frequency entanglement present in the two-photon system. The Schmidt number, defined as $K = 1/\sum_k \lambda_k^2$, quantifies the number of TM pairs required to describe the properties of the generated state, with $K = 1$ for a single-mode (separable) state and $K \gg 1$ for a multimode (entangled) state [15–17]. The Schmidt number is related to the spectral purity of the individual signal photons generated, which are generally described by the mixed density matrix

$$\hat{\rho}_s = \text{Tr}_i(\hat{\rho}_{\text{PDC}}) = \sum_k \lambda_k |A_k\rangle \langle A_k| \quad (10)$$

with a purity of

$$\mathcal{P}_s = \text{tr}(\hat{\rho}_s^2) = \frac{1}{K}. \quad (11)$$

For PDC-generated photons, this quantity is directly experimentally accessible through the marginal second-order correlation function (i.e., unheralded signal photons) as $g^{(2)}(0) = 1 + \mathcal{P}_s$ [18–20].

In summary, we have introduced the continuous time-frequency structure of PDC and connected it to the discrete TM picture through the Schmidt decomposition. Such analysis naturally describes the two-photon entanglement from PDC, the squeezed modes of a pulsed OPO, and the spectral purity of the generated photons. In most configurations, PDC generates

highly correlated states with a large Schmidt number, yielding low-purity heralded photons if no additional spectral filtering is applied. We will shift our focus in the next section to how proper engineering of the PDC process can overcome this limitation and facilitate the direct generation of pure single photons.

3. PDC ENGINEERING

Although multimode PDC states with the usual frequency anti-correlations, as shown in Fig. 2, have found many applications in quantum science [21–23], full control over the modal structure of the PDC state would make a new range of applications possible. For example, high-visibility quantum interference between distinct nodes in a photonic network requires pure PDC sources, i.e., sources that emit in a single temporal mode. Without dispersion engineering, intrinsic frequency anti-correlations between signal and idler are imposed by energy conservation of the pump, reflected by the -45° angle of the pump function in the joint spectral amplitude (see Fig. 2), resulting in highly multimode systems. To realize single-mode PDC, researchers have tailored the phase-matching function to produce separable JSAs, allowing for high-quality heralded photons without any need for additional spectral filtering.

A. Group-Velocity Matching for Single-Mode Emission

At the turn of the millennium, several groups studied the spectral characteristics of PDC photon pairs and identified a connection between the photon spectra and the dispersion of the nonlinear medium [24–26]. It was shown that with properly selected nonlinear material, polarizations, and photon central frequencies, the frequency correlations between the signal and idler photons can be eliminated [27]. Later this work was further developed in Ref. [16], where the authors showed that the relationship between the group velocities of interacting fields plays an essential role in tailoring the phase-matching function $\phi(\omega_s, \omega_i)$ and consequently the JSA.

To understand the underlying physics, we perform a Taylor expansion of the phase mismatch (defined in Section 2) up to the first order. Assuming that the process is perfectly phase matched at the center frequencies and that group-velocity dispersion through the nonlinear medium is negligible, we obtain

$$\Delta k(\omega_s, \omega_i) \approx (u_s^{-1} - u_p^{-1})\omega_s + (u_i^{-1} - u_p^{-1})\omega_i, \quad (12)$$

where the $u_j \equiv \frac{\partial \omega_j}{\partial k_j}$ are the group velocities of the pump, signal, and idler fields. In this context, it is useful to define the group-velocity mismatch contrast ξ as

$$\xi = \frac{u_s^{-1} - u_p^{-1}}{u_i^{-1} - u_p^{-1}}. \quad (13)$$

The group-velocity mismatch contrast is related to the angle of the phase-matching function in the (ω_s, ω_i) -plane by $\theta_{\text{PM}} = -\arctan(\xi)$ [16].

Among all possible group-velocity arrangements, two special cases received particular attention. In the first case, dubbed *asymmetric group-velocity matching* (aGVM), the pump propagates with the same group velocity as either the signal photon ($\xi \rightarrow 0$) or the idler photon ($\xi \rightarrow \infty$). If the pump is group-velocity matched to the signal photon, the JSA from Eq. (3) is reduced to

$$f(\omega_s, \omega_i) \approx \alpha(\omega_s + \omega_i)\phi(\omega_i). \quad (14)$$

As seen in Fig. 3(b), as the phase-matching bandwidth shrinks to be much narrower than the pump bandwidth, the JSA becomes more and more separable. The single-modedness of the system can be increased by using wider pump bandwidths or tightening the phase-matching function with longer nonlinear interactions [16]. In this scenario, the signal and idler photon will have drastically different spectral bandwidths.

In the second case, the group velocity of the pump is exactly between the group velocities of signal and idler ($\xi \rightarrow -1$), referred to as *symmetric group-velocity matching* (sGVM) or *extended phase matching*, which results in a JSA of the form

$$f(\omega_s, \omega_i) \approx \alpha(\omega_s + \omega_i)\phi(\omega_s - \omega_i). \quad (15)$$

As seen in Fig. 3(c), if the phase-matching bandwidth equals the pump bandwidth, the JSA is a perfectly separable circle,

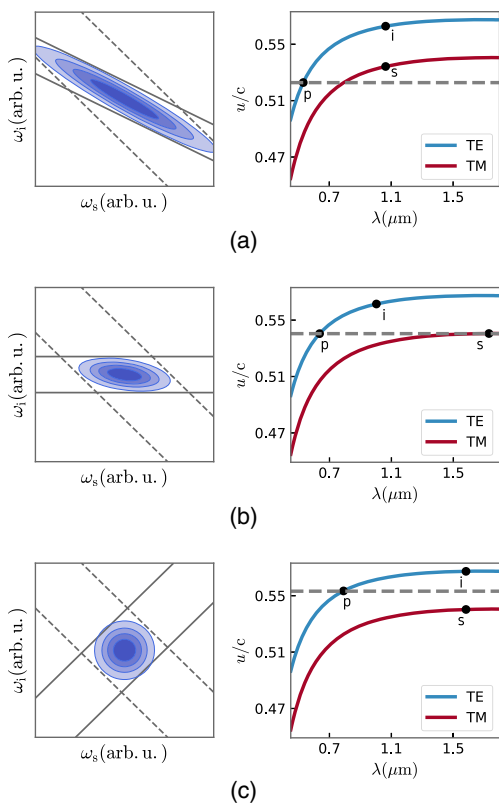


Fig. 3. Three different group-velocity matching condition. The JSA of each case is plotted on the left side, with the respective group velocities u_i of the pump, signal, and idler fields plotted on the right side. The group velocities (normalized over the speed of light in vacuum) are exemplary for TE- and TM-polarized light in a z-cut KTP crystal. (a) Typically without dispersion engineering, the long-wavelength signal and idler photons both have a larger group velocity than the pump ($\xi > 0$). This leads to a negative phase-matching angle and consequently to a correlated JSA as shown on the left. In this example, $\xi \approx 0.4$. (b) In the case of aGVM ($\xi \rightarrow 0$), one photon (here the signal) propagates at the same velocity as the pump. This yields a phase-matching function that is aligned with the signal or idler frequency axis. If the pump spectral bandwidth is larger than the phase-matching bandwidth, a separable JSA is generated. (c) For sGVM ($\xi \rightarrow -1$), the group velocity of the pump lies between the group velocities of signal and idler. This leads to a $+45^\circ$ phase-matching angle and, given that the pump spectral bandwidth matches the phase-matching bandwidth, a separable JSA with potentially indistinguishable signal and idler.

allowing for pure single photons with identical spectral properties. This phase-matching configuration also allows for two-photon states with positive spectral correlations (and negative temporal correlations) when the pump is broader than the phase-matching function [28–30], useful for certain quantum synchronization and dispersion-cancellation techniques.

B. Experimental High-Purity Photon Sources

The first experimental demonstrations of separable photon-pair generation were realized in nonlinear bulk crystals. In these systems, the spatial and spectral properties of the photon pairs can be linked during generation, depending on the focus of the pump and collection optics [31]. In 2007, Torres's group demonstrated control over the spectral correlations using this spectral-spatial coupling for photon pairs at 810 nm generated in LiIO_3 [32]. By adapting the spatial mode of the pump, the generated photon pairs could be tuned from spectrally correlated to separable. This was verified by a measurement of the joint spectral intensity (JSI), $|f(\omega_s, \omega_i)|^2$.

In 2008, Walmsley's group demonstrated engineered PDC under aGVM conditions in a bulk KDP crystal [33] with photon pairs produced around 830 nm. In addition to JSI measurements, the authors demonstrated Hong–Ou–Mandel interference [34] between heralded photons from two different PDC sources with a visibility of 94.4%.

Also in 2008, Wong's group designed and analyzed a source of telecom photon pairs produced under sGVM conditions in periodically poled KTiOPO_4 (ppKTP) crystal [35]. To measure correlations, the photons were upconverted in a second nonlinear crystal by a short gate pulse. By scanning the relative delay of the photons and the gate, the authors were able to measure the joint *temporal* intensity, explicitly showing the possibility of temporal anti-correlation under sGVM conditions. This demonstrated for the first time that changing the spectral bandwidth of the pump facilitates control over the time-frequency correlations of the pair photons.

KTP is particularly appealing as a source for dispersion-controlled photons. As seen in Fig. 3, it exhibits both aGVM and sGVM conditions at different frequencies. In particular, through the sGVM condition, it can be used to produce photon pairs with degenerate spectra in the highly useful telecommunications wavelength regime. In 2011, researchers at NIST presented a highly pure and spectrally degenerate telecom PDC source realized in bulk ppKTP [36], demonstrating the indistinguishability of the photon pair through 95% visibility in signal-idler Hong–Ou–Mandel interference.

To achieve the long interaction lengths necessary for narrow phase-matching functions, sources in guided-wave media are essential. In addition, the tight field confinement provides significant increases in the source brightness, and the spectral and spatial degrees of freedom are largely decoupled in a waveguide. In 2011, Silberhorn's group presented the first separable PDC source in a waveguide [19], based on rubidium-exchanged ppKTP. The tight field confinement contributed to a high brightness, with $\langle \hat{n}_{\text{PDC}} \rangle \approx 2.5$ photons per pulse at pump pulse energies as low as 70 pJ, and the purity of the source was confirmed through both JSI and $g^{(2)}$ measurements. A further refinement of the source offered a signal-idler indistinguishability of around 94% confirmed with Hong–Ou–Mandel interference, and a photon spectral purity of up to 86.7% was obtained from interfering the

photon with a classical reference field [37]. Since then, sGVM sources have been incorporated into dual-pumped Sagnac schemes to construct degenerate and highly pure photon pair sources with polarization entanglement [38,39].

C. Problem with Side Lobes

To put these results into context, we next consider the limitations imposed by the phase-matching function in Eq. (5). In Fig. 4, we plot the JSAs resulting from this phase-matching function along with possible broadband spectral filtering. It becomes immediately obvious that the side lobes of the sinc-shaped phase-matching function introduce undesired frequency anti-correlations, limiting the maximum purity of heralded photons to around 86% in the sGVM case. With filters chosen to transmit the main peak of the JSA but block as many of the correlated side lobes as possible, it is possible to increase the source performance, but limitations are still present. In the case of aGVM depicted in Fig. 4(a), the idler filter can be chosen to be much narrower than the signal filter. In this example, if the idler is filtered and serves as a herald, the maximum purity for the heralded signal increases to 97%. In contrast, if the signal is filtered and serves as a herald, the heralded idler photon has a maximum purity of about 92%. Note that this value can be increased with a larger pump bandwidth. In the sGVM example shown in Fig. 4(b), the signal and idler photons are indistinguishable, and the filtering shown in either case leaves the other photon with a purity of about 94% when heralded. We note that these numbers can be further increased when choosing smaller filter bandwidths at the cost of decreased heralding rates [40,41].

Luckily, there are elegant methods to shape the phase-matching function in order to avoid the spectral filtering. These methods rely on engineering the phase-matching distribution through modulation of the poling patterns and, in the case of integrated devices, tailoring the geometry of the waveguided structures. Since the phase-matching function is the Fourier transform of the quasi-phase-matching (QPM) grating $[\chi(z)]$ in Eq. (4), the nonlinearity profile along the interaction can be smoothed or *apodized* to a Gaussian function by modulating the QPM grating. The first experimental demonstration of phase-matching apodization was realized by Fejer's group [42], where 13 dB suppression of the side lobes is shown. This simple apodization method reduces the peak efficiency and broadens the width of the phase-matching function, as expected from the

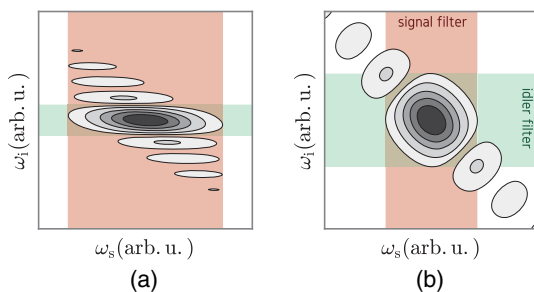


Fig. 4. Joint spectral amplitudes (absolute value) with standard periodic poling and filters on the individual photons. (a) In an aGVM source, the idler can be filtered to remove the side lobes and herald pure signal photons. However, filtering on the signal arm cannot be used to remove the side lobes. (b) In sGVM sources, the JSA is symmetric. Filtering either signal or idler leaves the other with a purity of about 94%.

Fourier analysis. Apart from custom QPM gratings, the authors also investigate different waveguide geometries effective for eliminating the phase-matching side lobes. Later, many other methods were proposed and demonstrated to efficiently apodize the phase-matching function, such as modulation of the poling periodicity [43], modulating the poling pattern's duty-cycle [44,45], and optimizing the orientation of each domain [46–49]. These techniques grant purities in excess of 99% without spectral filtering, opening new avenues to engineer the TM structure of PDC states by arbitrary shaping of the phase-matching function.

D. Controlled Generation of Temporal Modes

Finally, we want to highlight two possibilities to accurately control the generated PDC state beyond separability. For applications that exploit TMs as the encoding basis, the targeted generation of states with a user-defined TM structure is highly desirable. Complementary techniques arise for PDC state engineering through spectrally shaping the pump pulse in aGVM and sGVM sources, the former providing pure shaped single photons while the latter provides flexible sources for high-dimensional TM entanglement.

In the aGVM case, as seen in Eq. (14), the spectrum of the idler photon is almost entirely dependent on the phase matching, while the spectrum of the signal photon is dependent on the shape of the pump. By manipulating the spectral shape of the pump, the shape of the signal photon can be programmed on the fly, as seen in Figs. 5(a)–5(c). So long as the phase matching is narrow relative to the finest features of the desired spectral shape, the JSA remains separable. This was recently demonstrated in KTP waveguides under birefringent phase-matching conditions, providing high-purity shaped photons at 1411 nm [50].

In contrast, PDC states that comprise a user-defined number of TMs can be generated in the sGVM configuration. Again, this is achieved by spectral shaping of the pump pulses. One example of this is a PDC driven by a pump pulse with a first-order Hermite–Gaussian spectrum [51], as depicted in Fig. 5(e). In this case, the generated state is a TM Bell state of the form

$$|\psi\rangle_{\text{Bell}} = \frac{1}{\sqrt{2}}(|0\rangle_s|1\rangle_i + e^{i\phi}|1\rangle_s|0\rangle_i), \quad (16)$$

where $|0\rangle_j$ ($|1\rangle_j$) labels the j photon occupying a Gaussian (first-order Hermite–Gaussian) spectrum and $j = (s, i)$. To add additional TMs to this state, it is sufficient to increase the order of the Hermite–Gaussian spectrum of the pump pulse, which is easily achieved with conventional pulse shaping [52]. Although this provides a state with finite number of Schmidt modes, the generated TMs are generally not equally occupied (i.e., they can have different $\sqrt{\lambda_k}$) [51], and thus the generated TMs are not maximally entangled. Another alternative pump shape to control the Schmidt modes is a superposition of time bins or, equivalently, cosine functions in the frequency domain, as shown in Fig. 5(g) [12]. This provides a flexible and versatile source that generates maximally entangled states with an arbitrary dimension without the need for changing any hardware.

As the last remark in this section, we want to point out that the theoretical description of the PDC process presented here, using the first-order perturbation theory, is only valid when the process is weakly pumped (also referred to as the low-gain regime) [53,54]. A full description of such nonlinear optical processes requires the time-ordered treatment of the involved Hamiltonians

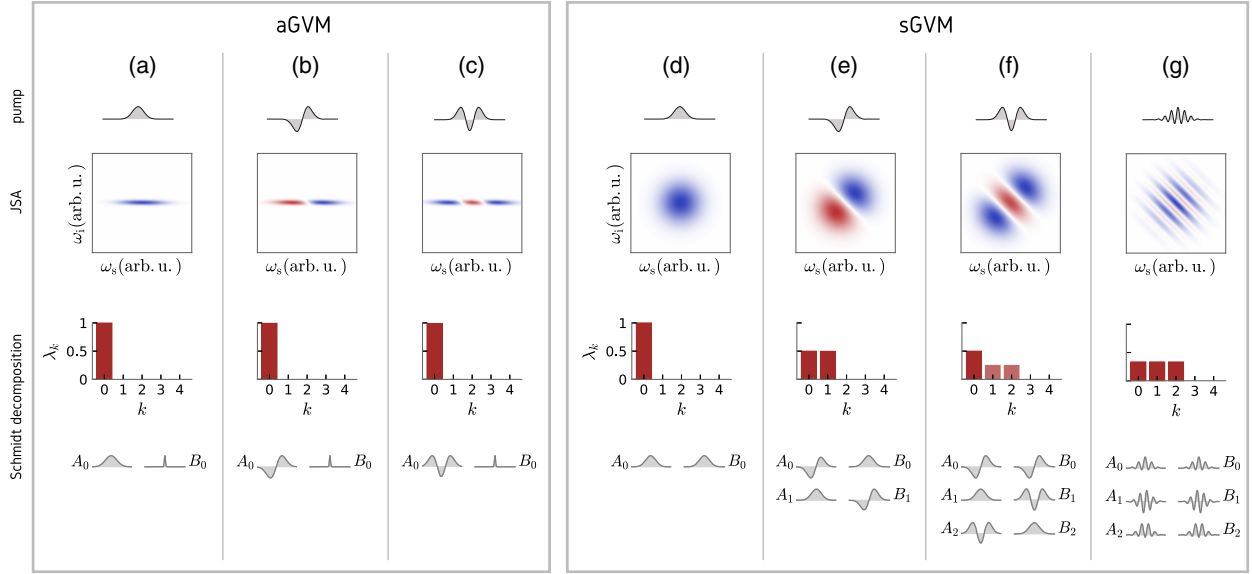


Fig. 5. Orchestrating Schmidt modes via group-velocity matching and pump pulse shaping. (a)–(c) JSAs for a PDC source with an aGVM setting. The weights of the first five Schmidt modes λ_k are shown under each JSA. The state remains single-mode regardless of the pump shape. The only significant Schmidt modes of signal A_0 and idler B_0 photons are shown at the bottom, where we plot TM amplitudes versus frequency. The idler photon shape is invariant to the pump, while the TM of the signal photon reflects the TM of the pump field. (e)–(g) A sGVM PDC can be used to control the exact number of excited TMs. For example, driving the source with a first-order Hermite–Gaussian pump pulse as in (e) results in exactly two TMs. This can be extended with higher orders of Hermite–Gaussian pulses as in (f), but the different Schmidt modes are not occupied with the same probability. A balanced Schmidt-mode distribution can be achieved when the source is pumped with time-bin superpositions, as in (g).

and consideration of the presence of multi-photon components. In the high-gain regime (with intense pump powers and PDC mean photon numbers $\gg 1$), the time ordering leads to significant changes of the Schmidt modes and the respective squeezing in each mode. Despite this, in the high-gain regime it is possible to generate bright squeezed states that are interesting to study a range of quantum phenomena at mesoscopic scales [55–57].

To conclude, PDC state engineering is now at a point where we can exert close-to-arbitrary control over the TM structure of the generated state. This brings into reach the realization of TM-based quantum information processing (QIP) applications and provides us with a very clean laboratory system for the generation of Hilbert spaces with well-defined dimensions.

4. MANIPULATION AND MEASUREMENT OF TEMPORAL MODES

With a variety of sources available for both pure and entangled TM-encoded photons, the next piece of the complete TM-based QIP toolbox is a quantum device capable of accessing a TM out of a multimode input. In other words, we require a special quantum-mechanical beam splitter that operates on a customizable basis of TMs. A promising tool to build such a device is engineered frequency conversion (FC).

Frequency conversion has been recognized as means to translate the central frequency of a photonic quantum state while preserving its non-classical signatures. The first proposal in 1990 considered the frequency-translation of squeezed states of light [58]. Different experiments have since confirmed that FC retains quadrature squeezing [59–62], quantum coherence and entanglement [63–66], anti-bunching of single photons [67,68], and non-classical photon correlations [69,70]. Since FC can be highly

efficient [71–73], it provides a useful tool for improved detection schemes [74–78] and an interface for dissimilar nodes in future quantum networks [79–89].

However, there is more to frequency conversion. In 2010, Raymer *et al.* proposed an interpretation of FC as a two-color beam splitter [90], enabling for example Hong–Ou–Mandel interference [34] of photons of different color. If the FC is set to 50% efficiency, and if two monochromatic photons that are centered at the two linked frequencies (red and blue) are sent into the process, simultaneous sum-frequency generation (SFG) or difference-frequency generation (DFG) occurs and both photons will exit the FC either at the blue frequency or the red frequency. The conversion process links the two frequency bands in a beam splitter fashion, as has been demonstrated with single-photon signals exhibiting Ramsey interference [91] and two-color Hong–Ou–Mandel interference [92].

The proposal of Ref. [90] also considers the case of spectrally broadband FC, where a specific input frequency ω_{in} is mapped to a plethora of output frequencies ω_{out} and vice versa, as determined by the Heisenberg-picture Bogoliubov transformations,

$$\hat{a}^\dagger(\omega_{in}) \mapsto \int d\omega'_{in} G_{aa}(\omega_{in}, \omega'_{in}) \hat{a}^\dagger(\omega'_{in}) + \int d\omega'_{out} G_{ac}(\omega_{in}, \omega'_{out}) \hat{c}^\dagger(\omega'_{out}), \quad (17)$$

$$\hat{c}^\dagger(\omega_{out}) \mapsto \int d\omega'_{in} G_{ca}(\omega_{out}, \omega'_{in}) \hat{a}^\dagger(\omega'_{in}) + \int d\omega'_{out} G_{cc}(\omega_{out}, \omega'_{out}) \hat{c}^\dagger(\omega'_{out}). \quad (18)$$

Here, \hat{a}^\dagger and \hat{c}^\dagger are creation operators in the input and frequency-converted output modes, respectively, and the G_{ij}

are Green's functions that describe the mapping between the two. By applying a Schmidt decomposition to the Green's functions, an interpretation of broadband FC as a beam splitter that links sets of input TMs to output TMs becomes apparent [90]. Similar to PDC, this process will generally be multimode.

Inspired by the previously outlined work in PDC engineering, the mode structure of FC can be tailored through dispersion engineering. It turns out that a configuration that is similar to asymmetric group-velocity matching facilitates single-mode operation; when the input signal propagates through the nonlinear medium at the same velocity as the bright pump, but the output is group-velocity mismatched, one specific TM is selected and converted to the output frequency, while all other TMs are simply transmitted [93]. The single-mode FC has been dubbed the *quantum pulse gate* (QPG) to reflect that it selects, or gates, one broadband TM. The reversal of this process, when the output light shares the group velocity of the pump, has been proposed as a TM shaper [94].

In the following we briefly outline the QPG formalism. The interaction Hamiltonian that describes a general FC process is given by

$$\hat{H}_{\text{int}} = \theta \int d\omega_{\text{in}} d\omega_{\text{out}} F(\omega_{\text{in}}, \omega_{\text{out}}) \hat{a}(\omega_{\text{in}}) \hat{c}^\dagger(\omega_{\text{out}}) + \text{h.c.}, \quad (19)$$

where \hat{a} and \hat{c} are annihilation operators in the input and upconverted modes, respectively, and θ is a coupling of the process incorporating the power of the QPG pump and the strength of the material nonlinearity. The *transfer function* $F(\omega_{\text{in}}, \omega_{\text{out}})$ describes the mapping from input to output frequencies, equivalent in the low-efficiency regime to the Green's function $G_{\text{RB}}(\omega_{\text{in}}, \omega_{\text{out}})$ and analogous to the JSA in PDC processes. The transfer function, as in the case of PDC, is a product of pump amplitude and phase matching,

$$F(\omega_{\text{in}}, \omega_{\text{out}}) = \alpha(\omega_{\text{out}} - \omega_{\text{in}}) \phi(\omega_{\text{in}}, \omega_{\text{out}}). \quad (20)$$

Similar to PDC, we can apply a Schmidt decomposition to the mapping function and define our operators in the TM basis [compare Eqs. (3)–(9)], obtaining

$$\hat{H}_{\text{int}} = \theta \sum_{k=0}^{\infty} \sqrt{\lambda_k} \hat{A}_k \hat{C}_k^\dagger + \text{h.c.}, \quad (21)$$

with $\sum_k \lambda_k = 1$. Despite the similarity to the Schmidt decomposition of the PDC state as formulated in Eq. (9), there is a fundamental difference in the meaning of the decomposition and the Schmidt modes in each case. While the PDC decomposition expresses the modes of a *state*, in the case of the FC we have a SFG *operation*. The Hamiltonian in Eq. (21) generates operator transformations

$$\hat{A}_k \rightarrow \cos(\sqrt{\lambda_k} \theta) \hat{A}_k + \sin(\sqrt{\lambda_k} \theta) \hat{C}_k, \quad (22)$$

$$\hat{C}_k \rightarrow \cos(\sqrt{\lambda_k} \theta) \hat{C}_k - \sin(\sqrt{\lambda_k} \theta) \hat{A}_k. \quad (23)$$

These can be interpreted as k independent beam splitters with reflectivities $\sin^2(\sqrt{\lambda_k} \theta)$, which connect the input \hat{A}_k to an output \hat{C}_k .

As previously derived for PDC, the phase-matching function can be written in terms of the group-velocity mismatch, $\Delta k(\omega_{\text{in}}, \omega_{\text{out}})$. Assuming that the nonlinear medium is periodically poled to ensure phase matching at the center frequencies, this phase mismatch can be written to the first order in analogy to Eq. (12) as

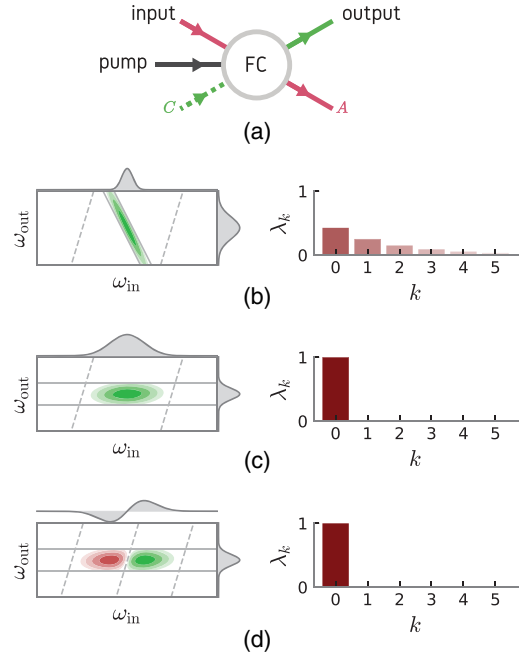


Fig. 6. Frequency conversion process and its transfer function. (a) Outline of a general frequency conversion process with pump, input and output fields. (b)–(d) Sum-frequency conversion transfer functions $F(\omega_{\text{in}}, \omega_{\text{out}})$ with its marginal distributions (left) and its first few Schmidt coefficients $\sqrt{\lambda_k}$. (b) A non-engineered SFG with significant frequency correlations and a $K \approx 3.7$. (c) and (d) present a tailored SFG process with aGVM condition with pump functions $\alpha(\omega_{\text{out}} - \omega_{\text{in}})$ of Gaussian and first-order Hermite–Gauss, respectively, and a $K \approx 1.01$.

$$\Delta k(\omega_{\text{in}}, \omega_{\text{out}}) \approx (u_{\text{in}}^{-1} - u_{\text{p}}^{-1})\omega_{\text{in}} - (u_{\text{out}}^{-1} - u_{\text{p}}^{-1})\omega_{\text{out}}. \quad (24)$$

For the case of aGVM where the input signal propagates at the same velocity as the pump ($u_{\text{in}} = u_{\text{p}}$), the first-order phase-matching function is only dependent on the upconverted frequency $\phi(\omega_{\text{in}}, \omega_{\text{out}}) \approx \tilde{\phi}(\omega_{\text{out}})$. If the phase matching is spectrally narrow enough that the output frequency spread is negligible compared to the input, the contribution of the pump field is approximately dependent on only the frequency of the input field, $\alpha(\omega_{\text{out}} - \omega_{\text{in}}) \approx \tilde{\alpha}(\omega_{\text{in}})$. If these approximations hold, the transfer function can be rewritten simply as

$$F(\omega_{\text{in}}, \omega_{\text{out}}) \approx \tilde{\alpha}(\omega_{\text{in}}) \tilde{\phi}(\omega_{\text{out}}). \quad (25)$$

As the phase-matching function tightens, the transfer function becomes more and more separable, as illustrated in Figs. 6(c) and 6(d).

For a separable transfer function, the Schmidt decomposition yields only one single non-zero Schmidt coefficient, and the interaction Hamiltonian reduces to the desired QPG Hamiltonian,

$$\hat{H}_{\text{QPG}} = \theta \hat{A}_0 \hat{C}_0^\dagger + \text{h.c.}, \quad (26)$$

and we obtain the following operator transformations:

$$\hat{A}_0 \rightarrow \cos(\theta) \hat{A}_0 + \sin(\theta) \hat{C}_0, \quad (27)$$

$$\hat{C}_0 \rightarrow \cos(\theta) \hat{C}_0 - \sin(\theta) \hat{A}_0, \quad (28)$$

$$\hat{A}_k \rightarrow \hat{A}_k \quad \text{for } k \neq 0, \quad (29)$$

$$\hat{C}_k \rightarrow \hat{C}_k \quad \text{for } k \neq 0. \quad (30)$$

Hence, the ideal QPG selects one single input TM and converts it to an output TM with an efficiency of $\sin^2(\theta)$, while all orthogonal TMs pass through the QPG unconverted and undisturbed. The selected input TM \hat{A}_0 is defined by the shape of the bright pump pulse that drives the conversion ($\hat{\alpha}(\omega_{\text{in}})$), whereas the shape of the output TM \hat{C}_0 is given by the envelope of the phase-matching function ($\hat{\phi}(\omega_{\text{out}})$) [93,94]. By shaping the spectral amplitude and phase of the QPG pump pulse, the mode selected by the QPG can be adapted on the fly. While most works have motivated the QPG towards Hermite–Gauss TMs, it can also be set to select arbitrary superpositions as well as entirely different mode bases (e.g., time or frequency bins) by reshaping the pump pulse. While other group-velocity conditions exist that enable nearly single-mode sum-frequency generation, the aGVM case outlined here has been shown to be optimal [95].

Although ideal QPG operation as described in Eq. (26) requires perfect GVM between the pump and input, one can still realize a nearly single-mode QPG if the group-velocity mismatch is small with respect to the temporal width of each field. To compare different scenarios, we redefine the group-velocity mismatch contrast, which was introduced in Eq. (13) as

$$\xi = \frac{u_{\text{in}}^{-1} - u_{\text{p}}^{-1}}{u_{\text{out}}^{-1} - u_{\text{p}}^{-1}}. \quad (31)$$

An aGVM condition between the pump and input fields means $\xi \rightarrow 0$. This definition can help us to study the feasibility of building a QPG in different nonlinear materials with different dispersion properties, which will be discussed in the next section.

More detailed studies followed this first proposal for a QPG, which focused in particular on the behavior of a QPG as a function of conversion efficiency. In this context, implementations based on both four-wave mixing and SFG were investigated [95]. The figure of merit that was defined is the so-called *selectivity* S of the QPG, which is defined as

$$S = \eta_0 \cdot \frac{\eta_0}{\sum_{k=0}^{\infty} \eta_k} \leq 1, \quad (32)$$

where $\eta_k = \sin^2(\sqrt{\lambda_k}\theta)$ is the conversion efficiency for the k th TM. The selectivity measures both the single-modedness of the QPG and the conversion efficiency for this mode.

An ideal QPG operates on only one TM and converts this mode with unit efficiency ($S = 1$). In a more realistic scenario, the QPG becomes multimode when approaching high conversion efficiencies, owing to non-perturbative interaction dynamics often referred to as *time-ordering* effects in the quantum context [53,95,96]. For a single QPG, a maximum selectivity of $S \approx 83\%$ has been determined [95]. Figure 7 shows the change in the transfer functions for increasing pump powers [95].

In Ref. [97], Reddy *et al.* proposed a scheme to overcome this limitation, dubbed *temporal-mode interferometry*. Using two QPGs in a Mach–Zehnder-like configuration, they show it is possible to achieve selectivities approaching unity. In this scheme, two QPGs are operated at 50% conversion efficiency—similar to two balanced beam splitters—and the phases between the two QPGs are adjusted such that interference leads to complete conversion of the targeted input TM. Since each QPG operates at a moderate conversion efficiency, the individual processes are still close to single-mode, and an overall selectivity of more than 98% can be achieved.

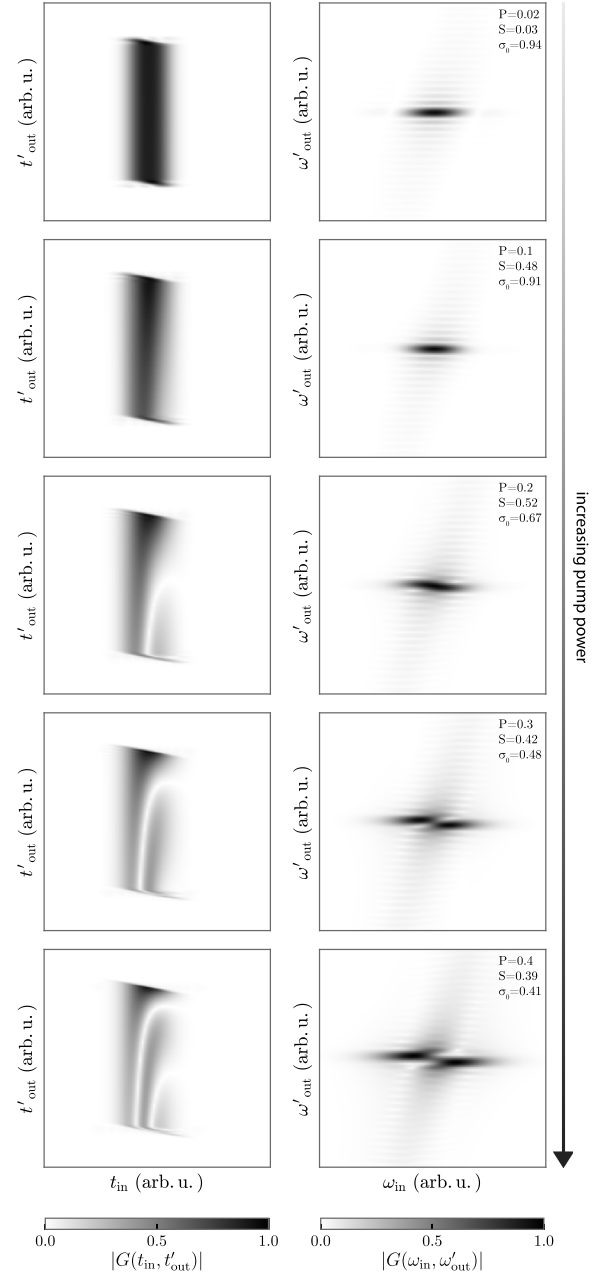


Fig. 7. Absolute value of the temporal (left) and spectral (right) transfer functions for broadband frequency conversion. The left column shows the mapping from input times t_{in} to output times t_{out} for increasing pump powers (top to bottom), corresponding to increasing conversion efficiencies. The relative pump energy P , selectivity S , and separability σ_0 are printed on top-right corner of each row. This leads to simultaneous forward and backward conversion, which is reflected by the oscillations in the mapping function. The functions were calculated by numerically solving the Heisenberg equations for the input and output field operators. The right column shows the respective spectral mapping functions. It can be seen that the general shape of the function broadens and that additional correlations are introduced for stronger pump powers. These correlations do not show up in a perturbative approach.

Despite this advance, simultaneously achieving high efficiency and isolating orthogonal modes is a significant experimental challenge. In scenarios where the QPG is used for temporal-mode

reconstruction and measurement, efficiency may not be the dominant concern. Instead, one might simply need to know how well the upconverted signal identifies the presence of the target TM. To isolate this criterion, often the *separability* σ_j for a given mode j among a d -dimensional basis is quantified, defined as [98]

$$\sigma_j = \frac{\eta_j}{\sum_{k=0}^d \eta_k} \leq 1. \quad (33)$$

This quantifies how well the QPG isolates a single mode from a mixture irrespective of incomplete conversion. Additionally, oftentimes the suppression or *extinction ratio* for mode j is reported [99,100],

$$\text{E.R.}_j(\text{dB}) = 10 \log_{10} \frac{\eta_j}{\max_{k \neq j} \eta_k}, \quad (34)$$

which defines to what extent the QPG suppresses signals from modes orthogonal to the target mode.

5. EXPERIMENTAL PROGRESS ON TM SELECTION

In this section, we provide an overview of experimental work on temporal-mode-selective devices built with pulse shaping and dispersion engineering. To start, it is imperative to find nonlinear materials and interactions that satisfy the aGVM conditions, i.e., minimize $|\xi|$ in Eq. (31). This condition can be met for SFG processes in multiple materials, as mapped out in Fig. 8. In particular, it naturally occurs near degeneracy in materials with type-0 or type-I phase-matching conditions (i.e., where the QPG pump and input have the same polarization and approximately the same frequency). However, in these near-degenerate configurations, the second harmonic of the QPG pump adds a strong source of phase-matched background noise for single-photon operation, and suppressing it by detuning the signal from degeneracy quickly degrades the mode selectivity of the device, as

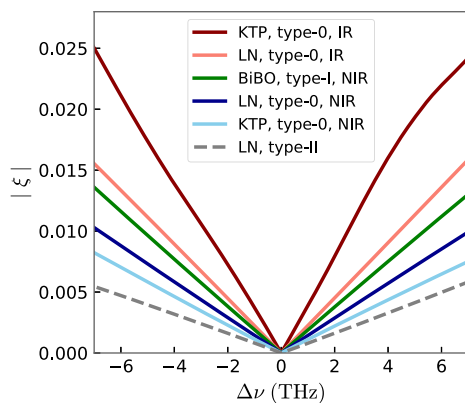


Fig. 8. Group-velocity mismatch contrast ξ (such that 0 is perfectly matched) for processes in lithium niobate (LN) waveguides, potassium titanyl phosphate (KTP) waveguides, and bulk bismuth borate (BiBO), as the input signal is detuned from the optimal group-velocity matching. The grey dashed line corresponds to the type-II process in LN, where GVM is found for a 1550 nm signal, 875 nm pump, and 560 nm upconverted [99]. All other processes have degenerate signal and QPG pump for group-velocity matching, and IR (NIR) corresponds to 1550 nm (800 nm) signal and QPG pump. Signal detuning or noncollinear geometry is necessary in all cases except for type-II LN to overcome the second harmonic of the QPG pump.

seen in the rising ξ values in Fig. 8. To operate with “perfect” group-velocity matching, specific conditions can be found in type-II or frequency-nondegenerate configurations. For example, in z-cut lithium niobate, a 1550 nm ordinarily polarized input signal may interact with a 875 nm extraordinarily polarized QPG pump to produce an ordinarily polarized upconverted signal in the green range of the visible spectrum [93,99]. Since the SHG process for the QPG pump is both phase mismatched and in the blue range, the upconverted signal can be effectively isolated at the optimal GVM wavelength. However, the type-II nonlinear strength is considerably weaker than the type-0, necessitating stronger pump fields.

While broadband temporal modes find a natural use in quantum applications, similar concepts have been proposed and explored for classical communications. By taking a broad flat-top optical pulse and manipulating its spectral phase with a pulse shaper, one can generate sets of orthogonal pulses based on, for example, Hadamard codes. If a decoder applies the correct decoding phase sequence, the ultrashort pulse becomes Fourier limited once more, with a commensurate increase in peak power [101]. This concept can be merged with dispersion-engineered sum-frequency generation to enable ultrashort-pulse code-division multiple access. If a broadband pulse is sent through a long nonlinear crystal for second-harmonic generation (SHG), and the crystal is group-velocity mismatched such that the SHG light walks off from the input light, and the second harmonic will be temporally lengthened and spectrally narrowed. If a frequency-dependent phase is applied to the pulse, it will only be efficiently frequency doubled if the phase is symmetric. If two users each have access to half of the spectral bandwidth of an ultrashort pulse, the pulse will cease to upconvert in this medium if they apply orthogonal phase codes [102,103]. This effect is due to interference within the broadband pulse structure and enabled by the group-velocity walkoff in the nonlinear medium. This scheme was demonstrated by Weiner’s group using a 20-mm-long bulk PPLN sample with a broad input pulse at telecommunications wavelength split into 16 channels. The SHG from mismatched codes exhibited an extinction ratio of over 27 dB when filtering the central frequency component [102]. Using entangled photon pairs to supply the same effective spectral narrowing as the group-velocity mismatched SHG, analogous encoding schemes have been demonstrated with biphoton upconversion [104].

Recent realizations of the QPG allow for the analysis and reconstruction of the temporal modes of distant single-photon level pulses. These experiments can generally be described by the apparatus of Fig. 9. In Silberhorn’s group, a quantum pulse gate was constructed using a type-II interaction in titanium-indiffused PPLN waveguides with short poling periods (4.4 μm) [99], where an orthogonally polarized and group-velocity matched telecom (1535 nm) input signal and a Ti:sapphire (875 nm) QPG pump mix to produce a signal in a green (550 nm) upconverted beam. The broad GVM of this process allows it to be used for sub-picosecond pulses (approximately 300 fs FWHM), with the selected mode exactly matching the spectral profile of the QPG pump in the low-efficiency regime, as seen in Fig. 10. In Ref. [99], an efficiency of nearly 88% was observed for the primary Gaussian mode with a single-photon-level coherent state input, with a demonstrated extinction ratio of approximately 7 dB, limited by the resolution of the pulse shaper. With improved QPG pump pulse shaping, this experiment was

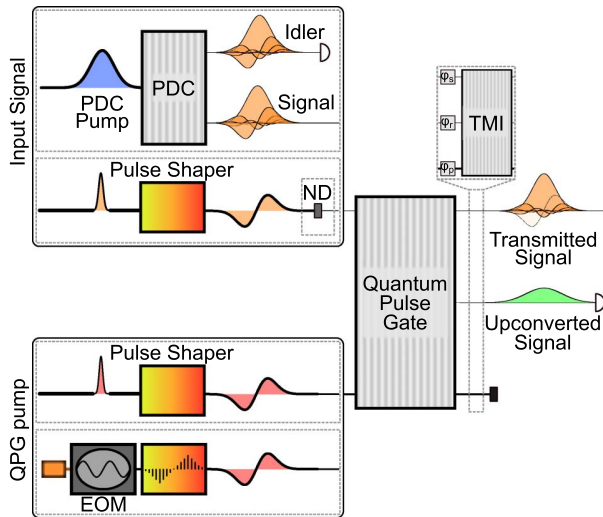


Fig. 9. Generic experimental situation for a quantum pulse gate. A TM-encoded single photon or weak coherent state is prepared through PDC or through shaping a spectrally broad input pulse and attenuating with a neutral density (ND) filter. A strong QPG pump is prepared using similar pulse shaping methods, or through electro-optic modulation (EOM) of a strong cw laser to produce a frequency comb, which is modulated in a tooth-by-tooth fashion by a pulse shaper [100]. The two are mixed in a group-velocity-matched $\chi^{(2)}$ waveguide, and the upconverted signal in the register mode is measured. For temporal-mode interferometry (TMI) [97], the QPG is split into two 50% efficient steps with phase shifts in between.

extended to measure PDC photons from a spectrally pure source with an extinction ratio of 12.8 dB and shaped coherent laser light with an extinction ratio of over 20 dB, although with a greatly reduced conversion efficiency (approximately 20%) [105]. Experimental SFG transfer functions using this system can be seen in Fig. 10.

An approximate approach to mode-selective measurement without strict group-velocity matching was later put forth by Huang and Kumar [106]. Although the optimal mode-selective

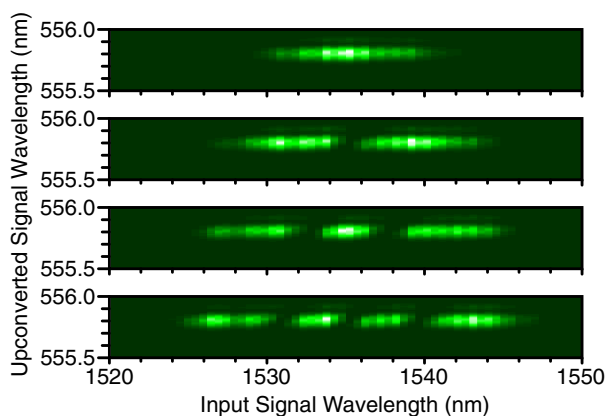


Fig. 10. Experimental spectral-intensity transfer functions for the first four Hermite–Gaussian temporal modes (top–bottom), as measured in the experimental apparatus of Ref. [165]. The QPG in question was built from a 17-mm-long PPLN waveguide phasematched for a type-II interaction (875 nm + 1540 nm to 555.7 nm), with the group-velocity matching necessary to produce highly separable SFG transfer functions.

frequency conversion configuration has been shown to be group-velocity matched [93,95], they found that reasonably single-mode frequency conversion could be realized through numerically optimized pump shaping so long as the bandwidth of the phase matching function is significantly narrower than the bandwidth of the pump. By generating a 20 GHz pulse train through electro-optically modulating a strong CW laser, Kowligy *et al.* produced a 17-element frequency comb for both the input signal and QPG pump, with each tooth individually addressable in phase and amplitude. With this scheme, they were able to experimentally demonstrate efficiencies near 80% and 8 dB extinction ratios using a 6 cm type-II PPKTP waveguide [100]. In follow-up work, they reverted to a nearly group-velocity matched configuration using a near-degenerate type-0 SFG in a 52 mm PPLN waveguide with input signals around 1550 nm. Applying their waveform generation and numerical optimization to this situation, they were able to demonstrate efficiencies above 75% for a four-dimensional Hermite–Gaussian alphabet with separabilities above 65% and as high as 87% for picosecond-scale Gaussian pulses [98]. These results have been extended to novel mode-selective pulse-shaping schemes based on overconversion in SFG [107] and demonstrations of mode-selective upconversion with efficiencies and selectivities high enough to outperform time-frequency filtering for signal isolation [108].

In the low-efficiency regime, the spectral shape prepared for the pump pulse corresponds exactly to the temporal mode selected by the QPG. In the high-efficiency regime, this first-order treatment breaks down due to the time-ordering effects outlined in the previous section and Fig. 7 [53,96,97]. Reddy and Raymer have investigated this regime with a QPG based on a 5-mm PPLN waveguide phase matched for a type-0 interaction between an 812-nm input signal, an 821-nm QPG pump, and a 408-nm register (output) mode [109,110]. By operating with nearly degenerate pump and signal, the group-velocity mismatch between the two red modes is negligible compared to the violet upconverted mode, and the type-0 PPLN interaction provides an extremely high nonlinearity. This allowed them to saturate the QPG efficiency at reasonable QPG pump powers (85% with 3.5 mW at 76 MHz with 500-fs pulses) [109]. They also confirmed numeric predictions that, in the high-efficiency regime, greater conversion efficiencies and mode selectivities can be reached with QPG pump shapes that differ from their analytically calculated low-efficiency regime counterparts.

With 50% conversion efficiency, enhanced mode selectivity is possible through temporal mode interferometry (TMI), where phase reshaping between two 50% efficient QPGs suppresses higher-order corrective terms [97,111,112]. By passing through the same waveguide twice (necessary to ensure identical phase-matching conditions), Reddy and Raymer were able to show mode-selective Ramsey interference with enhanced efficiency and mode selectivity relative to numerically calculated single-stage expectations [110]. This enhancement was present using the analytic low-efficiency-regime QPG pump mode shapes, removing the need for efficiency-dependent numerical optimization.

A. Mode Selection in Quantum Memories

A further possibility to manipulate TMs is by tailored light-matter interactions in single-mode quantum memories, in particular Raman ensemble memories. Here, the optical light field interacts with an ensemble of atoms with a Λ energy level

configuration. A strong control pulse drives a two-photon Raman transition, which maps the addressed input TM onto a so-called spinwave, which can be transferred back into an optical field by applying another strong control pulse. Similar to a QPG, the underlying equations describing this interaction can be cast into the form of a broadband beam splitter, where the shape of the strong control pulse determines the TMs that are stored and retrieved [113]. In contrast to QPGs, quantum memories give access to a wide range of accessible spectral bandwidths ranging from a few megahertz (MHz) up to terahertz (THz), depending on the physical system used to realize the memory. Recent results have shown the potential usefulness of these types of memories for the storage and manipulation of multimode quantum frequency combs [114] and the frequency and bandwidth conversion of photons [115,116]. By performing a process tomography, Walmsley's group has demonstrated the single-TM operation of a Raman memory [117]. Similar to the single-stage QPG, the Raman memory shows a degrading single-modedness with increasing efficiency. One way around this problem is to place the memory inside a cavity, which enables both high efficiency and mode selectivity simultaneously [118].

B. Multimode Manipulations with Sum-Frequency Generation

While group-velocity engineered waveguides and mode-selective interfaces are powerful tools, by definition they are unable to reshape the structure of multimode fields except as resource-intensive add/drop devices [51]. Applied temporal mode encodings may need multimode reshaping, for example, to match the central frequencies and bandwidths of PDC photons to the acceptance range of a solid-state memory interface [119], or to develop resource-efficient rotations and manipulations in the temporal mode basis. Initially, single-photon SFG was explored in the context of upconversion detectors, which efficiently shifts the frequency of photons from the telecom regime to the visible, where more efficient avalanche photodiodes exist [71,77]. While advances in superconducting nanowire detectors have eased telecom detection requirements, such processes have continued to find quantum applications, including frequency conversion for connecting quantum network nodes [119–121] and ultrafast signal gating [35,122,123]. Multimode SFG processes have been shown to add little noise, evidenced through experiments that have confirmed entanglement preservation in time bin [63] and polarization [66,124] degrees of freedom after frequency conversion and bandwidth manipulation.

For more general transformations, we can look to concepts from temporal imaging [125,126], which describes manipulations to the temporal structure of light in much the same way that spatial imaging describes the actions of lenses and diffractive propagation. Temporal imaging systems require the ability to implement phase shaping in both the spectral and temporal domains. Spectral domain manipulations can be accomplished simply with phase-only pulse shaping or standard dispersion-compensation techniques [52], but temporal phase manipulation (often called “time lensing”) is more difficult for sub-picosecond pulses, especially at the quantum level. Recently, groups have shown that dispersion and sum-frequency generation provides an effective toolbox for manipulating the bandwidth and time scale of PDC photons [127] as well as reshaping the time-frequency structure of entangled photon pairs [128]. These

techniques work in the exact opposite regime as the QPG, in that broad, non-restrictive phase matching is desired, i.e., all three fields must stay approximately group-velocity matched through the interaction. This often limits SFG-based time lenses to short nonlinear crystals, but the process can in principle reach high efficiency without the same time-ordering roadblocks as mode-selective measurement [95,129,130]. Note that temporal imaging can be accomplished in analogous ways through four-wave mixing [131,132]. Alternatively, other groups have shown deterministic time lensing using electro-optic modulation [133–135] and cross-phase modulation [136]. Taking concepts from the work done on quantum temporal imaging and applying them to temporal-mode manipulation is an exciting direction for future research.

6. TOWARDS APPLICATIONS OF TEMPORAL MODES IN QUANTUM INFORMATION SCIENCE

Finally, in this section, we outline experimental progress towards harnessing mode-selective upconversion for quantum technologies. The experiments referenced above have shown that quantum pulse gates can be realized with high efficiencies and high selectivities. In order to apply them for quantum signal processing, high signal-to-noise ratios are absolutely essential to separate quantum from classical signals and to protect resources such as entanglement and squeezing.

To exploit temporal modes as a high-dimensional coherent quantum resource, the selectivity must be maintained for a high-order alphabet as well as over the complete set of possible superposition states, as illustrated in Fig. 11. The security of quantum key distribution, for instance, relies entirely on the ability to measure complementary observables. For tomographic reconstruction of d -dimensional quantum states, projective measurements onto at least d^2 states spanning the total Hilbert space are required. A complete set of $d + 1$ mutually unbiased bases [137,138] provides a sufficient set of projections, examples of

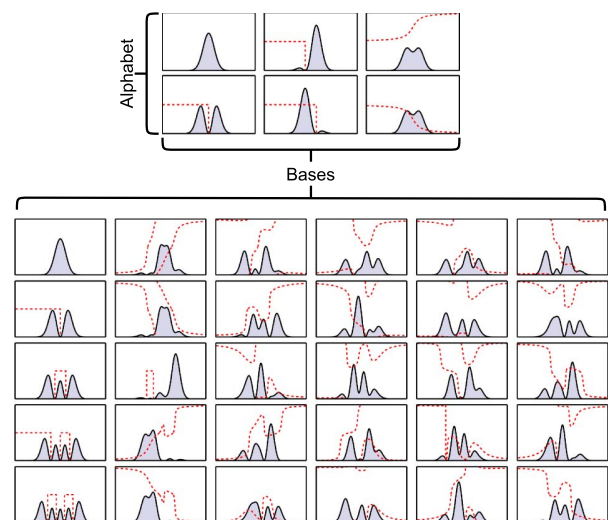


Fig. 11. Spectral field amplitudes spanning a complete set of mutually-unbiased bases for Hermite-Gauss modes in two (top) and five (bottom) dimensions [165,137]. In order to completely access the Hilbert space, effective projections on all of these states must be realizable. The normalised spectral intensity is shown in grey and the red line corresponds to the spectral phase (on the interval $0-2\pi$).

which in the Hermite–Gauss basis are shown in Fig. 11. High-dimensional two-qudit state tomography of entangled photons has been demonstrated with encodings in time-binned modes [84,139], spectral-binned modes [140,141], and orbital angular momentum spatial modes [142]. To avoid the intense resource devotion needed for full tomographic reconstruction, properties such as entanglement can be verified with witnesses instead [143–146]. However, these techniques still require the ability to project in complementary bases.

Utilizing the time-frequency degree of freedom for high-dimensional quantum information protocols has generally been confined to the context of time- or frequency-bin temporal modes, where the computational-basis modes are directly distinguishable in intensity. In particular, time bins have become the temporal-mode basis of choice behind the longest-distance Bell inequality violations over fiber networks [147–149], many commercial QKD systems [150], and high-dimensional entanglement-enabled quantum communication schemes [151–153]. By passing a photonic signal through an unbalanced Mach–Zehnder interferometer, such that the reflected arm acquires an overall delay and adjustable phase relative to the transmitted signal, a superposition of arrival times can be prepared or measured [154]. Extensions to higher dimensions have been realized with multi-path interferometers [155], cascaded Mach–Zehnder interferometers with different delays [84,153], and time-to-polarization conversion enabled by cross-phase modulation [139]. However, the interferometers in the first two techniques require detectors with time resolution fine enough to separate non-interfering events, and the latter technique is limited in which superpositions can be directly measured. By using SFG with chirped inputs as a time-to-frequency converter, it has been demonstrated that projective measurements can be made on superpositions of time-bin photonic states on time scales well below detector resolution [156]. While this technique was effective enough to convincingly violate a Bell inequality and reconstruct time-bin qubit density matrices, it is limited to a maximum efficiency of $1/d$ for a given projection.

SFG has also been key to frequency-bin encoded schemes, particularly those involving the recombination of a PDC photon pair in a second nonlinear crystal [157,158]. By creating spectrally entangled photons and slicing their spectra into bins, researchers have used this method to demonstrate novel high-dimensional encoding schemes [104] and violate high-dimensional Bell inequalities [140]. However, since these experiments rely on recombination of the two photons, they are difficult to extend to quantum network applications. Recent work using low-noise electro-optic modulators to create sidebands from a frequency comb source has enabled projective measurements on frequency-bin entangled photons from frequency comb sources without needing the two photons to recombine [141,159,160]. These tools have been demonstrated to enable deterministic frequency-bin rotations [161,162] and fast feed-forward frequency shifting for spectrally multiplexed photon sources [163].

The dispersion-engineered techniques outlined in Section 4 have the key advantage that so long as the transfer function of Eq. (20) remains separable, they are capable of projecting onto temporal modes in arbitrary bases, including both the binned modes and field-overlapping pulse modes. To be effective for high-dimensional quantum protocols, dispersion-engineered mode-selective SFG must be both low-noise and coherent, in

the sense that it remains effective for not only the basis modes but also general superpositions. Progress has been made towards applying the quantum pulse gate to photonic state characterization and manipulation, but it remains an active field of research.

Using the configuration of Ref. [99] with input from a spectrally pure PDC source, it was confirmed that the QPG output maintains nonclassical photon number correlations (i.e., the heralded $g^{(2)}$ of both the input and register modes was measured to be $0.32 \pm 0.01 < 1$) [164]. By shaping the QPG pump over a tomographically complete set of TMs, this setup has been used to reconstruct the one-qudit TM density matrix of PDC photons varied from single- to multimode configurations, with both intensity- and phase-correlated multimode structure [105]. However, worse performance was noted for higher-dimensional reconstructions. The device's performance was fully characterized through temporal-mode detector tomography [165], which showed that a system based on a 17-mm PPLN waveguide could reconstruct the TM density matrix in seven dimensions with a fidelity higher than 80%. By calibrating the QPG with this detector tomography, the reconstruction algorithm could be altered to reconstruct randomly generated seven-dimensional coherent superpositions of temporal modes with a fidelity of $(98.8 \pm 0.4)\%$. These experiments are, to date, the only dispersion-engineered TM measurements performed with a quantum light source rather than attenuated coherent light.

In a continuous-variable context, where quantum information is encoded in field quadratures rather than superpositions of discrete qudit states, temporal modes still serve an important purpose in SPOPOs. However, for these to work, continuous-variable operations must operate in a mode-selective fashion. Trep's group showed that QPG techniques can work as a mode-selective photon subtractor, a key non-Gaussian component of the continuous-variable toolkit [166–168]. Since the SPOPO emits squeezed light over many temporal modes, a mode-selective beam splitter is necessary to ensure that the heralded photon subtraction is matched to the desired temporal mode. Using a noncollinear frequency-degenerate phase matching in bulk bismuth borate (BiBO) supplemented with spectral filtering and shaped weak coherent states ($\bar{n} < 1$), Ra *et al.* were able to reconstruct the temporal-mode subtraction matrix in both the spectral bin and Hermite–Gauss basis [168], which characterizes the modal purity of the subtraction process. For a seven-dimensional HG superposition, the subtraction matrix was found to have a purity of 96% regardless of whether the signal was bright or on the single-photon level. Since the photon-subtraction method requires weak coupling in order to minimally disturb the quantum state, a QPG with a low efficiency (0.1%) was used, equivalent to a low-reflectivity beam splitter [166].

7. OUTLOOK AND CHALLENGES

We have shown that dispersion-engineered waveguides provide a capable toolbox for generating and measuring photon temporal modes. By constructing photon-pair sources simultaneously pure in both spatial and temporal degrees of freedom as shown in Section 3, it is possible to efficiently create pure heralded single photons, capable of providing the high-visibility quantum interference necessary for multiphoton quantum logic. By exploiting the group-velocity matching of these systems, it was also shown that the temporal shape and entangled structure of the temporal modes can be customized, providing a versatile resource for

quantum state engineering. In Section 4, it was shown that these same engineered techniques can be applied to sum-frequency generation, providing the necessary tools to manipulate and measure this structure. In Sections 5 and 6, we outlined the considerable experimental progress that has been made towards realizing this toolbox.

Many challenges remain to push toward practical application. Temporal-mode-selective devices have been demonstrated in the sub-picosecond or few-picosecond regime, where commercially available pulse shapers exist. Such time scales are natural for PDC processes, but come with difficult synchronization challenges for long-distance quantum communication or entanglement distribution. Moving to longer, less jitter-sensitive regimes through memory-based interfaces or resonant cavities [169] relaxes this concern, but increases the burden of pulse shaping. Four-wave mixing techniques have more complicated noise landscapes for quantum tasks, but offer considerably longer interaction lengths and are currently understudied for temporal-mode management. In all cases, for high-dimensional tasks, devices that isolate a single temporal mode are difficult to scale, requiring multiple shaped pulses and physical media to construct a multi-output measure. Techniques that demultiplex a set of pulsed temporal modes into spatial or spectral bins, equivalent to the orbital angular momentum mode sorter in space [170], are essential to scale these techniques to high-dimensional networks. A promising avenue for these temporal-mode demultiplexers is through multi-peak phase-matching structures [171,172].

By accessing the temporal mode structure of quantum light, we can open a new frontier in photonic quantum information science. By tailoring PDC sources to directly generate pure photon pairs, an important step towards scalable quantum networks has been taken. With measurements sensitive to the time-frequency structure in arbitrary phase-dependent bases, quantum pulse gates may open the door to novel ultrafast measurement schemes. We have outlined some of the significant advances that have been made in the past 10 years from numerous researchers across the globe. With an active and engaged community, we eagerly anticipate the next 10 years.

Funding. European Union's (EU) Horizon 2020 Framework Programme (H2020) (665148); Deutsche Forschungsgemeinschaft (DFG) (TRR 142); Natural Sciences and Engineering Research Council of Canada (NSERC).

Acknowledgment. The authors thank M. Santandrea, D. V. Reddy, H. Herrmann, and E. Meyer-Scott for useful discussions and suggestions.

REFERENCES

- W. Grice and I. Walmsley, "Spectral information and distinguishability in type-II down-conversion with a broadband pump," *Phys. Rev. A* **56**, 1627–1634 (1997).
- D. S. Hum and M. M. Fejer, "Quasi-phaseshifting," *C. R. Phys.* **8**, 180–198 (2007).
- C. K. Law, I. A. Walmsley, and J. H. Eberly, "Continuous frequency entanglement: effective finite Hilbert space and entropy control," *Phys. Rev. Lett.* **84**, 5304–5307 (2000).
- J. Ghalbouni, I. Agha, R. Frey, E. Diamanti, and I. Zaquine, "Experimental wavelength-division-multiplexed photon-pair distribution," *Opt. Lett.* **38**, 34–36 (2013).
- N. C. Menicucci, P. van Loock, M. Gu, C. Weedbrook, T. C. Ralph, and M. A. Nielsen, "Universal quantum computation with continuous-variable cluster states," *Phys. Rev. Lett.* **97**, 110501 (2006).
- M. Pysker, Y. Miwa, R. Shahrokhshahi, R. Bloomer, and O. Pfister, "Parallel generation of quadripartite cluster entanglement in the optical frequency comb," *Phys. Rev. Lett.* **107**, 030505 (2011).
- S. Yokoyama, R. Ukai, S. C. Armstrong, C. Sornphiphatphong, T. Kaji, S. Suzuki, J.-I. Yoshikawa, H. Yonezawa, N. C. Menicucci, and A. Furusawa, "Ultra-large-scale continuous-variable cluster states multiplexed in the time domain," *Nat. Photonics* **7**, 982–986 (2013).
- M. Chen, N. C. Menicucci, and O. Pfister, "Experimental realization of multipartite entanglement of 60 modes of a quantum optical frequency comb," *Phys. Rev. Lett.* **112**, 120505 (2014).
- G. J. De Valcarcel, G. Patera, N. Treps, and C. Fabre, "Multimode squeezing of frequency combs," *Phys. Rev. A* **74**, 061801 (2006).
- O. Pinel, P. Jian, R. M. de Araújo, J. Feng, B. Chalopin, C. Fabre, and N. Treps, "Generation and characterization of multimode quantum frequency combs," *Phys. Rev. Lett.* **108**, 083601 (2012).
- W. Wasilewski, A. I. Lvovsky, K. Banaszek, and C. Radzewicz, "Pulsed squeezed light: simultaneous squeezing of multiple modes," *Phys. Rev. A* **73**, 063819 (2006).
- G. Patera, C. Navarrete-Benlloch, G. J. de Valcarcel, and C. Fabre, "Quantum coherent control of highly multipartite continuous-variable entangled states by tailoring parametric interactions," *Eur. Phys. J. D* **66**, 1–14 (2012).
- J. Roslund, R. M. de Araújo, S. Jiang, C. Fabre, and N. Treps, "Wavelength-multiplexed quantum networks with ultrafast frequency combs," *Nat. Photonics* **8**, 109–112 (2014).
- S. Gerke, J. Sperling, W. Vogel, Y. Cai, J. Roslund, N. Treps, and C. Fabre, "Full multipartite entanglement of frequency-comb Gaussian states," *Phys. Rev. Lett.* **114**, 050501 (2015).
- H. Huang and J. H. Eberly, "Correlations and one-quantum pulse shapes in photon pair generation," *J. Mod. Opt.* **40**, 915–930 (1993).
- A. B. U'Ren, C. Silberhorn, K. Banaszek, I. A. Walmsley, R. Erdmann, W. P. Grice, and M. G. Raymer, "Generation of pure-state single-photon wavepackets by conditional preparation based on spontaneous parametric downconversion," *Laser Phys.* **15**, 146–161 (2005).
- Y. M. Mikhailova, P. Volkov, and M. Fedorov, "Biphoton wave packets in parametric down-conversion: spectral and temporal structure and degree of entanglement," *Phys. Rev. A* **78**, 062327 (2008).
- A. Christ, K. Laiho, A. Eckstein, K. N. Cassemiro, and C. Silberhorn, "Probing multimode squeezing with correlation functions," *New J. Phys.* **13**, 033027 (2011).
- A. Eckstein, A. Christ, P. J. Mosley, and C. Silberhorn, "Highly efficient single-pass source of pulsed single-mode twin beams of light," *Phys. Rev. Lett.* **106**, 013603 (2011).
- K. Wakui, Y. Eto, H. Benichi, S. Izumi, T. Yanagida, K. Ema, T. Numata, D. Fukuda, M. Takeoka, and M. Sasaki, "Ultrabroadband direct detection of nonclassical photon statistics at telecom wavelength," *Sci. Rep.* **4**, 4535 (2014).
- M. B. Nasr, B. E. Saleh, A. V. Sergienko, and M. C. Teich, "Demonstration of dispersion-canceled quantum-optical coherence tomography," *Phys. Rev. Lett.* **91**, 083601 (2003).
- V. Giovannetti, S. Lloyd, and L. Maccone, "Quantum-enhanced positioning and clock synchronization," *Nature* **412**, 417–419 (2001).
- V. Averchenko, D. Sych, G. Schunk, U. Vogl, C. Marquardt, and G. Leuchs, "Temporal shaping of single photons enabled by entanglement," *Phys. Rev. A* **96**, 043822 (2017).
- T. Keller and M. Rubin, "Theory of two-photon entanglement for spontaneous parametric down-conversion driven by a narrow pump pulse," *Phys. Rev. A* **56**, 1534–1541 (1997).
- R. Erdmann, D. Branning, W. Grice, and I. A. Walmsley, "Restoring dispersion cancellation for entangled photons produced by ultrashort pulses," *Phys. Rev. A* **62**, 053810 (2000).
- V. Giovannetti, L. Maccone, J. H. Shapiro, and F. N. C. Wong, "Extended phase-matching conditions for improved entanglement generation," *Phys. Rev. A* **66**, 043813 (2002).
- W. P. Grice, A. B. U'Ren, and I. A. Walmsley, "Eliminating frequency and space-time correlations in multiphoton states," *Phys. Rev. A* **64**, 063815 (2001).
- O. Kuzucu, M. Fiorentino, M. Albota, F. N. C. Wong, and F. Kärtner, "Two-photon coincident-frequency entanglement via extended phase matching," *Phys. Rev. Lett.* **94**, 083601 (2005).

29. T. Lutz, P. Kolenderski, and T. Jennewein, "Demonstration of spectral correlation control in a source of polarization-entangled photon pairs at telecom wavelength," *Opt. Lett.* **39**, 1481–1484 (2014).
30. V. Ansari, B. Brecht, G. Harder, and C. Silberhorn, "Probing spectral-temporal correlations with a versatile integrated source of parametric down-conversion states," arXiv:1404.7725 (2014).
31. R. S. Bennink, "Optimal collinear Gaussian beams for spontaneous parametric down-conversion," *Phys. Rev. A* **81**, 053805 (2010).
32. A. Valencia, A. Cere, X. Shi, G. Molina-Terriza, and J. P. Torres, "Shaping the waveform of entangled photons," *Phys. Rev. Lett.* **99**, 243601 (2007).
33. P. J. Mosley, J. S. Lundeen, B. J. Smith, P. Wasylczyk, A. B. U'Ren, C. Silberhorn, and I. A. Walmsley, "Heralded generation of ultrafast single photons in pure quantum states," *Phys. Rev. Lett.* **100**, 133601 (2008).
34. C. Hong, Z.-Y. Ou, and L. Mandel, "Measurement of subpicosecond time intervals between two photons by interference," *Phys. Rev. Lett.* **59**, 2044–2046 (1987).
35. O. Kuzucu, F. N. C. Wong, S. Kurimura, and S. Tovstonog, "Joint temporal density measurements for two-photon state characterization," *Phys. Rev. Lett.* **101**, 153602 (2008).
36. T. Gerrits, M. J. Stevens, B. Baek, B. Calkins, A. Lita, S. Glancy, E. Knill, S. W. Nam, R. P. Mirin, R. H. Hadfield, R. S. Bennink, W. P. Grice, S. Dorenbos, T. Zijlstra, T. Klapwijk, and V. Zwiller, "Generation of degenerate, factorizable, pulsed squeezed light at telecom wavelengths," *Opt. Express* **19**, 24434–24447 (2011).
37. G. Harder, V. Ansari, B. Brecht, T. Dirmeier, C. Marquardt, and C. Silberhorn, "An optimized photon pair source for quantum circuits," *Opt. Express* **21**, 13975–13985 (2013).
38. R.-B. Jin, R. Shimizu, K. Wakui, M. Fujiwara, T. Yamashita, S. Miki, H. Terai, Z. Wang, and M. Sasaki, "Pulsed Sagnac polarization-entangled photon source with a PPKTP crystal at telecom wavelength," *Opt. Express* **22**, 11498–11507 (2014).
39. M. M. Weston, H. M. Chrzanowski, S. Wollmann, A. Boston, J. Ho, L. K. Shalm, V. B. Verma, M. S. Allman, S. W. Nam, R. B. Patel, S. Slussarenko, and G. J. Pryde, "Efficient and pure femtosecond-pulse-length source of polarization-entangled photons," *Opt. Express* **24**, 10869–10879 (2016).
40. A. B. U'Ren, K. Banaszek, and I. A. Walmsley, "Photon engineering for quantum information processing," *Quantum Inf. Comput.* **3**, 480–502 (2003).
41. E. Meyer-Scott, N. Montaut, J. Tiedau, L. Sansoni, H. Herrmann, T. J. Bartley, and C. Silberhorn, "Limits on the heralding efficiencies and spectral purities of spectrally filtered single photons from photon-pair sources," *Phys. Rev. A* **95**, 061803 (2017).
42. J. Huang, X. Xie, C. Langrock, R. Roussev, D. Hum, and M. Fejer, "Amplitude modulation and apodization of quasi-phase-matched interactions," *Opt. Lett.* **31**, 604–606 (2006).
43. A. M. Brańczyk, A. Fedrizzi, T. M. Stace, T. C. Ralph, and A. G. White, "Engineered optical nonlinearity for quantum light sources," *Opt. Express* **19**, 55–65 (2011).
44. P. Ben Dixon, J. H. Shapiro, and F. N. C. Wong, "Spectral engineering by Gaussian phase-matching for quantum photonics," *Opt. Express* **21**, 5879–5890 (2013).
45. C. Chen, C. Bo, M. Y. Niu, F. Xu, Z. Zhang, J. H. Shapiro, and F. N. C. Wong, "Efficient generation and characterization of spectrally factorable biphotons," *Opt. Express* **25**, 7300–7312 (2017).
46. A. Dosseva, L. Cincio, and A. M. Brańczyk, "Shaping the joint spectrum of down-converted photons through optimized custom poling," *Phys. Rev. A* **93**, 013801 (2016).
47. J.-L. Tambasco, A. Boes, L. G. Helt, M. J. Steel, and A. Mitchell, "Domain engineering algorithm for practical and effective photon sources," *Opt. Express* **24**, 19616–19626 (2016).
48. F. Graffitti, D. Kundys, D. T. Reid, A. M. Brańczyk, and A. Fedrizzi, "Pure down-conversion photons through sub-coherence-length domain engineering," *Quantum Sci. Technol.* **2**, 035001 (2017).
49. F. Graffitti, P. Barrow, M. Proietti, D. Kundys, and A. Fedrizzi, "Independent high-purity photons created in domain-engineered crystals," arXiv:1712.07140 (2017).
50. V. Ansari, E. Roccia, M. Santandrea, M. Doostdar, C. Eigner, L. Padberg, I. Gianani, M. Sbroscia, J. M. Donohue, L. Mancino, M. Barbieri, and C. Silberhorn, "Heralded generation of high-purity ultra-short single photons in programmable temporal shapes," *Opt. Express* **26**, 2764–2774 (2018).
51. B. Brecht, D. V. Reddy, C. Silberhorn, and M. G. Raymer, "Photon temporal modes: a complete framework for quantum information science," *Phys. Rev. X* **5**, 041017 (2015).
52. A. M. Weiner, "Femtosecond pulse shaping using spatial light modulators," *Rev. Sci. Instrum.* **71**, 1929–1960 (2000).
53. A. Christ, B. Brecht, W. Mauere, and C. Silberhorn, "Theory of quantum frequency conversion and type-II parametric down-conversion in the high-gain regime," *New J. Phys.* **15**, 053038 (2013).
54. N. Quesada and J. E. Sipe, "Time-ordering effects in the generation of entangled photons using nonlinear optical processes," *Phys. Rev. Lett.* **114**, 093903 (2015).
55. S. Lemieux, M. Manceau, P. R. Sharapova, O. V. Tikhonova, R. W. Boyd, G. Leuchs, and M. V. Chekhova, "Engineering the frequency spectrum of bright squeezed vacuum via group velocity dispersion in an SU(1, 1) interferometer," *Phys. Rev. Lett.* **117**, 183601 (2016).
56. G. Harder, T. J. Bartley, A. E. Lita, S. W. Nam, T. Gerrits, and C. Silberhorn, "Single-mode parametric-down-conversion states with 50 photons as a source for mesoscopic quantum optics," *Phys. Rev. Lett.* **116**, 143601 (2016).
57. G. Harder, V. Ansari, T. J. Bartley, B. Brecht, and C. Silberhorn, "Harnessing temporal modes for multi-photon quantum information processing based on integrated optics," *Philos. Trans. A Math. Phys. Eng. Sci.* **375**, 20160244 (2017).
58. P. Kumar, "Quantum frequency conversion," *Opt. Lett.* **15**, 1476–1478 (1990).
59. J. Huang and P. Kumar, "Observation of quantum frequency conversion," *Phys. Rev. Lett.* **68**, 2153–2156 (1992).
60. C. E. Vollmer, C. Baune, A. Sambrowski, T. Eberle, V. Händchen, J. Fiurášek, and R. Schnabel, "Quantum up-conversion of squeezed vacuum states from 1550 to 532 nm," *Phys. Rev. Lett.* **112**, 073602 (2014).
61. C. Baune, J. Gniesmer, A. Schönbeck, C. E. Vollmer, J. Fiurášek, and R. Schnabel, "Strongly squeezed states at 532 nm based on frequency up-conversion," *Opt. Express* **23**, 16035–16041 (2015).
62. W. Liu, N. Wang, Z. Li, and Y. Li, "Quantum frequency up-conversion of continuous variable entangled states," *Appl. Phys. Lett.* **107**, 231109 (2015).
63. S. Tanzilli, W. Tittel, M. Halder, O. Alibart, P. Baldi, N. Gisin, and H. Zbinden, "A photonic quantum information interface," *Nature* **437**, 116–120 (2005).
64. T. Honjo, H. Takesue, H. Kamada, Y. Nishida, O. Tadanaga, M. Asobe, and K. Inoue, "Long-distance distribution of time-bin entangled photon pairs over 100 km using frequency up-conversion detectors," *Opt. Express* **15**, 13957–13964 (2007).
65. K. De Greve, L. Yu, P. L. McMahon, J. S. Pelc, C. M. Natarajan, N. Y. Kim, E. Abe, S. Maier, C. Schneider, M. Kamp, S. Höfling, R. H. Hadfield, A. Forchel, M. M. Fejer, and Y. Yamamoto, "Quantum-dot spin-photon entanglement via frequency downconversion to telecom wavelength," *Nature* **491**, 421–425 (2012).
66. S. RameLOW, A. Fedrizzi, A. Poppe, N. K. Langford, and A. Zeilinger, "Polarization-entanglement-conserving frequency conversion of photons," *Phys. Rev. A* **85**, 013845 (2012).
67. S. Zaske, A. Lenhard, C. A. Keßler, J. Kettler, C. Hepp, C. Arend, R. Albrecht, W.-M. Schulz, M. Jetter, P. Michler, and C. Becher, "Visible-to-telecom quantum frequency conversion of light from a single quantum emitter," *Phys. Rev. Lett.* **109**, 147404 (2012).
68. S. Ates, I. Agha, A. Gulinatti, I. Rech, M. T. Rakher, A. Badolato, and K. Srinivasan, "Two-photon interference using background-free quantum frequency conversion of single photons emitted by an InAs quantum dot," *Phys. Rev. Lett.* **109**, 147405 (2012).
69. M. T. Rakher, L. Ma, O. Slattery, X. Tang, and K. Srinivasan, "Quantum transduction of telecommunications-band single photons from a quantum dot by frequency upconversion," *Nat. Photonics* **4**, 786–791 (2010).
70. H. J. McGuinness, M. G. Raymer, C. J. McKinstrie, and S. Radic, "Quantum frequency translation of single-photon states in a photonic crystal fiber," *Phys. Rev. Lett.* **105**, 093604 (2010).
71. A. P. Vandevender and P. G. Kwiat, "High efficiency single photon detection via frequency up-conversion," *J. Mod. Opt.* **51**, 1433–1445 (2004).
72. A. P. VanDevender and P. G. Kwiat, "Quantum transduction via frequency upconversion," *J. Opt. Soc. Am. B* **24**, 295–299 (2007).
73. J. S. Pelc, L. Ma, C. R. Phillips, Q. Zhang, C. Langrock, O. Slattery, X. Tang, and M. M. Fejer, "Long-wavelength-pumped upconversion single-photon detector at 1550 nm: performance and noise analysis," *Opt. Express* **19**, 21445–21456 (2011).

74. M. A. Albota and F. N. Wong, "Efficient single-photon counting at 1.55 μm by means of frequency upconversion," *Opt. Lett.* **29**, 1449–1451 (2004).
75. R. V. Roussev, C. Langrock, J. R. Kurz, and M. Fejer, "Periodically poled lithium niobate waveguide sum-frequency generator for efficient single-photon detection at communication wavelengths," *Opt. Lett.* **29**, 1518–1520 (2004).
76. C. Langrock, E. Diamanti, R. V. Roussev, Y. Yamamoto, M. M. Fejer, and H. Takesue, "Highly efficient single-photon detection at communication wavelengths by use of upconversion in reverse-proton-exchanged periodically poled LiNbO₃ waveguides," *Opt. Lett.* **30**, 1725–1727 (2005).
77. R. T. Thew, S. Tanzilli, L. Krainer, S. Zeller, A. Rochas, I. Rech, S. Cova, H. Zbinden, and N. Gisin, "Low jitter up-conversion detectors for telecom wavelength GHz QKD," *New J. Phys.* **8**, 32 (2006).
78. M. Legré, R. Thew, H. Zbinden, and N. Gisin, "High resolution optical time domain reflectometer based on 1.55 μm up-conversion photon-counting module," *Opt. Express* **15**, 8237–8242 (2007).
79. G. Giorgi, P. Mataloni, and F. De Martini, "Frequency hopping in quantum interferometry: efficient up-down conversion for qubits and ebits," *Phys. Rev. Lett.* **90**, 027902 (2003).
80. Y. Ding and Z. Ou, "Frequency downconversion for a quantum network," *Opt. Lett.* **35**, 2591–2593 (2010).
81. H. Takesue, "Single-photon frequency down-conversion experiment," *Phys. Rev. A* **82**, 013833 (2010).
82. R. Ikuta, Y. Kusaka, T. Kitano, H. Kato, T. Yamamoto, M. Koashi, and N. Imoto, "Wide-band quantum interface for visible-to-telecommunication wavelength conversion," *Nat. Commun.* **2**, 1544 (2011).
83. N. Curtz, R. Thew, C. Simon, N. Gisin, and H. Zbinden, "Coherent frequency-down-conversion interface for quantum repeaters," *Opt. Express* **18**, 22099–22104 (2010).
84. R. Ikuta, T. Kobayashi, S. Yasui, S. Miki, T. Yamashita, H. Terai, M. Fujiwara, T. Yamamoto, M. Koashi, M. Sasaki, Z. Wang, and N. Imoto, "Frequency down-conversion of 637 nm light to the telecommunication band for non-classical light emitted from NV centers in diamond," *Opt. Express* **22**, 11205–11214 (2014).
85. P. S. Kuo, J. S. Pelc, O. Slattery, Y.-S. Kim, M. M. Fejer, and X. Tang, "Reducing noise in single-photon-level frequency conversion," *Opt. Lett.* **38**, 1310–1312 (2013).
86. Y.-H. Cheng, T. Thomay, G. S. Solomon, A. L. Migdall, and S. V. Polyakov, "Statistically background-free, phase-preserving parametric up-conversion with faint light," *Opt. Express* **23**, 18671–18678 (2015).
87. F. Steinlechner, N. Hermosa, V. Pruneri, and J. P. Torres, "Frequency conversion of structured light," *Sci. Rep.* **6**, 21390 (2016).
88. H. Rütz, K.-H. Luo, H. Suche, and C. Silberhorn, "Quantum frequency conversion between infrared and ultraviolet," *Phys. Rev. Appl.* **7**, 024021 (2017).
89. N. Maring, P. Farrera, K. Kutluer, M. Mazzer, G. Heinze, and H. de Riedmatten, "Photonic quantum state transfer between a cold atomic gas and a crystal," *Nature* **551**, 485–488 (2017).
90. M. Raymer, S. van Enk, C. McKinstrie, and H. McGuinness, "Interference of two photons of different color," *Opt. Commun.* **283**, 747–752 (2010).
91. S. Clemmen, A. Farsi, S. Ramelow, and A. L. Gaeta, "Ramsey interference with single photons," *Phys. Rev. Lett.* **117**, 223601 (2016).
92. T. Kobayashi, R. Ikuta, S. Yasui, S. Miki, T. Yamashita, H. Terai, T. Yamamoto, M. Koashi, and N. Imoto, "Frequency-domain Hong-Ou-Mandel interference," *Nat. Photonics* **10**, 441–444 (2016).
93. A. Eckstein, B. Brecht, and C. Silberhorn, "A quantum pulse gate based on spectrally engineered sum frequency generation," *Opt. Express* **19**, 13770–13778 (2011).
94. B. Brecht, A. Eckstein, and C. Silberhorn, "Controlling the correlations in frequency upconversion in PPLN and PPKTP waveguides," *Phys. Status Solidi C* **8**, 1235–1238 (2011).
95. D. V. Reddy, M. G. Raymer, C. J. McKinstrie, L. Mejling, and K. Rottwitz, "Temporal mode selectivity by frequency conversion in second-order nonlinear optical waveguides," *Opt. Express* **21**, 13840–13863 (2013).
96. N. Quesada and J. E. Sipe, "Effects of time ordering in quantum nonlinear optics," *Phys. Rev. A* **90**, 1–13 (2014).
97. D. V. Reddy, M. G. Raymer, and C. J. McKinstrie, "Efficient sorting of quantum-optical wave packets by temporal-mode interferometry," *Opt. Lett.* **39**, 2924–2927 (2014).
98. P. Manurkar, N. Jain, M. Silver, Y.-P. Huang, C. Langrock, M. M. Fejer, P. Kumar, and G. S. Kanter, "Multidimensional mode-separable frequency conversion for high-speed quantum communication," *Optica* **3**, 1300–1307 (2016).
99. B. Brecht, A. Eckstein, R. Ricken, V. Quiring, H. Suche, L. Sansoni, and C. Silberhorn, "Demonstration of coherent time-frequency Schmidt mode selection using dispersion-engineered frequency conversion," *Phys. Rev. A* **90**, 030302 (2014).
100. A. S. Kowligy, P. Manurkar, N. V. Corzo, V. G. Velev, M. Silver, R. P. Scott, S. J. B. Yoo, P. Kumar, G. S. Kanter, and Y.-P. Huang, "Quantum optical arbitrary waveform manipulation and measurement in real time," *Opt. Express* **22**, 27942–27957 (2014).
101. J. A. Salehi, A. M. Weiner, and J. P. Heritage, "Coherent ultrashort light pulse code-division multiple access communication systems," *J. Lightwave Technol.* **8**, 478–491 (1990).
102. Z. Zheng and A. Weiner, "Spectral phase correlation of coded femtosecond pulses by second-harmonic generation in thick nonlinear crystals," *Opt. Lett.* **25**, 984–986 (2000).
103. Z. Zheng, A. Weiner, K. Parameswaran, M. Chou, and M. Fejer, "Low-power spectral phase correlator using periodically poled LiNbO₃ waveguides," *IEEE Photon. Technol. Lett.* **13**, 376–378 (2001).
104. J. M. Lukens, A. Dezfouliyan, C. Langrock, M. M. Fejer, D. E. Leaird, and A. M. Weiner, "Orthogonal spectral coding of entangled photons," *Phys. Rev. Lett.* **112**, 133602 (2014).
105. V. Ansari, J. M. Donohue, M. Allgaier, L. Sansoni, B. Brecht, J. Roslund, N. Treps, G. Harder, and C. Silberhorn, "Tomography and purification of the temporal-mode structure of quantum light," *arXiv 1607.03001* (2018).
106. Y.-P. Huang and P. Kumar, "Mode-resolved photon counting via cascaded quantum frequency conversion," *Opt. Lett.* **38**, 468–470 (2013).
107. P. Manurkar, N. Jain, P. Kumar, and G. S. Kanter, "Programmable optical waveform reshaping on a picosecond timescale," *Opt. Lett.* **42**, 951–954 (2017).
108. A. Shahverdi, Y. M. Sua, L. Tume, and Y.-P. Huang, "Quantum parametric mode sorting: beating the time-frequency filtering," *Sci. Rep.* **7**, 6495 (2017).
109. D. V. Reddy and M. G. Raymer, "Engineering temporal-mode-selective frequency conversion in nonlinear optical waveguides: from theory to experiment," *Opt. Express* **25**, 12952–12966 (2017).
110. D. V. Reddy and M. G. Raymer, "High-selectivity quantum pulse gating of photonic temporal modes using all-optical Ramsey interferometry," *Optica* **5**, 423–428 (2018).
111. D. V. Reddy, M. G. Raymer, and C. J. McKinstrie, "Sorting photon wave packets using temporal-mode interferometry based on multiple-stage quantum frequency conversion," *Phys. Rev. A* **91**, 012323 (2015).
112. N. Quesada and J. E. Sipe, "High efficiency in mode-selective frequency conversion," *Opt. Lett.* **41**, 364–367 (2016).
113. J. Nunn, I. Walmsley, M. Raymer, K. Surmacz, F. Waldermann, Z. Wang, and D. Jaksch, "Mapping broadband single-photon wave packets into an atomic memory," *Phys. Rev. A* **75**, 011401 (2007).
114. Z. Zheng, O. Mishina, N. Treps, and C. Fabre, "Atomic quantum memory for multimode frequency combs," *Phys. Rev. A* **91**, 031802 (2015).
115. K. A. G. Fisher, D. G. England, J.-P. W. MacLean, P. J. Bustard, K. J. Resch, and B. J. Sussman, "Frequency and bandwidth conversion of single photons in a room-temperature diamond quantum memory," *Nat. Commun.* **7**, 11200 (2016).
116. P. J. Bustard, D. G. England, K. Heshami, C. Kupchak, and B. J. Sussman, "Quantum frequency conversion with ultra-broadband tuning in a Raman memory," *Phys. Rev. A* **95**, 053816 (2017).
117. J. H. Munns, S. Park, B. Brecht, and I. A. Walmsley, "Temporal amplitude & phase: algorithmic reconstruction via time-domain interferometry (teAPARTI)," in *Frontiers in Optics* (Optical Society of America, 2017), paper JW3A-34.
118. J. Nunn, J. H. D. Munns, S. Thomas, K. T. Kaczmarek, C. Qiu, A. Feizpour, E. Poem, B. Brecht, D. J. Saunders, P. M. Ledingham, D. V. Reddy, M. G. Raymer, and I. A. Walmsley, "Theory of noise suppression in λ -type quantum memories by means of a cavity," *Phys. Rev. A* **96**, 012338 (2017).

119. D. Kielpinski, J. F. Corney, and H. M. Wiseman, "Quantum optical waveform conversion," *Phys. Rev. Lett.* **106**, 130501 (2011).
120. I. Agha, S. Ates, L. Sapienza, and K. Srinivasan, "Spectral broadening and shaping of nanosecond pulses: toward shaping of single photons from quantum emitters," *Opt. Lett.* **39**, 5677–5680 (2014).
121. G. Heinze, H. de Riedmatten, K. Kutluer, M. Mazzer, N. Maring, and P. Farrera, "Photonic quantum state transfer between a cold atomic gas and a crystal," *Nature* **551**, 485–488 (2017).
122. M. Allgaier, V. Ansari, C. Eigner, V. Quiring, R. Ricken, J. M. Donohue, T. Czerniuk, M. Alßmann, M. Bayer, B. Brecht, and C. Silberhorn, "Streak camera imaging of single photons at telecom wavelength," *Appl. Phys. Lett.* **112**, 031110 (2018).
123. J.-P. W. MacLean, J. M. Donohue, and K. J. Resch, "Direct characterization of ultrafast energy-time entangled photon pairs," *Phys. Rev. Lett.* **120**, 053601 (2018).
124. J. M. Donohue, J. Lavoie, and K. J. Resch, "Ultrafast time-division demultiplexing of polarization-entangled photons," *Phys. Rev. Lett.* **113**, 163602 (2014).
125. B. H. Kolner and M. Nazarathy, "Temporal imaging with a time lens," *Opt. Lett.* **14**, 630–632 (1989).
126. C. Bennett, R. Scott, and B. Kolner, "Temporal magnification and reversal of 100 Gb/s optical data with an up-conversion time microscope," *Appl. Phys. Lett.* **65**, 2513–2515 (1994).
127. J. Lavoie, J. M. Donohue, L. G. Wright, A. Fedrizzi, and K. J. Resch, "Spectral compression of single photons," *Nat. Photonics* **7**, 363–366 (2013).
128. J. M. Donohue, M. Mastrovich, and K. J. Resch, "Spectrally engineering photonic entanglement with a time lens," *Phys. Rev. Lett.* **117**, 1–15 (2016).
129. J. M. Donohue, M. D. Mazurek, and K. J. Resch, "Theory of high-efficiency sum-frequency generation for single-photon waveform conversion," *Phys. Rev. A* **91**, 1–11 (2015).
130. G. Patera and M. I. Kolobov, "Temporal imaging with squeezed light," *Opt. Lett.* **40**, 1125–1128 (2015).
131. R. Salem, M. A. Foster, A. C. Turner, D. F. Geraghty, M. Lipson, and A. L. Gaeta, "Optical time lens based on four-wave mixing on a silicon chip," *Opt. Lett.* **33**, 1047–1049 (2008).
132. J. Shi, G. Patera, M. I. Kolobov, and S. Han, "Quantum temporal imaging by four-wave mixing," *Opt. Lett.* **42**, 3121–3124 (2017).
133. M. Karpiński, M. Jachura, L. J. Wright, and B. J. Smith, "Bandwidth manipulation of quantum light by an electro-optic time lens," *Nat. Photonics* **11**, 53–57 (2016).
134. L. J. Wright, M. Karpiński, C. Söller, and B. J. Smith, "Spectral shearing of quantum light pulses by electro-optic phase modulation," *Phys. Rev. Lett.* **118**, 023601 (2017).
135. S. Mittal, V. V. Orre, A. Restelli, R. Salem, E. A. Goldschmidt, and M. Hafezi, "Temporal and spectral manipulations of correlated photons using a time lens," *Phys. Rev. A* **96**, 043807 (2017).
136. N. Matsuda, "Deterministic reshaping of single-photon spectra using cross-phase modulation," *Sci. Adv.* **2**, e1501223 (2016).
137. S. Bandyopadhyay, P. O. Boykin, V. Roychowdhury, and F. Vatan, "A new proof for the existence of mutually unbiased bases," *Algorithmica* **34**, 512–528 (2002).
138. W. K. Wootters and B. D. Fields, "Optimal state-determination by mutually unbiased measurements," *Ann. Phys.* **191**, 363–381 (1989).
139. S. J. Nowierski, N. N. Oza, P. Kumar, and G. S. Kanter, "Tomographic reconstruction of time-bin-entangled qudits," *Phys. Rev. A* **94**, 042328 (2016).
140. S. Schwarz, B. Bessire, and A. Stefanov, "Experimental violation of a d-dimensional Bell inequality using energy-time entangled photons," *Int. J. Quantum Inf.* **12**, 1560026 (2014).
141. M. Kues, C. Reimer, P. Roztocky, L. R. Cortés, S. Sciara, B. Wetzell, Y. Zhang, A. Cino, S. T. Chu, B. E. Little, D. J. Moss, L. Caspani, J. Azaña, and R. Morandotti, "On-chip generation of high-dimensional entangled quantum states and their coherent control," *Nature* **546**, 622–626 (2017).
142. M. Agnew, J. Leach, M. McLaren, F. S. Roux, and R. W. Boyd, "Tomography of the quantum state of photons entangled in high dimensions," *Phys. Rev. A* **84**, 062101 (2011).
143. J. M. Arrazola, O. Gittsovich, and N. Lütkenhaus, "Accessible nonlinear entanglement witnesses," *Phys. Rev. A* **85**, 062327 (2012).
144. M. Krenn, M. Huber, R. Fickler, R. Lapkiewicz, S. Ramelow, and A. Zeilinger, "Generation and confirmation of a (100 × 100)-dimensional entangled quantum system," *Proc. Natl. Acad. Sci. USA* **111**, 6243–6247 (2014).
145. Z. Huang, L. Maccone, A. Karim, C. Macchiavello, R. J. Chapman, and A. Peruzzo, "High-dimensional entanglement certification," *Sci. Rep.* **6**, 27637 (2016).
146. P. Erker, M. Krenn, and M. Huber, "Quantifying high dimensional entanglement with two mutually unbiased bases," *Quantum* **1**, 22 (2017).
147. W. Tittel, J. Brendel, H. Zbinden, and N. Gisin, "Violation of Bell inequalities by photons more than 10 km apart," *Phys. Rev. Lett.* **81**, 3563–3566 (1998).
148. I. Marcikic, H. De Riedmatten, W. Tittel, H. Zbinden, M. Legré, and N. Gisin, "Distribution of time-bin entangled qubits over 50 km of optical fiber," *Phys. Rev. Lett.* **93**, 180502 (2004).
149. R. Valivarthi, Q. Zhou, G. H. Aguilar, V. B. Verma, F. Marsili, M. D. Shaw, S. W. Nam, D. Oblak, and W. Tittel, "Quantum teleportation across a metropolitan fibre network," *Nat. Photonics* **10**, 676–680 (2016).
150. A. Muller, T. Herzog, B. Huttner, W. Tittel, H. Zbinden, and N. Gisin, "Plug-and-play systems for quantum cryptography," *Appl. Phys. Lett.* **70**, 793–795 (1997).
151. T. Zhong, H. Zhou, R. D. Horansky, C. Lee, V. B. Verma, A. E. Lita, A. Restelli, J. C. Bienfang, R. P. Mirin, T. Gerrits, S. W. Nam, F. Marsili, M. D. Shaw, Z. Zhang, L. Wang, D. Englund, G. W. Wornell, J. H. Shapiro, and F. N. C. Wong, "Photon-efficient quantum key distribution using time-energy entanglement with high-dimensional encoding," *New J. Phys.* **17**, 022002 (2015).
152. Z. Xie, T. Zhong, S. Shrestha, X. Xu, J. Liang, Y.-X. Gong, J. C. Bienfang, A. Restelli, J. H. Shapiro, F. N. Wong, and C. W. Wong, "Harnessing high-dimensional hyperentanglement through a biphoton frequency comb," *Nat. Photonics* **9**, 536–542 (2015).
153. T. Ikuta and H. Takesue, "Four-dimensional entanglement distribution over 100 km," *Sci. Rep.* **8**, 817 (2018).
154. J. D. Franson, "Bell inequality for position and time," *Phys. Rev. Lett.* **62**, 2205–2208 (1989).
155. R. T. Thew, A. Acin, H. Zbinden, and N. Gisin, "Bell-type test of energy-time entangled qutrits," *Phys. Rev. Lett.* **93**, 010503 (2004).
156. J. M. Donohue, M. Agnew, J. Lavoie, and K. J. Resch, "Coherent ultrafast measurement of time-bin encoded photons," *Phys. Rev. Lett.* **111**, 153602 (2013).
157. K. A. O'Donnell and A. B. U'Ren, "Time-resolved up-conversion of entangled photon pairs," *Phys. Rev. Lett.* **103**, 123602 (2009).
158. A. Pe'er, B. Dayan, A. A. Friesem, and Y. Silberberg, "Temporal shaping of entangled photons," *Phys. Rev. Lett.* **94**, 073601 (2005).
159. L. Olislager, J. Cussey, A. T. Nguyen, P. Emplit, S. Massar, J.-M. Merolla, and K. P. Huy, "Frequency-bin entangled photons," *Phys. Rev. A* **82**, 013804 (2010).
160. J. A. Jaramillo-Villegas, P. Imany, O. D. Odele, D. E. Leaird, Z.-Y. Ou, M. Qi, and A. M. Weiner, "Persistent energy-time entanglement covering multiple resonances of an on-chip biphoton frequency comb," *Optica* **4**, 655–658 (2017).
161. J. M. Lukens and P. Lougovski, "Frequency-encoded photonic qubits for scalable quantum information processing," *Optica* **4**, 8–16 (2017).
162. H.-H. Lu, J. M. Lukens, N. A. Peters, O. D. Odele, D. E. Leaird, A. M. Weiner, and P. Lougovski, "Electro-optic frequency beamsplitters and tritters for high-fidelity photonic quantum information processing," *Phys. Rev. Lett.* **120**, 030502 (2018).
163. M. Grimau Puigibert, G. Aguilar, Q. Zhou, F. Marsili, M. Shaw, V. Verma, S. Nam, D. Oblak, and W. Tittel, "Heralded single photons based on spectral multiplexing and feed-forward control," *Phys. Rev. Lett.* **119**, 083601 (2017).
164. M. Allgaier, V. Ansari, L. Sansoni, C. Eigner, V. Quiring, R. Ricken, G. Harder, B. Brecht, and C. Silberhorn, "Highly efficient frequency conversion with bandwidth compression of quantum light," *Nat. Commun.* **8**, 14288 (2017).
165. V. Ansari, G. Harder, M. Allgaier, B. Brecht, and C. Silberhorn, "Temporal-mode measurement tomography of a quantum pulse gate," *Phys. Rev. A* **96**, 063817 (2017).

166. V. A. Averchenko, V. Thiel, and N. Treps, "Non-linear photon subtraction from a multimode quantum field," *Phys. Rev. A* **89**, 063808 (2014).
167. V. Averchenko, C. Jacquard, V. Thiel, C. Fabre, and N. Treps, "Multimode theory of single-photon subtraction," *New J. Phys.* **18**, 083042 (2016).
168. Y.-S. Ra, C. Jacquard, A. Dufour, C. Fabre, and N. Treps, "Tomography of a mode-tunable coherent single-photon subtractor," *Phys. Rev. X* **7**, 031012 (2017).
169. D. V. Reddy and M. G. Raymer, "Photonic temporal-mode multiplexing by quantum frequency conversion in a dichroic-finesse cavity," arXiv:1708.01705 (2017).
170. G. C. Berkhout, M. P. Lavery, J. Courtial, M. W. Beijersbergen, and M. J. Padgett, "Efficient sorting of orbital angular momentum states of light," *Phys. Rev. Lett.* **105**, 153601 (2010).
171. M. Asobe, O. Tadanaga, H. Miyazawa, Y. Nishida, and H. Suzuki, "Multiple quasi-phase-matched LiNbO₃ wavelength converter with a continuously phase-modulated domain structure," *Opt. Lett.* **28**, 558–560 (2003).
172. M. Silver, P. Manurkar, Y.-P. Huang, C. Langrock, M. M. Fejer, P. Kumar, and G. S. Kanter, "Spectrally multiplexed upconversion detection with C-band pump and signal wavelengths," *IEEE Photon. Technol. Lett.* **29**, 1097–1100 (2017).